Karlsruher Institut für Technologie

IEKP-KA/2013-1

Entwicklung von neuen Sensorkonzepten und Untersuchungen an strahlenharten Silizium-streifensensoren für CMS am Large Hadron Collider in der Hochluminositätsphase

Karl-Heinz Hoffmann

Zur Erlangung des akademischen Grades eines
DOKTORS DER NATURWISSENSCHAFTEN
von der Fakultät für Physik des
Karlsruher Institut für Technologie (KIT)

genehmigte

DISSERTATION

von

Dipl.-Phys. Karl-Heinz Hoffmann
aus Temeschburg

Tag der mündlichen Prüfung: 01.02.2013

Referent: Prof. Dr. Thomas Müller, Institut für Experimentelle Kernphysik
Korreferent: Prof. Dr. Willem de Boer, Institut für Experimentelle Kernphysik

Deutsche Zusammenfassung

Das Standardmodell der Teilchenphysik beschreibt die Elementarteilchen und ihre Wechselwirkungen in einer zusammenfassenden Theorie. Es wurde in den letzten Jahren durch zahlreiche Experimente untersucht und bestätigt. Trotzdem gibt es noch einige offene Fragen. Um diese Fragen zu klären, wurde der Large Hadron Collider LHC am CERN[1] gebaut. Der Teilchenbeschleuniger wird Protonen mit einer Schwerpunktsenergie von bis zu 14 TeV an vier Wechselwirkungspunkten zur Kollision bringen. Einer von vier Teilchendetektoren am LHC ist der Compact Muon Solenoid (CMS). Der Detektor besteht unter anderem aus einem hochauflösenden Spurdetektor aus Siliziumpixel- und Siliziumstreifensensoren mit ca. 206 m^2 aktiver Sensorfläche. Die Streifensensoren werden über die geplante Laufzeit einer Strahlenbelastung mit Fluenzen von bis zu 2×10^{14} n_{eq} cm^{-2} ausgesetzt sein. Ein Upgrade des seit 2010 mit stetig steigender Schwerpunktsenergie und Luminosität laufenden LHC ist bereits in Planung, wobei es dann zu einer Luminositätssteigerung um einen Faktor fünf bis zehn, auf 10^{35} $cm^{-2}s^{-1}$ kommen soll. Um bei der damit verbundenen höheren Teilchenspurdichte und den gesteigerten Fluenz zuverlässig zu funktionieren, benötigt der Spurdetektor strahlenhärtere Sensoren und neue Sensorkonzepte.

Strahlenschäden im Silizium verändern die Sensoreigenschaften und vermindern die Sensorqualität. Die effektive Dotierung der Sensoren ändert sich, was bei hohen Fluenzen zu einer Erhöhung der Depletionsspannung führt. Der Leckstrom nimmt zu und die Ladungssammlung wird auf Grund von Ladungsträgereinfang und der erhöhten Depletionsspannung, falls diese die maximale Versorgungsspannung überschreitet, reduziert. Des Weiteren hat das Ausheilen der Strahlenschäden einen Einfluss auf die Sensoreigenschaften.

Ein Teil dieser Arbeit ist die Untersuchung unterschiedlicher Siliziumstreifensensoren vor und nach Bestrahlung, sowie zwischen den Ausheilschritten. Die Sensoren wurden auf diversen Siliziummaterialien und in verschiedenen Dicken von einem einzigen Hersteller produziert. Neben n-Typ Silizium wurde auch p-Typ Silizium (mit zwei verschiedenen Streifenisolationstechniken) untersucht. Die Sensoren wurden mit Protonen und Neutronen entsprechend den erwarteten Fluenzen für den Spurdetektor bestrahlt.

Neben den Sensorgrößen Leckstrom und Depletionsspannung wurden Streifenparameter wie Streifenleckstrom, Biaswiderstand, Kopplungskapazität, Leckstrom über das Oxid, Zwischenstreifenwiderstand und -kapazität bestimmt. Mit einer Sr90-Quelle wurden die Ladungssammlung und das Signal-zu-Rausch-Verhältnis und deren Entwicklung überprüft.

Die meisten Streifenparameter zeigten keine nennenswerten Änderungen, lediglich der Zwischenstreifenwiderstand fiel stark ab, blieb jedoch noch ausreichend hoch, um eine gute Streifenisolierung zu gewährleisten. Damit konnte gezeigt werden, dass beide für p-Typ Silizium angewendeten Isolationstechniken bis zu den hier erreichten Fluenzen eingesetzt werden können. Der temperaturabhängige Leckstrom stieg für alle Sensoren an und zeigte dabei etwas höhere Werte als aus einer Studie an Dioden erwartet wurde. Daher lässt sich abschätzen, dass der Energieverbrauch eines Spurdetektors höher sein wird als bisher angenommen und eine ausreichende Kühlung des Spurdetektors benötigt wird. Die Depletionsspannung steigt besonders für die 300 µm dicken Sensoren

[1] Conseil Européen pour la Recherche Nucléaire

rasch an und führt zu einer Reduzierung der Ladungssammlung und damit auch des Signal-zu-Rausch-Verhältnisses. Dennoch zeigen diese Sensoren auch bei den hier erreichten Fluenzen noch vergleichbare Werte für die Ladungssammlung und das Signal-zu-Rausch-Verhältnis wie die 200 µm Sensoren. Besonders die 300 µm p-Typ Sensoren funktionieren auch nach längeren Ausheilzeiten noch gut, vergleichbar wie die dünnen Sensoren, während die Werte für den 300 µm n-Typ Sensor hingegen stark abfallen.
Da die Untersuchungen noch für höhere Fluenzen fortgesetzt werden, kann eine endgültige Auswahl allerdings noch nicht getroffen werden. Zusammenfassend kann gesagt werden, dass für die hier maximale Fluenz von 1.5×10^{15} n_{eq} cm^{-2}, was einem radialen Abstand vom Wechselwirkungspunkt bei CMS von 20 cm entspricht, die 300 µm p-Typ Sensoren ausreichend gut funktionieren.
Ein weiterer Teil dieser Arbeit ist die Untersuchung einer neuen Sensorgeometrie, um der erhöhten Spurdichte nach dem Upgrade gerecht zu werden. Dazu wurde ein Sensor entworfen und produziert, der über eine vierfache Streifensegmentierung verfügt und dabei die Sensorauslese weiterhin am Sensorrand stattfindet. Der in zwei identische Hälften aufgeteilte Sensor verfügt im zentralen Sensorbereich über Streifen, deren Signal über Aluminiumauslesestreifen zum Sensorrand geführt werden. Bei den Signalmessungen mit Quelle und Laser wurde ein ungewolltes Signalkoppeln auf diesen Aluminiumauslesestreifen festgestellt. Durch Simulationen konnte die Ursache dafür identifiziert und eine Lösung gefunden werden. Eine abschirmende Struktur von mit Bor hoch dotiertem Silizium konnte bei einem p-Typ Sensor den Aluminiumauslesestreifen, durch ein elektrisches Gegenfeld, ausreichend abschirmen und die Signalkopplung verhindern. Daher wurde eine verbesserte Iteration dieses Sensors mit der abschirmenden Struktur entworfen und mit dem ITE Warschau produziert. Die neuen Sensoren wurden getestet und deuteten auf die nun hergestellte Funktionsfähigkeit des Sensors hin, ließen aber aufgrund einer ungenügenden Streifenisolierung keine endgültigen Schlüsse zu. Daher wurde eine weiter Produktion eines solchen Sensors gestartet.
Sollte diese Produktion gut verlaufen und der Sensor einwandfrei funktionieren, ist er eine Alternative zum aktuellen Sensorkonzept für das Upgrade, welches momentan mit einem zweifach segmentierten Sensor plant.

Karlsruher Institut für Technologie

IEKP-KA/2013-1

Development of new Sensor Designs and Investigations on Radiation Hard Silicon Strip Sensors for CMS at the Large Hadron Collider during the High Luminosity Phase

Karl-Heinz Hoffmann

Zur Erlangung des akademischen Grades eines
DOKTORS DER NATURWISSENSCHAFTEN
von der Fakultät für Physik des
Karlsruher Institut für Technologie

genehmigte

DISSERTATION

von

Dipl.-Phys. Karl-Heinz Hoffmann
aus Temeschburg

Tag der mündlichen Prüfung: 01.02.2013

Referent: Prof. Dr. Thomas Müller, Institut für Experimentelle Kernphysik
Korreferent: Prof. Dr. Willem de Boer, Institut für Experimentelle Kernphysik

Contents

Introduction v

1. The CMS Experiment at the Large Hadron Collider 1
1.1. The Large Hadron Collider . . . 1
1.1.1. The Accelerator Complex . . . 3
1.2. The Compact Muon Solenoid (CMS) Experiment . . . 4
1.3. The LHC Upgrade . . . 6
1.4. CMS Tracker Upgrade . . . 7
1.4.1. Requirements for a new Tracker . . . 7
1.4.2. The 2S module . . . 10

2. Silicon and Silicon Detectors 13
2.1. Properties of Silicon . . . 13
2.1.1. Crystal Structure . . . 13
2.1.2. Energy Bands . . . 14
2.1.3. Intrinsic Semiconductors . . . 15
2.1.4. Extrinsic Semiconductors . . . 17
2.1.5. Carrier Transport in Semiconductors . . . 18
2.1.6. Carrier Generation and Recombination in Semiconductors . . . 19
2.2. Basic Semiconductor Devices . . . 23
2.2.1. The pn-Junction . . . 23
2.2.2. The Metal-Insulator-Semiconductor Structure . . . 26
2.2.3. Silicon Strip Detectors . . . 27
2.2.4. Noise Sources . . . 29

3. Radiation Damage in Silicon 33
3.1. Damage Mechanisms . . . 33
3.2. Macroscopic Effects of Radiation Damages on Silicon Detector Parameters . . . 37
3.2.1. Leakage Current . . . 38
3.2.2. Depletion Voltage . . . 39
3.2.3. Type Inversion . . . 41
3.2.4. Trapping . . . 42
3.2.5. Beneficial Effect of high Oxygen Concentration . . . 42

4. Irradiation Facilities and Sensor Teststations 45
4.1. Irradiation Facilities 45
4.1.1. Proton Irradiation - The Compact Cyclotron Karlsruhe 45
4.1.2. Neutron Irradiation - Reactor Infrastructure Center Ljubljana 47
4.2. Sensor Test Stations 49
4.2.1. Probe-station 49
4.2.2. ALiBaVa Setup 54

5. Campaign to identify the Baseline Sensor Technology for Future CMS Tracking Detectors 59
5.1. Central European Consortium - R&D Proposal 59
5.1.1. Overview 59
5.1.2. Objectives within the R&D Proposal related to this thesis 60
5.2. R&D for thin Single-Sided Sensors with Hamamatsu Photonics - HPK campaign . . 60
5.2.1. Overview 61
5.3. Details on Structures and Measurements 65
5.3.1. Diodes 65
5.3.2. Strip Sensors 66
5.3.3. Multi-geometry Sensors 67
5.3.4. New Sensor Designs 71
5.3.5. 2nd Metal Layer Structures 72

6. Designing new structures and sensors 75
6.1. Manufacturing of Silicon Strip Sensors 75
6.1.1. Techniques of Silicon Wafer Production 75
6.1.2. Process Steps in Planar Technology 77
6.1.3. Technological Sequence for Pad Detectors with Bias Resistors and AC Coupling 81
6.2. LayoutEditor 85
6.2.1. Using the software 85
6.2.2. Designing a Strip Sensor 87
6.3. Sensors and Structures 91
6.3.1. The Standard Strip Sensors 91
6.3.2. Sensor with Fourfold Segmented Strips and Readout at the Edge - FOSTER . 93
6.3.3. Sensor with Integrated Pitch Adapter 97
6.3.4. Sensors with Integrated Pitch Adapters in a Second Metal Layer 98
6.3.5. Pitch Adapters for Multi-geometry-sensors 99
6.3.6. Summary 100

7. Initial Sensor Qualification and Irradiation Studies for the HL-LHC 101
7.1. The Wafers 101

7.2. Qualification of Non-Irradiated Sensors and Development of Sensor Characteristics under Irradiation . . . 102
7.2.1. Full Depletion Voltage . . . 102
7.2.2. Total Lakage Current . . . 107
7.2.3. Strip Leakage Current . . . 112
7.2.4. Coupling Capacitances and Pinholes . . . 114
7.2.5. Bias Resistors . . . 116
7.2.6. Inter-strip Resistance . . . 117
7.2.7. Inter-strip Capacitances . . . 120
7.2.8. Charge Collection . . . 120
7.3. Annealing Study . . . 128
7.4. Conclusion on Material and Technology Study . . . 135

8. Studies on new Sensor Designs **137**
8.1. Sensor with Fourfold Segmented Strips and Readout at the Edge - FOSTER . . . 137
8.1.1. Electrical characterization . . . 138
8.1.2. Laser and Source Measurements . . . 141
8.1.3. Simulations . . . 150
8.1.4. Sensor Production with ITE Warsaw . . . 157
8.2. Conclusion on new sensor design . . . 161

Summary **163**

A. Technical Drawings **165**
A.1. Jig Design . . . 165

B. ALiBaVa **171**
B.1. Charge Calibration . . . 171

C. Measurements **177**
C.1. FOSTER . . . 177

List of Figures **179**

List of Tables **184**

Index **186**

Bibliography **186**

Introduction

Today's largest all-silicon tracking detector is used in the Compact Muon Solenoid (CMS) experiment at CERN, which analyzes the proton-proton collisions at the Large Hadron Collider (LHC). The CMS detector consists of more than 200 m^2 of silicon pixel and silicon strip sensors. The strip layers have to withstand fluences of about $\Phi_{eq} = 2 \times 10^{14}\ cm^{-2}$ during the service life time. Thereafter a high luminosity upgrade of the Large Hadron Collider HL-LHC is planned for about 2022. As the luminosity will be increased by a factor of ten, a completely new tracker will be required, being able to cope with the higher track density and the higher radiation damage.
Radiation damage changes the sensor properties by creating lattice defects in the silicon. The leakage current increases, which leads to a higher noise and power consumption of the modules. The depletion voltage rises and trapping centers generated by the radiation are created within the silicon bulk. The trapping and a depletion voltage above the operating voltage lead to a decrease in the charge collection and signal-to-noise ratio.

In this thesis, the most promising sensor materials and technologies for a new tracker for the HL-LHC have been investigated within the CMS tracker upgrade collaboration and the central european consortium. The study includes float zone and magnetic Czochralski silicon sensors of several active thicknesses (120 µm, 200 µm, 320 µm), thinned by different techniques. The sensors have been delivered in n-bulk and p-bulk versions with two isolation techniques, p-stop and p-spray, for the p-bulk sensors. After an initial electrical characterization of the sensor properties and signal measurements with a Sr90 source, the sensors have been irradiated with neutrons and protons. The fluences of the irradiations have been selected according to the expected fluences for the CMS tracker after the upgrade, reaching from R=40 cm to R=10 cm, the radial distance from the interaction point. The changes of strip parameters, leakage currents, depletion voltages, charge collection and the signal-to-noise ratio after the irradiations have been evaluated. The studies of radiation hardness have been supplemented by a final annealing study, carried out in multiple steps to investigate the partial recovery of radiation damage and its influence on the sensor properties.
Furthermore, a new sensor design has been developed to cope with the increased track density after the upgrade. The sensor geometry is fourfold segmented, which increases the granularity by a factor of four and allows standard wire bonding to the readout chips, as readout pads are at the sensor edge.
The first chapter shortly introduces the CMS experiment at the LHC and describes the tasks of the various detector systems. In chapter two the basic properties of semiconductors, with an emphasis on the material silicon are discussed, while in the third chapter the effect of radiation on silicon and the associated changes to its properties are shown. Chapter four gives an overview of the irradiation

facilities and the used infrastructure at the IEKP in Karlsruhe. Moreover, the measurement devices which have been extended by a cold jig are presented. Chapter five describes the measurement campaign. In chapter six, the necessary process steps for the production of silicon strip sensors, the planar process, is depicted. The free software tool LayoutEditor, used to create sensor designs for the campaign, is introduced and a detailed overview of the newly designed sensors and structures is given. The measurement results of the sensor qualification are shown in chapter seven, illustrating the influence of radiation damage to the sensor properties and the change of sensor parameters. In chapter eight, first investigations on the newly designed fourfold segmented sensor with readout at the edge are discussed. Finally, chapter nine summarizes the results of this thesis.

Chapter 1.

The CMS Experiment at the Large Hadron Collider

The Standard Model of particles and forces summarizes our present knowledge of particle physics. It has been tested by various experiments. However, our understanding of the universe is incomplete. The Standard Model leaves some unsolved questions, which the Large Hadron Collider will help to answer. The search for the Higgs boson seems to have come to a successful outcome on 4 July 2012 by observing a new particle, which behaves like the expected Standard Model Higgs. Further questions like the nature of the dark matter, which makes up more than 80% of the matter in the universe, are still open.

1.1. The Large Hadron Collider

The Large Hadron Collider (LHC) is a gigantic particle accelerator at CERN[1] near Geneva, crossing the border between Switzerland and France, see figure 1.1. It is the largest and highest-energy particle accelerator, designed to collide counter rotating beams of protons at four interaction points at a foreseen energy of 7 TeV per beam, or heavy ions at 2.75 TeV per nucleon.
The LHC is built in the 27 km long former LEP[2] tunnel between 50 and 175 m underground. The counter rotating beams travel in separated beam pipes at a speed close to the speed of light. They are guided around the accelerator ring by a strong magnetic field, supplied by using superconducting electromagnets that are cooled down to about -271 °C.
In 2012 the LHC has run at proton beams of 4 TeV and delivered an integrated luminosity of about 23.3 fb^{-1}.

At each of the four interaction points at least one experiment is housed. There are two large experiments, ATLAS[3] and CMS[4], two medium-sized specialized experiments ALICE[5] and LHCb[6] and two smaller-sized experiments TOTEM[7] and LHCf[8] [CER]. Here follows an overview of the four main experiments in alphabetical order:

[1] **C**onseil **E**uropéen pour la **R**echerche **N**ucléaire
[2] **L**arge **E**lectron-**P**ositron Collider
[3] A Toroidal Lhc ApparatuS
[4] Compact Muon Solenoid
[5] A Large Ion Collider Experiment
[6] Large Hadron Collider beauty experiment
[7] TOTal Elastic and diffractive cross section Measurement
[8] Large Hadron Collider forward

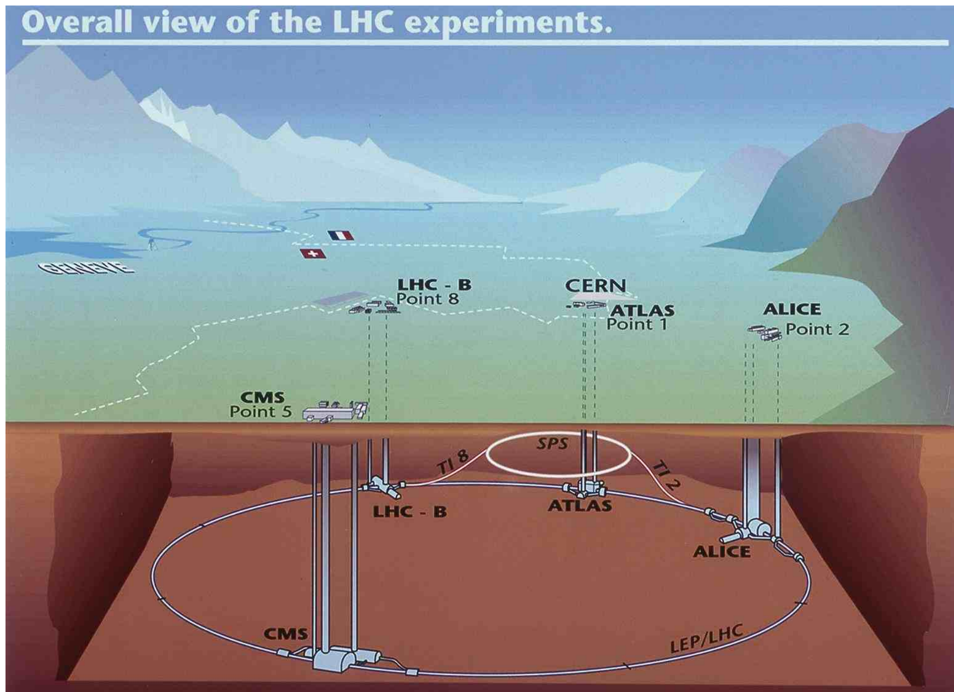

Figure 1.1.: Overview of the LHC experiments straddling the boarder between France and Switzerland near Geneva [Car98]. Using the 27 km long former LEP tunnel situated 50 to 175 m underground and its infrastructure, the LHC houses two multipurpose experiments ATLAS and CMS accompanied by two special experiments LHCb and ALICE.

- **ALICE** is a detector optimized to study the heavy ion collisions at the LHC. The result of these Pb-Pb collisions at $\sqrt{s} = 5.5\ TeV$ are temperatures and conditions that existed right after the Big Bang. It is expected, that a state of matter, wherein the quarks and gluons are deconfined is generated. It is planned to study the so called quark-gluon plasma as it expands and cools. The ALICE detector is unit26m long, 16 m high, 16 m wide and weights 10000 t.

- **ATLAS** is a general-purpose detector. It investigates a wide range of physics, capable to fully exploit the physics of high energy proton-proton collisions and heavy ion collisions. The main goal of ATLAS is to find the Higgs boson, but it has also the ability to improve measurements of the Standard Model and the top quark, search for dark matter and investigate the CP violation. The detector is one of the largest particle detectors, it is 46 m long, 25 m high, 25 m wide and weights 7000 t.

- **CMS** is also a general-purpose detector. Its goals are similar to ATLAS, but it uses different detector technologies, which will be presented in section 1.2. The detector is one of the heaviest particle detectors. It is 21.5 m long, 15 m in diameter and weights 12500 t.

- **LHCb** is a detector built to explore the differences between matter and antimatter, to solve the question why antimatter disappeared seconds after the Big Bang, while matter builds up the universe. LHCb therefore studies the b quark and its anti-b quark, as they are generated in billions and decay rapidly. The detector is 21 m long, 10 m high, 13 m wide and weights

about 5600 t.

1.1.1. The Accelerator Complex

The CERN accelerator complex is a succession of particle accelerators that can reach increasingly higher energies. Each accelerator boosts the speed of a beam of particles, before injecting it into the next one in the sequence [Lef09]. Figure 1.2 illustrates the boost cycle beginning with a bottle of hydrogen. First the orbiting electrons get stripped of the hydrogen atoms and the protons are accelerated in the LINAC2 to 50 MeV before they reach the PS Booster. The Booster accelerates them to 1.4 GeV and the following Proton Synchrotron (PS) to 25 GeV. The final pre-accelerator Super Proton Synchrotron (SPS) accelerates to 450 GeV before the bunch of protons reaches the LHC where it can reach its final energy of 7 TeV after several minutes. The beams are then stored in the LHC for hours, meanwhile the collisions take place at the four intersection points inside the four main experiments.

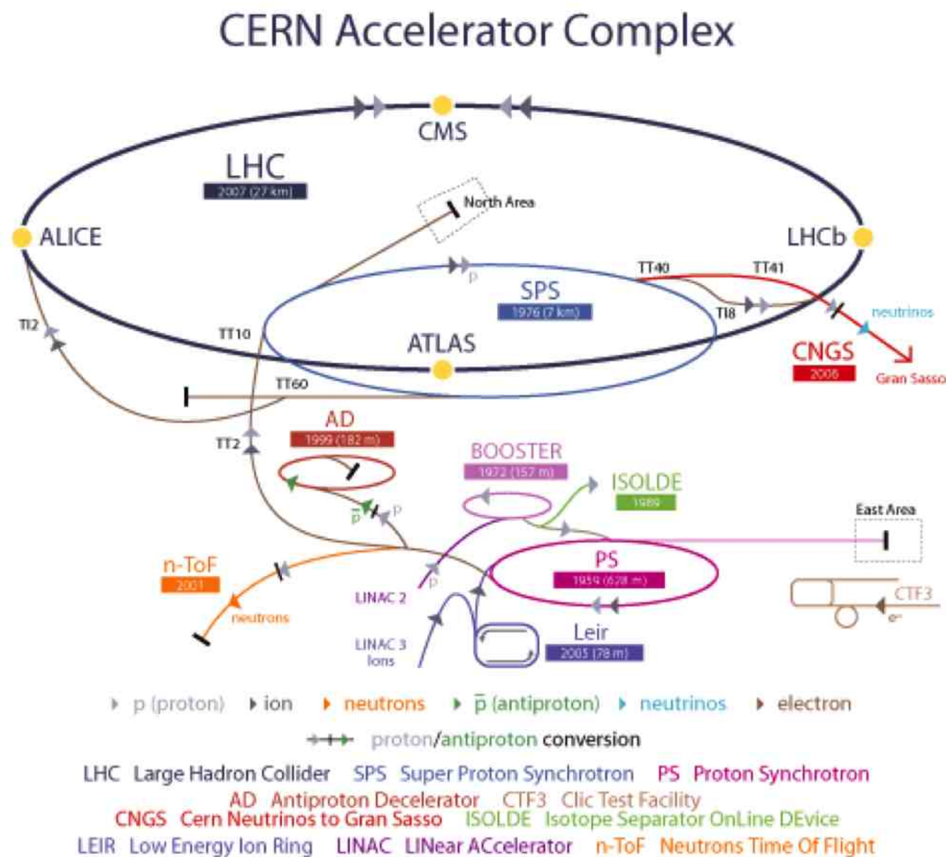

Figure 1.2.: Overview of the accelerator complex of the LHC [Lef09]. Beginning with a bootle of hydrogen atoms, the electrons get stripped of, while the protons get their first acceleration to 50 MeV at the LINAC2. Then the beam of protons reaches via the PS Booster (acceleration to 1.4 GeV) the Proton Synchrotron (PS), where it is accelerated to 25 GeV. Before it finally is inserted into the LHC, the Super Proton Synchrotron (SPS) has accelerated the proton beam to 450 GeV. In the LHC the beam can reach its nominal energy of 7 TeV after an acceleration time of 20 minutes.

1.2. The Compact Muon Solenoid (CMS) Experiment

As the work in this thesis is directly related to the CMS experiment the following section will describe this experiment.
CMS is a huge multi-purpose detector built up like a cylindrical onion consisting of detector layers of different materials as shown in figure 1.3. Each layer exploits its special properties to track, stop or measure the particles generated by the collisions. The energy and momentum of the particles allow conclusions on the particles identity.
The detector can be divided in three larger parts. The most inner part is the Tracker, a high precision detector composed of a silicon pixel and a silicon strip detector, visualizing the particles trajectory. The Tracker is surrounded by the electromagnetic and the hadronic calorimeters (ECAL and HCAL). While the ECAL measures the energy of photons and electrons, the HCAL detects particles made up of quarks. These inner parts are encircled by a superconducting solenoid inducing a homogeneous magnetic field of 4 T, which in turn is encased by the iron magnet return yoke and the muon detectors.

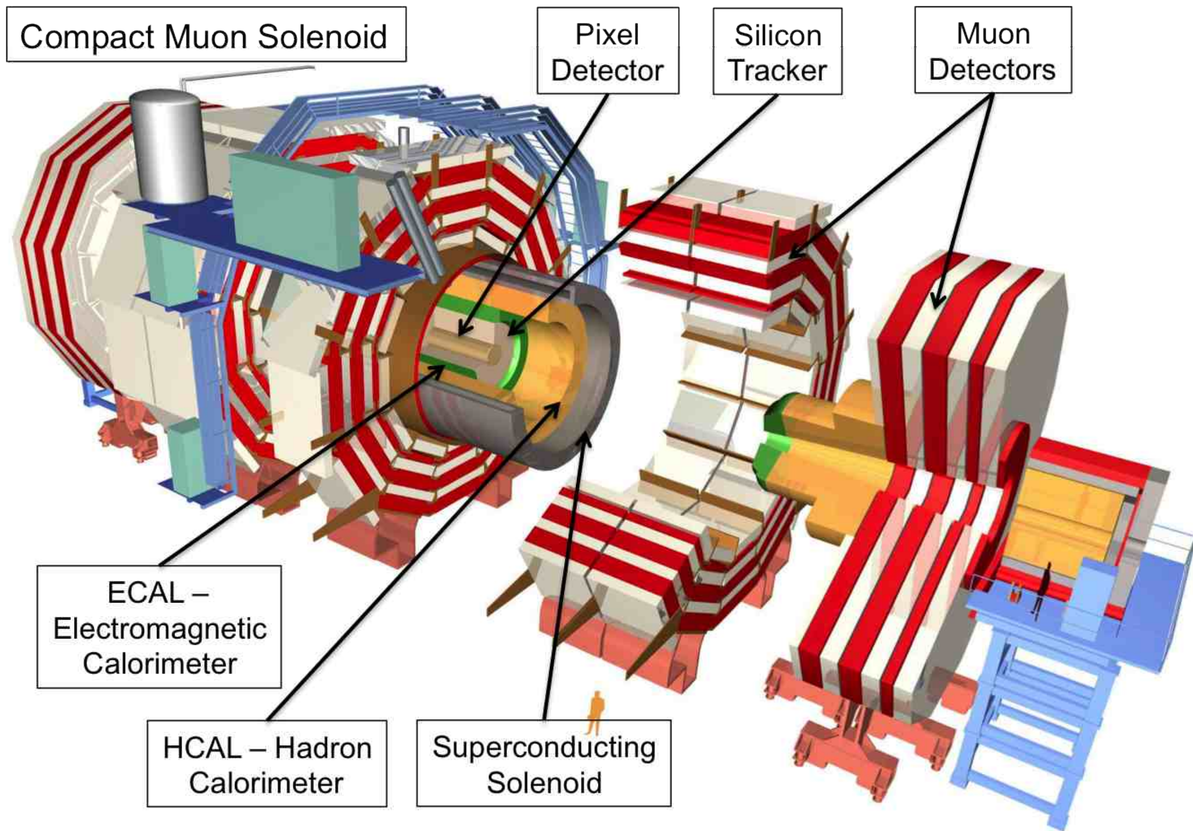

Figure 1.3.: Expanded view of the CMS detector [Tay].

Each particle traveling through CMS leaves behind a characteristic pattern in the different layers, allowing to identify it (see figure 1.4). The huge amount of data, produced by the billions of interactions each second, can not be read out and stored in that short time. Therefore an online event selection process (trigger system) reduces the huge data rate to the final output rate of about

100Hz for storage and subsequent analysis [Fel09]. The first event reconstruction is done on the CERN computer center (Tier0) before the data is then sent to Tier1 computer centers all over the world, where the event reconstruction is redone in more detail, using further informations from the experiments.

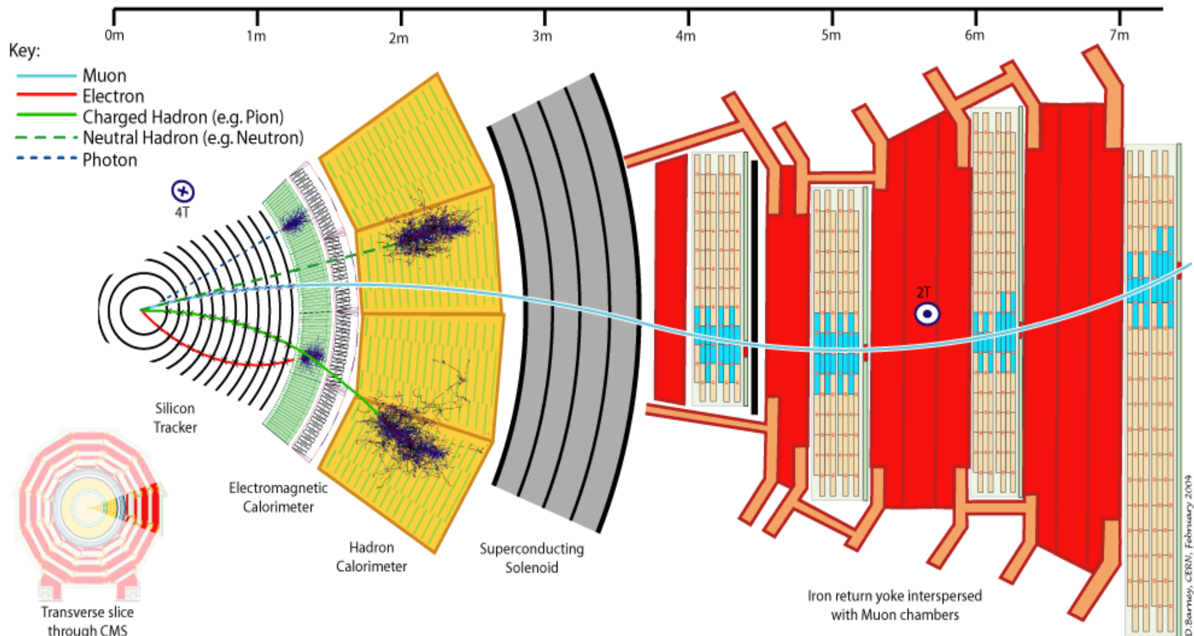

Figure 1.4.: Tracking of all systems together [Lap12].

The several systems shown in figure 1.4 are:

The Tracking System

CMS has designed and installed the largest silicon tracking detector, with more than 200 m^2 area of active silicon detectors. The CMS tracker is geometrically divided into substructures, shown in figure 1.5. The pixel detector is close to the interaction point and surrounded by the Silicon Strip Tracker (SST). The SST consists of the inner barrel detector (TIB), the inner discs (TID), the outer barrel (TOB) and of the two end cap detector systems (TEC+ and TEC-). The over all length of the tracker is 5.4 m and its outer diameter is 2.4 m [Kra12].

The hit positions of a particle coming from the interaction point are measured by the tracker. Combining the hit position measurements of all detector layers allows the reconstruction of the track of the particle. Charged particles follow a spiraling path in the CMS magnetic field. The momentum and the energy of the particle can be evaluated from the curvature of it's path.

The Calorimetry Systems

Composed of the Electromagnetic Calorimeter (ECAL) and the Hadronic Calorimeter (HCAL), the calorimeter system measures the energy of the particles by completely stopping them. The ECAL, enclosing the tracker measures the energy of electrons and photons by electromagnetic interaction.

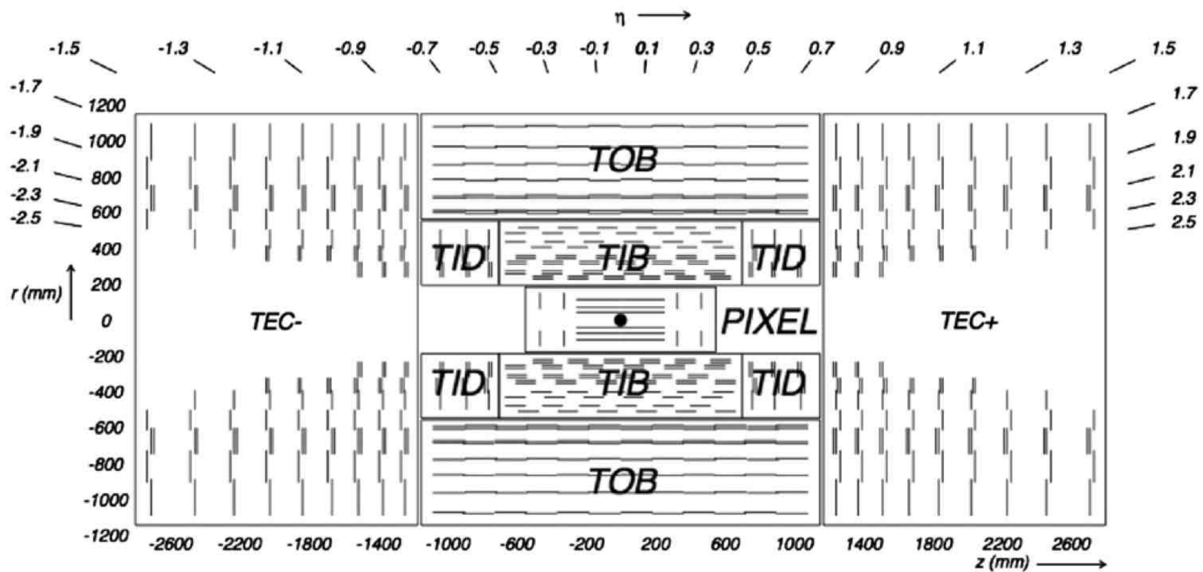

Figure 1.5.: Schematic cross-section through the CMS tracker. Each line represents a detector module. Double lines indicate back-to-back modules which deliver stereo hits [Kra12].

The ECAL is surrounded by the HCAL, that measures the energy of hadrons using the strong interaction.

The Muon Detectors
The only particles that have not already been stopped are muons and only weakly interacting particles like neutrinos. The muon system measures the muons in dedicated muon chamber detectors, getting also an information on their momenta from the bending of the paths in the magnetic field. As neutrinos pass the muon detectors without interacting, their momenta and positions can be calculated by adding up the momenta of all detected particles. For this it is important to guarantee hermetic coverage of the detector.

1.3. The LHC Upgrade

The LHC is expected to operate at a luminosity of $\mathcal{L} = 10^{34}\text{cm}^{-2}s^{-1}$ and reach a center-of-mass energy of $\sqrt{s}$ = 14 TeV. Therefore the CMS detector has been designed to cope with the high radiation and event rate expected for this luminosity. However there is a strong motivation to increase the performance of the machine in order to expand the physics potential of the LHC. Thus the LHC will need a major upgrade. The aim is to increase the luminosity by a factor of 5-10, and provide $3000fb^{-1}$ in 10 to 12 years [Sut12]. Scheduled for the years 2013 until 2022 the LHC accelerator complex will gradually be upgraded. Figure 1.6 shows the scheduled time line for the upgrade.

The physics potential of the upgraded High Luminosity LHC (HL-LHC) can be divided into the following topics [Gia05]:

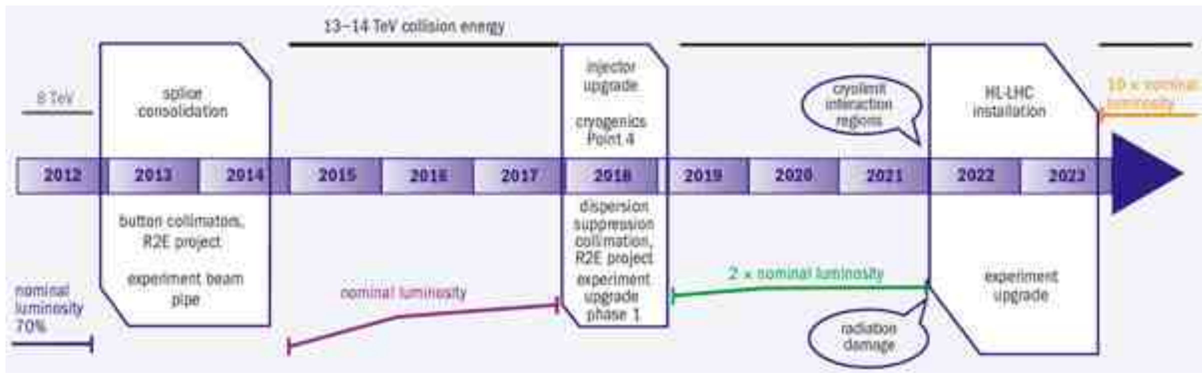

Figure 1.6.: Long-term program of the LHC. The upgrade will happen by gradually upgrading the accelerator chain, ending approximately in 2022, reaching 5-10 times the nominal luminosity [Sut12].

- Improvement of the accuracy in the determination of Standard Model (SM) parameters.
- Improvement of the accuracy in the determination of parameters of New Physics possibly discovered at the LHC.
- Extension of the discovery reach in the high-mass region.
- Extension of the sensitivity to rare processes.

For more details about the High Luminosity upgrade and the HiLumi LHC Design Study, see http://cern.ch/HiLumiLHC.

1.4. CMS Tracker Upgrade

After the LHC has been upgraded by a factor of 5-10 more in peak luminosity, also the experiments need major upgrades. More luminosity, which is equivalent to more produced particles per bunch crossing and time, leads to an increased occupancy and radiation damage of the tracking detectors. This very high luminosity of $\mathcal{L} = 10^{35}\text{cm}^{-2}s^{-1}$ requires a completely new tracker and an further improved trigger system.

1.4.1. Requirements for a new Tracker

As shown in figure 1.7, the track density within the tracker will increase significantly by going to higher luminosities. The detector, and thus the silicon strip sensors, will have to cope with more tracks, closer to each other. The possibility, that one single strip is hit by several particles will increase and may result in two or more hits on this single strip. These hits can not be separated and are detected as only one hit. The track reconstruction will lose efficiency as not all tracks will be resolved.

Therefore one major challenge for the tracking system is, to reconstruct the tracks of all the particles produced in the collisions by increasing the granularity of the tracker. This can be achieved by shortening the strips. Reducing the strip length makes it possible to detect two hits separately

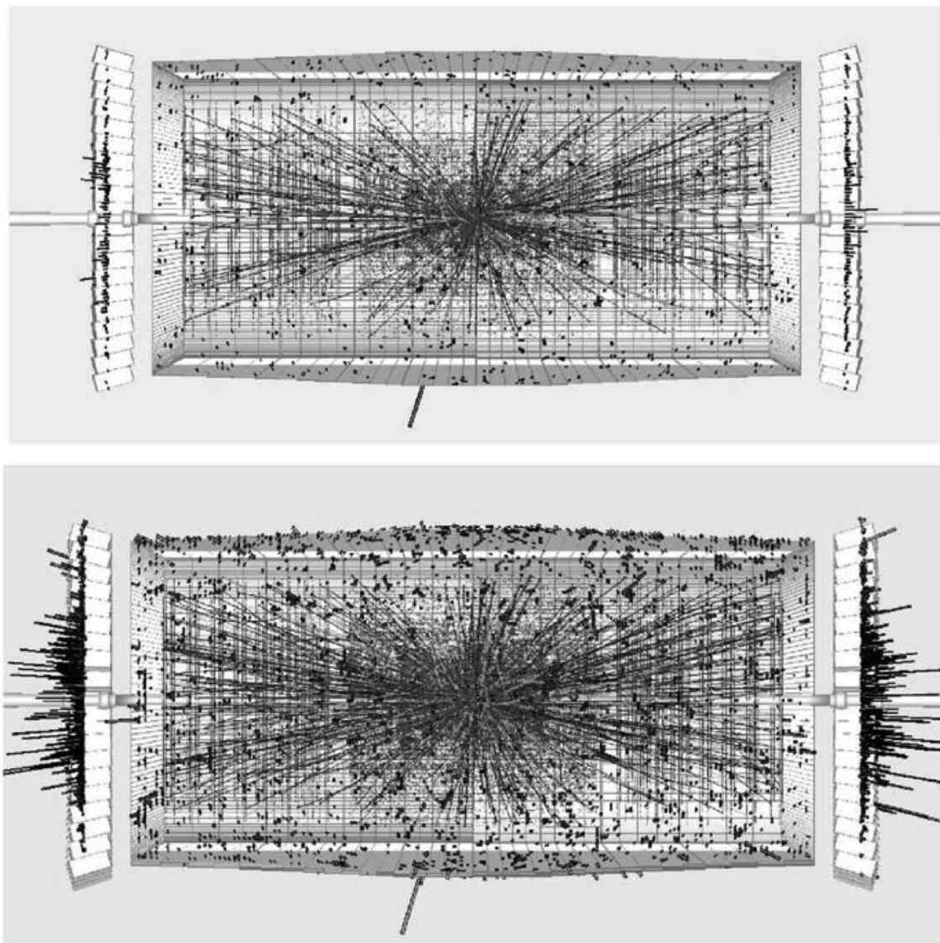

Figure 1.7.: Tracks in the CMS tracker as they are expected for bunch crossing at luminosities of $10^{34}cm^{-2}s^{-1}$ (top) and $10^{35}cm^{-2}s^{-1}$ (bottom) [Vir03].

on two strips, instead of two hits on one long strips resulting in only one hit. Shortening the strips means at the same time to increase the number of strips, which could be a problem for the module design, as all strips have to be connected to the readout chips. This is typically done at the sensor edge, by wire bonding the strips to the readout. One promising sensor design, that leads to an increased granularity by a factor of four, is the FOSTER. The sensor design, investigation and evaluation is one major part of this thesis.

Another challenge for the tracker upgrade that comes with the increased luminosity and the associated higher track density is the radiation damage. The high number of generated particles that irradiate the tracker damage the sensors and the electronics by degrading their efficiency and functionality. Comparing the electron signals for pixel sensors and strip sensors at the current LHC and at the upgraded LHC, it can be seen that the fluence levels for both are shifted by one order of magnitude to higher fluences. The signals decrease to less than 5000 electrons, making it impossible to detect any particles. Figure 1.8 shows the shifted fluences for pixel and strip sensors at the upgraded LHC and illustrates the necessity of more radiation hard silicon sensors.

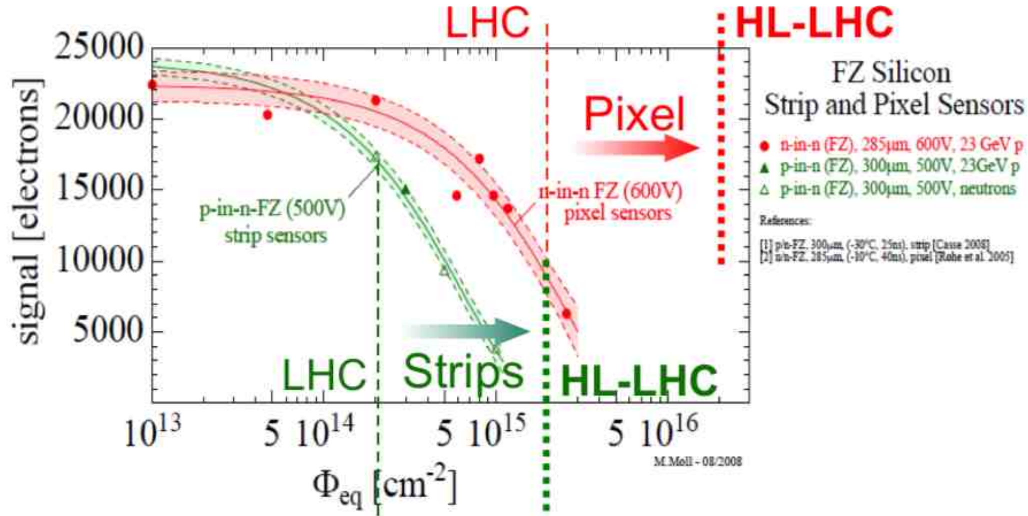

Figure 1.8.: Signal reduction with increasing fluence [Mol08].

Irradiated sensors loose not only signal, they also produce high leakage currents, suffer from trapping and need to be operated at higher voltages. As the impact of radiation to the sensor performance is crucial, an upgraded tracker needs more radiation hard sensors. In this thesis, various silicon materials are investigated before and after irradiation to conclude on their behavior and to find a sensor solution for the upgrade. There are n-in-p and p-in-n sensors with different isolation techniques and in different silicon materials under investigation.

Simultaneously to the challenges for the sensors, it is foreseen that the tracker provides a trigger information to contribute to the Level-1 trigger. As not all data can be transferred and recorded, the data reduction on the detector level is necessary. The trigger rate of the Level-1 trigger has to stay below 100 kHz, to ensure the higher level trigger to keep the final output rate of about 100 Hz for storage and analysis. As the charged particle transverse momentum spectrum, shown in figure 1.9 mainly consists of low p_T tracks that are not interesting, cutting p_T tracks below a certain threshold away would substantially reduce the number of tracks and thus the trigger rate, helping to keep it below 100 kHz [Hal11].

The CMS collaboration started a campaign to identify radiation hard silicon sensors and new sensor designs in order to find suitable solutions (see chapter 5.2). Higher granularity can be achieved by shortening the strips, which on the other hand increases the number of readout channels and thus could increase the power consumption. One option to provide a tracking information to the Level-1 trigger will be shortly discussed in the following section.

In summary, the CMS tracker for the HL-LHC has to cope with a higher track density and an increased irradiation. These two challenges originating from the increased number of particle interactions are accompanied by the need of the contribution to the Level-1 trigger, helping to keep the trigger rate below 100 kHz. In this thesis, new sensor designs and the radiation hardness are investigated and suitable solutions for the upgrade requirements are provided.

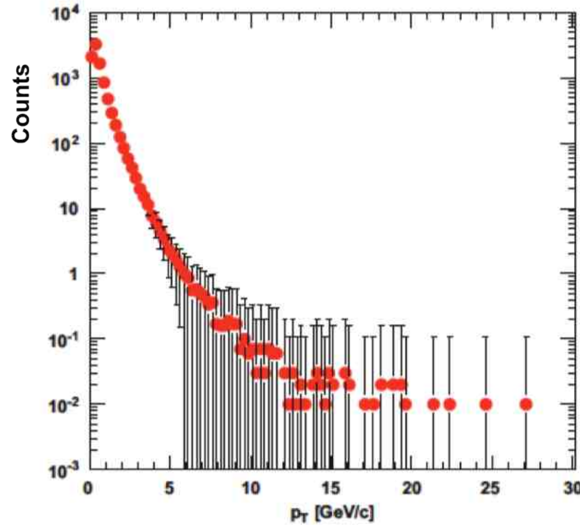

Figure 1.9.: Transverse momentum spectrum of charged tracks in HL-LHC conditions [Hal11].

1.4.2. The 2S module

Current developments, concerning the implementation of the tracking trigger focus on the rejection of low p_T tracks, which will be done locally in the module front-end. Rejecting particles with p_T below 1-2 GeV would reduce the bandwidth requirements by at least one order of magnitude [Hal11], see figure 1.9. The discrimination of high and low p_T tracks is done by correlating signals in two closely spaced sensors. Figure 1.10 shows the principle of the discrimination. Particles with low p_T are strongly bent, due to the magnetic field of the CMS solenoid. In figure 1.10 the "fail" particle hits two strips in the first sensor and three strips in the second sensor. Correlating the cluster sizes in the two sensor planes and the distance between the sensors with the particle p_T allows the discrimination. The "pass" particle with high p_T is hardly bent in the magnetic field. It hits one strip in the first plane and two strips in the second. A pair of hits that fulfills the selection cut is called a "stub".

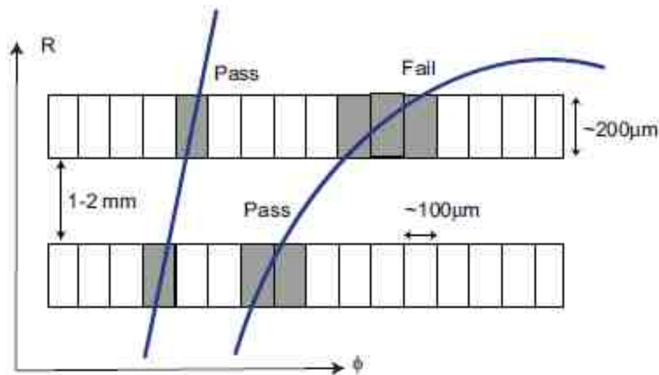

Figure 1.10.: The concept of a p_T-module is to discriminate between high and low p_T tracks by determining the cluster width. Tracks with high p_T are hardly bent, while tracks with low p_T are strongly bent.

The spacing of the sensors depends on the position the module will have in the tracker, varying from 1 mm for the barrel to 4 mm for the end caps.
A simple p_T module would be the 2S module, a sandwich of two silicon sensors that are read out by the same electronics. The signals from both sensors will be correlated on the module which allows the discrimination between high or low p_T. A 3D model of the 2S module are shown in figure 1.11.

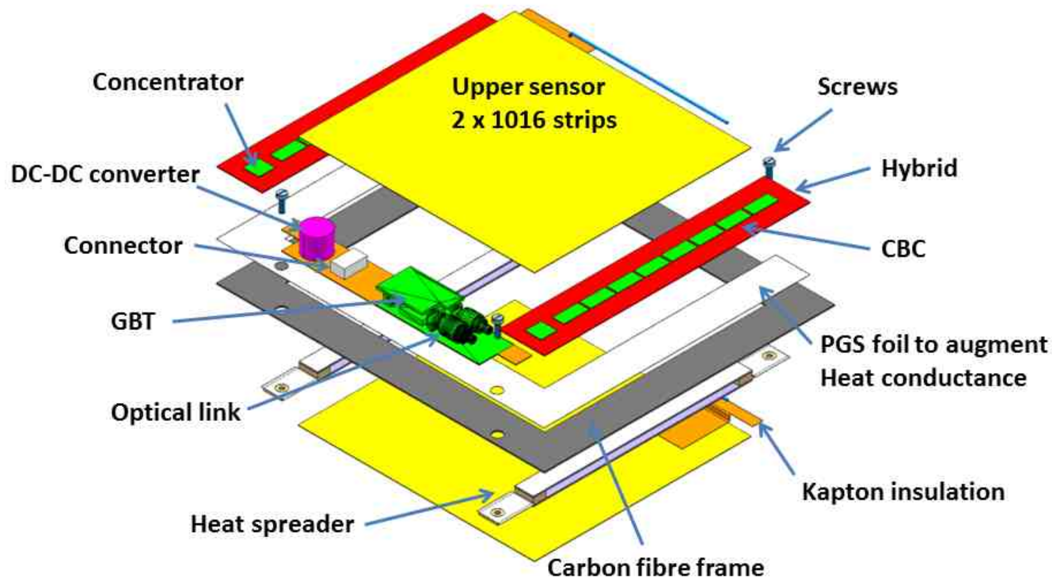

Figure 1.11.: The design drawing shows the 2S module broken down into its individual parts. The main parts of the module are the two strip sensors with the readout at the edges [Abb11].

The choice of new sensors for the tracker upgrade is driven by the new module concept. The sensors currently foreseen for the 2S module will have a size of 10 cm $\times$ 10 cm and the strips will be twofold segmented with a length of 5 cm. The sensors will have 2 $\times$ 1016 strips with a pitch of 90 µm. The sensors have the readout connection at the sensor edge in order to do the alternating bonding of the strips of the two sensors to the binary readout chip. The readout chip (CBC) will have 254 channels and be bump bonded to the hybrid. The bonding from the sensors to the hybrid will be done by wire bonding.
In this thesis a new sensor geometry will be introduced and investigated that would be a good candidate for the 2S module, see section 6.3.2.

Chapter 2.

Silicon and Silicon Detectors

Since the early 90ies most high energy physics experiments, as for example the CMS experiment at the LHC, use silicon strip sensors as tracking detectors.
Silicon is the second most abundant element in the Earth's crust and is also mainly used in semiconductor industry. Together with its properties, this makes it a favorable material for radiation detectors at low cost. This chapter will introduce the basics of silicon properties and the functionality of silicon strip sensors.

2.1. Properties of Silicon

2.1.1. Crystal Structure

Silicon as single crystal has a diamond lattice type as shown in figure 2.1. Each atom is surrounded by four close neighbors and they are arranged in a tetrahedron, with each atom sharing its four outer electrons with its neighbors, forming covalent bonds.

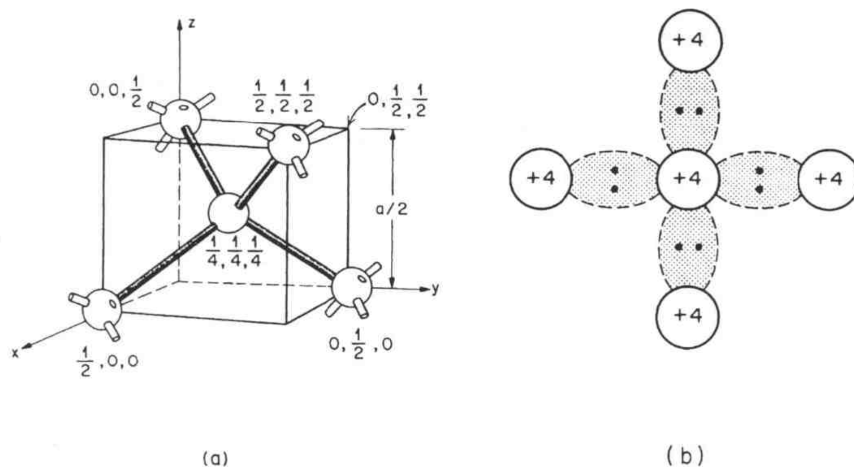

Figure 2.1.: Silicon atoms (a) tetrahedron bond and (b) shown in a two-dimensional representation [Lut].

Silicon, with the atomic number 14 belongs to the fourth main group of the periodic table of elements. Tabel 2.1 summarizes some quantitative properties.

Table 2.1.: Properties of silicon [Har08].

Parameter	Symbol	Unit	Value
Atomic number			14
Relative atomic weight			28.0855
Structure			diamond
Lattice constant	a_0	Å	5.4307
Electron configuration			$1s^2 2s^2 2p^6 3s^2 3p^2$
Density	ρ	gcm^{-3}	2.328
Melting point	T_m	°C	1414
Boiling point	T_b	°C	2355
Gap energy (300K) / (0K)	E_g	eV	(1.124) / (1.170)
Dielectric constant	ϵ_r		11.7
Intrinsic carrier density	n_i	cm^{-3}	1.45×10^{10}
Mobility of electrons	μ_e	$cm^2[Vs]^{-1}$	1350
Mobility of holes	μ_h	$cm^2[Vs]^{-1}$	450
Effective density of states			
- of the conduction band	N_c	cm^{-3}	3.22×10^{19}
- of the valence band	N_v	cm^{-3}	1.83×10^{19}
Max. electrical filed	E_{max}	$V\mu m^{-1}$	30
Thermal expansion coefficient		1 / °C	2.5×10^{-6}
Intrinsic resistivity		kΩ	235

2.1.2. Energy Bands

Silicon atoms arranged in a diamond structure form so called energy bands. Figure 2.2 shows the band formation. The valence band, the highest filled energy band with its upper energy border E_v and the conduction band, the lowest non filled energy band with its lower energy border E_c are separated by the band gap E_g.

$$E_g = E_c - E_v \tag{2.1}$$

At low temperatures (T=0K) the valence band is fully occupied while the conduction band is empty. At higher temperatures the valence electrons can transit from the valence band to the conduction band, due to lattice vibrations. Phonons, being the quasi-particle of the temperature dependent lattice vibrations, excite the electrons.
Depending on the size of the band gap three solids can be distinguished, see figure 2.3. Metals have

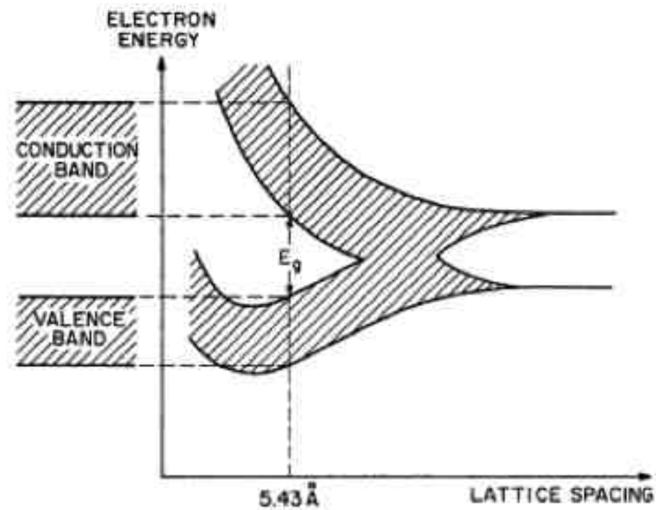

Figure 2.2.: Energy levels of silicon atoms as a function of lattice spacing [Lut].

the Fermi level within the conduction band, while the Fermi level for semiconductors and insulators lies between conduction and valence band.

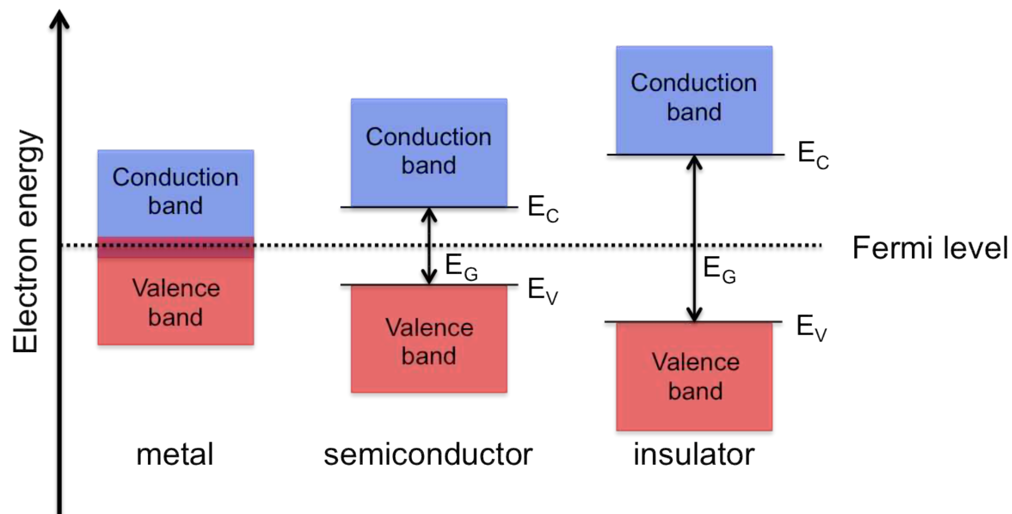

Figure 2.3.: Illustration of the simplified band structure to classify solids into metal, semiconductor and insulator. If the Fermi level lies in the conduction band, the material is a metal, if the Fermi level lies between the conduction and the valence band, the material is either a semiconductor or an insulator. The difference is only in the size of the band gap.

2.1.3. Intrinsic Semiconductors

In a semiconductor, at finite temperatures the probability for the transition of an electron is given by the Fermi-Dirac function:

$$F(E) = \frac{1}{1 + \exp \frac{E - E_F}{k_B T}} \tag{2.2}$$

where E is the energy of the electronic state, k_B is the Boltzmann constant, T is the temperature and E_F is the Fermi energy level at which the occupation probability is one half. If $|E-E_F|>3k_BT$, this expression can be approximated for electrons and holes to:

$$F_n(E) \approx \exp -\frac{E-E_F}{k_BT} \quad and \quad F_p(E) = 1 - F_n(E) \approx \exp -\frac{E_F-E}{k_BT} \tag{2.3}$$

The density of states near the bottom of the conduction band for low carrier densities and temperatures is given by:

$$N(E) = \frac{(2m_D^*)^{\frac{3}{2}}}{2\pi^2\hbar^3}\sqrt{E-E_C} \tag{2.4}$$

with the Planck's constant $\hbar$, the energy of the conduction band E_c and the density-of-state effective mass for electrons m_D^*=0.32m_e, which depends on the silicon lattice orientation [Kit05]. Convoluting the state density N(E) with the corresponding occupation probability F_n(E) gives the free electron density n:

$$n = \int_{E_C}^{\infty} N(E)\cdot F(E)dE = \frac{2}{\hbar^3}(2\pi m_D^* k_BT)^{\frac{3}{2}} \exp -\left(\frac{E_C-E_F}{k_BT}\right) = N_C \exp -\left(\frac{E_C-E_F}{k_BT}\right) \tag{2.5}$$

Respectively the free holes density p:

$$p = N_V \exp -\left(\frac{E_F-E_V}{k_BT}\right) \tag{2.6}$$

Figure 2.5(a) shows an illustration of the energy band structure, the density of states, the occupation probability and the carrier concentration for intrinsic semiconductors.

In an intrinsic semiconductor, without any defects or dopants, the concentration of electrons and holes are equal in thermal equilibrium $n = p = n_i$ with $n_i \approx 1.45 \cdot 10^{10}\text{cm}^{-3}$ at 300K. The density of charge carriers is then:

$$n_i = \sqrt{N_C N_V} \exp\left(-\frac{E_g}{2k_BT}\right) \tag{2.7}$$

and the Fermi energy in the intrinsic case can be calculated to:

$$E_i = \frac{E_C+E_V}{2} + \frac{3k_BT}{4} ln\left(\frac{m_p}{m_n}\right) \tag{2.8}$$

2.1.4. Extrinsic Semiconductors

The properties of intrinsic semiconductors can be modified by adding foreign atoms to the silicon lattice, which is called doping. Doping the silicon by adding elements of the fifth main group, like phosphorus, increases the number of negative charge carriers. The dopant acts as a donor, as the weakly bound fifth valence electron can easily be excited to the conduction band. It introduces an energy state E_D, just 0.044 eV below the conduction band. The silicon is then called N type silicon. Adding elements of the third main group, like boron increases the number of positive charge carriers. The dopant acts as acceptor, as it captures electrons. It creates an energy state E_A just 0.045 eV above the valence band. The silicon is then called P type silicon. The upper part of figure 2.4 shows the crystal lattice for n-doped and p-doped silicon, while the lower part visualizes the energy levels of the doped silicon types.

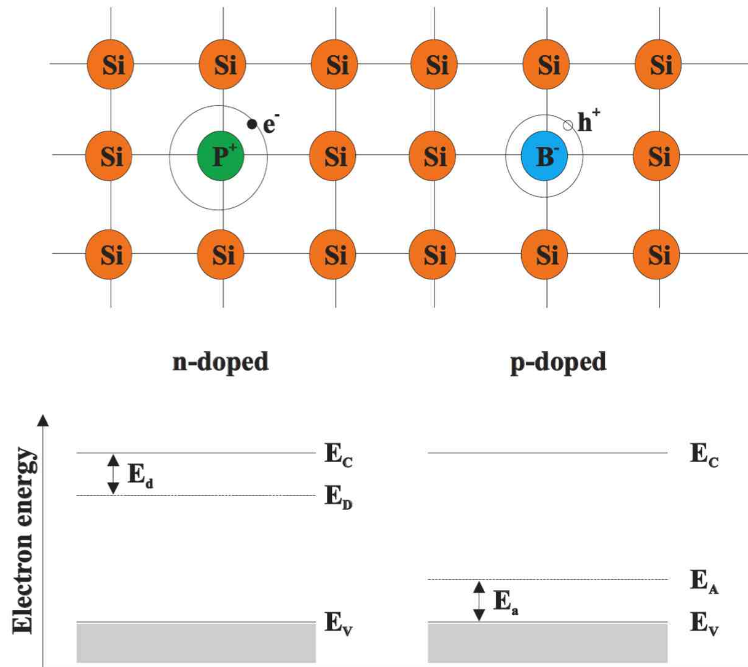

Figure 2.4.: Impact of adding foreign atoms to the silicon lattice by doping changes the electric properties. If a silicon atom is replaced by an element of the fifth main group (on the left side), the additional electron acts as a donor and creates an energy state below the conduction band. Replacing an silicon atom by an element of the third main group (on the right side), the missing electron is a trap, acting as an acceptor and creates an energy state above the valence band [Fur05].

The doping concentration is usually higher than the intrinsic concentration of charge carriers and thus the electron and hole densities are equal to the number of donor and acceptor atoms:

$$n = N_D \quad \text{for N type silicon} \quad and \quad p = N_A \quad \text{for P type silicon} \tag{2.9}$$

The new Fermi levels read:

$$E_C - E_F = k_B T \; ln \frac{N_C}{N_D} \quad \text{for N type silicon} \tag{2.10}$$

$$E_F - E_V = k_B T \; ln \frac{N_V}{N_A} \quad \text{for P type silicon} \tag{2.11}$$

The Fermi level defines the electron and hole concentration in general:

$$n = n_i \exp\left(\frac{E_F - E_i}{k_B T}\right) \tag{2.12}$$

$$p = n_i \exp\left(\frac{E_i - E_F}{k_B T}\right) \tag{2.13}$$

With the mass-action law from the definitions:

$$n \cdot p = n_i^2 \tag{2.14}$$

One type of charge carriers can only increase in density if the other type decreases. Figure 2.5(b),(c) shows the energy band structure, the density of the states, the occupation probability and the carrier concentration for n-doped and p-doped silicon.

For low temperatures the occupation follows the Fermi-Dirac statistic:

$$N_D^+ = N_D \left[1 - \frac{1}{1 + \frac{1}{2}\exp\left(\frac{E_D - E_F}{k_B T}\right)}\right] \quad \text{for donors} \tag{2.15}$$

$$N_A^+ = N_A \left[\frac{1}{1 + 4\exp\left(\frac{E_A - E_F}{k_B T}\right)}\right] \quad \text{for acceptors} \tag{2.16}$$

The Fermi level must be determined by solving the neutrality condition $n = N_D^+ + p$ leading to:

$$n \approx \sqrt{\frac{N_D N_C}{2}} \exp\left(-\frac{E_d}{2 k_B T}\right) \tag{2.17}$$

with $E_d = E_C - E_D$ and $N_D \gg \frac{1}{2} N_C \exp\left(\frac{E_d}{k_B T}\right) \gg N_A$. In the temperature range from $\sim$ 100K to 500K all donors are ionized and $N_D^+ = N_D$ is valid.

2.1.5. Carrier Transport in Semiconductors

So far the semiconductor has been in equilibrium, with homogeneous concentrations, electrically neutral without any external influences like electric or magnetic fields. The following section will consider phenomena that occur either by applying an external electric field or because of inhomogeneous distribution of movable charge carriers.
The charge carriers, electrons in the conduction band and holes in the valence band, can move freely within the semiconductor. Their mean kinetic energy is $\frac{3}{2} k_B T$ which results in a mean velocity at room temperature of about $10^7 \frac{cm}{s}$. They can scatter on imperfections, impurities and defects within the lattice, yielding in a mean free path of about 10^{-5}cm and a mean free time of 10^{-12}s [Lut].

Drift

In the case of a zero field, the average displacement of a charge carrier is also zero. By applying an electric field, the charge carriers will begin to drift suitable along the electric field and randomly collide, obtaining an average drift velocity of:

$$\nu_n = -\frac{q \cdot \tau_c}{m_n}\varepsilon = -\mu_n \varepsilon \tag{2.18}$$

$$\nu_p = \frac{q \cdot \tau_c}{m_p}\varepsilon = \mu_p \varepsilon \tag{2.19}$$

For high fields, strong deviations from linearity are observed and the drift velocities become independent of the electric field.
As scattering occurs due to thermal vibrations and impurities the mobilities μ_n and μ_p are dependent on temperature and doping concentration. For more details see [Sze81].

Diffusion

In case of inhomogeneous distribution of charge carriers in a semiconductor, carriers will move from regions of higher concentrations to regions of lower concentrations. This effect is called diffusion and results in a smoothening of the charge distribution. Mathematically it is described by:

$$\vec{F_n} = -D_n \vec{\nabla} n \quad and \quad \vec{F_p} = -D_p \vec{\nabla} p \tag{2.20}$$

where F_n (F_p) is the flux of carriers and D_n (D_p) the diffusion constant.
Mobility and diffusion are related to each other by the Einstein equation:

$$D_n = \frac{kT}{q}\mu_n \quad and \quad D_p = \frac{kT}{q}\mu_p \tag{2.21}$$

Combining the effects of drift and diffusion the current densities are:

$$\vec{J_n} = q\mu_n n\varepsilon + qD_n \vec{\nabla} n \quad and \quad \vec{J_p} = q\mu_p p\varepsilon + qD_p \vec{\nabla} p \tag{2.22}$$

2.1.6. Carrier Generation and Recombination in Semiconductors

Free charge carriers are created by lifting electrons from the valence band into the conduction band. What occurs is a free electron and a free hole. The necessary energy for this process can be accomplished by various mechanisms such as thermal agitation, optical excitation and by ionization. There is also the possibility to increase the number of free charge carriers by injecting carriers through forward biasing or to deplete the number by applying a reverse bias voltage. In the following, some mechanisms for charge carrier generation and recombination will be discussed.

Thermal Generation of Charge Carriers

As seen in the previous sections, the probability of exciting an electron from the valence band into the conduction band in an intrinsic semiconductor is very low. Ionizing shallow dopants is much easier as they create energy levels near the middle of the band gap. Such intermediate states in the band gap appear in reality due to defects and imperfections in the lattice or by doping.
Thermally generated charge carriers are usually disturbing the sensor functionality as they act as noise and superimpose the signal. For direct semiconductors with a small band gap, electrons can be excited directly from the valence to the conduction band and create free charges overlaying the real signal. Operating these detectors cooled is a possible solution.
For semiconductors with a large band gap the probability of direct excitation is low. The excitation has then to be done using the intermediate states created by impurities. In indirect semiconductors the energy for a band-to-band transition is not only the energy of the band gap. An additional momentum has to be transferred to account to the differently located momenta.

Generation of Charge Carriers by Electromagnetic Radiation

This is the basic principle of photo detectors. Electrons and holes are generated by the absorption of photons. The photon interacts with an electron which thus transits from the valence band to the conduction band. If the photon energy is larger than the band gap, the created electron and hole will move toward the band gap edge, emitting energy in form of phonons. For photons with energies smaller than the band gap an absorption is only possible if intermediate states within the band gap exist [Lut].

Generation by Charged Particles

A traversing charged particle looses kinetic energy through elastic collisions with the electrons. The basic theory for this process has been developed by Bohr and later by Bethe, Bloch and Landau. The Bethe-Bloch formula is given by [Lut] as:

$$\frac{dE}{dx} = 2\pi N_L r_e^2 m_e c^2 \rho \frac{Zz^2}{A\beta^2} \left[ln \left(\frac{2m_e\gamma^2 v^2 W_{max}}{I^2} \right) - 2\beta^2 - \delta - 2\frac{C}{Z} \right] \tag{2.23}$$

where x is the path length in g/cm^2,
$2\pi N_L r_e^2 m_e c^2$ =0.1535MeVc^2/g,
$r_e = \frac{e^2}{4\pi m_e c^2}$ =2.817×10^{-13}cm and is the classical electron radius,
m_e is the electron mass,
$N_L = 6.022 \times 10^{23}$ is the Avogadro's number,
I is the effective ionization potential averaged over all electrons,
Z is the atomic number of the medium,
A is the atomic weight of the medium,
ρ is the density of the medium,
z is the charge of the traversing particle,
$\beta = v/c$, the velocity of a traversing particle in units of speed of light,

$\gamma = \frac{1}{\sqrt{1-\beta^2}}$,
δ is a density correction,
C is a shell correction and
W_{max} is the maximum energy transfer in a single collision.
According to equation 2.23 electrons with an energy of 1.5MeV have the lowest energy loss in silicon and thus deposit the lowest charge in the sensor. Such an electron is called MIP[1] and sensors for particle detection are developed to detect also these MIPs. Therefore the most important sensor parameter, the signal-to-noise ratio, is defined for a MIP.

The energy loss calculated by 2.23 describes the mean energy loss per traversed material. The fluctuation around this mean value is described by the Landau distribution. The probability $\phi(E)dE$ that a charged particle looses energy between E and E ± dE is given to:

$$\phi(E)dE = \frac{2\pi N_L e^4 Z}{m_e v^2 A} \frac{1}{E^2} \tag{2.24}$$

This and the mean energy loss by Bethe-Bloch formula lead to the deviation from the mean value $\lambda = E - E_{mean}$ [Moy55]:

$$\omega(\lambda) = \frac{1}{\pi} \int_0^\infty e{-}uln(u) - \lambda(u) \sin \pi u du \approx \frac{1}{\sqrt{2\pi}} \tag{2.25}$$

Recombination

For indirect semiconductors like silicon, the direct band-to-band recombination is suppressed as it requires a large momentum transfer to the crystal lattice. In contrast to that, recombination is realized by a two step process of capturing and emitting electrons and holes at states within the band gap caused. For n-type semiconductors the recombination time τ_r is given by $\frac{1}{\beta n_0}$ and for indirect semiconductors the recombination factor β is given by [Lut]:

$$\beta = \frac{N_t v_{th,n} \sigma_n v_{th,p} \sigma_p}{v_{th,n}\sigma_n[n + n_i \exp(\frac{E_t - E_i}{k_B T})] + v_{th,p}\sigma_p[p + n_i \exp(\frac{E_i - E_t}{k_B T})]} \tag{2.26}$$

with the initial doping concentration n_0.

[1] minimum ionizing particle

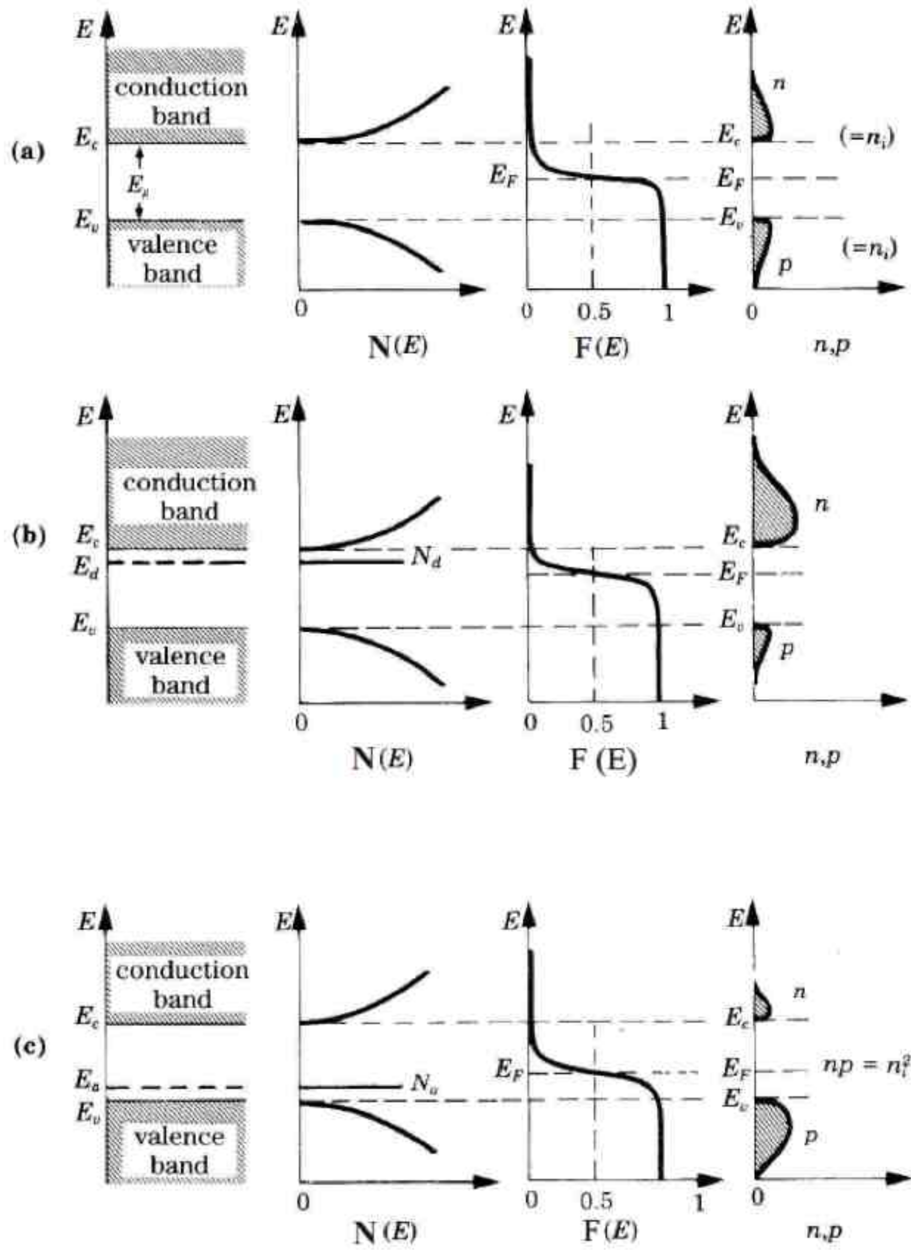

Figure 2.5.: Illustration of the energy band structure, the density of states, the occupation probability and the carrier concentration for (a) intrinsic semiconductors, (b) N type silicon and (c) P type silicon [Sap94].

2.2. Basic Semiconductor Devices

2.2.1. The pn-Junction

One of the most important electronic structures is the pn-junction. Created by bringing together two extrinsic semiconductors of opposite doping, it works as a diode, conducting current basically in one direction.
Starting with the separated n-doped and p-doped regions in thermal equilibrium figure 2.6(a) shows the energy bands. Bringing the two regions together as shown in figure 2.6(b), electrons will diffuse from the n-doped region to the p-doped region and recombine, while the holes from the p-doped region will do the same vice versa. The surplus of ionized donors and acceptors creates an electric field that counteracts the diffusion. The resulting region is called space charge region (SCR) and is practically free of charge carriers.

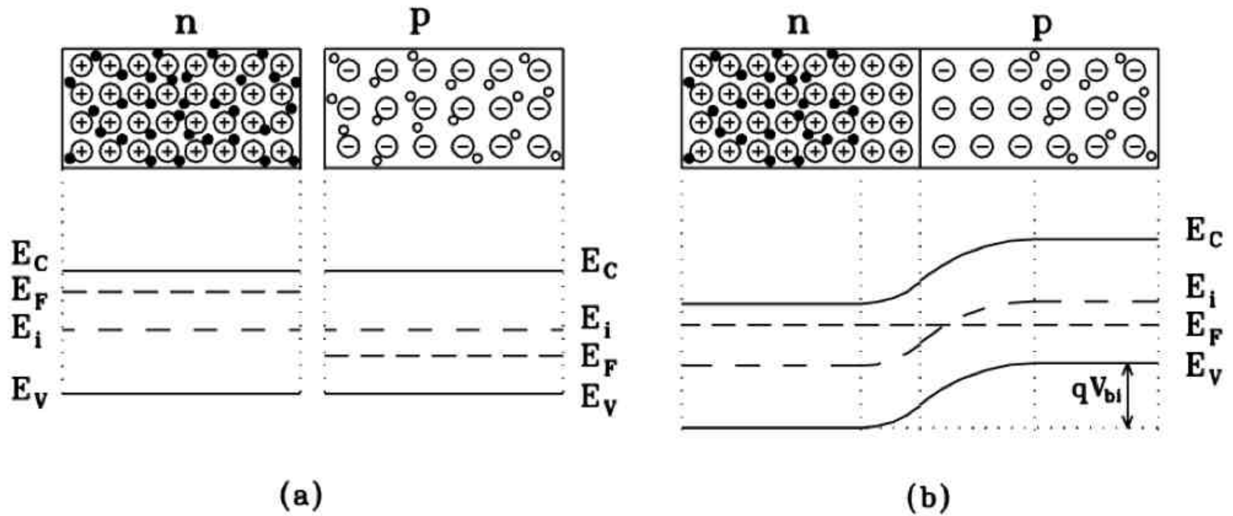

Figure 2.6.: A pn-junction in thermal equilibrium. In (a) the n-doped and the p-doped regions are separated and in (b) the regions are brought together [Lut]. By joining the regions together, the electrons move to the n-side with the lower Fermi levels, while the holes move to the p-side with the higher Fermi levels. Around the contact region, a so called space charge region without free charge carriers is built.

The evolved electric potential is called built-in voltage:

$$V_{bi} = \frac{1}{q}(E_i^p - E_i^n) = \frac{k_B T}{q} ln \frac{N_A N_D}{n_i^2} \tag{2.27}$$

Figure 2.7 shows the space charge region with the width d=d$_p$+d$_n$, the charge distribution, the resulting electric field and the electric potential distribution.

The width of the space charge region d and the maximum electric field are given by [Lut]:

$$d = d_p + d_n = \sqrt{\frac{2\epsilon\epsilon_0 V_{bi}}{q(N_A + N_D)}} \left[\sqrt{\frac{N_A}{N_D}} + \sqrt{\frac{N_D}{N_A}}\right] = \sqrt{\frac{2\epsilon\epsilon_0 (N_A + N_D) V_{bi}}{q N_A N_D}} \tag{2.28}$$

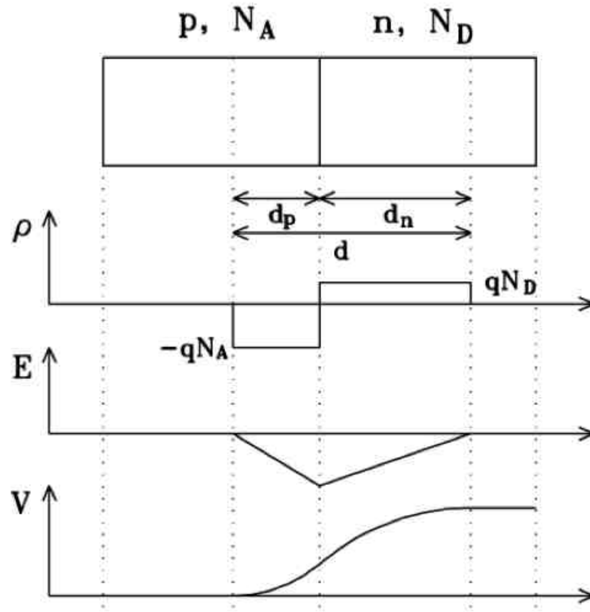

Figure 2.7.: Illustration of a pn-junction showing from top to bottom: the space charge region, the the charge distribution, the resulting electric field and the electric potential distribution [Lut].

$$E_{max} = \frac{q}{\epsilon\epsilon_0} N_D x_n = \sqrt{\frac{2q}{\epsilon\epsilon_0} \frac{N_A N_D}{N_A + N_D} V_{bi}} \tag{2.29}$$

For a silicon diode, a low doped bulk region and a highly doped thin layer are used to form the pn-junction. In this case, where $N_A \gg N_D$, equation 2.28 becomes:

$$d = \sqrt{\frac{2\epsilon\epsilon_0}{qN_D} V_{bi}} \tag{2.30}$$

If an external voltage is applied the width of the space charge region will change, depending on the polarity. Applying a forward bias will shrink the region, operating at a reverse bias will expand the region. Replacing the built-in voltage V_{bi} with V_{bi}-V and assuming $N_A \gg N_D$ the voltage at which the space charge region reaches the thickness D of the diode is:

$$V_{fd} = \frac{q}{2\epsilon\epsilon_0} |N_{eff}| D^2 \tag{2.31}$$

where V_{fd} is the full depletion voltage and $|N_{eff}| = N_D - N_A$.
The current-voltage characteristics can be derived from the minority carrier concentration at the edge of the neutral region:

$$n_p = n_n e^{-q\frac{V_{bi}-V}{k_B T}} = n_{p0} e^{q\frac{V}{k_B T}} \tag{2.32}$$

$$p_n = p_{n_0} e^{q\frac{V}{k_B T}} \tag{2.33}$$

As the minority carrier diffusion current is proportional to the deviation from thermal equilibrium,

the current can be expressed as:

$$J = (J_{S_n} + J_{S_p})(e^{\frac{qV_{bias}}{k_B T}} - 1) = J_S(e^{\frac{qV_{bias}}{k_B T}} - 1) \tag{2.34}$$

and J_S is the total reverse bias saturation current:

$$J_S = q\left(\frac{n_{p0}D_n}{\sqrt{D_n\tau_{r_n}}} + \frac{p_{n0}D_p}{\sqrt{D_p\tau_{r_p}}}\right) \tag{2.35}$$

where $\tau_{r_{n(p)}}$ is the charge carrier lifetime, $D_{n(p)}$ is the diffusion constant and n_{p0}(p_{n0}) is the electron or hole density at the edge of the neutral p or n region at thermal equilibrium. For reverse biased diodes with $n \cdot p \ll n_i^2$ the thermal generation dominates and the volume current is given by:

$$J_V \approx -q\frac{n_i}{\tau_g}W \tag{2.36}$$

with the width of the pn-junction W.

The capacitance-voltage characteristics depends on the effective doping concentration and can be used to determine the full depletion voltage, see equation 2.31. When the space charge region is increased from x to $x + dx$, the surface charge of the p-side will increase by $qN_D dx$ causing an electric field change of $\frac{qN_D dx}{\epsilon\epsilon_0}$ and a surface voltage change of $x\frac{qN_D dx}{\epsilon\epsilon_0}$. Integrated over the width of the space charge region W gives total charge Q_P and total potential ϕ_P:

$$Q_P = -\int_0^W qN_D(x)dx \tag{2.37}$$

$$\phi_P = \int_0^W \frac{qN_D(x)}{\epsilon\epsilon_0}xdx \tag{2.38}$$

ϕ_P must be equal to $V_{bi} - V_{bias}$. The capacitance per area of the diode is given by [Lut]:

$$C = \frac{\partial Q_P}{\partial V} \approx \frac{\epsilon\epsilon_0}{W} \tag{2.39}$$

and the doping concentration N_D can be calculated using:

$$\frac{\partial(1/C^2)}{\partial V} = \frac{\partial(1/C^2)/\partial W}{\partial V/\partial W} = \frac{2W/(\epsilon\epsilon_0)^2}{qN_D W/(\epsilon\epsilon_0)} = \frac{2}{qN_D\epsilon\epsilon_0} \tag{2.40}$$

The capacitance of a fully depleted diode is given by:

$$C = \begin{cases} A\sqrt{\frac{q\epsilon\epsilon_0 N_D}{2V_{bias}}} & , V_{bias} \leq V_{fd} \\ A\frac{\epsilon\epsilon_0}{d} & , V_{bias} \geq V_{fd} \end{cases} \tag{2.41}$$

with the area A, the thickness d and the external bias voltage V_{bias}.

2.2.2. The Metal-Insulator-Semiconductor Structure

Since the common insulators in the case of silicon are oxides, the Metal-Oxide-Semiconductor device (MOS) consists of a semiconductor and a metal, separated by a insulating oxide layer. The MOS can be used to investigate the quality of the insulating oxide layer and surface effects of the semiconductor.

In an ideal case, identical work functions for metal and semiconductor and no space charges in the oxide can be assumed.

The operation of a MOS, depending on the externally applied voltage can then be divided into four conditions shown in figure 2.8.

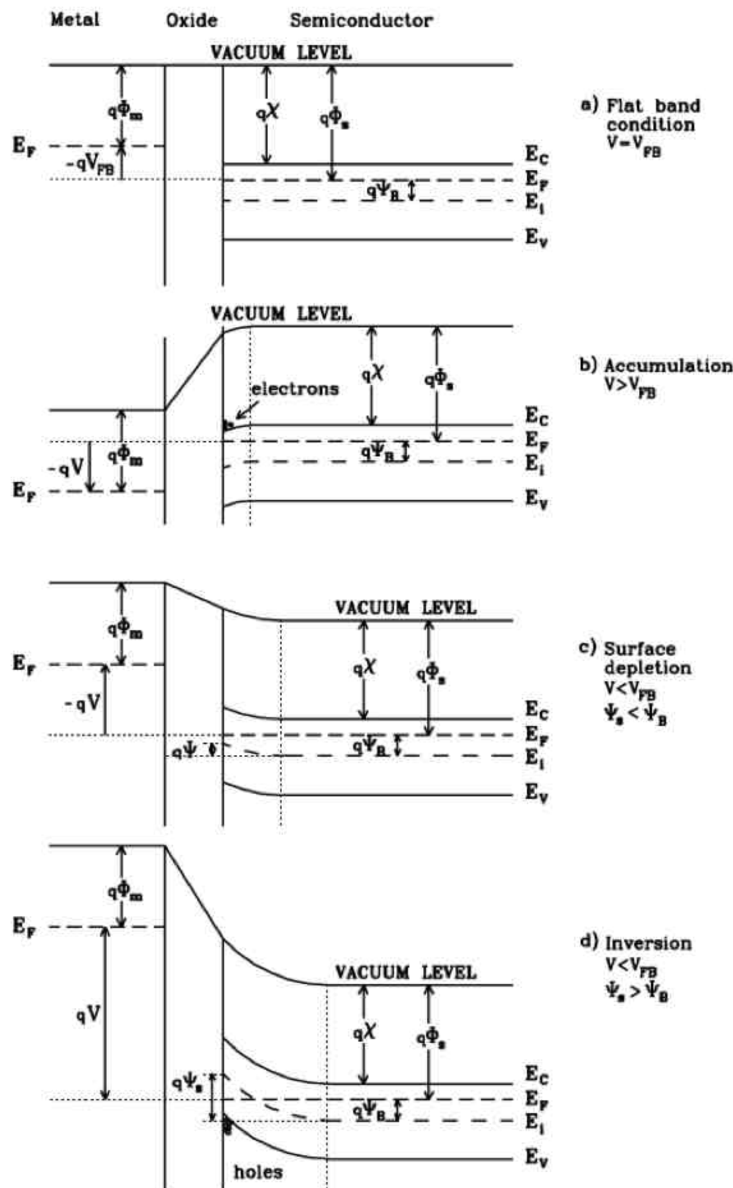

Figure 2.8.: An n-type MOS structure in the band model without oxide charges: (a) The flat-band condition, (b) accumulation, (c) surface depletion and (d) inversion. [Lut].

Flat-Band condition

In this condition, the applied electric field forms a flat conduction and valence band as shown in figure 2.8(a) with a constant vacuum level throughout the device, assuming no oxide charges. The flat-band voltage is given by:

$$V_{FB} = \phi_m - \phi_s \tag{2.42}$$

Accumulation $V > V_{FB}$

If a higher voltage than the flat band voltage is applied across the structure, the energy bands get bent towards the Fermi level as shown in figure 2.8(b). The electron concentration will increase, fulfilling the thermal equilibrium condition $\frac{n}{n_i} = e^{\frac{E_F - E_i}{k_B T}}$. The result is a very thin charge layer at the silicon-oxide interface with a surface charge of:

$$Q_{acc} = -\epsilon_{ox}\epsilon_0 \frac{V - V_{FB}}{d_{ox}} = C_{ox}(V - V_{FB}) \tag{2.43}$$

where C_{ox} is the oxide capacitance per unit area.

Depletion $V \leq V_{FB}$

If a lower voltage than the flat band voltage is applied, the energy bands get bent downwards, see figure 2.8(c). The concentration of electrons near the interface will decrease, building up a depleted region. The depth of the region is given by:

$$d_s = \sqrt{\frac{\epsilon_s \epsilon_0}{q N_D}(V_{FB} - V) + \left(\frac{\epsilon_s}{\epsilon_{ox}} d_{ox}\right)^2} - \frac{\epsilon_s}{\epsilon_{ox}} d_{ox} \tag{2.44}$$

Inversion $V \leq V_{FB}$

If the voltage is much lower than the flat band voltage, such that intrinsic level at the interface will reach the Fermi level ($\Psi_s \leq \Psi_B$), the hole concentration at the silicon-oxide interface increases, see figure 2.8(d). The surface charge density of the inversion layer is then given as:

$$Q_{inv} = (V_T - V C_{ox}) \tag{2.45}$$

with the threshold voltage $V_T = V_{FB} - 2\Psi_B - \frac{d_{ox}}{\epsilon_{ox}\epsilon_0}\sqrt{4 q N_D \epsilon_s \epsilon_0 \Psi_B}$. The depletion depth equals $d_{max} = \sqrt{\frac{4\epsilon_s\epsilon_0\Psi_B}{q N_D}}$.

2.2.3. Silicon Strip Detectors

Silicon strip detectors are used to get a position information of a traversing radiation particle. The detector has therefore a segmentation. Figure 2.9 shows a cross section of a n-type silicon strip sensor.

A n-doped silicon bulk of 300 µm thickness has strip segmentation in the form of highly p-doped regions at the bulk surface. These p+ strips are covered by a thin oxide layer which is again topped

by aluminium strips (AC coupling). The aluminum strips run above the p+ implants being a little bit wider in order to reduce the electric field strength at the implants. This design feature increasing the voltage robustness is called metal overhang.
The back side of the n-bulk consists of a highly n-doped layer covered by aluminium in order to get a good ohmic contact and is called backplane.
To operate the sensor, a bias voltage is applied between the backplane and the strips to fully deplete the sensor, by extending the space charge region of the many pn-junctions at the strips over the whole sensor thickness. An ionizing particle that traverses the sensor will create electron-hole-pairs along its track. Due to the electric field, the charges will drift towards the electrodes. The p+ implants on top of the sensor will collect the charges and couple the signal to the aluminium strip, which is connected to the readout electronics where amplification and signal processing take place.

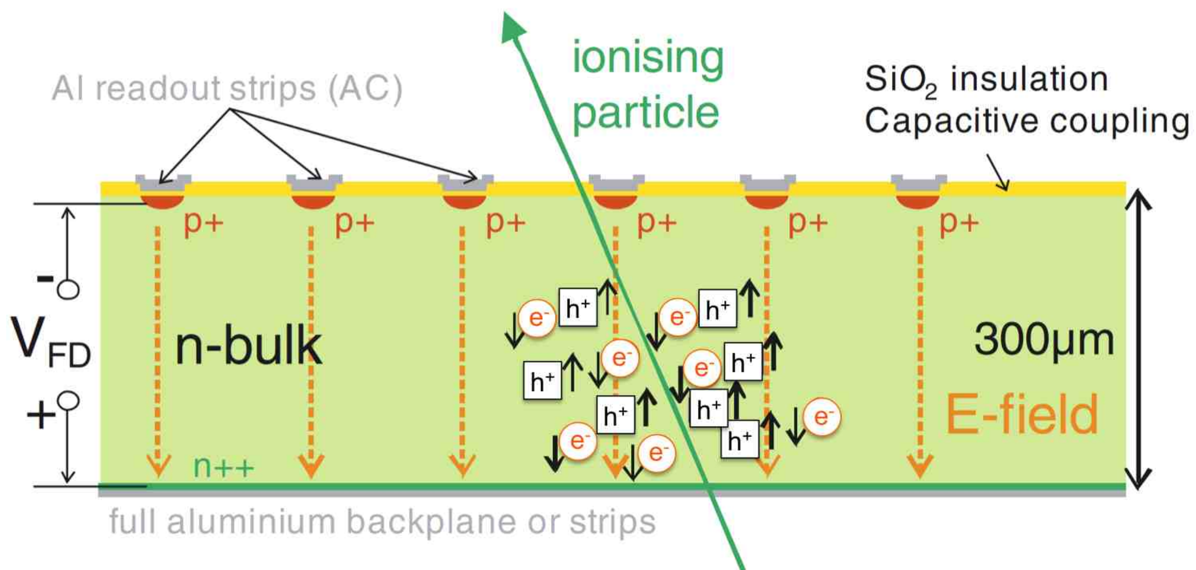

Figure 2.9.: Cross section of a n-type silicon strip sensor. It consists of a n-doped silicon bulk with a strip segmentation of p+ implants separated by a oxide layer from the readout strips on one side, and a highly doped layer of n++ covered by aluminium on the other side. Transversing ionizing particles create electron-hole-pairs along its track which drift towards the electrodes due to the electric field of the applied reverse bias voltage. The signal of the holes is coupled from the p+ implants to the aluminum readout strip that is connected with the readout electronics [Har08].

A more detailed view of a silicon strip sensor can be seen in the 3D sketch in figure 2.10. The sensor periphery consists of a highly n-doped ring surrounding the sensor connected by vias to an aluminium layer where alignment markers are placed and some sensor information is written on. The bias ring is set to ground and connected via bias resistors to the p+ implants, while a high positive potential is connected to the sensor backplane. The guard ring is placed around the bias ring, it shapes the electrical field in the active sensor area. The readout electronics is connected to the AC pads via wire bonding while the DC pads are only for quality testing purpose. To protect the structures, the whole sensor is covered with a passivation layer of silicon dioxide with openings at the contact pads.
A standard strip consists of the implant strip separated by an oxide from the aluminium readout

strip . The AC contact pads are favorably placed at the sensor edge, allowing to bond the readout electronics by wire bonding to the AC pads.

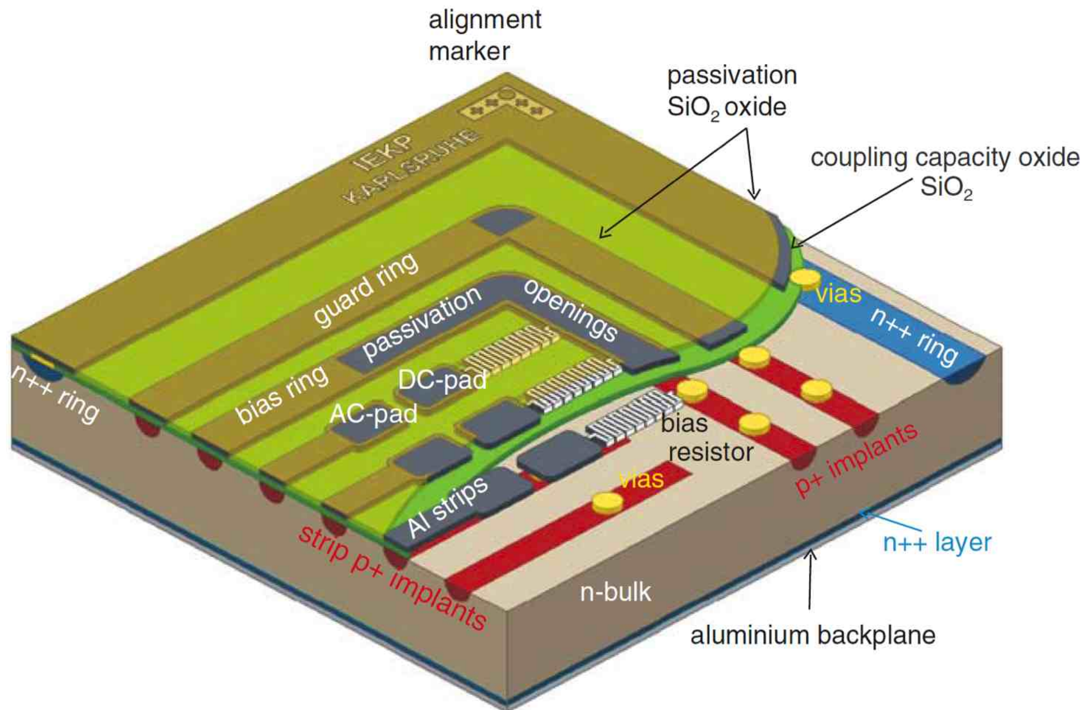

Figure 2.10.: 3D sketch of a n-type silicon strip sensor. At the edge of the sensor a highly n-doped ring surrounds the hole sensor to protect the sensor from edge effects like high dark currents due to the sensor cutting, and to ensure homogeneous field distributions. The bias ring is set to ground and connected to the p+ implant strips via bias resistors to provide the same potential to all implant strips. A floating guard ring surrounds the bias ring in order to ensure a defined drop of the bias voltage shaping a homogeneous electric field. The readout electronics is connected to the AC pads, while the DC pads are only implemented for quality testing purpose. [Har08].

Sensors with p-bulk have n+ implants on top and a highly doped p++ backplane. They are also reversed biased, but with high negative voltage at the backplane collecting electrons at the implants. Other than n-type sensors, the p-type sensors need an additional strip isolation. As the positive charges in the oxide attract an accumulation layer of negative charge carriers at the oxide-substrate interface, this accumulation layer shorts the n-doped strips. To separate them, an additional implantation of p-doped areas between the n+ strips is necessary. There are two main isolation techniques, the so-called p-stop technique with a narrow but deep highly p-doped area and the p-spray technique with a uniform but low p-doped surface. Figure 2.11 shows both techniques plus a combination of both.

2.2.4. Noise Sources

There are several sources of noise in an electronic element. This section will name them and give a rough overview of their influence on the total noise:

- **thermal noise** with a serial thermal noise contributed by the resistance of the metal strip in

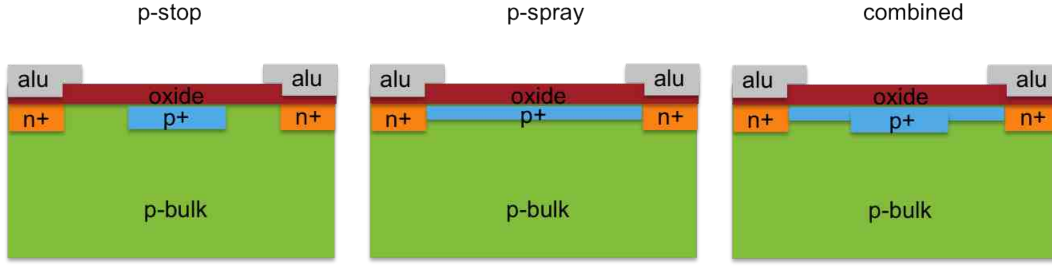

Figure 2.11.: Isolation techniques for p-type silicon strip sensors. From left to right there are the p-stop isolation with a highly p-doped area, the p-spray isolation with a low uniform p-doped surface and the combination of both.

series with the readout line:

$$\frac{d\overline{U^2_{n,strip}}}{df} = 4k_BTR_{metal} \tag{2.46}$$

and a parallel thermal noise by thermal fluctuations of the electron distribution in the bias resistors:

$$\frac{d\overline{I^2_{n,bias}}}{df} = \frac{4k_BT}{R_{bias}} \tag{2.47}$$

- **shot noise** based on the statistic fluctuations in the number of charge carriers:

$$\frac{\langle dI^2_{shot} \rangle}{df} = 2eI_{leakage} \tag{2.48}$$

- **preamplifier's input transistor** whose equivalent noise charge contribution at the proper amplifier is:

$$Q_{n,p} = -u_{n,amp}(C_{strip} + C_{in} + C_f) \tag{2.49}$$

for parallel noise and

$$Q_{n,s} = u_{n,amp}C_{strip,bulk} \tag{2.50}$$

for serial noise, where the total capacitance of a strip C_{strip} is given by:

$$C_{strip} = \frac{C_c(2C_{int} + C_{back})}{C_c + (2C_{int} + C_{back})} \approx 2C_{int} + C_{back} \tag{2.51}$$

with the coupling capacitance C_c, the inter-strip capacitance C_{int} and the back plane capacitance C_{back} extracted from the CV curve divided by the number of strips $\frac{C_{tot}}{N_{strips}}$.

The total noise is the quadratic sum of the components:

$$Q^2_{total} = 2eI_{leakage}T_sF_i + \frac{4k_BT}{R_{bias}}T_sF_i + F_uC^2_{strip}4k_BTR_{metal} + F_uC^2_{strip}u^2_{n,amp} \tag{2.52}$$

with the pulse shaping time T_s and the pulse shaping correlated form factors F_u for noise voltage and F_i for noise currents. With the pulse response function W(t), F_i and F_u are given by:

$$F_i = \frac{1}{2T_s} \int_{-\infty}^{\infty} W(t)^2 dt, \qquad F_u = \frac{T_s}{2} \int_{-\infty}^{\infty} \left[\frac{dW(t)}{dt} \right]^2 dt \tag{2.53}$$

This short overview of noise contributing parameters has been done in order to illustrate the influence of several sensor parameters that will be measured and discussed in chapter 7.2. A more detailed treatment of the noise components can be found in [Die03] or [Lut].

Chapter 3.

Radiation Damage in Silicon

To ensure proper operation of silicon strip detectors over the lifetime of an experiment it is necessary to understand the effects of radiation damage on sensor properties and performance. This chapter will give an introduction to the radiation damage mechanisms and the changes of material properties.

3.1. Damage Mechanisms

Ionization is one of the important processes of interaction of radiation with matter. Generating electron-hole pairs by interactions of the radiation with the electron cloud creates no permanent damage and is reversible, but interactions with the silicon lattice causes permanent damage by displacing lattice atoms. The following processes are important for the lattice:
The minimum recoil energy to kick a silicon atom from its lattice site is around 15 eV. The energy at which the probability to displace an atom is one half is $E_d = 20$ eV [Lin79], since it depends on the recoil direction. Below this value the energy is dissipated as phonons. Particles with energies above this limit kick a silicon atom out of the lattice and create vacancy interstitial pairs, called Frenkel pairs. The maximum recoil energy $E_{R_{max}}$ of a particle with mass m and energy E in a head-on collision with silicon ($M \approx 28\ m_p$) is:

$$E_{R_{max}} = \frac{4Mm}{(M+m)^2}E \tag{3.1}$$

Table 3.1 gives an overview of the maximum and average recoil energies for the electron, the proton, the neutron and the silicon atom.

The first silicon atom hit (primary knock-on atom, PKA) moves through the crystal creating further damage along its track. The range R is given by [Lin79]:

$$R \approx 32\frac{nm}{keV}\sqrt{E_R} \quad for \quad E_R < 10keV \tag{3.2}$$

where E_R is the recoil energy of the PKA. The rate of energy loss can be derived from the range as $\frac{dE_R}{dz} \sim \sqrt{E_R}$. For recoil energies in the range of $1-2\ keV$ only isolated (point) defects will be created. For higher recoil energies $E_R \geq 10\ keV$ several clusters[1] and additional point defects will be produced. Both the energy loss and the mean free path between two interactions decrease with decreasing recoil energy.

[1]Dense agglomeration of point defects that appear at the end of a recoil silicon track.

Table 3.1.: Characteristics of interaction of radiation with silicon [Lut]. The table shows the interaction process, the maximum and average recoil energy at a particle energy of 1 MeV and the minimum energy needed to create point defects or cluster.

Radiation	Electrons	Protons	Neutrons	Si^+
Interaction	Coulomb scattering	Coulomb and nuclear scattering	Elastic nuclear scattering	Coulomb scattering
$E_{R_{max}}$ [eV]	155	133700	133900	1000000
$E_{R_{av}}$ [eV]	46	210	50000	265
E_{min} [eV]				
- point defect	260000	190	190	25
- cluster defect	4600000	15000	15000	2000

In figure 3.1 the most frequent lattice defects in a silicon crystal are pictured. There are displaced silicon atoms, called interstitials or missing silicon atoms in the silicon lattice, called vacancies and other defects created by foreign atoms of oxygen, phosphorus, boron, or carbide. All of the shown defects can also be clustered in larger defect regions.

The displacement damage can be calculated by:

$$D(E) = \sum_i \sigma_i(E) \int_0^{E_{R_{max}}} f_i(E, E_R) P(E_R) dE_R \tag{3.3}$$

where the sum runs over all possible interactions of the radiation particle with the energy E and the silicon atoms that lead to displacements. σ_i is the cross section of the corresponding interaction, $f_i(E,T)$ is the probability for the generation of a PKA with the recoil energy E_R. $P(E_R)$ is the Lindardt Partition function [LN62] and gives the fraction of energy, which is spent for displacement. Some values are: $P(E_R) \approx 50\%$ for 10 MeV protons, $P(E_R) \approx 42\%$ for 24 GeV protons and $P(E_R) \approx 43\%$ for 1 MeV neutrons.

The NIEL[2] scaling hypothesis tries to compare the radiation damage induced by different particles and particle energies. Thereby it is assumed, that the damage scales linearly with the fluence. The reference particles are neutrons at an energy of 1 MeV. Their damage factor is defined to be $D_{neutrons}(1\ MeV) = 95\ MeV mb$. The hardness factor k defined as the ratio of fluence to equivalent fluence is:

$$k = \frac{\int D(E)\phi(E)dE}{D(1MeV)\int \phi(E)dE} = \frac{\phi}{\phi_{eq}} \tag{3.4}$$

with the fluence $\phi(E)$. Figure 3.2 shows the displacement damage function D(E) of neutrons, protons, pions and electrons normalized to 95 MeV mb.

[2]Non-Ionizing Energy Loss

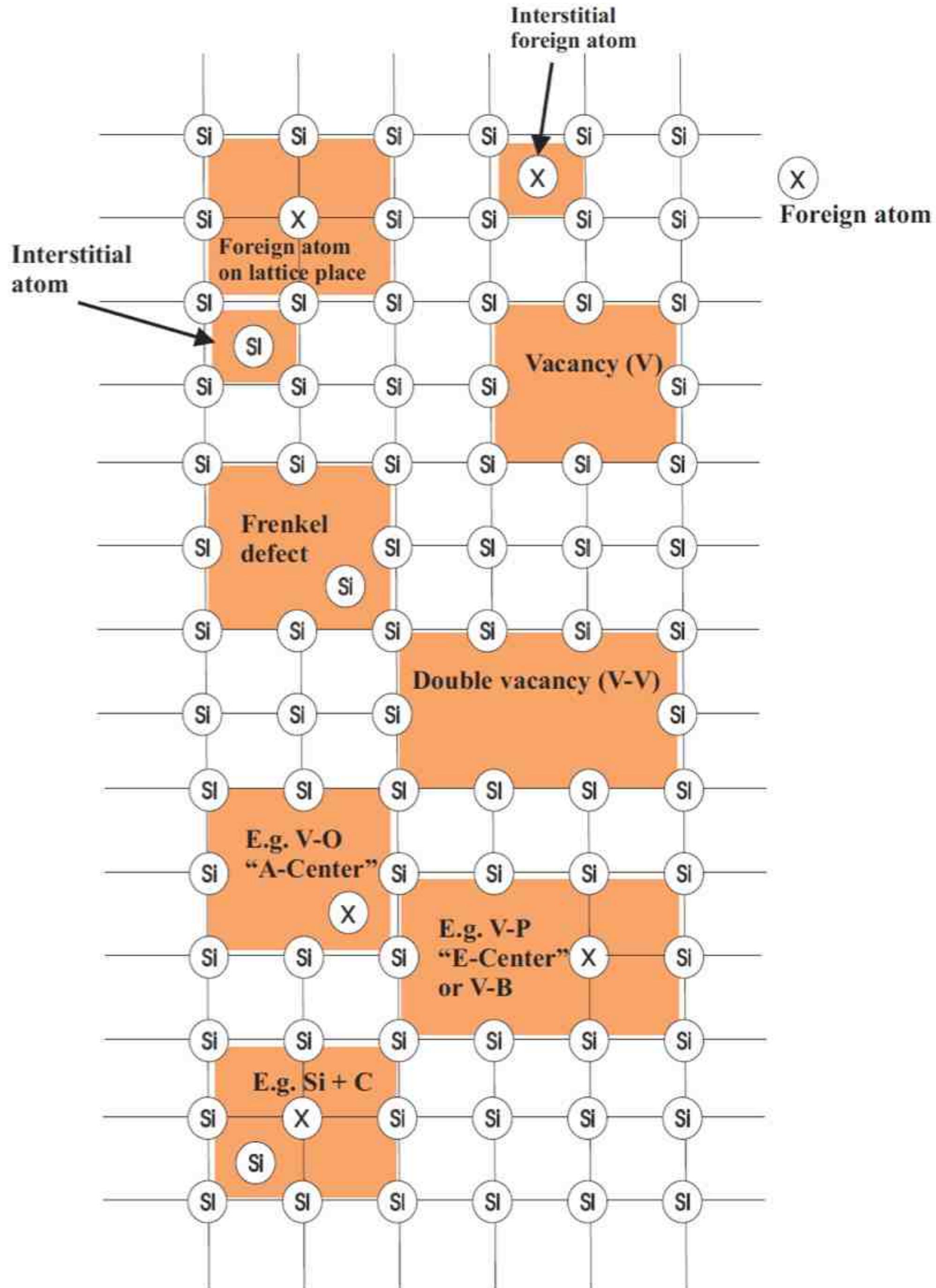

Figure 3.1.: Illustration of important defects in silicon [Fur05].

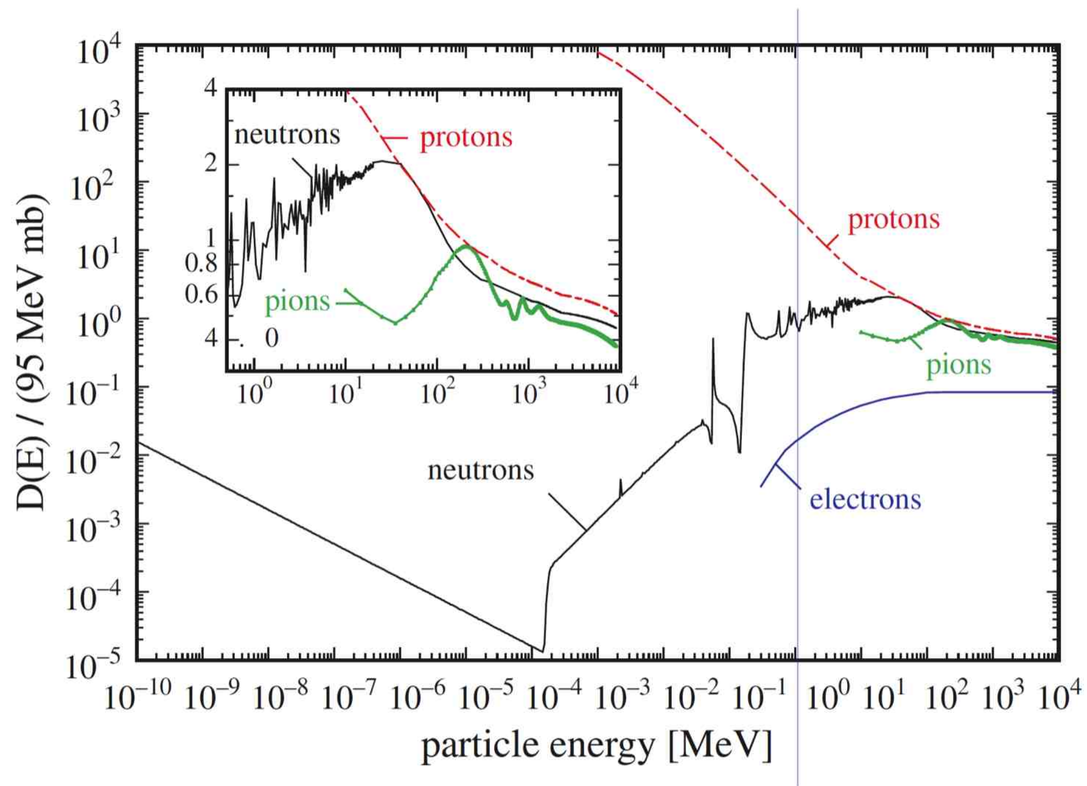

Figure 3.2.: Displacement damage function for different particles [Lin03], normalized to 95MeV mb.

3.2. Macroscopic Effects of Radiation Damages on Silicon Detector Parameters

Additional energy levels in the band gap created by radiation change the sensor properties. The following main consequences of energy levels in the band gap, as shown in figure 3.3, will be discussed. They can

- act as **recombination-generation centers** capturing and re-emitting electrons and holes, which increases the leakage current.
- **change the charge density in the space charge region** which will have an impact on N_{eff} and V_{depl}.
- act as **trapping centers** capturing and re-emitting electrons and holes with a time delay, which leads to a lower charge collection efficiency, as trapped charges do not contribute to the signal.

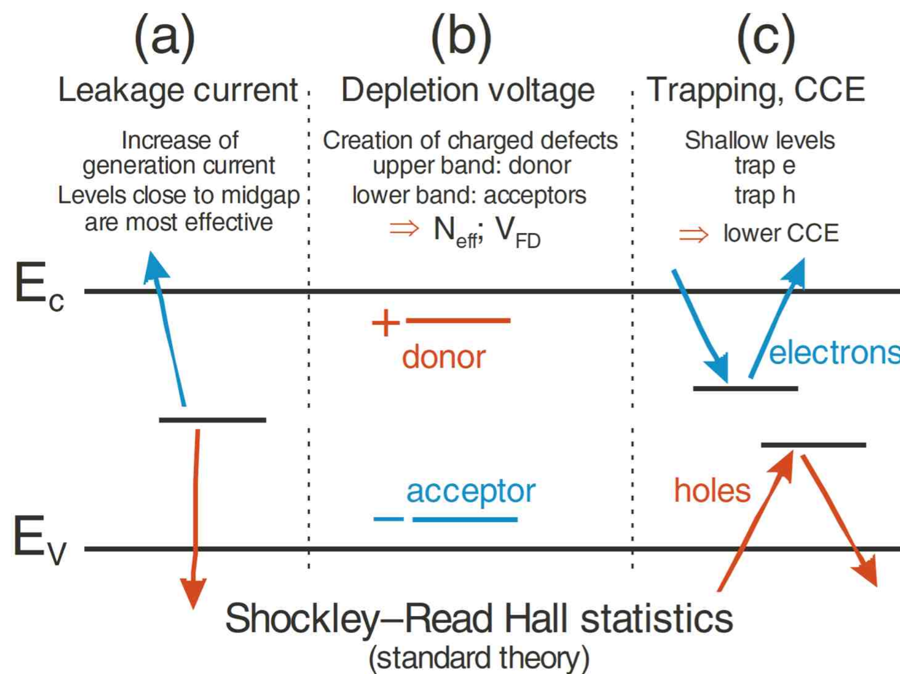

Figure 3.3.: Illustration of the defect energy levels responsible for the change of silicon properties [Har08]. (a) Energy levels in the band gap act as recombinaton-generation centers, increasing the leakage current. (b) Donor levels near the conduction band and acceptor levels near the valence band change the charge density in the space charge region and thus influence the depletion voltage. (c) Trapping centers close to the middle of the band gap reduce the charge collection efficiency by capturing and re-emitting charges with some time delay.

Considering thermal equilibrium, the capture rates for electrons and holes are given by:

$$R_n = \sigma_n v_{th,n} n_i N_d (1 - F) \exp \frac{E_F - E_i}{k_B T} \tag{3.5}$$

$$R_p = \sigma_p v_{th,p} n_i N_d (1 - F) \exp \frac{E_i - E_F}{k_B T} \tag{3.6}$$

and the electron generation rate:

$$G_n = N_d F \epsilon_n \tag{3.7}$$

with the Fermi level

$$F = F(E_d) = \frac{1}{1 + \exp \frac{E_d - E_F}{k_B T}} \tag{3.8}$$

The emission probabilities are calculated to:

$$\epsilon_n = \sigma_n v_{th,n} n_i \exp \frac{E_d - E_i}{k_B T} \tag{3.9}$$

$$\epsilon_p = \sigma_p v_{th,p} n_i \exp \frac{E_i - E_d}{k_B T} \tag{3.10}$$

for electrons and holes. For low fluences the ratio of charge states in the space charge region can be calculated to:

$$\frac{f^-}{f^+} = \frac{\epsilon_n}{\epsilon_p} = \frac{\sigma_n v_{th,n}}{\sigma_p v_{th,p}} \exp \left(2 \frac{E_d - E_i}{k_B T}\right) \tag{3.11}$$

Defects with an energy above the intrinsic Fermi Level E_i have a higher electron emission probability. Energy levels below E_i prevail electron capturing. For heavily irradiated pn-junctions the leakage current increases to large values and the charge ratio is then given by [Lut]:

$$\frac{f^-}{f^+} = \frac{\epsilon_n + p c_p}{\epsilon_p + n c_n} = \frac{c_n n_i \exp\left(\frac{E_d - E_i}{k_B T}\right) + p c_p}{c_p n_i \exp\left(-\frac{E_d - E_i}{k_B T}\right) + n c_n} \tag{3.12}$$

As shown in figure 3.3 radiation induced defects basically affect the leakage current, the full depletion voltage and the charge collection efficiency.

3.2.1. Leakage Current

The increase of leakage current is found to be proportional to the irradiation fluence [Mol99]:

$$\frac{\Delta I}{V} = \alpha \Phi_{eq} \tag{3.13}$$

where V is the volume of the diode and Φ_{eq} is the equivalent fluence of 1MeV neutrons. The current related damage rate α has proven by measurements found to be independent of the material, which can be seen in figure 3.4.

Observations showed that the leakage current and thus the *alpha*-parameter drops with time. Figure 5.3 shows the annealing behavior at different temperatures.

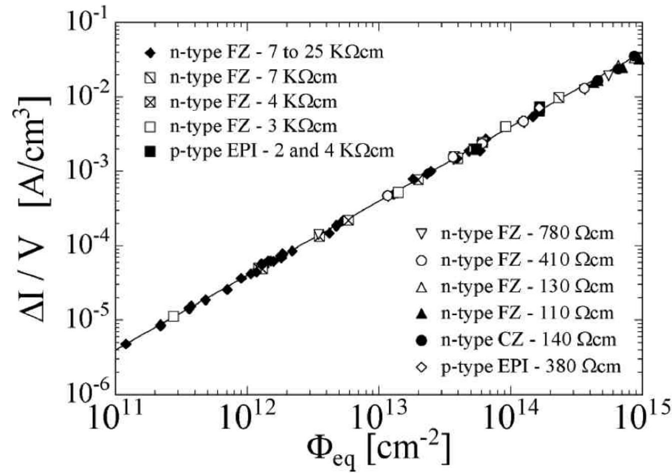

Figure 3.4.: Fluence dependence of the leakage current of different silicon materials [Mol99]. The slope, defining the current related damage rate α is material independent at a given temperature. After a heat treatment of 80 min at 60°C the value for α is $(3.99 \pm 0.03) \times 10^{-17}$ A/cm.

The following parametrization can be found for α [Mol99]:

$$\alpha(t) = \alpha_0 + \alpha_I \exp -\frac{t}{\tau_I} - \beta \cdot ln\frac{t}{t_0} \tag{3.14}$$

where $\alpha_I \sim 1.25 \times 10^{-17} A/cm$, $\beta \sim 3 \times 10^{-18} A/cm$ and t_0=1min. Table 3.2 shows the values of the temperature dependent parameters τ_I and α_0. The average damage rate after 80min at 60°C is $4 \times 10^{-17} A/cm$. This state of annealing is chosen, as the change in the effective doping concentration ΔN_{eff} has its minimum there [Mol99].

Table 3.2.: Parameters for the annealing of the leakage current from [Mol99]. Below room temperature τ_I becomes larger than 100 days. As the exponential term in equation 3.14 vanishes, there is almost no annealing any more.

Annealing temperature in °C	21	49	60	80
α_0 in $10^{-17} A/cm$	7	6	5	4
τ_I [min]	140000	260	94	9

3.2.2. Depletion Voltage

In order to guarantee full charge collection efficiency of a sensor, the space charge region has to cover the whole bulk. Therefore the sensor has to be operated at full depletion. As shown in equation 2.31 V_{fd} depends on N_{eff}, which changes during irradiation due to the creation of charged defects in the band gap, see figure 3.3. The change can be parametrized by the so called Hamburg model:

$$\Delta N_{eff} = N_C(\Phi_{eq}) + N_A(\Phi_{eq}, t) + N_Y(\Phi_{eq}, t) \tag{3.15}$$

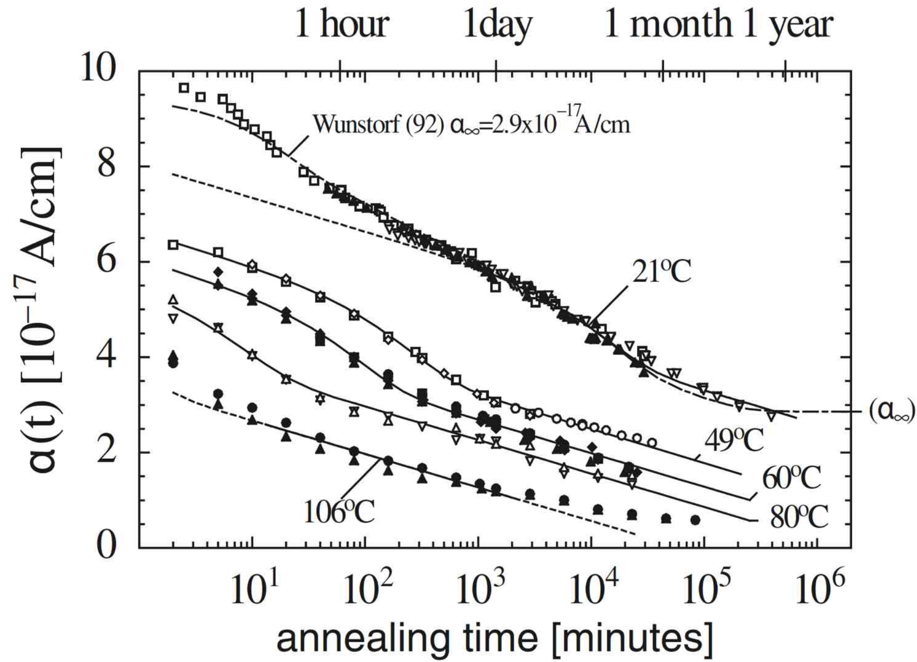

Figure 3.5.: The current related damage rate anneals with time [Mol99]. For higher temperatures α can reach even lower values.

where

1. $N_C(\Phi_{eq})$ is the **stable damage** and given by:

$$N_C(\Phi_{eq}) = N_{C,0}(1 - \exp(-c\Phi_{eq})) + g_c\Phi_{eq} \tag{3.16}$$

where the first term considers an incomplete donor removal of the initial effective doping concentration N_{eff} and the second term describes a continuous rise of stable acceptors. For standard FZ an average constant $g_c = (1.49 \pm 0.04) \times 10^{-2} cm^{-1}$ can be measured [Mol99].

2. $N_A(\Phi_{eq}, t)$ is the **beneficial** or **short term annealing**. Beneficial because N_{eff} increases with irradiation and if it was negative it becomes smaller, thus the depletion voltage drops. It can be summarized as:

$$N_A(\Phi_{eq}, t) = \Phi_{eq}\Sigma_i g_{a,i} \exp\left(-\frac{t}{\tau_{a,i}}\right) \tag{3.17}$$

where the introduction rate of the defect with the longest time constant was measured to be $g_a = (1.81 \pm 0.14) \times 10^{-2} cm^{-1}$. Some values for the time constant τ_a are listed in table 3.3.

3. $N_Y(\Phi_{eq}, t)$ is the **reverse annealing**. After long annealing times acceptor like defects have developed by a second order process:

$$N_Y(\Phi_{eq}, t) = N_{Y,\infty}\left(1 - \frac{1}{1 + k_y N_{Y,\infty} t}\right) \tag{3.18}$$

with the measured value: $N_Y(\Phi_{eq}, t) = (5.16 \pm 0.09) \times 10^{-2} cm^{-1}$. Values for τ_y are listed in table 3.3.

Table 3.3.: Temperature dependent time constants for short (beneficial) and long (reverse) annealing from [Mol99].

Annealing temperature in °C	-10	0	10	20	40	60	80
Short term annealing (τ_a)	306 d	53 d	10 d	55 h	4 h	19 min	2 min
Reverse annealing (τ_y)	516 y	61 y	8 y	475 d	17 d	21 h	92 min

3.2.3. Type Inversion

Type inversion occurs only in n-type sensors. Figure 3.6 shows the evolution of the full depletion voltage in dependence of fluence and annealing time. At a given annealing time, the full depletion voltage drops at low fluences until it reaches the inversion point, where the n-bulk sensor becomes an effective p-type sensor. After inversion the full depletion voltage rises with increasing fluence.
At a given fluence, the N_{eff} increases with annealing time, which for n-type sensors results in a decrease of the full depletion voltage before type inversion and an rise of the full depletion voltage after type inversion [Die03].

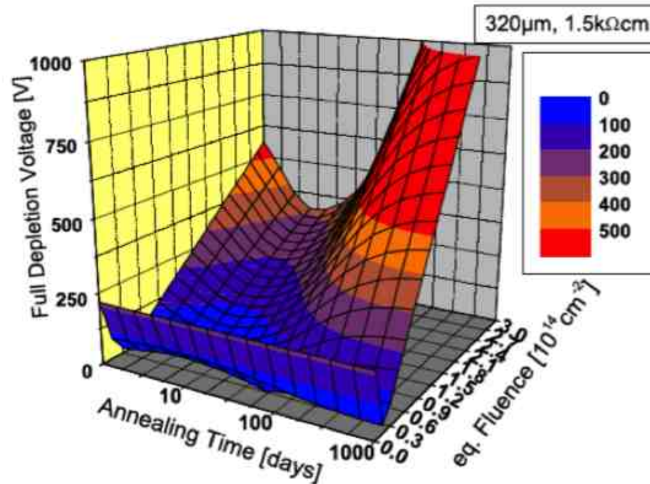

Figure 3.6.: Evolution of the full depletion voltage for n-type sensors according to the "Hamburg" model. At low fluences the full depletion voltage drops until type inversion and rises after that with further irradiation. The short annealing within the first two weeks leads to a decreasing full depletion voltage and the reverse annealing increases N_{eff}, saturating after a very long annealing [Die03].

The change of effective doping concentration in the sensor bulk under the influence of irradiation has been measured in float zone (FZ) n-type substrates. The full depletion voltage of the FZ n-type sensors first decreases, reaching even zero, before it increases almost linear. Figure 3.8 shows the development of V_{fd}.

3.2.4. Trapping

Another effect of radiation damage is trapping. Traps capture drifting electron-hole pairs on their way to the electrodes and emit them after some time delay. If the shaping time of the readout electronics is shorter than the time after which the trap emits the charge again, their part of the signal is lost and thus the total signal is reduced. Therefore trapping leads to a decrease of the charge collection efficiency. The more trapping centers are on the drift path, the higher is the trapping probability, decreasing the effective free drift time of the charge carriers:

$$\frac{1}{\tau_{tr}^{n(p)}} = \sigma_{n(p)} v_{th,n(p)} P_d^{n(p)} N_d \tag{3.19}$$

where $P_d^{n(p)}$ is the probability that a defect is in the more positive (negative) state.

3.2.5. Beneficial Effect of high Oxygen Concentration

The ROSE[3] collaboration (CERN-RD48) with its key idea to improve the radiation hardness of silicon by defect engineering has investigated the effect of oxygen and carbon enrichment on silicon devices [L+01a]. Figure 3.7 shows the differences on the effective doping concentration and the full depletion voltage as a function of the proton fluence. Beginning with comparable values of $|N_{eff}|$ and V_{depl} the effective donor concentration reduces to a minimum and increases afterwards with different slopes. The slope of $|N_{eff}|$ and V_{dep} after this minimum, which is declared as point of type inversion, is strongly dependent on the oxygen and carbon concentration. As a small $|N_{eff}|$ and thus a smaller V_{depl} are beneficial, the positive effect of the oxygen enrichment is clearly visible. Increasing the carbon concentration has even a bad influence.

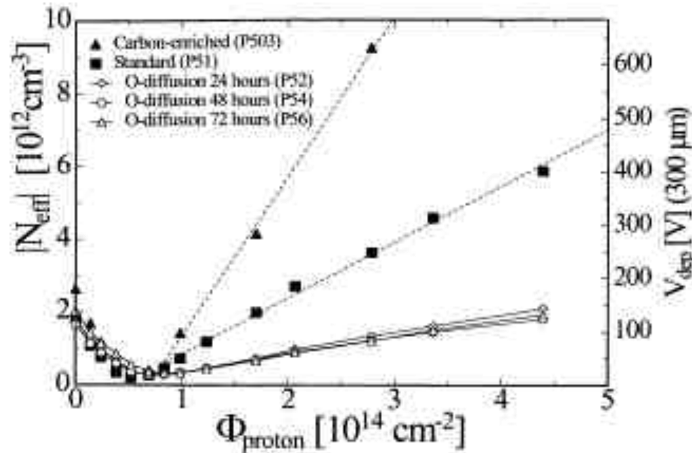

Figure 3.7.: Influence of carbon and oxygen on V_{dep} and $|N_{eff}|$ [L+01a]. The plot illustrates the beneficial influence of the oxygen concentration in FZ silicon on the depletion voltage and the effective doping concentration. Compared to the standard silicon, the oxygen enriched silicon shows a steady increase, while the carbon enriched silicon increases even worse.

This positive effect of oxygen enrichment with respect to proton irradiation has also been investi-

[3] **R**esearch and development **O**n **S**ilicon for future **E**xperiments

gated for neutron and pion irradiations [L+01b]. Figure 3.8 shows a comparison of V_{dep} and |Neff| for standard FZ and oxygen enriched FZ in dependence of the fluence and the particle type.

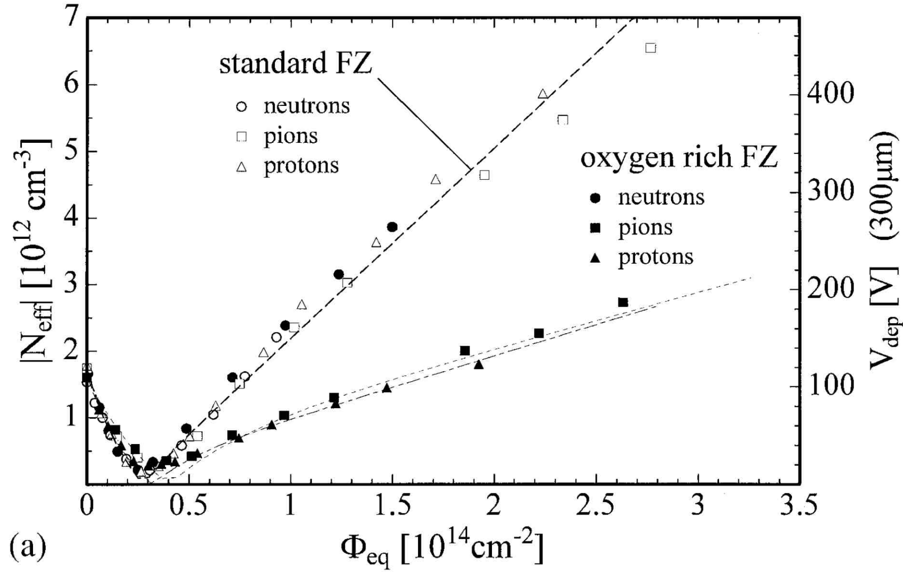

Figure 3.8.: Comparison of V_{dep} and $|N_{eff}|$ for standard FZ and oxygen enriched FZ in dependence of fluence and particle type[L+01b]. The plot illustrates the beneficial influence of the oxygen concentration in FZ silicon on the depletion voltage and the effective doping concentration for irradiation with pions and protons. For neutron irradiations there is no difference for standard FZ and the oxygenated FZ observable.

The beneficial effect of oxygen enrichment is observable for pion and proton irradiations, but not for neutron irradiations, except for low resistivity material [Ruz00].

Chapter 4.

Irradiation Facilities and Sensor Teststations

This chapter will give an overview of the irradiation facilities and the improved sensor test stations that have been used for this thesis. The irradiations carried out as described in 5.2 have been performed in Karlsruhe at the ZAG Zyklotron AG and in Ljubljana at the Reactor Infrastructure Center of the Jožef Stefan Institute.
The measurements presented in this thesis have been done using the sensor test stations of the IEKP. There are two sensor probe-stations and two ALiBaVa setups that will be introduced in the following sections.

4.1. Irradiation Facilities

All irradiations within the HPK campaign have been done in the framework of AIDA[1]. The aim of the AIDA project, with more than 80 institutes and laboratories from 23 european countries involved as beneficiaries or associate partners, is to upgrade, improve and integrate key european research infrastructures and develop advanced detector technologies for future particle accelerators (LHC upgrade, Linear Colliders, Neutrino facilities and Super-B factories).

4.1.1. Proton Irradiation - The Compact Cyclotron Karlsruhe

The proton irradiations are done by the IEKP itself, using the Compact Cyclotron. Operated by ZAG Zyklotron AG, a private company located on the Campus North of the KIT, the Compact Cyclotron can offer 25MeV protons. From an H^- source the H^- ions are accelerated to their required energy. By shooting the H^- ions through a stripping foil, the electrons are removed and the H^+ ions move to the beam line from where they are directed onto the target. The current produced at the foil where the electrons are stripped off is double the proton beam current and serves as a first proton beam current measurement. Our target box is placed 50 cm from the exit window of the beam. In figure 4.1 the beam line and the target box mounted on a XY-stage are shown. The beam coming from the left with a proton energy of about 23 MeV and a proton current of about 1.5 μA has a diameter of $4 - 8$ mm. In order to get a homogeneous irradiation, the objects needed to be irradiated have to be scanned by the beam spot. Therefore the objects are fixed to an aluminium frame, using Kapton® tape, which is then inserted into the thermally insulated target box with a

[1] **A**danced European **I**infrastructures for **D**etectors at **A**ccelerators

graphite absorber at the back. The front window is made of Kapton® foil which is attached to a GFK frame.

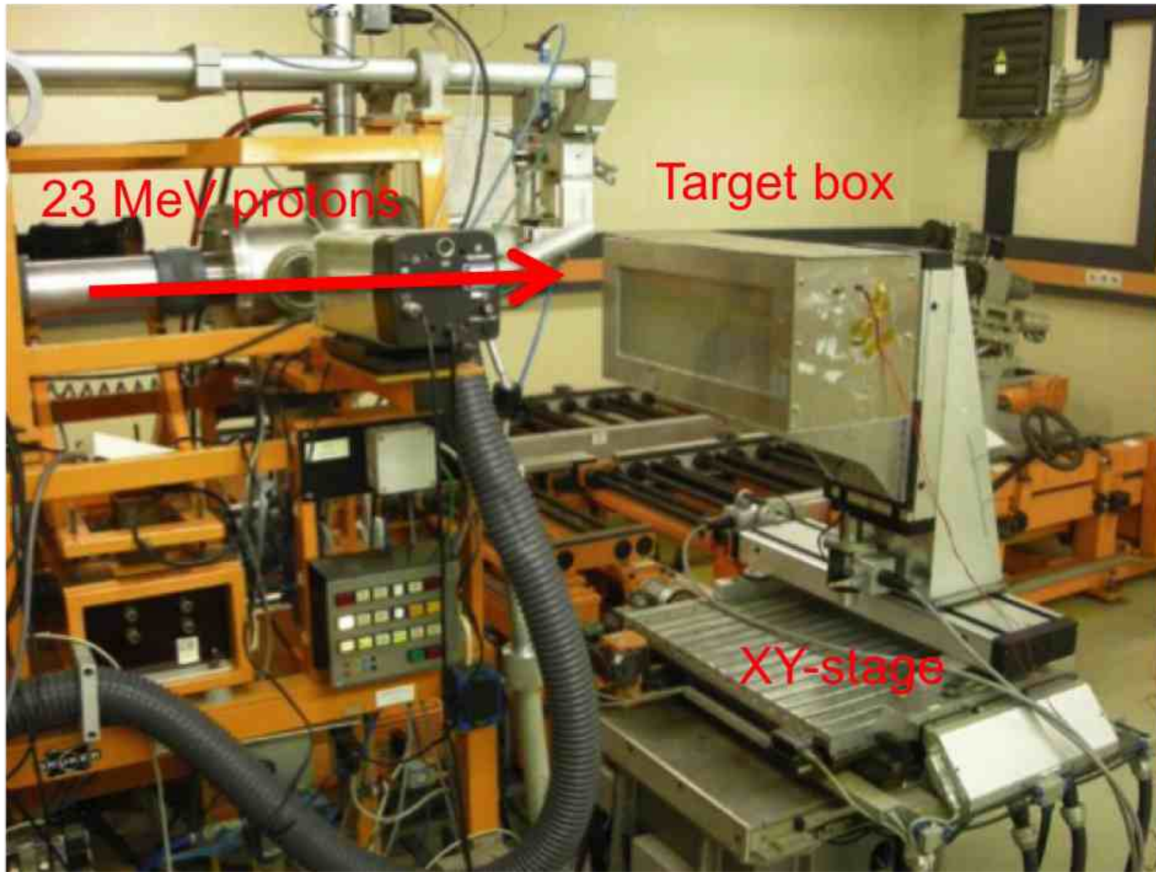

Figure 4.1.: Interior view of the Compact Cyclotron in Karlsruhe.

Figure 4.2 shows the irradiation box. The objects are fixed with Kapton® tape on an aluminum frame that is mounted in the box.

The box can house up to four frames, each frame offers an area of 44 cm × 17 cm. During the irradiation the box is flooded by cooled N_2 setting up a temperature of about -30°C in the box. The cooling is necessary in order to prevent uncontrolled annealing during the irradiation.
To estimate the fluence for given irradiation parameters, following formula from [Die03] is used:

$$F_{est} \approx \frac{n \cdot I}{q_{el} \cdot v_x \cdot \Delta z} \tag{4.1}$$

with the number of scans n, the proton beam current I, the electron charge q_{el}, the horizontal scan velocity v_x and the step width in vertical direction Δ_z. Irradiations to fluences in the order of $\Phi_{neq} = 1 \times 10^{15} cm^{-2}$ need, depending on the size of the object, 15min for a diode and about 45 min for a small sensor of few cm^2.
Post-irradiation dosimetry is provided by ZAG. Done by Ni57-activity measurement in Ni-foils that are attached to the structures during irradiation. More information can be found in the web: `http://www-ekp.physik.uni-karlsruhe.de/index.php?option=com_content&view=article&id=93&Itemid=`

Figure 4.2.: Front view of the irradiation box. The objects to be irradiated are fixed to the aluminium frame that is inserted into the box. During irradiation, the box is flooded by cooled N_2, setting the temperature in the box to about -30°C in order to avoid annealing.

12

4.1.2. Neutron Irradiation - Reactor Infrastructure Center Ljubljana

The neutron irradiations are done at the Reactor Infrastructre Center at Jožef Stefan Institute in Ljubljana. The 1966 build up TRIGA-Mark-III reactor with a power of 250kW and a maximum total flux of $4 \times 10^{12} cm^{-2} s^{-1}$ offers several in-core and ex-core irradiation channels. The in-core irradiation channels shown in figure 4.3 are mainly used for high fluence irradiations. Channel F-19 for small sized objects like diodes and very small sensors of a few cm^2 and the Triangular channel (TIC) for larger sensors up to 44 cm × 17 cm.

At full power, a fluence in the order of $\Phi_{neq} = 1 \times 10^{16} cm^{-2}$ is reached within one hour. For lower fluences the reactor power is trimmed. The dosimetry is done with an accuracy of 10%.
More information can be found in [SvT12] and in the web: `http://www.rcp.ijs.si/ric/index-a.htm`

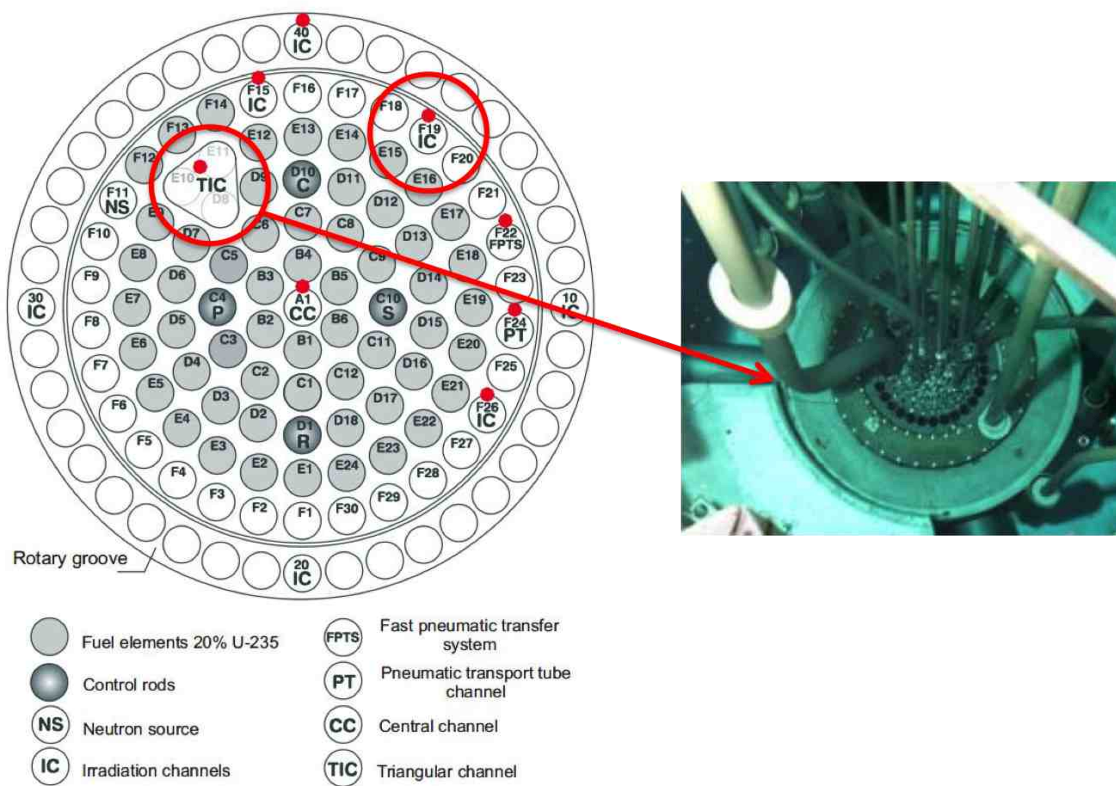

Figure 4.3.: Overview of the in-core irradiation channels of the TRIGA-Mark-III reactor at Ljubljana. Small objects are irradiated in the F-19 channel while larger objects are put in the triangular channel. At full power fluences of $\Phi_{neq} \circ 1 \times 10^{16} cm^{-2}$ are reached within one hour.

4.2. Sensor Test Stations

The IEKP offers several test stations for the qualification and investigation of silicon strip sensor properties. Currently there are two so called probe-stations for sensor qualification measurements and two ALiBaVa setups for charge collection efficiency measurements. This section will shortly describe these test stations and their measurements.

4.2.1. Probe-station

In 2008 the IEKP[2] was equipped with one functional probe-station. This half automatic probe-station enabled measurements of sensor characteristics like currents and capacitances, while applying high voltage to the sensors. Therefore the station offers a dark and temperature controlled environment. All apparatus and measurements are controlled via a self programmed LabView software. The measurements are described in section 4.2.1.
The probe-station was equipped with a coolable jig[3], where the sensors have been fixed by a vacuum suction system during the measurements. The cooling was realized by cooling pipes integrated in the jig. Designed for cold measurements at -10°C, the jig was connected to a chiller operated with a special coolant. More information and details on this jig design can be found in [Fre04].
As the upgrade of the LHC to the HL-LHC will increase the radiation damage for the sensors and thus the current, a new cold jig is required, being able to cool the sensors down to -20°C. Therefore, the first task of this thesis was the design and the participation in operation of a new coolable jig. Previous studies concerning the materials and the electrical parts of the jig have been made in the diploma thesis [Hof08], therein a prototype jig with Peltier cooling was built up and tested.
Taking this prototype as baseline the probe-station has been equipped with a new 18cm $\times$ 18cm coolable aluminium jig. Figure 4.4 gives an overview of the new jig and it's different layers.

Starting from the bottom, the new jig has a connector plate, which has two purposes. The connector plate houses the pin connector from the power supply and the circuit board that distributes the power to the Peltier elements. Technical drawings of the plate can be found in A.1 and A.2. On top of the connector plate is the cooling plate, separated by four GFK discs at the corners to keep electrical insulation. Drilled cooling pipes as shown in A.3 enable the pre-cooling by circulating water at 4°C. The complete cooling plate with bases for the Peltier elements can be found in A.4. This pre-cooling is meant to conduct the heat of the Peltier elements out of the jig. The six Peltier elements positioned at the six bases of the cooling plate are framed by two GFK plates with openings to allow a good thermal contact of the Peltier elements to both, the cooling plate below and the vacuum plate above. Figure 4.5 shows the GFK insulation layer with the openings for the Peltier elements.

The vacuum plate includes five separate vacuum fields: one for diodes, one for a small halfmoon[4], one for a large halfmoon, and two circular fields in the center for middle and large size sensors. A technical drawing is in the appendix A.5. A picture of the assembled jig in the probe-station can

[2]Institut für Experimentelle Kernphysik
[3]A support table built up of several layers that is set on high voltage.
[4]Set of test structures to monitor the sensor quality

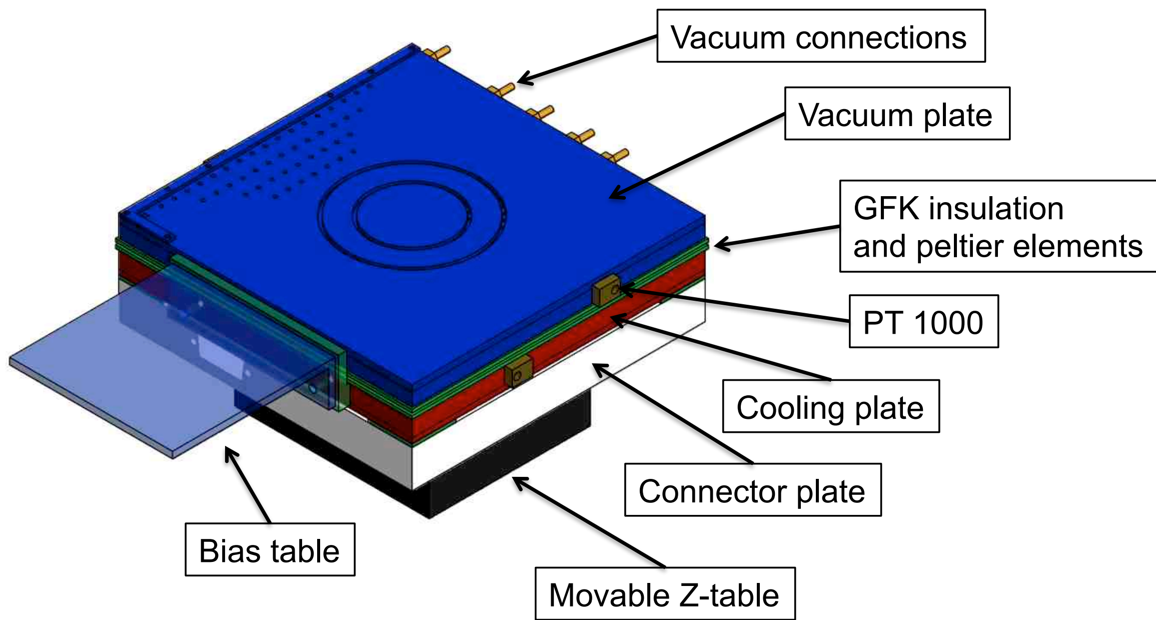

Figure 4.4.: 3D model of the jig with thermoelectric cooling.

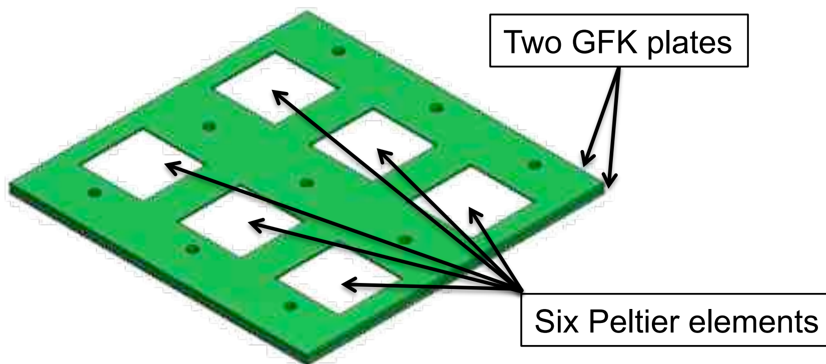

Figure 4.5.: Sandwich of the two GFK plates framing the six Peltier elements.

be seen in figure 4.6.

The Peltier elements of the jig are powered by a TDK Lambda GEN20-38, a programmable power supply with 0-20V and 0-38A. Four PT1000 resistance thermometers are mounted on the jig to monitor the temperature and one humidity sensor is close to the jig checking for the dew point. The temperature of the jig is controlled by a PID[5] controller, a generic control loop feedback mechanism, which is integrated in the LabView software of the probe-station. The temperature range of the jig goes from +80°C to -25°C with a stability of 0.5°C.
In addition to the already functional probe-station that has been equipped with the new cold jig, a second probe-station [Erf09] has been built up in order to cope with the numerous measurements of the impending HPK campaign (see chapter 5.2). Figure 4.7 shows the two probe-stations.

Both probe-stations are based on the same principle, run with the same LabView software and

[5]Proportional-Integral-Derivative

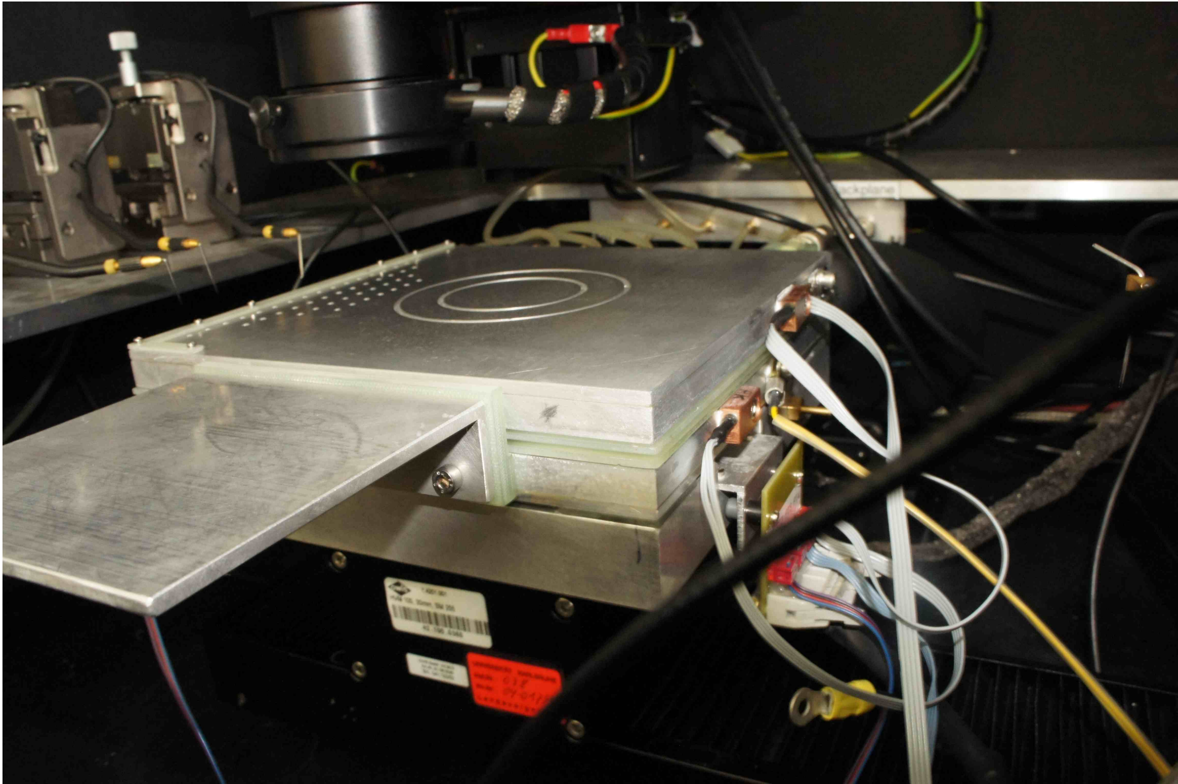

Figure 4.6.: Picture of the assembled jig in the probe-station mounted on the Z-table. The several layers of the jig, consisting of the connector plate, the cooling plate, the GFK insulation layer with the Peltier elements and the vacuum plate on top, can be seen.

share one chiller, which is pre-cooling the cold jigs of both stations. The measuring equipment is stored in racks, one next to each station with the following tools:

- Keithley K6517A electrometer, a power supply unit for voltages up to 1000V and current measurement device in the range of 10pA to 1mA, used to bias the sensor and measure the sensor currents.
- Keithley K617 power supply for low voltages up to 100V, used to apply voltages on selective parts of the sensor.
- Hewlett Packard LCR meter 4284A with a frequency range between 20Hz and 1MHz, used for all capacitance measurements.

All devices are controlled via a LabView software, that carries out the measurements, using a relay system to address the devices. Detailed information on the execution of the probe-station measurements can be found in [Fur05] and on the new second probe-station in [Erf09].
The following section will only give a short overview of the sensor parameters measured in the probe-station and their meaning.

(a) probe-station I

(b) probe-station II

Figure 4.7.: Pictures of the two self build probe-stations at the IEKP.

Measurements

Total Leakage Current
The measurement of the total leakage current versus the voltage (IV) describes the current that is generated in the sensor while the sensor is reverse biased. This current contributes to the shot noise, shown in 2.48, and should be small. There is a current limit of 1mA that should not be exceeded.

Total Capacitance
The measurement of the total capacitance versus the voltage (CV) characterizes the development of the depletion region of the sensor. Increasing the voltage between backplane and the bias ring leads to a growing space charge region, unless the whole sensor is depleted and the capacitance gets constant, see 2.31.

Strip Leakage Current
The single strip leakage current (I_{leak}) describes the fraction of one strip to the total leakage current. The sum of the single strip leakage currents results nearly in the total leakage current.

Coupling Capacitance
The coupling capacitance (CC) describes the capacitance between the implant strip and the aluminium readout strip. A high value is desired to have a good signal coupling. The thickness of the readout oxide, that has to guarantee electrical strength, affects the CC with common values of about $\frac{1pF}{cm \cdot \mu m}$.

Pinhole
This parameter specifies the current flow over the dielectric readout oxide. A pinhole is defined as a short or low ohmic connection between the implant and the aluminium readout strip. For a good oxide, the current is below 10pA. Strips with pinholes will later not be connected to the readout chips.

Bias Resistor
As the implant strips are connected via the bias resistors (R_{bias}) to the bias ring, all bias resistors of one sensor should be homogeneous, in order to put all implants on the same potential. According to 2.47 the bias resistors contribute to the thermal parallel noise and should therefor not be too small. Typical values are between 1 MΩ and 5 MΩ.

Inter-strip Resistance
A high inter-strip resistance (R_{int}) is necessary to guarantee a good strip isolation. For non irradiated sensors R_{int} is typically in the range of several GΩ and drops for irradiated sensors to hundreds of MΩ.

Inter-strip Capacitance
The inter-strip capacitance (C_{int}) has a basic contribution the capacitance load into the amplifier and thus to the detector noise as shown in 2.51. Compared to the CC the values for C_{int} have to be small, with a ratio between $\frac{C_{int}}{CC} = \frac{1}{30}$ and $\frac{C_{int}}{CC} = \frac{1}{60}$.

The comparative values are mostly taken from the CMS sensor production [Har08].

4.2.2. ALiBaVa Setup

Mechanical Setup

The ALiBaVa setup (see figure 4.8) allows to operate silicon strip sensors under realistic conditions, measuring the charge collection efficiency. The setup consists of a light and air tight box, wherein the other components are assembled. Figure 4.8 shows the setup with the test board, already screwed on top of the cooling bridge and the movable XYZ-table holding the source and the laser. The ALiBaVa readout system is split in a Motherboard and a Daughterboard [MH10] in order to protect the Motherboard from radiation or low temperatures. The Daughterboard is mounted on the test board and the Motherboard is outside the ALiBaVa box connected by a data cable.

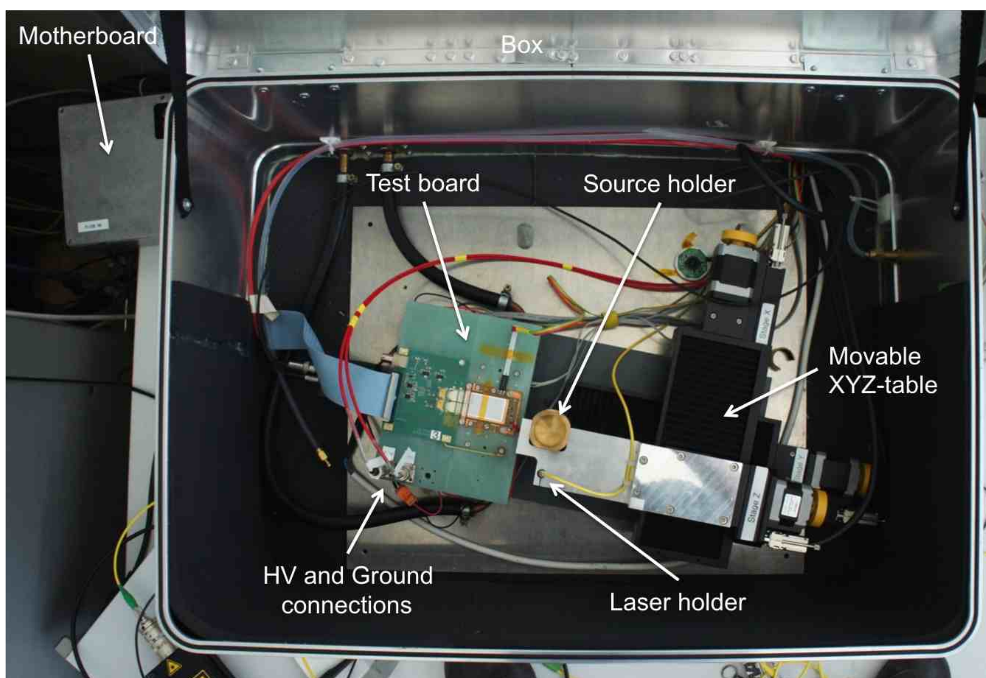

Figure 4.8.: Picture of the ALiBaVa setup. The air and light tight box houses a movable XYZ-table with the source and laser holder and a cooling bridge where the test board is mounted on. The blue data cable connects the Daughterboard to the Motherboard. The sensor is biased using the connectors on the test board.

The cooling system of the setup can not be seen in figure 4.8, as the test board is on top. Figure 4.9 shows the adjustment of the test board, the cooling bridge and the scintillator. The cooling bridge has a water pre-cooling and two Peltier elements, which allow measurements from +80°C to -25°C. The test board shown in figure 4.10 is screwed on top of the cooling bridge offering a good thermal connection between sensor and bridge. The opening in the bridge is necessary in order to provide the trigger information of the scintillator for the source measurements.

A daughterboard is composed of two beetle chips, each with 128 readout channels. These are connected via pitch adapters to the AC pads of a sensor. All data are conducted to the Motherboard via a flat band cable. The Motherboard serves several purposes. It processes the analog data from the Daughterboard, serves as a trigger input when using a β-source and the scintillator or generates

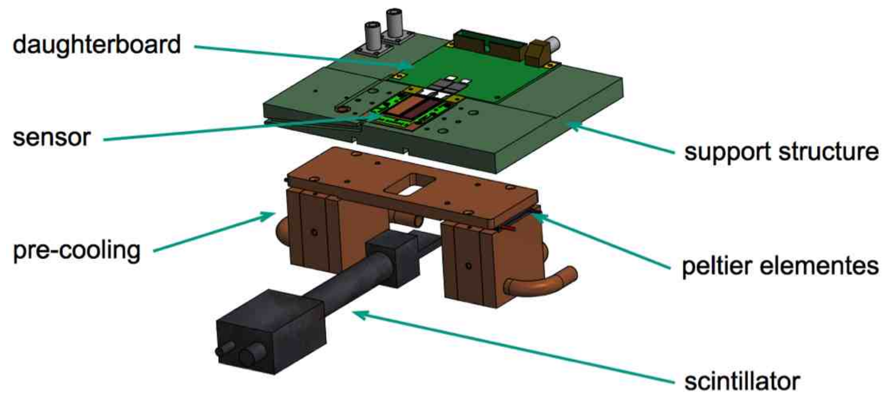

Figure 4.9.: 3D model of the adjustment of daughterboard, cooling bridge and scintillator. The daughterboard is screwed on top of the cooling bridge, establishing a good thermal contact. The cooling bridge has a water pre-cooling and two Peltier elements to control the sensor temperature. Below the opening in the cooling bridge is the scintillator used to trigger the readout for the source measurements.

triggers when used with a laser setup.

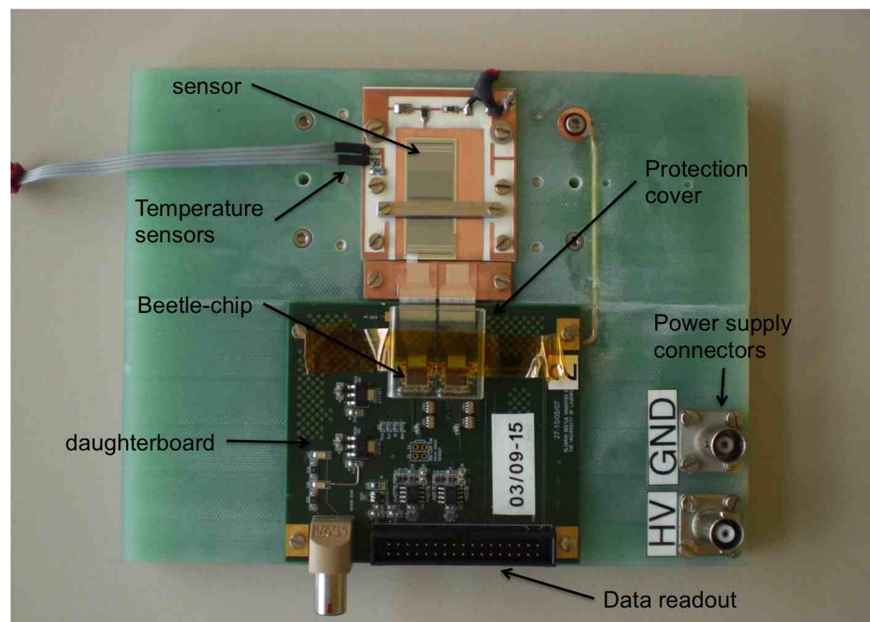

Figure 4.10.: Picture of the ALiBaVa test board and it's components. The daughterboard with the beetle chips is connected via pitch adapters to the sensor. The power supply connectors bias the sensor whose temperature is controlled by a PID controller integrated in the LabView software which runs the measurements.

For the β-source measurements a Sr90 source has been used. The Sr90 decays into Y90 and emits 546 keV electrons. The unstable Y90 decays into the stable Z90. There are two decay channels, for the main decay channel, a pure β-decay, the maximum electron energy is 2274 keV, but the mean energy with 939 keV is close to a MIP, see 2.23. To reduce the spot size of the Sr90 source a brass collimator with a opening window of 0.8mm has been used.
For the laser measurements an infrared laser with 1060 nm has been used. The laser beam penetrates the whole sensor, generating charge along its track.

Analysis Methods

The data analysis for the ALiBaVa measurements is based on the data analysis framework ROOT developed at CERN. The analysis is divided in two parts. In the first part, the raw data is processed, before in the second part collected charge and the signals are looked for. The raw data are the signals of the 256 readout channels of the Daughterboard recorded for each incoming or outgoing trigger signal. Additionally the temperature and a timestamp are logged.
In the following, the different analysis parameters and methods will be described:

Pedestals
The pedestal is the mean digitized read out charge of a channel i, averaged over a number of events N. The signals are recorded randomly without the presence of a physical signal. The pedestal is given in units of counts of an analog to digital converter (ADC). For a given channel, the pedestal is defined as:

$$Ped_i = \frac{\Sigma_{k=1}^{N} ADC_k}{N} \tag{4.2}$$

Pedestals are recorded before each measurement of a new sensor and at each temperature and voltage step.

Noise
The noise of a channel is defined as the width of the distribution of the ADC values for this channel i. Calculated by the fluctuations around the pedestal, the noise of one strip is given by:

$$\sigma_i = \sqrt{\frac{\Sigma_{k=1}^{N}(ADC_k - Ped_i)^2}{N}} \tag{4.3}$$

Common Mode
The common mode describes the shift of the signal heights of numerous channels by external influences. These signal changes have to be corrected, which is done by calculating the mean of the channel signals for all events subtracted by the pedestal:

$$CM_N = \frac{\sigma_{k=1}^{i}(ADC_{N,k} - Ped_k)}{i} \tag{4.4}$$

The distribution of the common mode is typically gaussian around zero.

Cluster
After determining the pedestal and the noise and correcting the signal data from the common mode, the search for signals generated by transversing particles begins. The analysis method to identify the signal is to look for the channel with the highest signal. If the signal-to-noise ratio (SNR) for this channel fulfills the criteria:

$$\frac{Signal}{Noise} = \frac{ADC_{corr_i}}{\sigma_i} \geq 5.0 \tag{4.5}$$

the channel is called seed. As a cluster consists of one or more channels, the next step is to look for the left and right neighbors of the seed channel.

Cluster Size

To determine of how many channels the cluster is made of, the criteria of the seed neighboring channels are:

$$\frac{ADC_{corr_{i\pm1}}}{\sigma_{i\pm1}} \geq 2.0 \tag{4.6}$$

The limits for the SNR are taken from the current CMS tracker. If a channel fulfills the criteria the analysis continues, if it does not it stops. This results in the number of channels that belong to the signal generated by the transversing particle.

Cluster Charge

The cluster charge is defined as the collected charge of all channels contributing to the cluster. The distribution of the cluster charge follows a gaussian convoluted landau. The most probable value (MPV) for the generated charge by a transversing particle can be determined by a gauss-landau-fit.

Cluster Noise

The cluster noise of the channels k, belonging to the cluster can be calculated using:

$$\sigma_{cl} = \sqrt{\Sigma_k = 1^K (\sigma_{i=k})^2} \tag{4.7}$$

Signal-to-Noise

The signal-to-noise ratio for the cluster of a given event i is defined as:

$$SNR_i = \frac{ADC_{cl}}{\sigma_c l} \tag{4.8}$$

A histogram over a large number of events would again result in a gauss-landau distribution, where the MPV of the gauss-landau-fit would be used as SNR.

Charge Collection Efficiency

The charge collection efficiency (CCE) is one major sensor parameter, essential for a proper detector functionality. It compares the collected charge of a sensor at different conditions.

Chapter 5.

Campaign to identify the Baseline Sensor Technology for Future CMS Tracking Detectors

Most work related to this thesis has been done in the framework of the Central Europe Consortium and on behalf of the CMS Tracker Sensor Working Group. The following chapter describes the R&D program and plans of the consortium. Beginning with the initial R&D proposal, the work package will be introduced in general and especially with focus on the work related to this thesis, which defined large parts of the program.

5.1. Central European Consortium - R&D Proposal

In 2008 some European institutes have grouped in the Central Europe Consortium (CEC), which is a formation of CMS members, to combine efforts and manpower in the participance in the CMS Tracker Upgrade.
The goal is to explore the current available materials and technologies for silicon sensor modules, with the effort to choose the most promising, that can be used for the upgrade of the CMS Tracker at the HL-LHC. The focus is on strip sensors and sensors with short strips. This study aims to provide fully developed modules with readout and cooling, showing up to which irradiation levels and occupancies these modules can be used in a future tracker. Since March 2008 the CEC is an approved CMS SLHC R&D [H⁺08b].

5.1.1. Overview

Starting with five member institutes the CEC has currently nine member institutes from all over Europe.
The R&D proposal from 2008 can be found on the CEC TWiki page[1] it covers several topics that are directly related to the LHC upgrade:

- Investigation of different sensor materials by the measurement of macroscopic performance parameters like currents, strip capacitances, resistivity and charge collection

[1]https://twiki.cern.ch/twiki/bin/view/CMS/CEC

- Development of Test Structures (TS) to monitor the processes during the sensor manufacturing
- Investigate new sensor geometries and routing designs
- Irradiation study with neutron, proton and mixed irradiations and investigation of annealing behavior
- Design of a complete module prototype

5.1.2. Objectives within the R&D Proposal related to this thesis

The focus of this thesis is set to strip sensors and their parameterization before and after irradiation, sensors with integrated pitch adapters and fourfold segmented sensors with short strips and edge readout. Therefore the following topics have been dealt with:

- Preparation of the probe-stations for measurements at -20°C and maintenance
- Designing the sensor layouts with the software package layout editor
- Investigating the sensor characteristics before and after irradiation to HL-LHC fluences
- Studying the feasibility of new routing and sensor designs
- Simulation of sensor properties

5.2. R&D for thin Single-Sided Sensors with Hamamatsu Photonics - HPK campaign

Central ingredient of the CEC program is the "R&D for thin Single-Sided Sensors with HPK" (HPK[2] campaign) [M^+08], started from the CMS tracker upgrade collaboration to identify the future sensor technology baseline for the Tracker Upgrade Phase II. Therefore an extensive R&D production of 6 inch wafers with a variety of different thicknesses and technologies have been ordered from HPK. The sensor properties and especially the behavior after irradiation are investigated for the different thicknesses on Float-Zone (FZ), Magnetic Czochralski (MCz) and Epitaxial silicon (Epi) material. The wafers come in p-on-n and n-on-p versions. For the n-on-p versions the insulation techniques p-stop and p-spray will be explored. In addition, some wafers have been produced with an additional routing in a second metal layer on selected structures to explore its feasibility.
The performance and functionality of new sensor designs and routing layouts are investigated. The Tracker Simulation Group will be supplied with detailed information about the sensor parameters in order to guarantee adequate simulations on the sensor and module operation.

[2]Hamamatsu Photonics K. K.

5.2.1. Overview

The goal of this R&D for Single-Sided Sensors with HPK is to investigate the characteristics and limits of the radiation tolerance of thin ($\leq$ 320 µm) single sided silicon strip sensors for the CMS HL-LHC Tracker upgrade. In order to ensure comparability, only one producer using the same process steps for all wafers, one mask design with many different devices for various purposes and one measurement and quality assurance protocol has been used. Table 5.1 gives an overview of the different materials, types and thicknesses for the campaign. HPK has been chosen, as most sensors of the current CMS Tracker have been produced by them and proofed to work reliably.

Table 5.1.: The wafer submission consists of six wafers per substrate type and active thickness.

substrate type	FZ	FZ	FZ	MCz	Epi	Epi	FTH	**Total**
active thickness	320µm	200µm	120µm	200µm	100µm	50µm	200µm	
on carrier		√	√		√	√		
p-on-n	6	6	6	6	6	6	6	42
n-on-p (p-spray)	6	6	6	6	6	6	6	42
n-on-p (p-stop)	6	6	6	6	6	6	6	42
2nd metal p-on-n		6						6
2nd metal n-on-p		6						6
2nd metal n-on-p		6						6
Total	18	36	18	18	18	18	18	**144**

The original order consisted of 126 wafers with a size of 6 inch, processed by Hamamatsu Photonics, which rose due to an additional delivery of 18 float zone thinned (FTH) sensors, with a physical thickness of 200 µm, to 144 wafers. Figure 5.1 shows the layout of the wafers.

For a meaningful conclusion it is necessary to investigate the dependence on sole proton and sole neutron irradiations as well as the dependence on the mixed irradiations. The wafer setup is almost symmetric and most structures are implemented twice. For the irradiation studies, a few selected structures are first irradiated with protons and with neutrons afterwards, while the other half of the structures are first irradiated with neutrons and then with protons. Having the irradiations and characterizations finished, some of them will undergo an annealing study. Figure 5.2 shows the full measurement and irradiation program for the Baby_Std sensors and diodes. In order to get consistent results, as many samples as possible are irradiated at once and one protocol to perform the measurements at several institutes has been used.

In order to find one radiation hard baseline technology for as much detector volume as possible, the irradiation studies are mainly driven by the expected HL-LHC fluences for the most inner regions of the tracker. Figure 5.3 shows the simulated fluences for the current CMS Tracker layout for different particles and in total. The fluences are extrapolated to the HL-LHC for an integrated luminosity of 3000fb^{-1}.

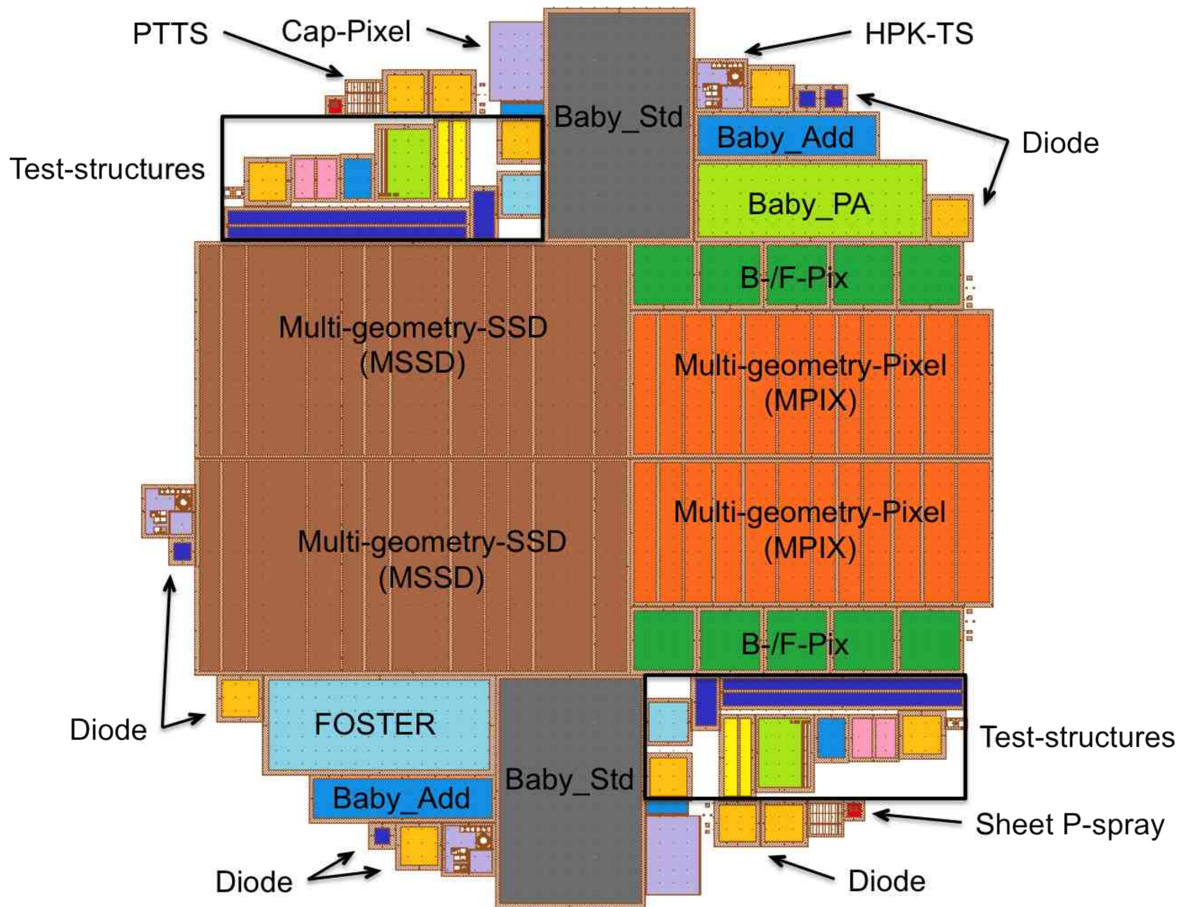

Figure 5.1.: Picture of the wafer layout: One wafer consists of 28 different structures, each with a different objective. In total one wafer holds 67 single structures.

As it is intended to equip as much tracker volume as possible with a single silicon sensor technology, all fluences, from the interaction point to the outer radial positions are investigated. Therefore our test wafers include the most promising sensor types for the tracker like pixels, short strip and standard strip sensors.
The fluence levels for the different radial positions are different for the dominant particle types. In the inner regions near the interaction point the total fluence is mostly dominated by charged hadrons, while the outer regions are more affected by neutrons. The fluences at representative positions at 5, 10, 15, 20 and 40 cm radial distance from the interaction point, marked with the black arrows in figure 5.3, are studied. Table 5.2 shows the extrapolated fluences that will be used for the campaign.

The irradiations are done at the Irradiation Center Karlsruhe (4.1.1) and the Ljubljana Neutron Irradiation Facility (4.1.2).
Between the irradiation steps a short annealing and a full characterization of the structures is done to get the sensor parameters in dependence on the pure proton and pure neutron irradiation. When the structures have received the real radius dependent mixed fluence they are again fully characterized and an annealing study is done. Table 5.3 lists the steps for the annealing study.

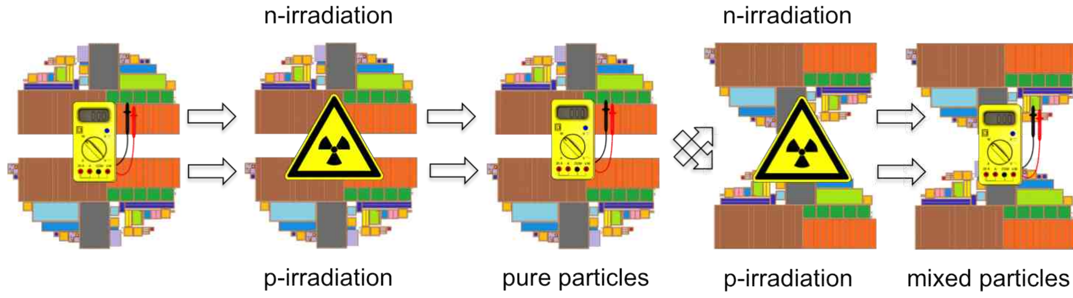

Figure 5.2.: Measurement and irradiation sequence for the Baby_Std sensors and for the diodes. After passing this sequence the investigation is completed by an annealing study.

Table 5.2.: Overview of the neutron and proton fluences for the different radial positions.

Fluences given in $10^{14}\phi_{neq}\mathrm{cm}^{-2}$				
Radius	p	n	Total	Ratio p/n
40	3	4	7	0.75
20	10	5	15	2.0
15	15	6	21	2.5
10	30	7	37	4.3
5	130	10	140	13

Between the steps IV and CV curves will be measured, as well as the charge collection.

Table 5.3.: Overview of the annealing steps.

Annealing after first irradiation: 10 minutes at 60°C							
Annealing after second irradiation: 10 minutes at 60°C							
Followed by an annealing study with the following steps:							
Step	1	2	3	4	5	6	7
Temperature [°C]	60	60	60	60	80	80	80
Time [minutes]	20	20	40	76	15	30	60
$\Sigma_{t@21°C}$ [days]	6.9	10.1	16.6	31.4	86.1	210.8	423.3

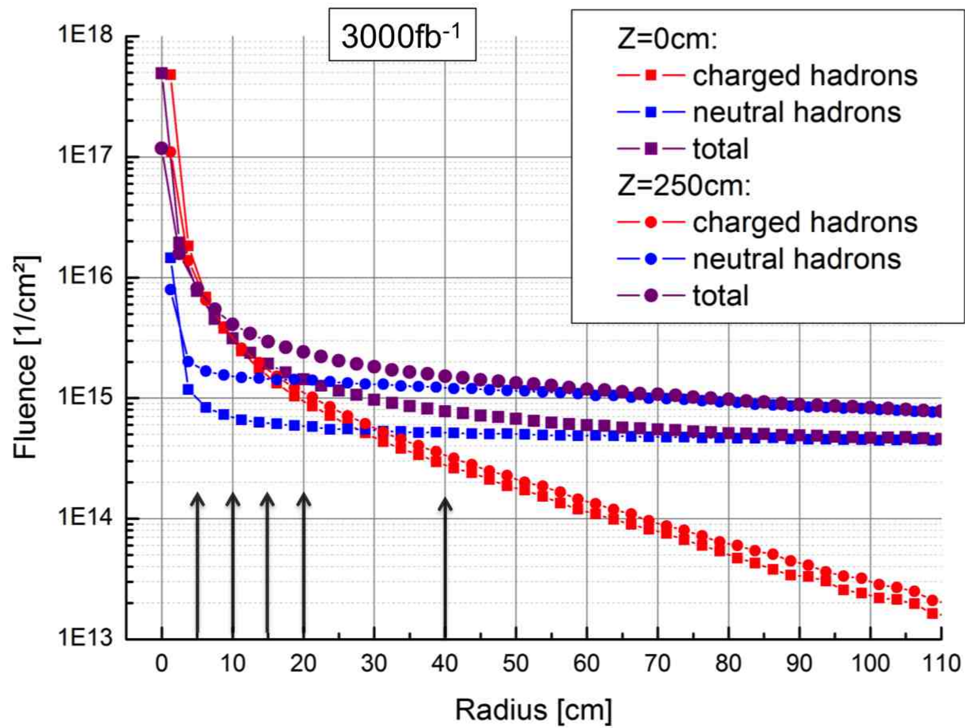

Figure 5.3.: The simulated particle fluence distributions for the central (z=0cm) and the end-cap (z=250cm) region for the HL-LHC at 3000 fb^{-1}, extrapolated from the expected LHC data for charged hadrons, neutral hadrons and in total in dependence of the radial position. The arrows mark the fluence points that are used for the campaign. Data from S. Müller [MBM11].

5.3. Details on Structures and Measurements

In the following section, details on some selected devices are given and the measurement and irradiation procedure is shown.

5.3.1. Diodes

The diodes are used for material studies giving information about the properties and the behavior of the different materials before and after irradiation as well as after annealing. There are twelve large diodes (7100 µm × 7100 µm named DiodeL) and four small diodes (4100 µm × 4100 µm named DiodeS) on one wafer. A picture of a DiodeL can be seen in figure 5.4.

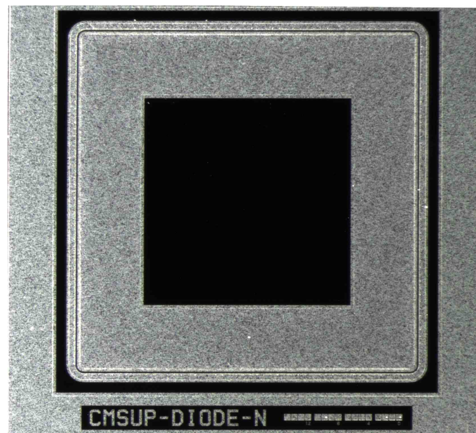

Figure 5.4.: Picture of a n-type DiodeL. The diode has one guard ring and a big opening in the center. Also the back side of the diode, which can be seen in figure 5.5, has openings in form of an aluminium grid, to allow short laser irradiation for the TCT measurements.

Diodes offer a good possibility to evaluate the changes of the bulk properties with irradiation. Next to standard qualification measurements like the current over voltage or capacitance over voltage measurements, they give access to further properties. The diodes have openings on the front side and on the back side (5.5), which allow to use the Transient Current Technique (TCT). By illuminating the diode at the openings with a short laser pulse, charge carriers are created within the volume of the diode. These charges are separated by an electric field that is applied between the front and the back side of the diode and move through it. Depending on which side of the diode the illumination with a red laser has been done, either electrons or holes move, while the other is directly absorbed. Accordingly an electron or a hole current will be measured on an oscilloscope. The measurements are done in a closed setup and at defined temperatures.

The TCT enables the measurement of time resolved currents and thus the extraction of the trapping times for electrons and holes, the shape of the electric field and the charge collection efficiencies.
As there a sixteen diodes on each wafer, the irradiation and annealing studies for them are extended.

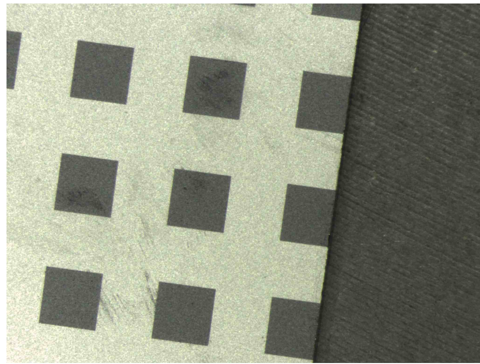

Figure 5.5.: Picture showing the metal grid on the wafer back side used on the complete wafer. The openings are needed to be able to generate charge carriers with a short laser pulse from the back side.

5.3.2. Strip Sensors

The Baby_Std sensors are the main topic of this theses. They are used to investigate the sensor properties before and after irradiation.
The initial characterization is done in the probe-station (4.2.1), where all important sensor parameters as the total current and the full depletion voltage are measured besides the strip parameters such as coupling capacitance, inter-strip capacitance, bias resistors, inter-strip resistance and strip currents. A description of these measurements can be found in section 4.2.1.
After the qualification in the probe-station, the sensors are bonded to pitch adapters and mounted to the daughter boards of a fast readout system. There are several fast readout systems, with a shaping time of about 25ns, that can be used. In Karlsruhe we use the ALiBaVa system [MH08], described in section 4.2.2. It offers the possibility to measure the charge collection efficiency (CCE), the signal(S), the noise(N) and the signal-to-noise ratio ($\frac{S}{N}$) with laser or source.
Next sensors are irradiated to the fluence of the corresponding irradiation step. For each radial position shown in 5.3 and 5.2 two Baby_Std sensors are irradiated. One with protons and the other with neutrons. Thereafter the qualification measurements in the probe-station and the ALiBaVa system are repeated to get the information of the pure proton or neutron irradiation, before each of the sensors are again irradiated with the missing particle fluence to receive the total fluence for that corresponding radial position. Again the measurements in the probe-station and the ALiBaVa system are done, before the sensors undergo an annealing study of several annealing steps, shown in figure 5.3.
After each irradiation the sensors have already been annealed for 10 minutes at 60°C.
Figure 5.6 shows the measurement sequence for the Baby_Std sensors.

Another strip sensor implemented on the HPK wafer, the Baby_Add sensor is mainly used for Lorentz angle measurements and for the calibration of the irradiation facilities. The Lorentz angle is investigated for different parameters like fluences, temperatures, voltages and magnetic fields. Changing the parameters allows a deeper understanding of the Lorentz angle behavior and its dependency especially with respect to the fluence.
The principle of the measurement can be seen in figure 5.7. A laser induces charges, which drift to

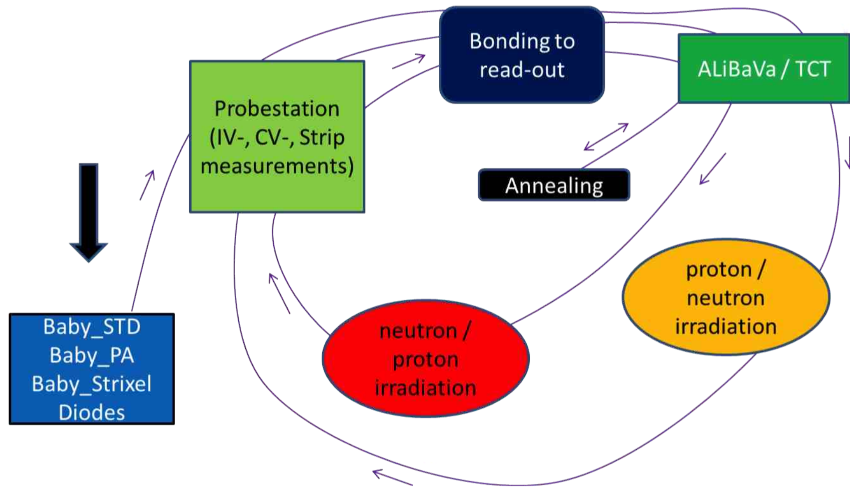

Figure 5.6.: The measuring sequence includes measurements and irradiation steps and a concluding annealing study. Following the arrows, each device will be characterized before irradiation, after a pure proton or neutron irradiation, after proton and neutron irradiation and finally after each of the several annealing steps, see table 5.3.

the strips due to an electric field, where they are collected. The charge carriers are slightly shifted by the magnetic field.

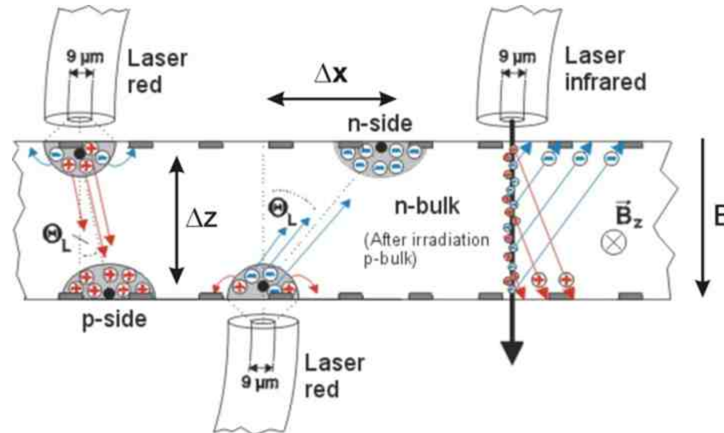

Figure 5.7.: Scheme of the Lorentz angle measurement: Laser induced charge carriers drift to the readout strips, on tracks bent by a magnetic field.

Figure 5.8 shows a picture of the 28120 µm × 7260 µm Baby_Add sensor on the top and the 35120 µm × 22620 µm Baby_Std sensor on the bottom.

Detailed information on the sensor designs can be found in section 6.3.

For completeness it is to mention that some strip sensors will be evaluated in an edge-TCT setup [KCM+10], similar to the TCT used for the diodes, but with the laser pulse injected from the side.

5.3.3. Multi-geometry Sensors

The multi-geometry sensors will be used for studies investigating the influence of different pitches, implant and aluminium widths and ratios of pitch to width on sensor parameters like breakdown

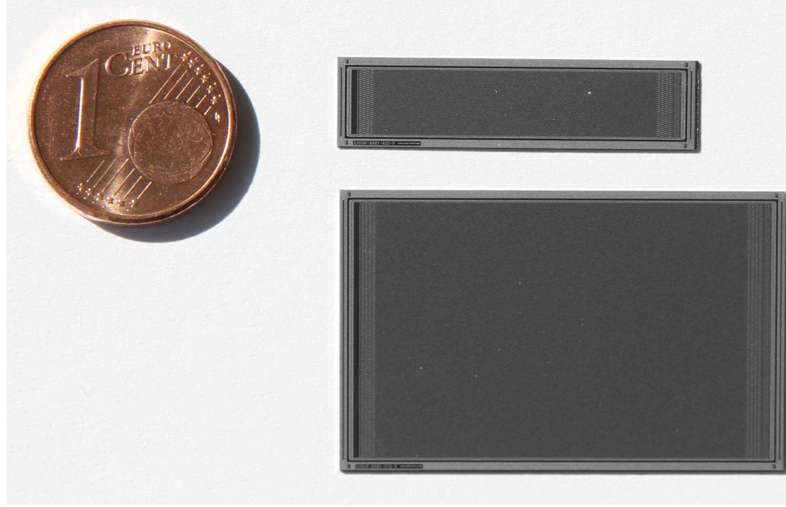

Figure 5.8.: Pictures of the Baby_Add (top) and the Baby_Std (bottom) sensor. The sensors are used for irradiation and annealing studies and for investigations on the Lorentz angle. Except for the size they do not differ.

voltages, capacitances, charge collection efficiencies and signal-to-noise ratios. There are two multi-geometry sensors on the wafer, the Multi-geometry-Strip-Sensor-Detector (MSSD) and the Multi-geometry-Pixel (MPix).
The (MSSD) is a strip sensor with 12 regions of different pitches, widths and pitch-to-width ratios. Each region has 32 strips and an exclusive bias ring, allowing the operation or exclusion of single regions. Figure 5.9 shows a GDS drawing of the MSSD and a table describing the regions.

Table 5.4.: Overview of the different regions of the MSSD. All length in µm.

region	1-120	2-240	3-80	4-70	5-120	6-240	7-80	8-70	9-120	10-240	11-80	12-70
pitch	120	240	80	70	120	240	80	70	120	240	80	70
implant width	17	35	11	9.5	29	59	19	16.5	41	83	27	23.5
alu width	24	42	18	16.5	36	66	26	23.5	47	90	34	30.5
$\frac{w}{p}$**-ratio**	0.142	0.146	0.138	0.136	0.242	0.246	0.238	0.236	0.342	0.346	0.338	0.336

Such kind of test structure has been investigated in previous studies [D+00] and [A+01]. The purpose of this sensor is the continuation of these studies, now for new materials and thicknesses below 320 µm. All strip parameters, as well as CCE and $\frac{S}{N}$ measurements can be investigated for the various regions. Especially the inter-strip capacitances are interesting on this multi-geometry-structure, as they dominate the load capacitance of the read-out chips and therefore the noise. Previous studies showed that at constant $\frac{w}{p}$ the load capacitance does not change. This result has to be verified for the new thinner sensors. The MSSD will not only be used for geometry studies but also for the irradiation campaign and beam tests, even though to a lower extent.
Figure 5.10 shows a test module assembled from a MSSD, several pitch adapters (introduced in section 6.3.5) and an TOB-Hybrid with APV readout chips. The connection of the MSSD to the readout system is done with a sequence of pitch adapters, in order to use the pitch adapter extensions which allow multiple bonding and thus saving hybrids. The MSSDs have to be bonded multiple

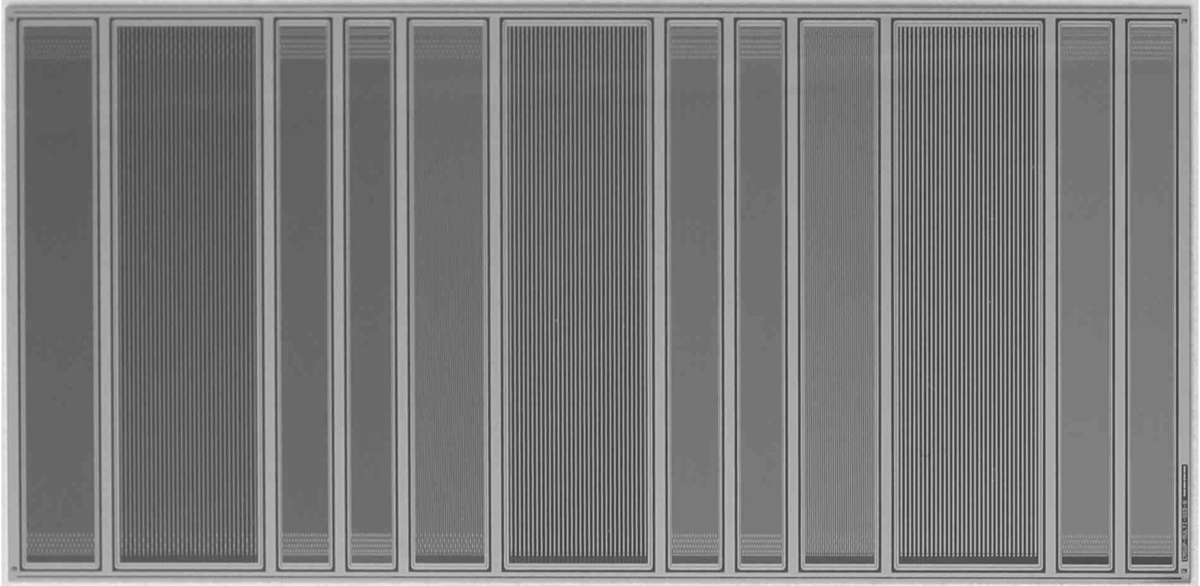

Figure 5.9.: Picture showing the different regions of the MSSD starting on the left with region 1-120. Table 5.4 gives an overview of the geometrical specifications for each region.

times, before irradiation and after each proton or neutron irradiation step.

Similar to the MSSD is the Multi-geometry-Pixel (MPix). Also divided into 12 regions, this structure has different pixel lengths of 1.25 mm and 2.5 mm, ratios of $\frac{w}{p}$ and different bias schematics using poly biasing and punch through biasing. Figure 5.11 shows the MPix and its different regions and table 5.5 gives an overview of the specifications.

Table 5.5.: Overview of the different regions of the MPix. All length in µm.

region	1	2	3	4	5	6	7	8	9	10	11	12
pitch	80	80	100	100	120	120	80	80	100	100	120	120
implant width	18	18	23	23	28	28	18	18	23	23	28	28
alu width	31	31	36	36	41	41	31	31	36	36	41	41
Pixel length	1250	1250	1250	1250	1250	1250	2500	2500	2500	2500	2500	2500

The measurements on the Multi-Pixel are similar to the ones for the MSSD.

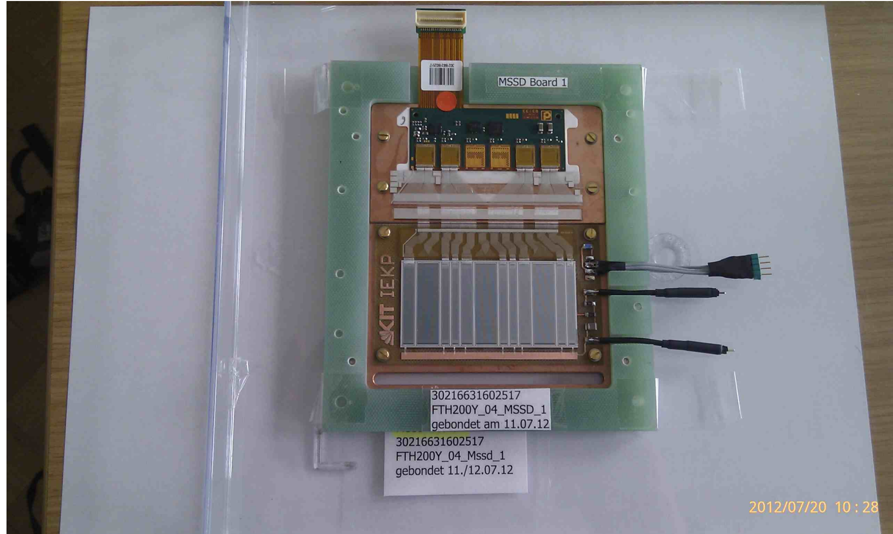

Figure 5.10.: Picture of a MSSD module. The MSSD sensor is wire bonded via several pitch adapters 6.3.5 to the TOB-Hybrid.

Figure 5.11.: Picture showing the different regions of the MPix starting on the left with region 1. Table 5.5 gives an overview of the geometrical specifications of each region.

5.3.4. New Sensor Designs

Two new sensor designs are tested within this campaign. One is realized in the Baby_PA sensor, a 128 strip sensor with an integrated pitch adapter implemented in the sensor's first metal layer. In figure 5.12 this integrated pitch adapter can be seen on the right edge of the sensor. The left side of the sensor shows several rows of contact pads which are used for the qualification measurements.

Figure 5.12.: Picture of the Baby_PA. The sensor has an integrated pitch adapter (on the right) in the first metal layer.

The implementation of the pitch adapter into the sensor saves the material of an additional glass substrate pitch adapter and thus reduces the material budget. A detailed view of the pitch adapter region is shown in figure 5.13. The aluminium readout strip on top of the implant ends a few millimeters away from the sensor edge and leads to the contact pads close to the edge. These contact pads fit to the APV25 readout chip pads and therefore can be directly bonded to the readout electronics.

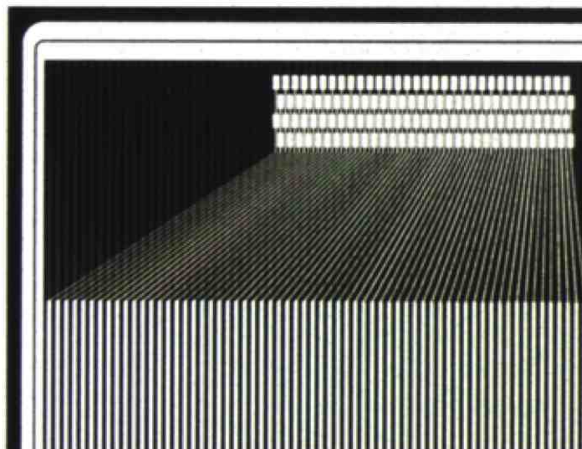

Figure 5.13.: Cut-out of the Baby_PA: The aluminium routing above the p^+implants ends at the point, where the routing diverges to the bond pads, which fit the APV25 pitch.

The functionality of this sensor is investigated, basically with respect to the signal-to-noise ratio in the pitch adapter region.

Another design study is realized in the FOSTER[3], a sensor with short strips and edge readout shown in figure 5.14. The investigation of this sensor is one major part of this thesis.

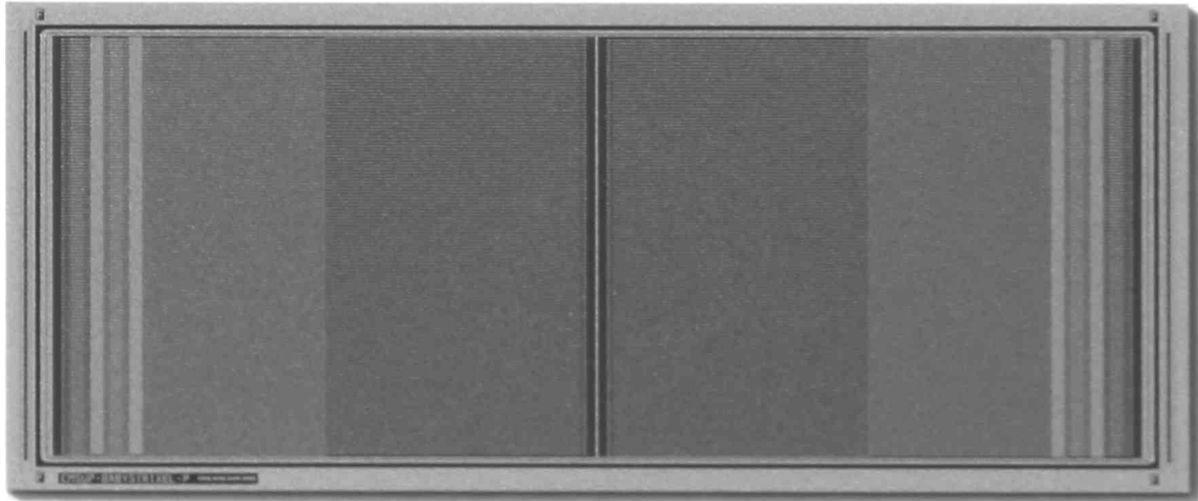

Figure 5.14.: Picture of the FOSTER, a fourfold segmented strip sensor with edge readout. This sensor increases the granularity by a factor of four and retains the readout at the sensor edge.

Section 6.3.2 will give detailed information on the design of the sensor, but also the picture in figure 5.14 and the schematic sketch in figure 5.15 show the differences to a standard strip sensor. The Foster has a fourfold segmentation, which can be seen by the differently shaded areas (dark grey in the center and light grey at the edges). Divided by a central bias line, each half of the sensor consists of two types of strips: near-strips and far-strips. The near-strips are built like standard strips, having an implant strip with an aluminum readout strip on top separated by a thin coupling oxide. The implants of the near-strips are connected to the bias ring at the sensor edge, where all AC contact pads are positioned. The near-strips are the strips near to the sensor edge, the far-strip are the ones in the center, see figure 5.15.

The far-strips have a slightly different design. Positioned in the center of the sensor, their implant is connected to the central bias line. The speciality of these strips is that the readout pads are positioned at the sensor edge, connected by a thin routing line running between the near-strips. Especially the crosstalk and coupling between the strips is of interest. Signal-to-noise ratio scans on selected regions, looking for induced signals on neighboring strips will be investigated.
In case the operability of the FOSTER is given, it would be a very promising candidate for using it in a p_T-module (see section 1.4.2) due to its high granularity and edge readout.

5.3.5. 2nd Metal Layer Structures

Some wafers are produced with a second metal layer on top of the first metal layer separated by a thick oxide. The idea of such a second metal layer is on the one hand to integrate the pitch adapter and the routing lines in that additional metal layer to reduce the material budget and on the other

[3]FOurfold segmented STrip sensor with Edge Readout.

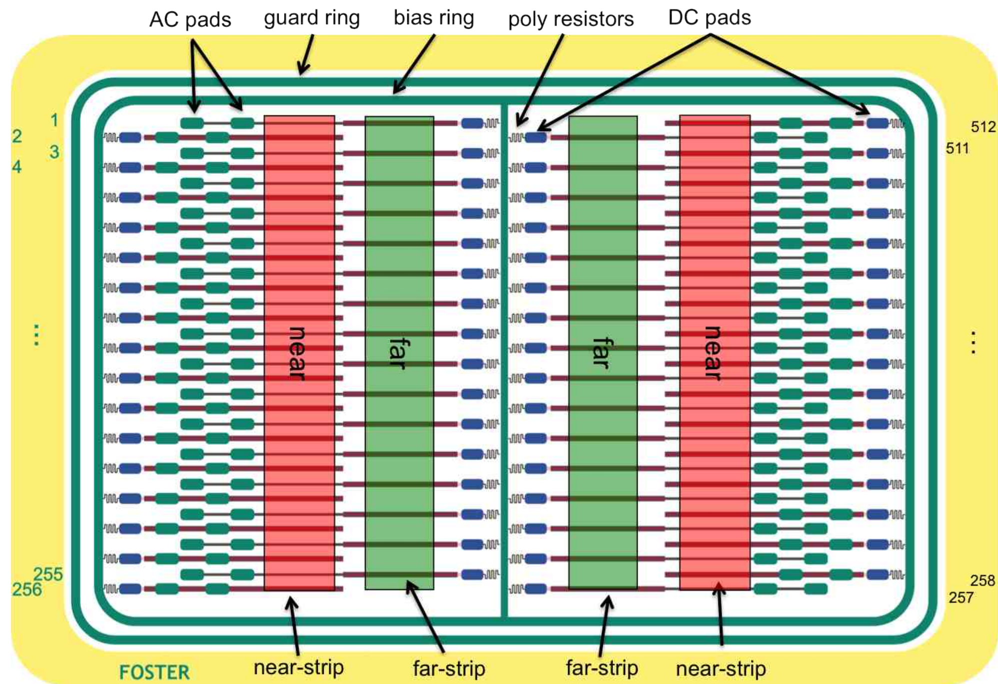

Figure 5.15.: Schematic view of the FOSTER [Kor11]. Divided by a central bias line the sensor is separated in two halves, and each of the halves is again divided into two regions. The region with the implants connected to the central bias line is called far region and its strips are called far-strips. The other region with the implants connected to the bias ring is called near region and its strips near-strips. Both far-strips and near-strips can be read out at the sensor edges allowing standard wire bonding to the readout chips.

hand to try to reduce coupling and crosstalk between implant strips, readout strips and routing lines. Several routing layouts are implemented on different structures. Section 6.3.4 gives detailed information on the design.

Chapter 6.

Designing new structures and sensors

In order to develop new sensor designs it is not only important to know how silicon strip sensors work (2.2.3), but also how they are produced. Therefore the first part of this chapter gives an introduction to the common known process technologies and process steps of planar silicon strip sensor production. The second part is dedicated to the layout tool that has been used to design our devices for the CEC and the HPK campaign. In part three the sensors and structures are specified.

6.1. Manufacturing of Silicon Strip Sensors

Nowadays the manufacturing steps for silicon strip sensors are mainly standard processes in semiconductor industry. This section shortly summarizes the production process steps from the natural quartz sand to high purity silicon wafers.

6.1.1. Techniques of Silicon Wafer Production

Although the crust of the earth is to about 25.8 weight per cent made of silicon, pure silicon does not exist in nature. It can be found in the form of quartz sand (SiO_2). First the quartz sand has to undergo several purification and melting processes to be transformed into raw silicon or metallurgical grade silicon with a purity $\geq$ 95 %. Which again passes purifying and melting steps, until it finally reaches Electronic Grade Silicon (EGS) with a purity of 99.999999999% or $\leq 1/100$ ppb.
Then the polycrystalline rod has to be turned into a single crystal ingot, where all needed dopants are included. The two most common techniques for the single crystal growth are the Float Zone process and the Czochralski process, shown in figure 6.1.

- **Float Zone (FZ) Silicon** growth is carried out on a polycrystalline silicon rod, that is placed on top of a single crystal seed, see figure 6.1(a). Using a radio frequency (RF) heating coil, the rod is melted zonally by moving the heating coil upwards along the rod. While the melted zone solidifies in a pure single crystal, the impurities move upwards staying within the melting zone, as they have different diffusion constants.
  The FZ growth is a very clean process, as the rod is melted in a gaseous atmosphere without being in contact with any crucible or other source of impurities. The growth and quality of the FZ silicon can be controlled by the RF temperature, the movement velocity of the coil

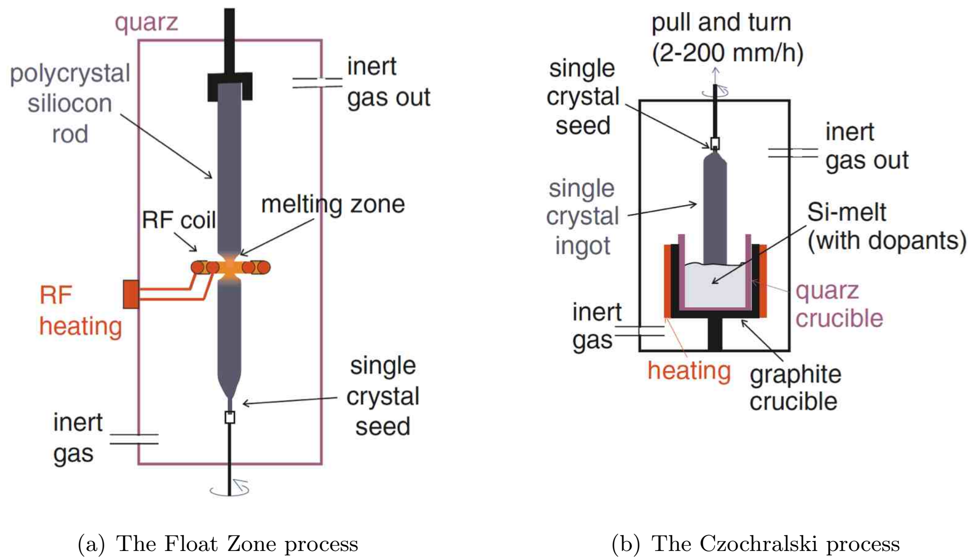

(a) The Float Zone process

(b) The Czochralski process

Figure 6.1.: Production techniques of single crystal ingots [Har08]. (a) The Float Zone process, where a polycrystalline silicon rod is put on top of a single crystal seed. By melting the silicon with a radio frequency coil that is moving upwards the rod, the silicon solidifies in a pure single crystal while the impurities move towards the end of the rod. (b) The Czochralski process uses a single crystal seed that is dipped in a crucible with melted silicon and dopants and then slowly pulled upwards while rotating.

and the rotation speed of the seed crystal. Due to its high purity, Float Zone silicon has been the standard material for the production of semiconductor sensors for years.

- **Czochralski (Cz) Silicon** growth is done by using the silicon melt, that is heated in a graphite crucible just a few degrees above the melting point. When a single crystal seed gets in contact with the melt and is slowly pulled upwards while steadily rotating, the single crystal growth out of the melt. By controlling the temperature of the melt, the pull rate and the rotation velocity of the crystal seed, the crystal pureness can be influenced.
  The Cz growth is a cheap technique, but due to the growing process prone to built in impurities in the silicon lattice. Therefore CZ silicon has also a higher oxygen concentration than FZ silicon.

- **Magnetic Czochralski (MCz) Silicon** growth is similar to the Czochralski process, except that a magnetic field is applied to the system. The magnetic field generates a Lorentz force that damps the fluctuations in the melt flow due to temperature gradients and thus increases the homogeneity of the impurities.
  The MCz crystal growth [SHR+02] is nowadays commonly used for the production of semiconductor sensors.

- Epitaxial (Epi) Silicon Epitaxial growth is the process of depositing a thin layer of single crystal material over a single crystal substrate, usually through chemical vapor deposition (CVD).

Besides the purity of the final crystal, also the resistivity and the oxide concentration are relevant parameters for the future usage as silicon sensors. Therefore dopants are added to the silicon lattice during the growth process. For FZ growth this is done by adding the dopants gaseous and for the Cz and MCz by putting them directly into the melt.
Usually the FZ silicon was preferred, as it was available as high resistivity material with typical oxygen concentrations of about 10^{16} atoms per cm^3 [BM05]. As recent studies showed higher radiation tolerance of materials with increased oxygen concentration, as can be seen in section 3.2.5, the Cz and MCz materials got more and more interesting, especially as they became available in high resistivity.
The diameter of such rods can be between 4 to 12 inch, but the manufacturers of silicon sensors are mainly capable of processing 4 to 6 inch wafers, only a few are extending to 8 inch wafers. For the sensor processing the rods need to be cut into wafers of typical thicknesses of 200 µm to 500 µm. These sliced wafers, either n- or p-type depending on the dopants during the growth, will then undergo several process steps to implement the sensor structure on it. Figure 6.2(a) shows silicon rods of different diameters and figure 6.2(b) the diced wafers of several hundred µm thickness.

(a) Silicon rods of different diameters [ZJOEC].

(b) Processed wafers of diameters from 2 to 8 inch [unk].

Figure 6.2.: Illustration of (a) silicon rods and (b) processed silicon wafers.

6.1.2. Process Steps in Planar Technology

The production of silicon strip sensors is done with a planar technology which is standard in the semiconductor industry. Nevertheless, certain requirements necessary for good quality silicon strip sensors are not common. Especially the device sizes of semiconductor industry products is small compared to silicon strip sensors. Therefore the strip sensor production requires knowledge of the single process steps and a good experience. In the following the process steps in planar technology are shortly introduced, more details can be found in [Hil08].

Thermal Oxidation

The oxide of silicon, silicon dioxide (SiO_2) has beneficial properties for the usage in semiconductor devices as it is mechanically stable and has good electrical properties. It acts as an electric insulator

and thus can be used to store charge and block current. SiO_2 can be grown in thin films on silicon wafers by thermal oxidation.
The High Temperature Oxidation (HTO) at temperatures between 800°C and 1200°C can be divided into two methods, the wet oxidation and the dry oxidation.

- **Dry oxidation** uses molecular oxygen and produces a high quality oxide.

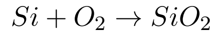

$$Si + O_2 \rightarrow SiO_2$$

  The oxide has a high density and a high breakthrough voltage but the growing process is slow and requires high temperatures. Therefore it is not possible to grow dry oxidation layers above doped areas without influencing the doping profile.

- **Wet oxidation** uses water vapor or pure H_2 and O_2.

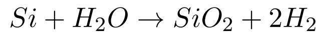

$$Si + H_2O \rightarrow SiO_2 + 2H_2$$

  The oxide grows faster and at lower temperatures due to a higher solubility of the water vapor in SiO_2, but the oxide has a less good quality and density and thus a less dielectric strength.

Doping Methods

The properties of semiconductors, especially the electrical properties like the conductivity can be manipulated by adding impurities. The creation of a p-n-junction, which is the basic principle of a silicon sensor, is realized by doping the semiconductor material with atoms of the third or the fifth group of the periodic table (see section 2.2.1), depending on the bulk doping which is done during the wafer fabrication. The structured doping of silicon is realized either by diffusion or ion implantation.

- **Diffusion** is a physical process based on thermal movement of atoms, molecules or charge carriers from regions of higher concentration to regions of lower concentrations. In the silicon crystal the impurities can fill empty places in the lattice, which are even present in a perfect single crystal, move in between the lattice or exchange places with silicon atoms. The diffusion stops either if the concentration is balanced or the temperature is lowered. A typical diffusion is done in two steps, first the dopant is led to the wafer at about 900°C and then the process is set in motion at about 1200°C. The diffusion process depends on the dopants, the concentration gradient, the temperature and the substrate and its crystallographic orientation. To structure the doping areas, the regions that should not be doped get masked with a silicon dioxide layer as shown in figure 6.3.

- **Implantation** is done by irradiating the wafer with ions. Regions that should not be doped get covered with a masking layer of photoresist. The penetration depth can be controlled by the accelerator voltage and as the irradiation is done at room temperature, earlier added dopants do not diffuse out. After placing the dopants in the silicon lattice, they have to be

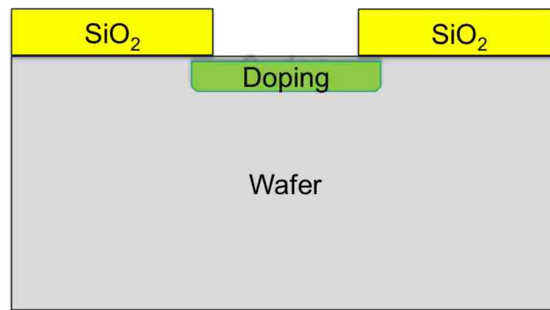

Figure 6.3.: Illustration of the diffusion process. Areas that are not meant to be doped, are masked with silicon dioxide. Due to laterally spreading of the dopants, the doped area is larger because the impurity atoms move beneath the oxide mask.

activated by high temperature process of about 1000°C, meanwhile the lattice damage due to the irradiation is healed.
The silicon atoms in the single crystal form so called "channels", see figure 6.4. Dopants moving parallel to the silicon atoms penetrate deep into the silicon as they do not scatter or react with the silicon atoms. In order to prevent the injected dopants to move parallel, a thin layer of oxide is put on top of the wafer. This layer deflects the ions and changes the incident angle which increases the probability of scattering.

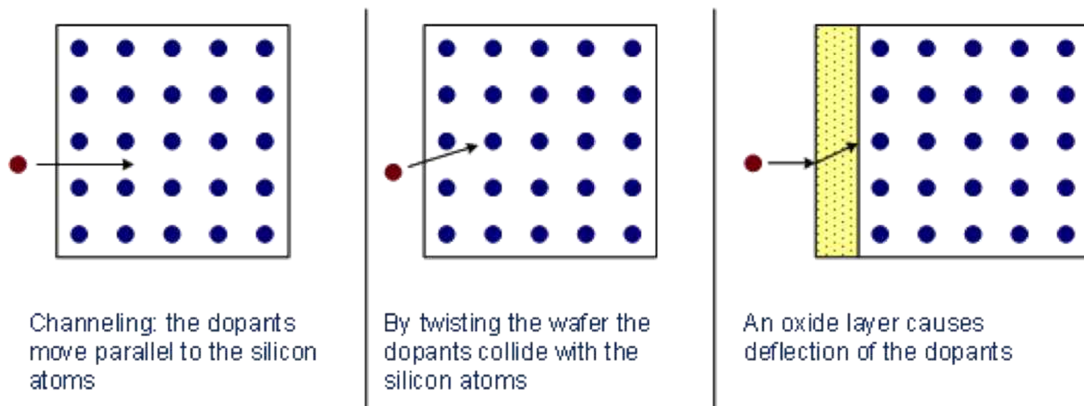

Figure 6.4.: Illustration how the "channeling" of the dopants can be prevented [Lau].

Deposition Methods

The deposition of thin films on a silicon surface can be realized by various techniques, only some of them mainly used in semiconductor processes will be explained.

- **chemical vapor deposition (CVD)** uses a gas phase of the desired constituents mixed with a tracer gas. The compounds are separated by heating and then deposited conformal on the surface. There are many different techniques like Atmospheric Pressure CVD (APCVD), Low Pressure CVD (LPCVD) and Plasma Enhanced CVD (PECVD) varying in the material that can be deposited, the needed temperature and the quality of the thin film.

- **physical vapor deposition (PVD)** uses physical processes such as sputtering or evaporation which deposits the thin films on the surface. Sputtering uses a plasma to knock particles out of a target, which then deposit on the substrate.

Besides, there is also the already mentioned epitaxial growth of crystalline film on a substrate.

Photolithography

The process of photolithography is used to form functional structures on a wafer by transferring them from a photomask. The photomask is built of a chrome film on a glass substrate forming the structure. To transfer the pattern to the wafer, it is necessary to coat the wafer with a thin film of photoresist. Then the wafer is illuminated as shown in figure 6.5 by the use of the photomask and the pattern is created after developing the photoresist. The remaining layer of photoresist can then be used as mask for further implantation or etching processes.

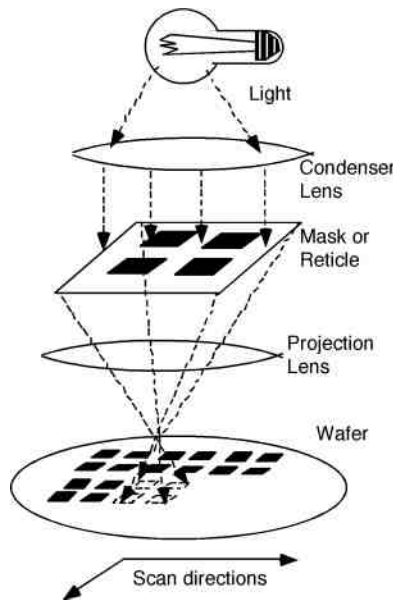

Figure 6.5.: Illustration of the photolithography. The structure on the photomask is transferred to the wafer, which is coated with photoresist, by illumination [Bar11].

Etching Methods

Etching is the basic method used to structure silicon wafers by removing unwanted layers. As the structures have a size of several μm, it is important to etch as accurate as possible which can be achieved by choosing etchants with suitable properties. Two important properties of etchants are the selectivity and the isotropy. The selectivity describes the difference in the etching rate of a given etchant applied to different materials. Figure 6.6 illustrates the difference between a good and a poor selectivity.

The isotropy describes the difference in the etching rate of a given etchant in different directions. This can lead to the so called "underetching" and has to be taken into account. Figure 6.7 visualizes the etch behavior of an anisotropic and an isotropic etchant.

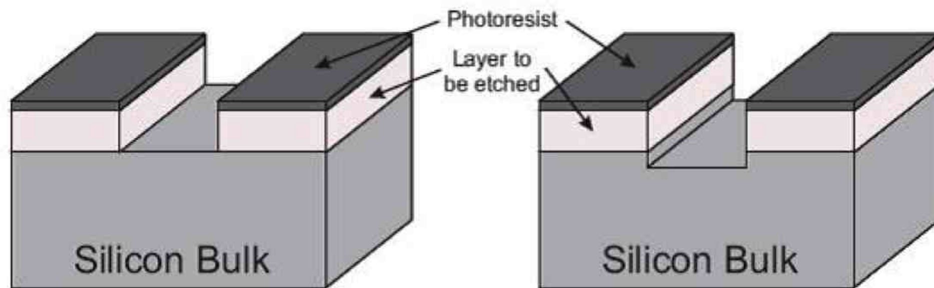

Figure 6.6.: Comparison of etchants with good selectivity (on the left) and poor selectivity (on the right). In the case of poor selectivity not only the top layer is removed, but also the underlying [Dra10].

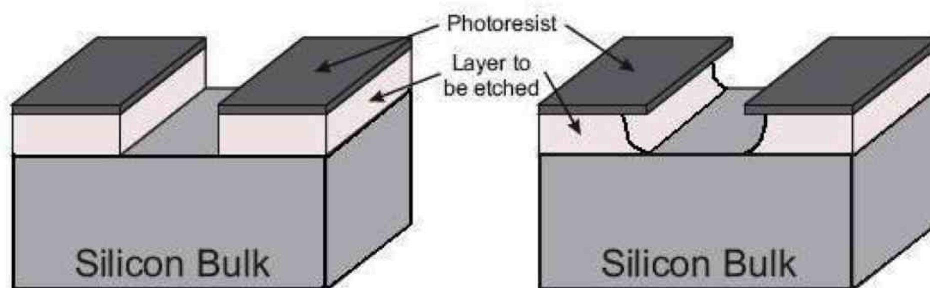

Figure 6.7.: Comparison of anisotropic and isotropic etchants. Anisotropic etchants can be used to produce exact structures (on the left) while isotropic etchants can lead to underetching [Dra10].

There are generally two categories of etching with different properties:

- **Wet etching** uses chemical solutions to remove material from the surface. There are several methods that offer a good selectivity but they are basically isotropic and have a low etch rate.
- **Dry etching** refers to the physical removal of material by ion bombardment. Common methods like ion beam etching or plasma etching are preferred in the semiconductor industry. They offer high and anisotropic etching rates.

6.1.3. Technological Sequence for Pad Detectors with Bias Resistors and AC Coupling

Using the process steps of planar technology, this section will visualize the production sequence of a silicon strip sensor beginning with a doped FZ silicon wafer. Each process step consists of several smaller processes and uses a different photomask. The sequence of steps is ordered in such a way, that the highest temperature step comes first, followed by steps of decreasing temperature. In this way one can prevent, that a high temperature step influences or damages a doping profile or structure of an already completed process step. It is also necessary to begin with the most inner

bulk structures first.
The following illustration of process steps is a short summary of the many processes needed to produce a silicon strip sensor. It shows the basic steps and should be sufficient to communicate the main principle. As each manufacturer uses individual parameters adjusted to their machines and technologies, this illustration is not generally, but goes along with the manufacturing processes of silicon sensors by ITE[1] Warsaw [Mar05].
The thickness of the layers are not to scale and many of the smaller steps in the fabrication process are omitted.

1. A plain n-type silicon FZ wafer to start with (see figure 6.8).

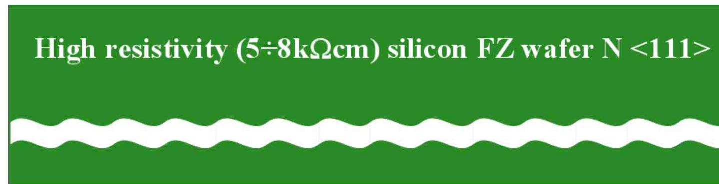

Figure 6.8.: A plain n-type FZ silicon wafer at the beginning [Mar05].

2. Oxide is grown on all sides of the wafer.

3. Removal of the back side SiO_2 in order to build a low ohmic contact.

4. Back side doping with phosphorus to generate the n+ contact by diffusion (see figure 6.9).

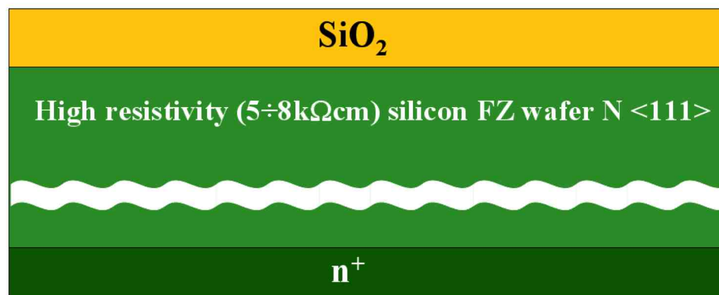

Figure 6.9.: A silicon wafer is oxidized, the oxide on the back side is removed and the back side n+ contact is diffused [Mar05].

5. Oxidation on front and back side for the following steps.

6. Photolithographic step to open doping windows on the front side (see figure 6.10).

7. Boron implantation on the front side at places without SiO_2.

8. Growing of a thin thermal oxide above the implanted area (see figure 6.11).

9. Deposition of a polysilicon layer on top to form the bias resistor.

[1] Institute of Electron Technology, Warsaw, Poland

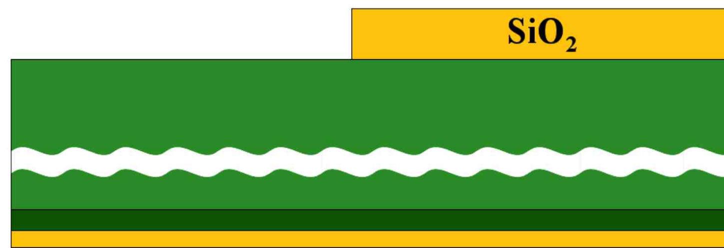

Figure 6.10.: After oxidation and photolithography, windows for the p+ doping are opened in the SiO_2 [Mar05].

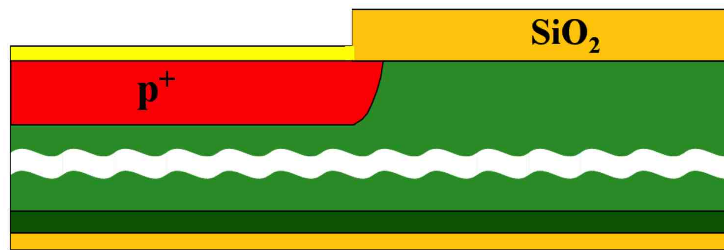

Figure 6.11.: After boron implantation a thin thermal oxide is grown over the implanted areas. This oxide will later represent the thin readout oxide, separating the implant strip from the aluminium read out strip [Mar05].

10. Doping of the polysilicon layer with boron to define the resistivity of the bias resistor (see figure 6.12).

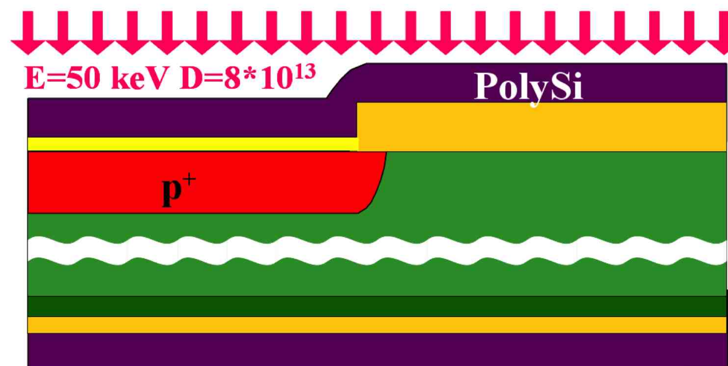

Figure 6.12.: Deposition of a polysilicon layer on top and doping it with boron defines the resistivity of the bias resistors [Mar05].

11. Oxidation for the next photolithographic step.

12. Patterning of the polysilicon layer by photolithography defines the shape of the bias resistor.

13. Removal of the polysilicon from the back side (see figure 6.13).

14. Defining the contacts to the resistors by photolithography.

15. Boron implantation to lower the resistivity of the contacts.

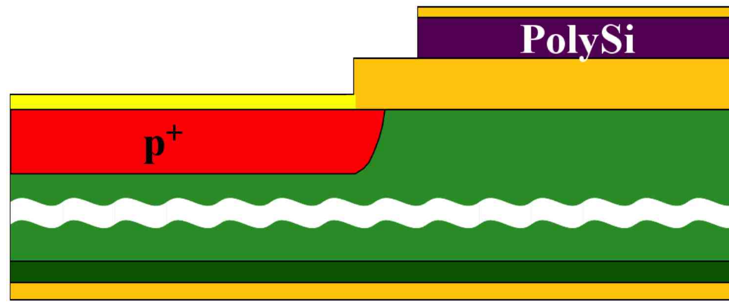

Figure 6.13.: After removing of the polysilicon surpluses the bias resistor is finished with oxide on top [Mar05].

16. Opening of the contacts to the p+ by photolithography (see figure 6.14).

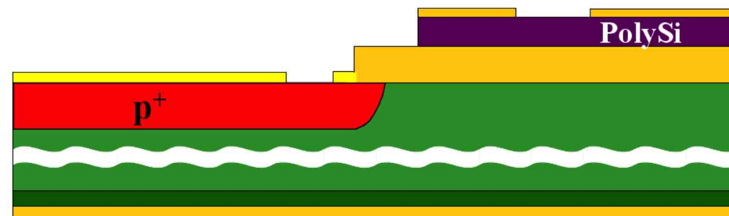

Figure 6.14.: The contacts to the resistors are defined by photolithography and boron implantation lowers the resistivity of the contacts. Annealing in nitrogen tunes the resistivity of the resistors. A thin insulation is deposited between polysilicon and metal, a photolithographic process defines the opening to the p+ contacts [Mar05].

17. Deposition of an aluminium-silicon-copper composition on both sides of the wafer.

18. Defining the pattern of the metallization by a photolithographic process (see figure 6.15).

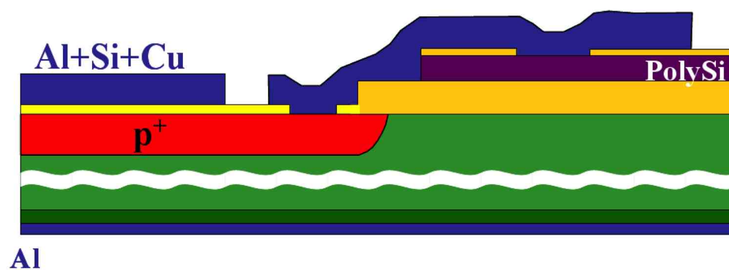

Figure 6.15.: Metal is deposited on the front and back side of the wafer. A photolithographic process defines the pattern of the metallization [Mar05].

19. Putting a SiO_2 passivation layer on top of the sensor with opening windows to the metal contacts.

20. A single metal AC coupled detector is ready. For a double metal detector, a thick oxide with vias would cover the front with a second metal layer above.

6.2. LayoutEditor

The wafer production as described in section 6.1.3 is based on photolithography. To process a standard silicon strip sensor on a n-type substrate at least 7 photo masks are needed to implement and build sensor specific structures as strips, contacts, vias and resistors (see 6.2.2).
The masks are in general designed with commercial software programs, intended for most complex ASIC design, that are extensive and expensive. The masks are then defined using the vector graphic format GDS II[2]. Trying different software programs, the open source program LayoutEditor[3] [Thi] fulfilled most of our requirements as it had almost the functionality needed and was easy to handle. Important features which have been missing in the original software could be implemented by Joachim Erfle [Erf09].
One of those features is the usage of macros, which allows simple design of structures with many repetitive parts, such as a silicon strip sensor. The following section will shortly describe how a standard silicon strip sensor is designed using the adjusted open source tool LayoutEditor.

6.2.1. Using the software

The design for the sensors and pitch adapters has been done with the LayoutEditor using the C++ macros which allow parameter handover. In a first step, a set of simple functions have been programmed. This set served as a basis for the design of more complex structures.
Larger devices have been divided into three parts. Part one is the outer region of the sensor with the sensor periphery, part two is an inter-region with the bias and guard rings and part three is the strip region. Figure 6.16 illustrates a section of the code of the main file for placing the strips.

Executing the main file, where all parameters like sizes and distances are defined, the three parts are drawn and the complete structure is displayed (see figure 6.17).

[2]GDS: Graphic Data System, is the standard database file format for data exchange of integrated circuit or IC layouts

[3]GPL-Version, Build: 20090105, Homepage: `http://www.layouteditor.net`

```
	//Drawing one strip
layout->executeMacro(rootpath+"parts/Strip.layout",
	rootpath,0,0,Height-2*OuterRingHeight-
	2*InterRingHeight+2*YStripOverhang,StripPitch,0);

	//Pointer to the cell of the strip
layout->drawing->setCell("Strip_0");
cell *local=layout->drawing->currentCell;

	//Change to main cell
layout->drawing->setCell("MiniSensor");

	//Using a loop to position the strips at their places
for(i=0;i<NumberOfStrips;i++)
	{
	p.setX(XCenter+StripPitch/2+((2*i-
	NumberOfStrips)*StripPitch)/2);
	p.setY(YCenter);
	element *e=layout->drawing->currentCell->addCellref(local,p);
	}
```

Figure 6.16.: Section of the C++ macro to place strips in LayoutEditor.

6.2.2. Designing a Strip Sensor

The complete design file for a strip sensor on a n-type silicon substrate is shown in figure 6.17. The p-type versions, one with p-stop and one with p-spray have been done by HPK.

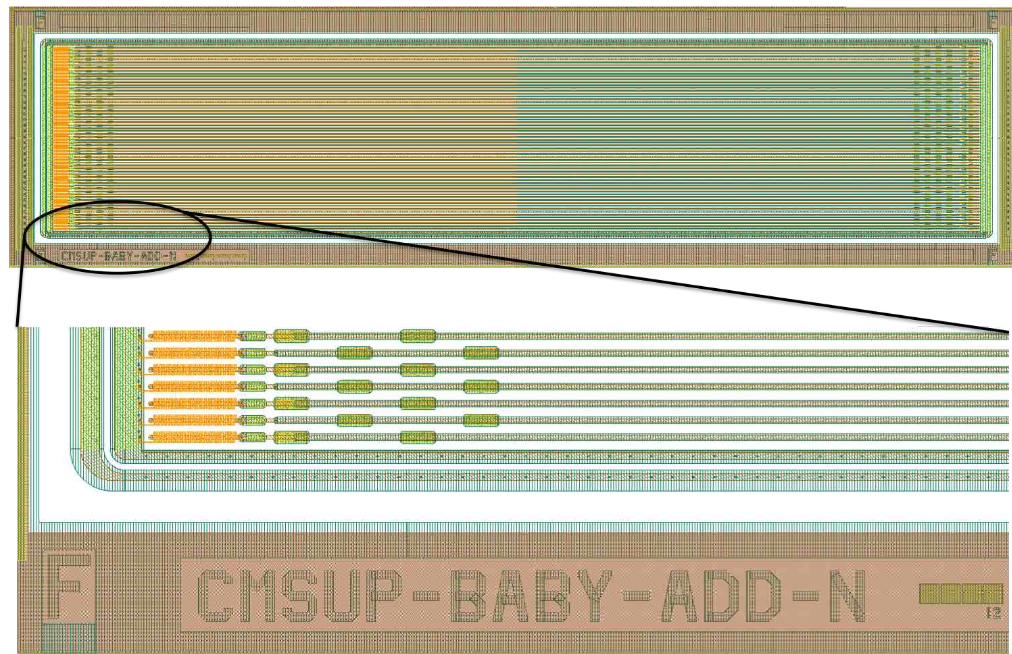

Figure 6.17.: Illustration of a complete design file (GDS II file) of a n-type strip sensor on the top and a zoom in on the bottom.

The design file consists of several layers. Each layer represents one photo mask and has its own color and purpose. Table 6.1 gives an overview of the layers and their function for n-type and p-type substrates, the numbering is done by HPK. P-type sensors need one additional mask, as the phosphorus doped implant strips need to be insulated (see 2.2.3). All layers on top of each other result in figure 6.17. The following listing will shortly describe each single layer for the n-type sensor:

- **Layer 8** defines the surrounding area of a sensor 6.19. It is phosphorus doped and isolating the active area from the high voltage and the surface currents.
- **Layer 9** defines the implanted strips of the sensor. The strips are boron doped in order to form a pn-junction with the phosphorus doped bulk substrate. Besides the strips, also the bias and guard ring are composed of a boron doped layer. The size of an implanted structure is always a bit bigger than the design due to underetching (see figure 6.7).
- **Layer 10** is the metal layer, usually aluminium. The mask provides the layout for the readout strips, the contact pads, the surrounding rings and the sensor periphery.
- **Layer 6** is used to shape the bias resistors and to stabilize the contact pads.
- **Layer 7** defines polysilicon heads that are important to improve the contact between the bias resistor and the aluminium by preventing the formation of a Schottky-Contact.

Table 6.1.: Overview of the layers and their function

Layer Number	p-type	n-type
1	p-stop	-
2	n+	-
3	via contact	via contact
4	aluminium	-
5	pad	pad
6	poly-silicon	poly-silicon
7	poly-n+	poly-n+
8	p+	n+
9	-	p+
10	-	aluminium

Figure 6.19.: The sensor area is surrounded by a highly phosphorus doped ring.

- **Layer 3** defines the aluminium vias. They provide a contact between the boron doped silicon and the aluminium topping.
- **Layer 5** is used for the protective passivation layer. This is a negative mask, which means that the mask structure will later be the region without passivation. This gives access to the contact pads and rings.

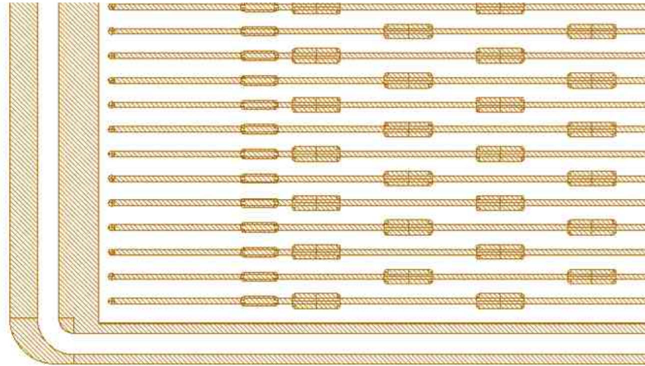

Figure 6.21.: The mask for the boron implantation forms the actual strips that collect the generated charges. They form together with the phosphorus doped bulk the pn-junction.

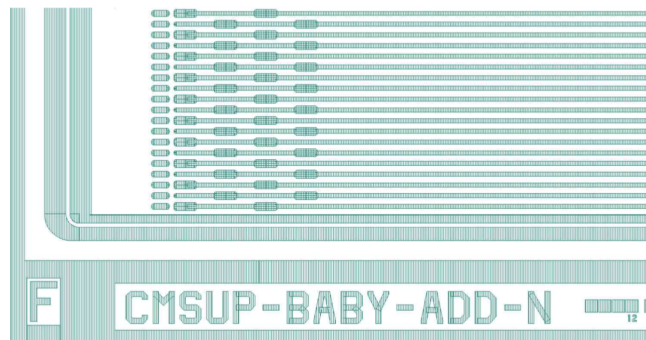

Figure 6.23.: The aluminium layer defines the readout strips, contact pads, the surrounding rings and the periphery.

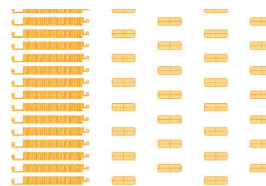

Figure 6.25.: The mask for the polysilicon is used to design the bias resistors and to form the contact pad.

Figure 6.27.: Polysilicon heads are used to improve the connection between the bias resistor and the aluminium.

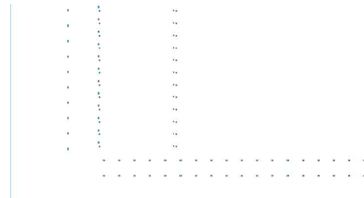

Figure 6.29.: The connection between regions of boron doped silicon and the metal layer is done by vias.

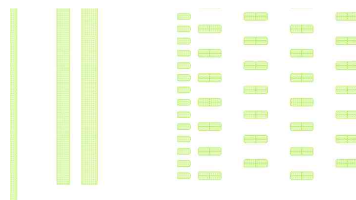

Figure 6.31.: The protective passivation layer covers the full sensor. There are openings at the pads and the rings, enabling to contact the aluminium for electrical characterization measurements.

6.3. Sensors and Structures

In order to comply with the risen requirements of the CMS upgrade to the detectors (section 1.3), it is not only essential to develop radiation hard sensors but also to investigate new sensor designs. The following section will give an overview of different sensors and pitch adapters that have been designed at IEKP. This was the first time that the gds[4] files were completely created in-house. The design has been made according to some design rules, for instance keeping the pitch-to-width ratio at 0.225 and technological guidelines. All structures have been designed for n-type silicon. The producer HPK adopted the files to their production processes and translated the designed n-type structures for the p-type wafers.

There are two standard strip sensors. One to analyze the influence of radiation damage on the characteristics of silicon strip sensors called Baby_Std and the other a smaller one called Baby_Add to investigate the Lorentz angle. There is a fourfold segmented sensor with short strips and the readout connection at the edges offering a high granularity called FOSTER (FOurfold segmented STrip sensor with Edge Readout) and a sensor with an integrated pitch adapter in the first or in a second metal layer, helping to reduce the material budget. Besides the sensors, several pitch adapters have been designed and produced to connect the different sensors to the various readout systems.

6.3.1. The Standard Strip Sensors

The standard strip sensors, one with 256 strips and the other with 64 strips, have a pitch of 80 µm. They are smaller (thus the prefix "Baby") and slightly changed reproductions of the standard strip sensors used for the current CMS tracker. The design of those two sensors is identical, they only differ in size and in the purpose of investigations.
The sensors have a standard periphery with the strip numbering, the sensor name, position markers and scratch pads. Figure 6.32 shows a section of the Baby_Std. The position markers, here in a shape of the letter "F" is used to position the sensor when assembling it to a module. The scratch pads assign the sensor a unique number, since there are two Baby_Std sensors on a wafer, six wafer per material and 21 different materials, see table 5.1.

The active sensor area with the strips is surrounded by the bias ring and the guard ring. Both rings are composed of a ring of highly boron doped silicon that is connected via vias to an aluminum ring above. Generally all aluminium layers on top of boron doped structures have an aluminium overhang, which is beneficial for the breakthrough behavior of the sensor. This aluminum ring has passivation openings in order to be able to contact the aluminium with probe needles to perform electrical characterizations. The bias ring is used to power the sensor, by connecting all implanted strips via bias resistors to ground while the sensor back side is on high voltage. The guard ring shapes the electric field at the borders and makes the sensor high voltage tolerant. This is necessary for the exact determination of the volume current and the full depletion voltage. A detailed view

[4]gds = Graphic Database System is the industry standard for data exchange of integrated circuit or IC layout artwork.

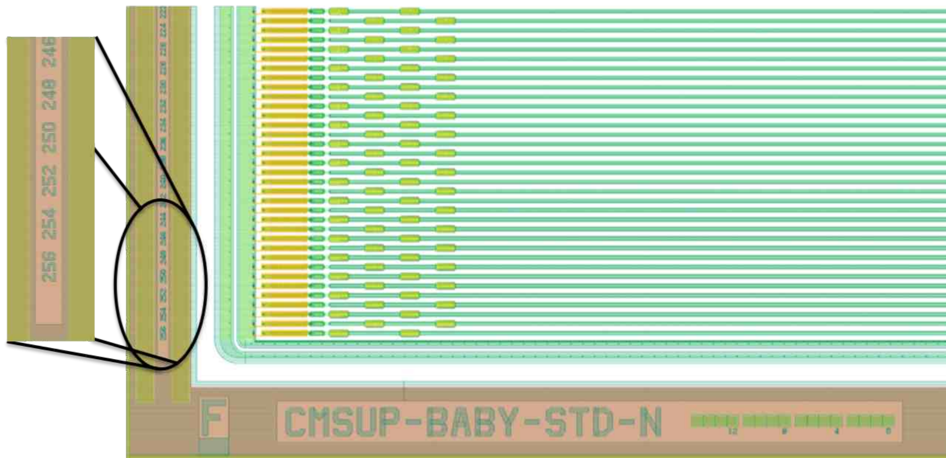

Figure 6.32.: Sketch of the gds file of a Baby_Std sensor showing the sensor periphery. The sensor has a standard periphery with strip numbering, position markers, the sensor name and a scratch pad to identify the sensor's wafer.

of these rings is shown in figure 6.33.

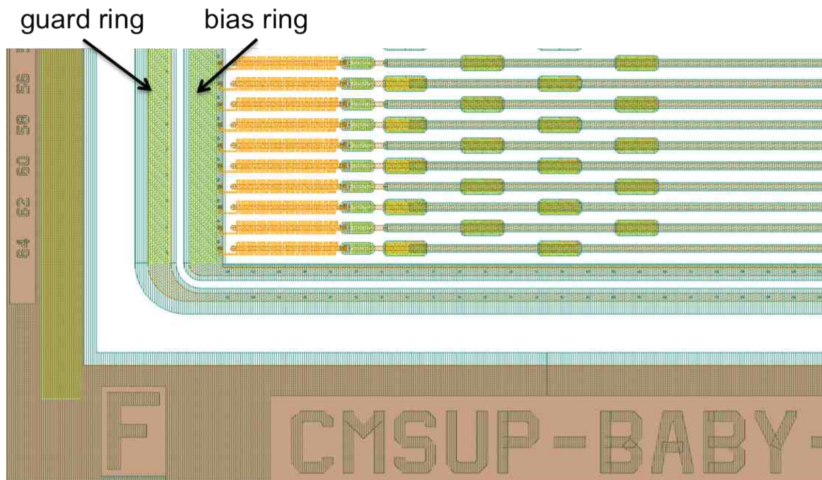

Figure 6.33.: Section of the gds file of a Baby_Std sensor depicting guard and bias ring. The guard ring is the outer of the two rings, typically floating, but necessary for the exact determination of the sensor current and the full depletion voltage. The inner bias ring is used to bias the sensor. It is connected via the bias resistors to the implant strips of the sensor.

The bias resistors are at one end connected to the bias ring and at the other to the DC pads, which connect through the oxide layer to the implant strips using vias. Figure 6.34 shows an overview of a sensor section. The implant extends from one edge of the sensor to the other beneath the aluminum readout strip, the contact pads and the bias resistors. In the design, the width of the implant is 18 µm and the aluminium readout strip on top has 31 µm due to the metal overhang.

The Baby_Add is exactly designed like the Baby_Std but has only 64 strips.

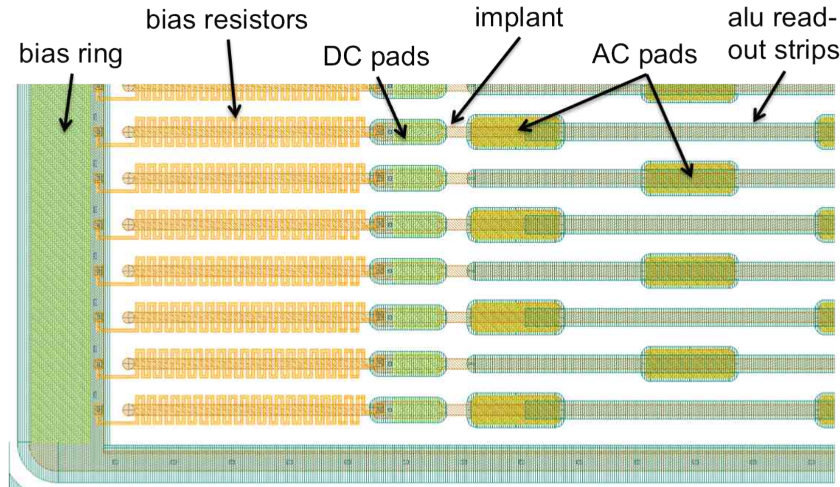

Figure 6.34.: Section of the gds file of a Baby_Std sensor showing the strip region. The implants run beneath the bias resistors, DC pads, AC pads and the aluminium readout strip from one edge of the sensor to the other. The DC pads connect the bias resistors to the implants and the AC pads connect to the readout strip. All pads and the bias ring have openings to contact the sensor for the electrical measurements.

6.3.2. Sensor with Fourfold Segmented Strips and Readout at the Edge - FOSTER

The FOSTER prototype is a 35 mm × 15 mm sensor with 2 x 256 strips. The strips have an implant strip length of 7.6 mm (about one quarter of the sensor length) and a pitch of 100 µm. The AC pads used to connect the strips to the readout electronics are all placed at the sensor edge. Before discussing the layout in detail, figure 6.35 gives a first schematic overview of the sensor. It is separated into two identical halves by an additional central bias line. Each of the halves is again divided into two regions called "near" and "far" with corresponding near-strips and far-strips.

To take a closer look at the sensor and its differences to a standard strip sensor three sections of the layout are discussed in detail:

- **edge of the sensor**
  The edge of the sensor shown in figure 6.36 is very similar to the edge of a standard sensor. There is no difference in the sensor periphery with strip numbering, guard and bias ring. The DC pads (94 µm × 38 µm) of the near-strips are connected via bias resistors to the outer bias ring. The AC pads (350 µm × 40 µm) of the near-strips and the far-strips are both positioned at the sensor edge. In the near region, where the aluminium routing lines of the far-strips run between the near-strips, the actual pitch is 50 µm.

- **overlap region**
  The overlap region between near and far is depicted in figure 6.37 and indicates the special feature of the sensor. The near-strips coming from the left side are designed like standard strips while the far-strips coming from the right side have an extended aluminium routing line to the sensor edge. For the near- and for the far-strips the implant width is 23 µm and the width of the aluminium readout strip on top of the implant is 36 µm, but the routing line of the far-strip that has no implant beneath is only 13 µm wide. The design difference between

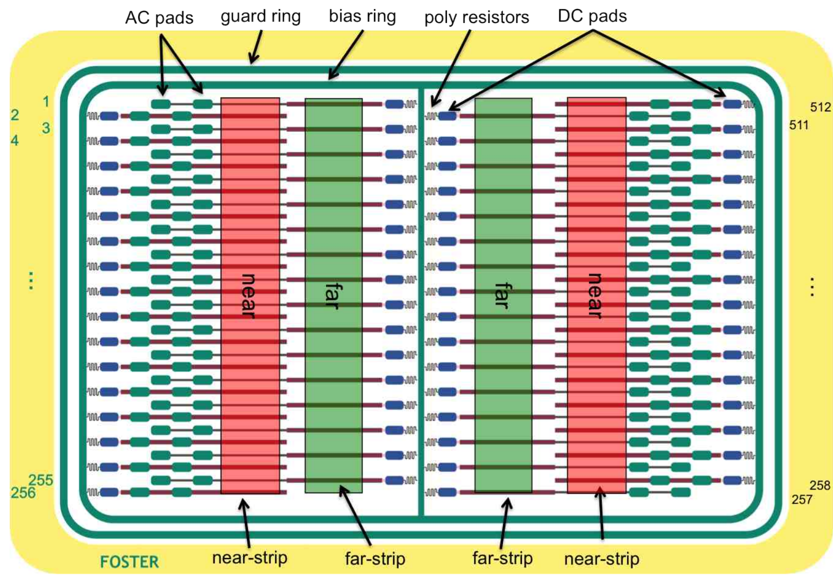

Figure 6.35.: Schematic view of the FOSTER [Kor11]. Divided by a central bias line the sensor is separated in two halves, and each of the halves is again divided into two regions. The region with the implants connected to the central bias line is called far region and its strips are called far-strips. The other region with the implants connected to the bias ring is called near region and its strips near-strips. Both far-strips and near-strips can be read out at the sensor edges allowing standard wire bonding to the readout chips.

near-strips and far-strips are shown in detail in figure 6.38.

- **central region**
  The additional bias line that can be seen in figure 6.35 connects via the bias resistors in the centre to the DC pads and the implants of the far-strips. The additional central bias line is crucial as it enables the fourfold segmentation of the sensor.

Looking at the current tracker upgrade plan [Abb11], which includes trigger-capable "2S-modules", such kind of sensor would even be beyond baseline, meeting all demands on a "2S-module"-sensor, AC pads placed at the sensor edge to preserve the possibility of standard wire bonding to connect the readout electronics and in addition to have more and shorter strips to increase the granularity.

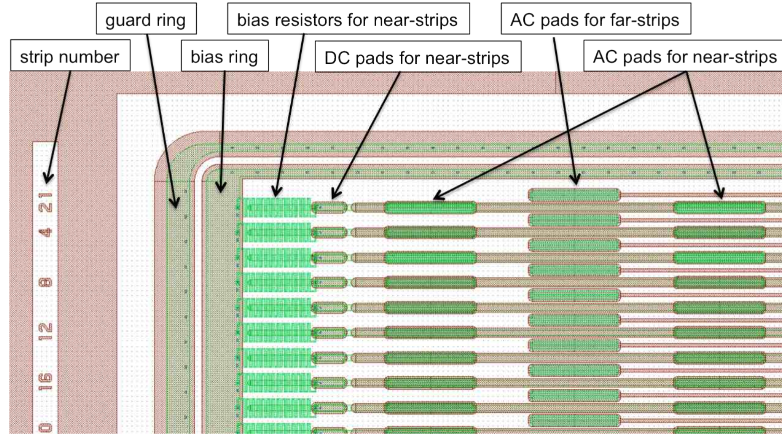

Figure 6.36.: Section of the FOSTER showing the upper left corner of the sensor. Starting on the left, the standard sensor periphery including strip numbering, guard ring and bias ring as electric field forming parts, is shown. The DC pads of the near-strips are connected to the bias ring via bias resistors. Due to the narrow spacing, the AC pads of the near-strips and the far-strips are staggered.

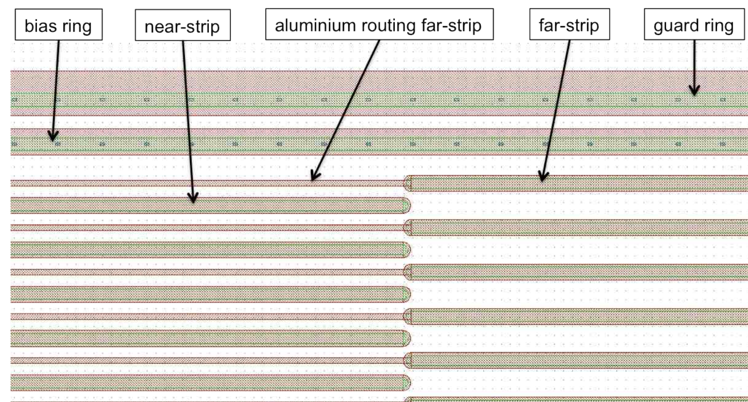

Figure 6.37.: Section of the FOSTER where the near-strips coming from the left meet the far-strips coming from the right. The thin aluminium routing of the far-strip continues between the near-strips to the sensor edge where the AC pads are located (figure 6.36). This allows the usage of a readout at the sensor edge.

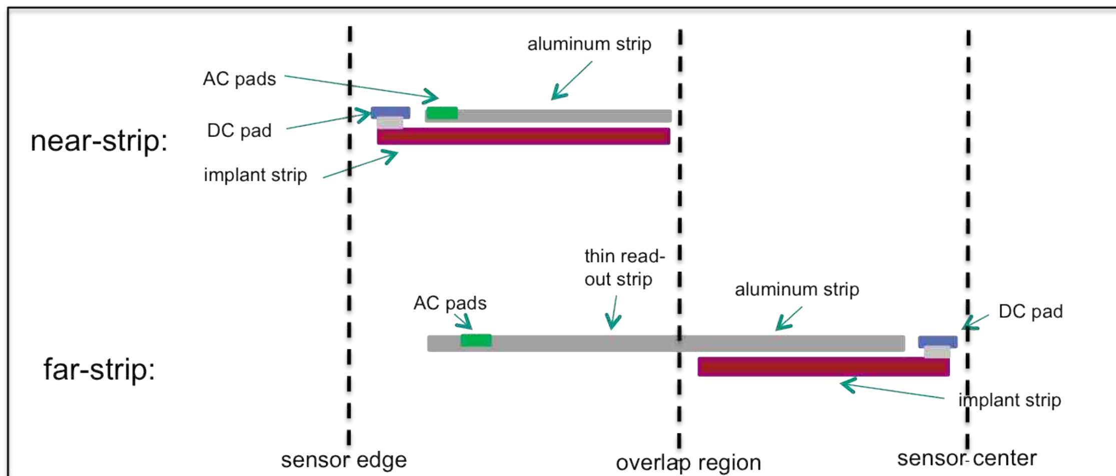

Figure 6.38.: Schematic drawing of the near-strip and far-strip highlighting the differences in the composition. The near-strip (on top) is designed like a standard strip while the far-strip (on bottom) is slightly different. The aluminium routing is not only above the implant strip but continues to the sensor edge where the AC pads are located. The DC pads of the far-strips are not positioned at the sensor edge but next to the central bias line.

6.3.3. Sensor with Integrated Pitch Adapter

The Baby_PA prototype is a 35 mm × 12.38 mm sensor with 128 strips and an integrated pitch adapter. Pitch adapters are used to adapt the sensor pitch to the pitch of the readout chip. The pitch adapter integrated on this sensor adapts from the strip pitch of 80 µm to the pitch of an APV25 readout chip with 44 µm. Typically the pitch adapter is produced on a glass substrate and bonded between sensor and readout chip. Integrating it into the sensor metal layer saves material. The Baby_PA is mostly built like a standard strip sensor. The only difference is the aluminium layer. Figure 6.39 shows the gds file of the Baby_PA with the integrated pitch adapter on the right side on the sensor.

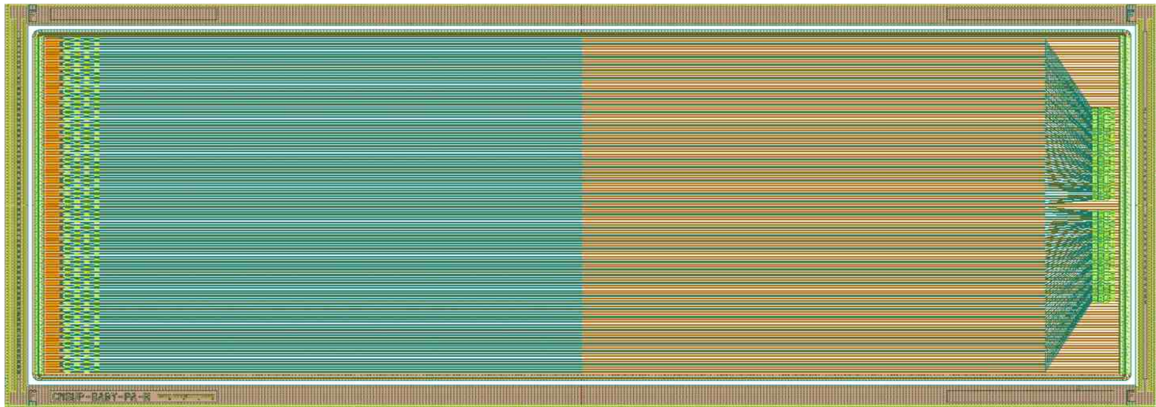

Figure 6.39.: Complete view of the designed Baby_PA prototype.

By zooming in the pitch adapter region as done in figure 6.40, the routing of the pitch adapter can be seen. While for a standard sensor the aluminium readout strips run on top of the implant strips separated by an insulating oxide layer from one side of the sensor to the other, the 31 µm wide readout strips of the Baby_PA end about 2.3 mm away from the edge. From there, they are connected with 10 µm wide aluminium routing lines to the pad pattern at the sensor edge, shown in figure 6.40(b). The pad pattern fits exactly to the APV25 readout chip. Therefore the sensor can directly be bonded to the chip, no additional pitch adapter on a glass substrate is needed.

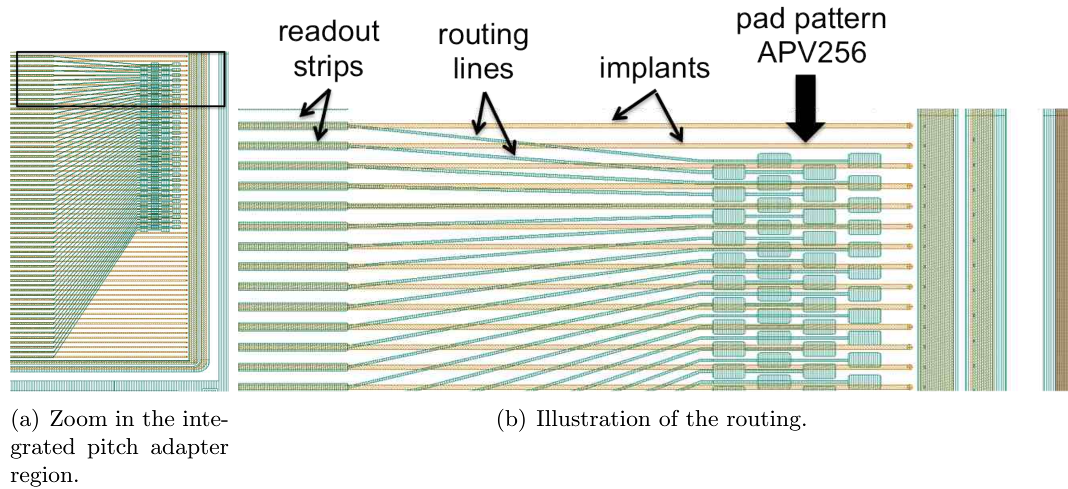

(a) Zoom in the integrated pitch adapter region.

(b) Illustration of the routing.

Figure 6.40.: Close look at the pitch adapter region. (a) Shows one half of the pitch adapter. (b) The aluminium readout strips running above the implant strips end close to the sensor edge (on the left) and route to the aluminium pads fitting the APV256 chip pads (on the right). The routing lines crossing on top of the implants are thinner then the readout lines that run straight on top of the implants.

The size of the here used integrated pitch adapter is about 2.2 mm, but of course the size and the geometrical structure of such an integrated pitch adapter can differ, see next section.

6.3.4. Sensors with Integrated Pitch Adapters in a Second Metal Layer

Eighteen of the FZ wafers are produced with a second metal layer. Therefore some sensors have an additional routing on top. For the Baby_Std and the Baby_PA different pitch adapter routings have been implemented in the second metal layer.
To process a wafer with a second metal layer two more masks, respectively two more layers in the gds file are needed. The first metal layer is untouched. One layer defines the contact vias from the aluminum in the first metal layer to the second, as the processed sensor with routing in the first layer is completely coated with a thick ($\geq$1 µm) insulating oxide layer. The other layer defines the pitch adapter routing in the second metal layer.
Several pitch adapter layouts have been implemented on the Baby_Std and Baby_Add sensors to investigate their influence on the sensor properties. Figure 6.41 shows four different pitch adapter layouts in the second metal layer on the Baby_Std. Figure 6.41(a) and figure 6.41(b) show the compact pitch adapters with a size of 2.2 mm and narrow routing lines while figure 6.41(c) and figure 6.41(d) show bigger pitch adapters with size of 3.7 mm and larger spacing between the routing lines. The bigger size and the larger spacing between the routing lines is due to routing the even strip numbers upwards and the odd strip numbers downwards in order to reduce crosstalk and signal coupling.

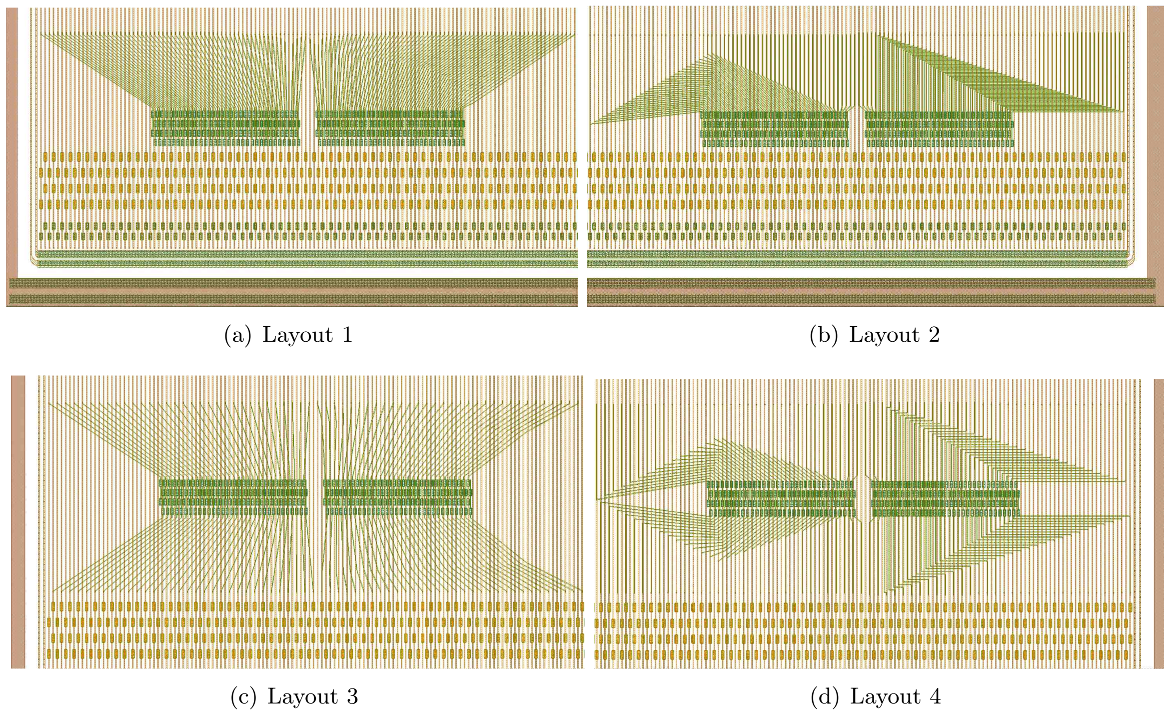

(a) Layout 1 (b) Layout 2

(c) Layout 3 (d) Layout 4

Figure 6.41.: Overview of the different pitch adapter layouts for the pitch adapters in the second metal layer on the Baby_Std. (a) and (b) show the compact pitch adapter layouts. (c) and (d) show the pitch adapter layouts with routing lines alternately upwards and downwards.

6.3.5. Pitch Adapters for Multi-geometry-sensors

As pitch adapters are needed to connect the sensors to the readout chips, each sensor that will be used with a readout system has its own pitch adapter. Especially the multi-geometry-sensors with several regions of different pitches need special pitch adapters.
To use the MPix and the MSSD sensors with an APV readout system several pitch adapters and pitch adapter extensions have been designed to offer multiple bonding. Figure 6.42 shows the gds file of the pitch adapter for the MPix called MPix_PA.

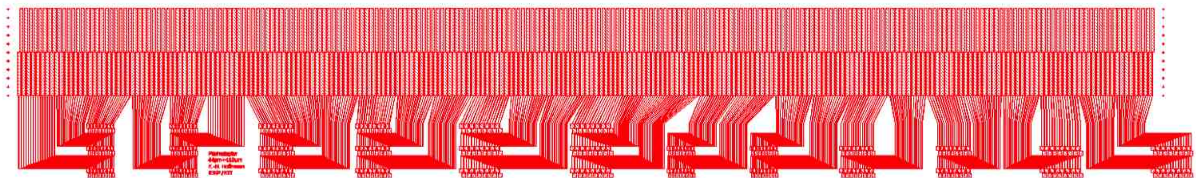

Figure 6.42.: Pitch adapter for the MPix called MPix_PA. This pitch adapter connects at one end to 480 pixels of the MPix and on the other end to a pitch adapter extension, that is further connected to the TOB_Hybrid via the TOB_Hybrid_PA.

Each of the twelve regions of the MPix is connected to the MPix_PA. For the regions 1-6 there are three rows of 16 pads per region and for the regions 7-12 there are two rows of 16 pads per region connected to the MPix_PA. The 480 pads are routed to two staggered rows of huge pads (160 µm

× 2000 µm). These pads allow multiple bonding. The advantage is, that the pitch adapter stays connected to the sensor during all measurements and irradiations and the bonding to the readout is always done using the huge pads. These pads are bonded to a pitch adapter extension, composed of 512 strips with 110 µm pitch and a length of 4000 µm. The pitch adapter extension is again connected to a pitch adapter called TOB_Hybrid_PA, that adapts to the TOB_Hybrid readout card. The TOB_Hybrid_PA is shown in figure 6.43.

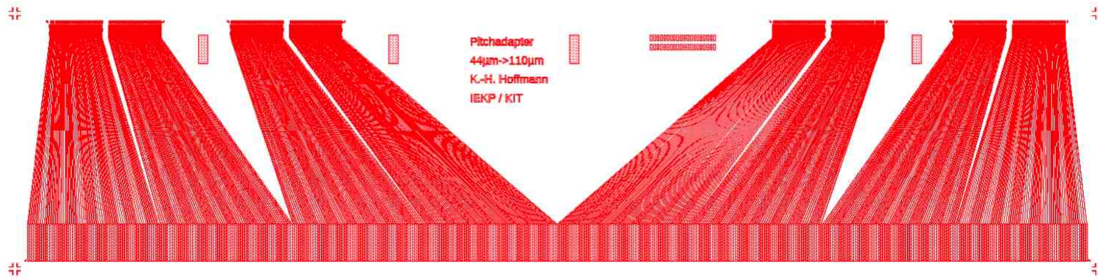

Figure 6.43.: Pitch adapter for the MPix called TOB_Hybrid_PA. This pitch adapter connects at one end to four APV25 readout chips and on the other end to a pitch adapter extension that is connected to the MPix sensor via the MPix_PA.

Figure 5.11 shows a picture of an assembled MPix module, using all the pitch adapters introduced in this section.

6.3.6. Summary

Before and during the HPK campaign several structures have been designed using the open source tool LayoutEditor. Starting with standard strip sensors and sensors with new routing designs also several pitch adapters have been composed. Table 6.2 summarizes the geometrical specifications of the designed sensors.

Table 6.2.: Overview of the geometrical specifications of the sensors

sensor	**Baby_Std**	**FOSTER**	**Baby_PA**	**Baby_Add**
size (µm)	35120 × 22620	35120 × 15120	35120 × 12380	28120 × 7260
no. of strips	256	512	128	64
pitch (µm)	80	100	80	80
alu width (µm)	31	36	31	31
implant width (µm)	18	23	18	18
width-to-pitch ratio	0.225	0.23	0.225	0.225

The development of a software framework to enable the flexible and quick design of sensors using the LayoutEditor was one major groundwork for the campaign and future sensor productions.

Chapter 7.

Initial Sensor Qualification and Irradiation Studies for the HL-LHC

Wafers of different silicon material, thickness and substrate type, introduced in chapter 5.2, offer valuable clues on the future sensor technology baseline for the Tracker Upgrade Phase II. Therefore the non-irradiated Baby_Std sensors are first used to investigate the production quality of the producer HPK and than for the irradiation study.
After the irradiation to different fluences, the sensors are tested again, to conclude on changes of sensor properties and functionality. The following chapter will only show a fraction of the performed measurements.

7.1. The Wafers

The wafers have been delivered in N, P and Y type, where P and Y are both p-type silicon but with different isolation techniques. The P wafers are made with p-stops while the Y wafers come with a p-spray. The sensors and also some of the diodes of the P wafer have no proper isolation between guard ring and bias ring / pad, which in some cases leads to strange current and capacitance values for voltages below 100V. At higher voltages the electric field seems to compensate these effects. The measurements with connected guard ring are necessary for later investigations, as the sensor volume is better defined with the guard ring connected to ground.
All wafers of float zone material, labeled FZ, come with a physical thickness of 320 µm ± 6 µm [Jun11]. The active thickness of the wafers is reduced to the ordered thickness by a process called deep diffusion from the wafer back side. There is not much information about that new process technology. Figure 7.1 shows a schematic illustration of the deep diffusion process compared to the commonly used wafer bonding technology.
Some additional wafers of float zone silicon with a physical thickness of 200 µm (FTH) have been delivered later for comparison with the deep diffusion FZ200. As these wafers arrived late, the qualification of these sensors before irradiation have only been done in a shortened manner.

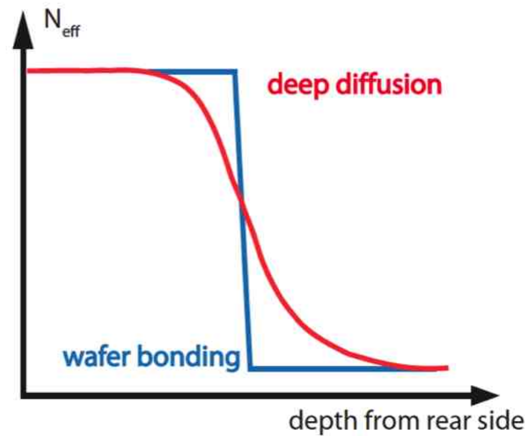

Figure 7.1.: Schematic illustration of the deep diffusion process, compared to the wafer bonding technology [Jun11]. The active wafer thickness depends strongly on the deep diffusion process, which can lead to imprecisenesses.

7.2. Qualification of Non-Irradiated Sensors and Development of Sensor Characteristics under Irradiation

The following measurements show the qualification of the non irradiated sensors and the development of their properties and functionality under the influence of radiation damage. According to the irradiation planning in table 5.2 the irradiations for all radii have not been finished yet. Some fluence steps are still missing. Therefore the measurement results in this section will only show the evolution of sensor properties for the R=40cm and R=20cm fluences, corresponding to the following materials and thicknesses:

- FZ320N FZ200N M200N FTH200N
- FZ320P FZ200P M200P FTH200P
- FZ320Y FZ200Y M200Y FTH200Y

In addition some measurements have also been done on FZ120 sensors for comparison.
The measurements have been done according to the measurement specifications written in [Die], for non irradiated sensors at T=20°C and RH<20% and for irradiated sensors at T=-20°C.

7.2.1. Full Depletion Voltage

The sensor capacity drops with increasing space charge region unless a saturation value is reached, when the whole sensor is depleted. The extraction of the full depletion voltage, which is the minimal operation voltage of the sensor, from a capacitance-voltage measurement can be done by at least two methods. Both, shown in figure 7.2, help to visualize the kink in the curve, where the full depletion voltage can be read. One procedure 7.2(a) uses logarithmic plotting of both axes, while the other 7.2(b) plots $\frac{1}{C^2}$ over the bias voltage. The full depletion voltage can be read as the intersection of two linear slopes fitted to the curve.

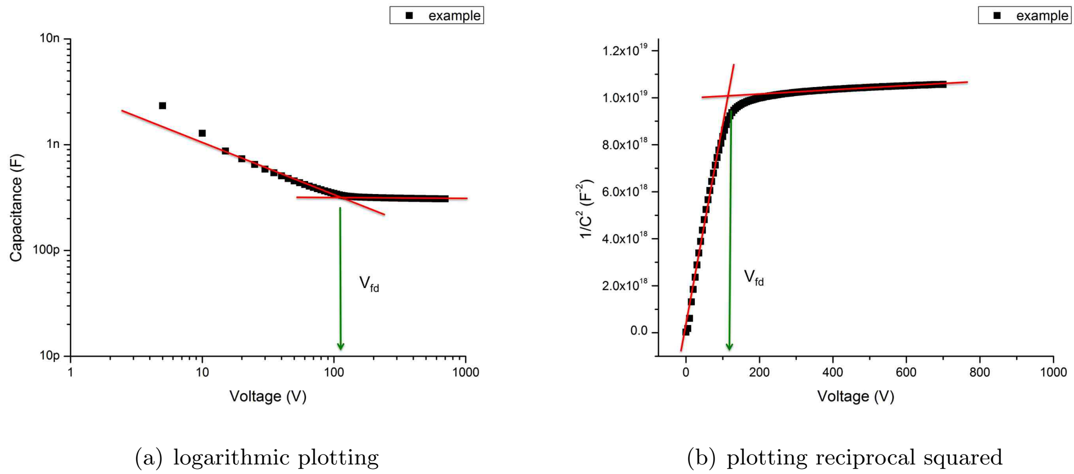

(a) logarithmic plotting (b) plotting reciprocal squared

Figure 7.2.: Illustration of two ways to extract the full depletion voltage from the capacitance-voltage measurement. Plotting both axes logarithmic 7.2(a) is one possibility to extract the full depletion voltage, while plotting $\frac{1}{C^2}$ over the bias voltage 7.2(b) gives another option. The full depletion voltage can be read as the intersection of two linear slopes fitted to the curve.

These methods work very well for non-irradiated sensors. For irradiated sensors and especially at higher fluences both procedures are hardly usable, as the linear slope at the beginning and the saturation plateau smear out. In the following the full depletion voltage extraction will be done by plotting $\frac{1}{C^2}$ over the voltage, taking the kink as V_{fd}. Figure 7.3 shows the development of the $\frac{1}{C^2}$ plot with increasing fluence.

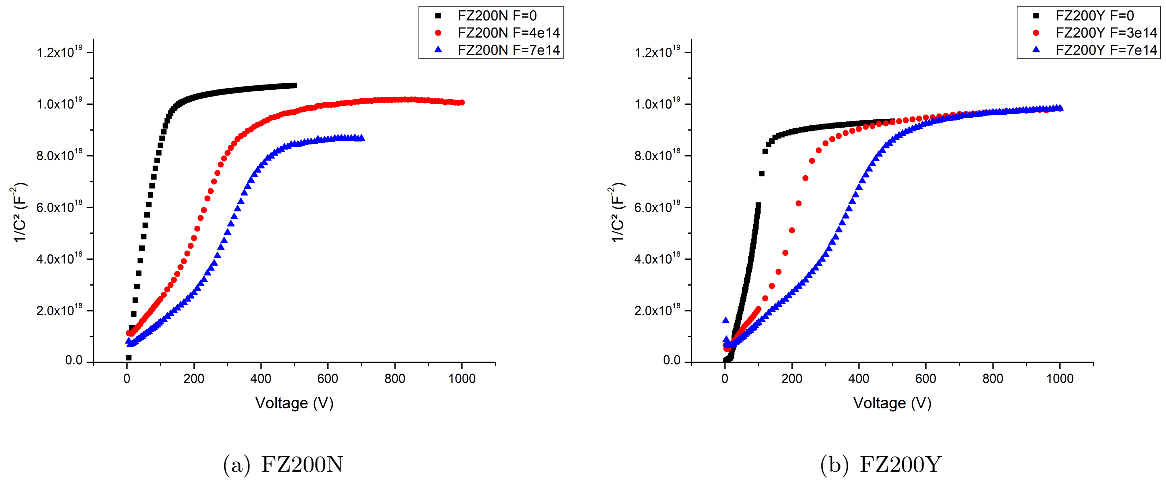

(a) FZ200N (b) FZ200Y

Figure 7.3.: Illustration of the change of the $\frac{1}{C^2}$ plot. With increasing fluence the kink of the curve smears out and gets harder to determine.

Figure 7.4 shows the measured CV curves for the non irradiated Baby_Std sensors in $\frac{1}{C^2}$ plots and table 7.1 summarizes the full depletion voltages for the different materials and thicknesses.

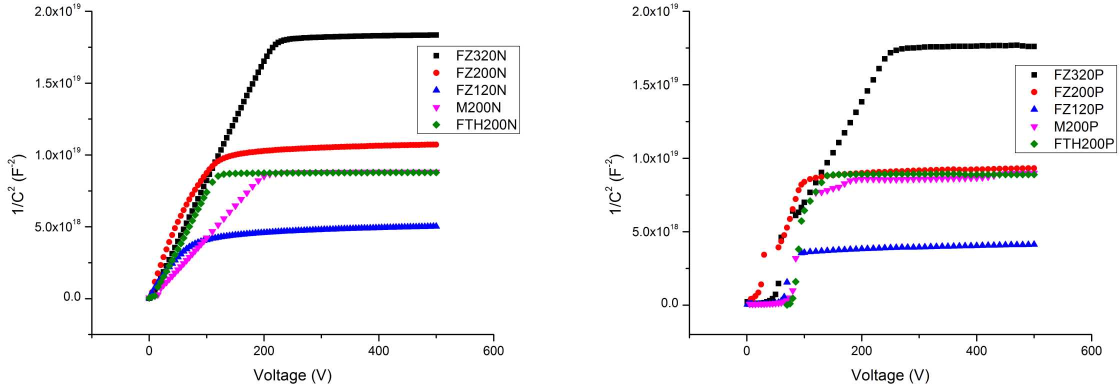

(a) CV curves for N type (b) CV curves for P type

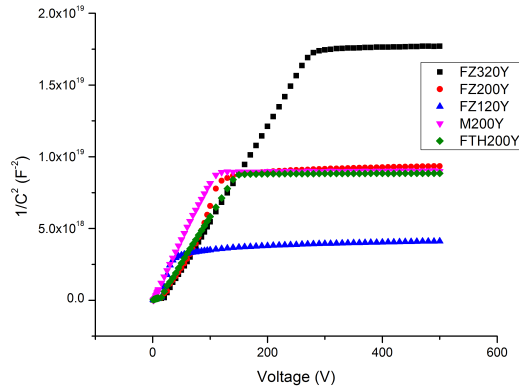

(c) CV curves for Y type

Figure 7.4.: CV curves for the different thicknesses separated by the material types: 7.4(a) N type, 7.4(b) P type and 7.4(c) Y type. The depletion voltage is read from the kink in the curve. For the P type Baby_Std some values below 100V are not plotted, due to a strange behavior caused by the improper isolation between bias and guard ring.

Table 7.1.: Overview of the full depletion voltages of the non irradiated Baby_Std sensors for the different materials and thicknesses, specified in V.

	FZ320	FZ200	FZ120	M200	FTH200
N	212.5±7.5	115±7.5	85±20	190±15	115±10
P	245±5	107.5±7.5	90±20	173.8±11.9	130±10
Y	265±5	118.8±6.9	85±20	107.5±8.8	146.3±8.8

All CV curves of the non-irradiated sensors show the expected characteristics. At the beginning, the $\frac{1}{C^2}$ curve has a constant slope, due to the growing depletion depth. The measured capacitance decreases, until the full depletion of a sensor is reached. The curve saturates at the capacitance value C_{end}. The 120 µm Baby_Std sensors are the ones that reach the saturation value of C_{end} first. At higher voltages the FZ200, M200 and FTH200 saturate, before lastly the FZ320 also reach the full depletion. Exceptions are the M200N and M200P sensors, which have higher depletion voltages as the comparable other 200 µm thick sensors, which points to a higher doping concentration.
C_{end} is the mean value of the capacitances above 1.2 times the V_{fd}. With the C_{end} values one can calculate the active wafer thickness d using the plate capacitor equation:

$$C_{end} = \epsilon_0 \epsilon_r \frac{A}{d} \tag{7.1}$$

with the active sensor area A limited by the guard ring. As this equation is valid for diodes, the calculation results summarized in table 7.2 have been done using the C_{end} values of the diode measurements.

Table 7.2.: Overview of the calculated sensor thicknesses, specified in µm, using C_{end} extracted from the CV curves of the diodes.

	FZ320	FZ200	FZ120	M200	FTH200
N type	302±1.2	231±1.7	150.1±3.5	202.3±3.1	204.8±4.7
P type	293±1.1	212.4±1.4	134.4±2.6	205±1.1	205.8± 5.1
Y type	291.9±1.2	211±1.5	133.8±2.7	205.8±5.7	204.5±5.4

It can clearly be seen, that there are differences between the expected thickness and the delivered thickness of the materials. While the magnetic Czochralski and the float zone thinned wafers are about the expected 200 µm thickness for all types, the float zone material deviates by several µm. The FZ320 has an active thickness of about 300 µm for all three types. The FZ200 N type is with about 231 µm little thicker than the P and Y types with about 211 µm and the FZ120 differs from the considered 120 µm by about 25%, with 150 µm for the N type and 134 µm for P and Y type. These deviations in the thickness do not harm the sensors functionality, but should be taken into account for further analysis, as for the volume current and the charge collection efficiency.
Another effect that can be seen in the $\frac{1}{C^2}$ curves is, that the capacitance after reaching the full depletion at the kink, further decreases. Especially for the FZ120 this is one reason for the large deviation from the measured to the ordered wafer thickness. This non saturation has been investigated in [Jun11] and related to a defect called E(61K), which changes the N_{eff} and thus the saturation properties of the CV curves.

As the full depletion voltage is an very important sensor parameter, affecting the active sensor volume that accounts for the collected charge of the sensor, the development under irradiation has to be reviewed. According to the fluences for the R=40 cm and R=20 cm irradiations, figure 7.5 shows the evolution of V_{fd} with a short annealing of 10min@60°C after each irradiation.

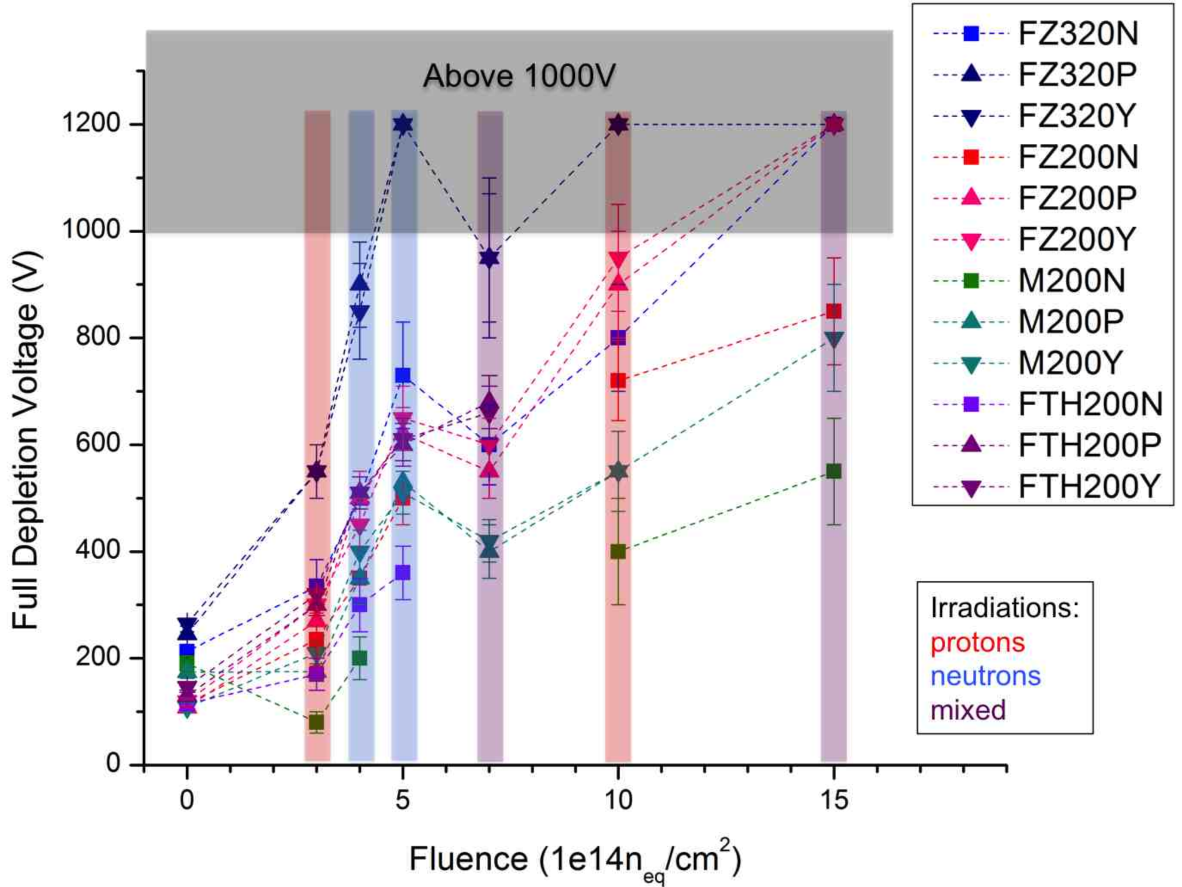

Figure 7.5.: Evolution of the V_{fd} with fluence. V_{fd} is shown for all sensors for only proton, only neutron and mixed irradiation. After the irradiation a short annealing of 10min@60°C has been done. Values within the grayish area are depletion voltages above 1000 V and plotted only for completeness. The measurements are done at −20°C, except the measurements on the non irradiated sensors that have been performed at 20°C.

After irradiation the full depletion voltage increases due to the changes of N_{eff}, as described in 3.15. Especially V_{fd} of the thick P and Y types increases very fast to full depletion voltages above 1000 V, which is the current voltage limit for the CV measurements. For the N type sensors the increase of V_{fd} is delayed due to the type inversion, see section 3.6. Therefore the full depletion voltages of the N type sensors are always below the full depletion voltages of the P type and Y type sensors. For the M200N, which had a higher initial doping concentration, and thus a higher initial depletion voltage, the irradiation to the lowest fluence of F=$3 \times 10^{14} n_{eq} cm^{-2}$ lead even to a decrease of V_{fd}. While the other N type sensors passed the type inversion below that first fluence point, the high concentration of donators in the M200N needed a higher fluence to be compensated by the acceptor like defects of the irradiation.
The decreased depletion voltages for the mixed irradiations with neutrons and protons at F=$7 \times 10^{14} n_{eq} cm^{-2}$ is due to an accidental annealing during the transportation of the sensors (90h at room

temperature). These sensors passed a beneficial annealing as described in section 3.15.
Taking into account that the current CMS tracker can at most be operated at 600 V, it can be seen that most sensors are no more fully depleted, except the M200N sensor with a depletion voltage of 550 V.

7.2.2. Total Lakage Current

As shown in section 2.2.4 the leakage current, which is strongly temperature dependent, contributes to the shot noise and should therefore be minimal. Especially with irradiation, the leakage current rises and only cooling the sensors keeps them operable. Studying the leakage current development with fluence is a reliable way to confirm the irradiation fluences.

Figure 7.6 shows the total current measurement for the different N type sensors. Clearly, the magnetic Czochralski material has a higher current as the float zone material. As the measurements are done under same conditions one would expect, that the current scales with the sensor volume and thus with the thickness. This is seen for the float zone sensors, but exactly in the opposite direction, the thinnest sensor has the largest current.

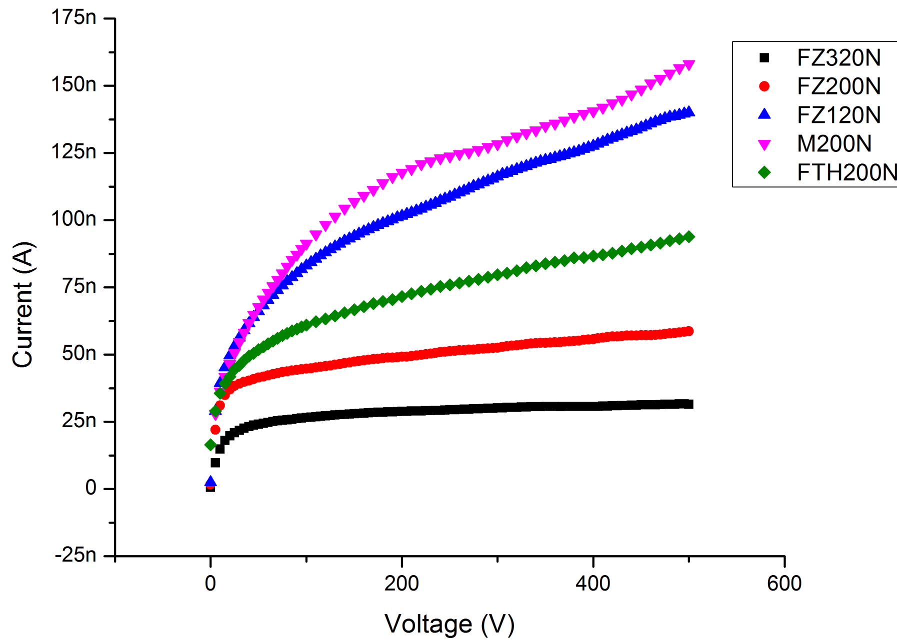

Figure 7.6.: Total leakage current for the non irradiated n-type Baby_Std sensors. One would expect a dependency of the leakage current to the sensor thickness, but this expectation is just reversed. The reason is due to the deep diffusion process, that leads to higher currents for the thinner sensors that are process using deep diffusion.

Measurements on the P type and Y type show the same effect, the thinner sensors have the higher currents. In figure 7.7 are the curves for the P and Y type sensors pictured. Again the magnetic

Czochralski material has a comparatively high current and the float zone shows the reverse volume scaling.

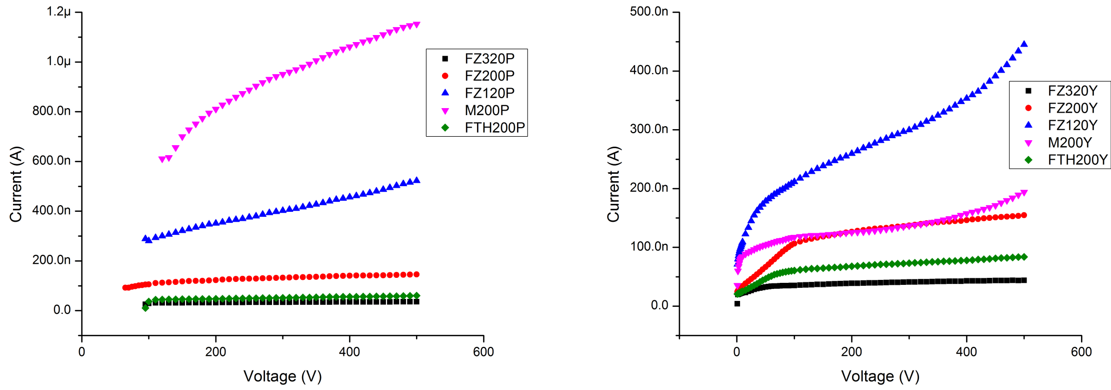

(a) Total Leakage Current - P sensors

(b) Total Leakage Current - Y sensors

Figure 7.7.: Measurements of the total leakage current for the different (a) P and (b) Y type sensors.

Investigations on this strange current behavior have been done in [Jun11]. Measuring the defect concentration of non irradiated float zone diodes using the DLTS[1], one candidate for causing the high current has been discovered. A deep acceptor called H(220K) defect, that is found in the thinner diodes processed with the deep diffusion technology is responsible for the higher current. The higher the concentration of this defect the higher is the leakage current. Figure 7.8 shows DLTS spectra illustrating the defect concentration for Y type float zone diodes.

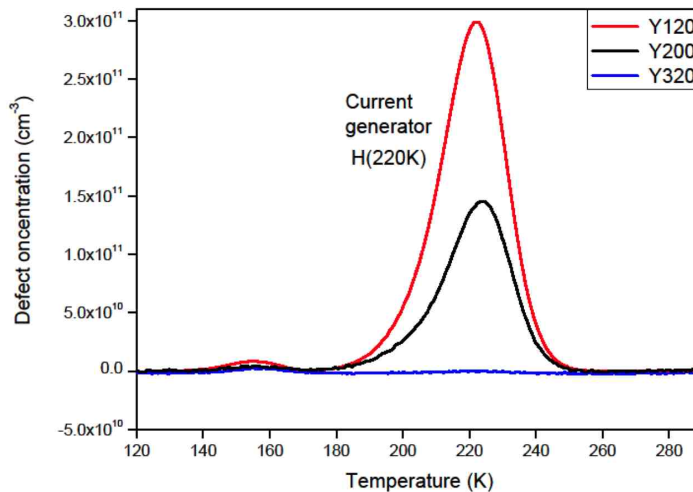

Figure 7.8.: DLTS spectra showing the defect concentration of defect H(220K) for Y float zone material [Jun11]. The thinner the sensor the higher the defect concentration, the higher the current.

[1]Deep Level Transient Spectroscopy

As the thinner diodes have a higher H(220K) defect concentration, they also have a higher current.

The magnetic Czochralski material shows very high currents and the FZ320 sensors have the lowest current. The effect of defect H(220K) leads for the FZ materials to higher currents for thinner sensors.

Nevertheless, all sensors can be biased up to 500 V with the guard ring connected and up to 700 V without guard ring connection. Some samples have also been tested up to 1000 V and did not show a breakdown.

After irradiation the leakage current increases strongly and the effect of defect H(220K) can't be seen in the curves any more. The concentration of defects due to the deep diffusion are small compared to the concentrations of irradiation induced defects [Jun11]. Figure 7.9 shows the leakage current of three float zone diodes irradiated with neutrons to $\Phi_{eq} = 1.1 \times 10^{14} cm^{-2}$.

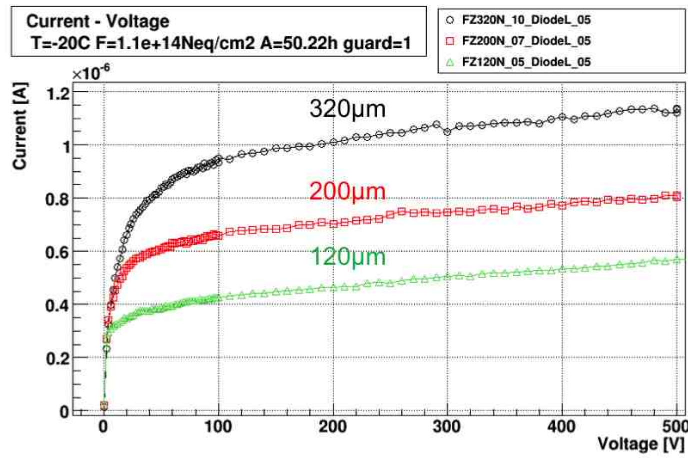

Figure 7.9.: Comparison of the leakage currents of diodes of different thicknesses after irradiation to $\Phi_{eq} = 1.1 \times 10^{14} cm^{-2}$. The measurements are done at -20°C.

For the Baby_Std sensors a comparison of the leakage current after irradiation is shown for the N type sensors in figure 7.10.

Before irradiation, the leakage current for FZ200 was higher than the leakage current for FZ320 sensors, see figure 7.6. After irradiation this situation has not been changed. Although the measured leakage current for the FZ320N is higher than the leakage current for the FZ200N, visualized by the squared and the round symbols in the lower part of figure 7.10, the volume scaled leakage current in the upper part shows that the leakage current of the FZ200N is still higher. It can only be assumed, that this is related to the H(220K) defect, or any other effect of the deep diffusion process.

The typical IV curves show a root-form increasing current until the sensor is fully depleted. Then, the leakage current should almost be constant. In figure 7.11, which shows the leakage currents for proton irradiated Baby_Std sensors, this current saturation can not be seen, although most sensors deplete below 1000 V (see figure 7.5).

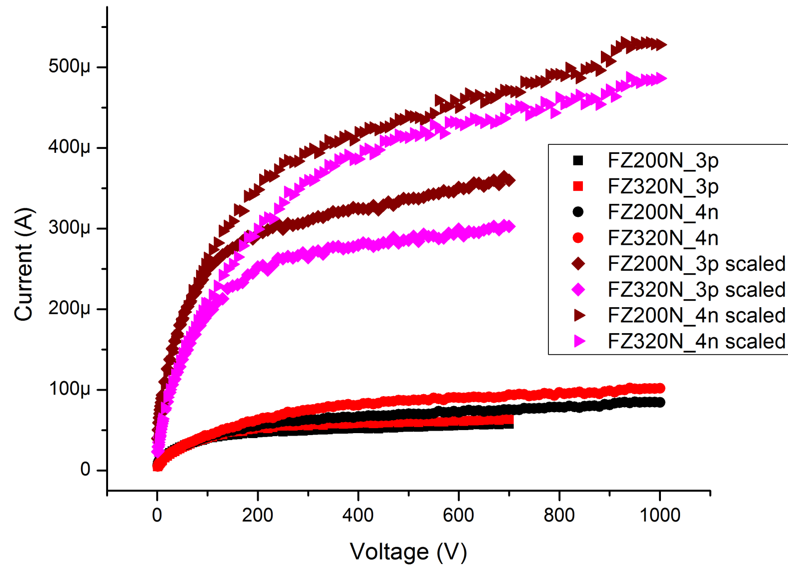

Figure 7.10.: Comparison of the leakage currents at -20°C of FZ320N and FZ200N Baby_Std sensors after irradiation to $\Phi_{eq} = 3 \times 10^{14} cm^{-2}$ and $\Phi_{eq} = 4 \times 10^{14} cm^{-2}$.

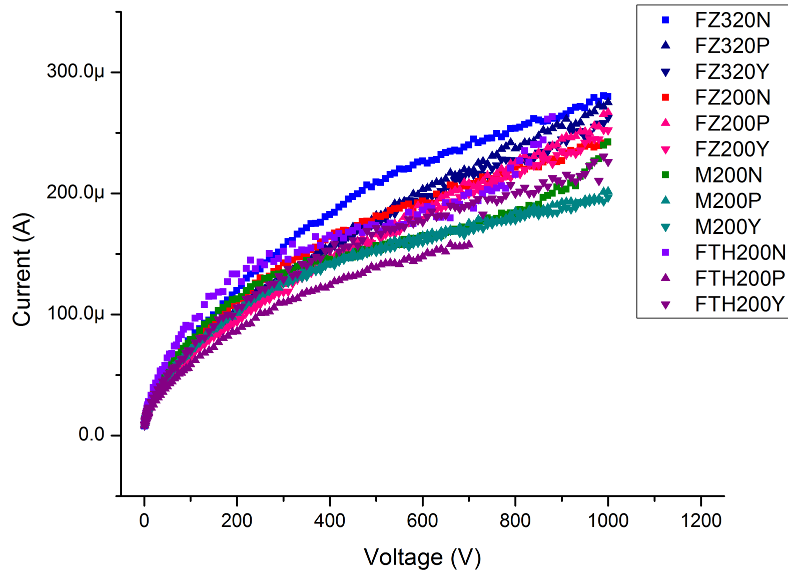

Figure 7.11.: Leakage currents of Baby_Std sensors irradiated with protons to $1 \times 10^{15} n_{eq} cm^{-2}$, measured at -20°C.

alpha Parameter

The current related damage rate, described in section 3.2.1 can be used to compare the leakage currents of the different sensors, as α is independent of the sensor material, the irradiation particles and energies.

Therefore in figure 7.12 the volume scaled current of the Baby_Std sensors measured at 600 V, which is the maximum voltage of the current CMS Tracker power supplies, are plotted versus the fluence. As the measurements after irradiation are all done at about $-19°C$ and the α extracted from the parameterization is calculated for 20°C, the measured currents have been scaled to 20°C using:

$$I(T) \propto T^2 \exp -\frac{1.21eV}{2k_B T} \tag{7.2}$$

taken from [Chi11]. The irradiated sensors have undergone a short annealing of 10min@60°C, except the mixed irradiated sensors at $\Phi_{eq} = 7 \times 10^{14} cm^{-2}$, which had an inadvertent annealing of 90h at room temperature during transportation. The expected α of $5.32 \times 10^{-17} A/cm$ is represented by the orange line, it depends on the annealing time and it taken from [Mol99].

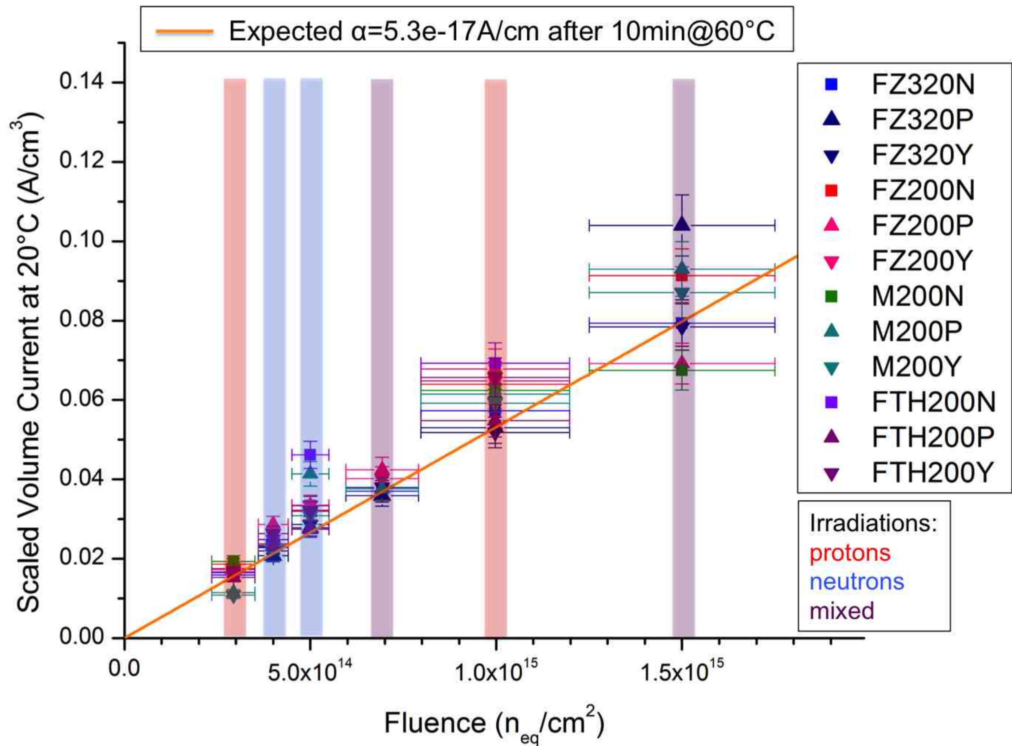

Figure 7.12.: Comparison of the volume scaled leakage currents measured at -20°C and scaled to 20°C for the Baby_Std sensors. The orange line represents the expected α for diodes after an annealing of 10min at 60°C.

The current densities, which are mainly influenced by the fluence, the annealing time and the temperature they are measured at, show the expected linear behavior. Nevertheless are most of the

measured *alpha* values above the expected α taken from diode measurements. There are several sources for the deviance. Additional surface currents on the sensors, due to the strip segmentation, leading to higher currents are one reason. Differences in the annealing times of the sensors caused during transportation or a wrong temperature measurement during the sensor probing are others. Hence, the α parameter can be seen as a lower limit for the current densities of the sensors, which means for use in the detector, that the leakage currents will be higher, than expected from the model by [Mol99].

7.2.3. Strip Leakage Current

The single strip leakage currents of the non irradiated Baby_Std sensors are measured at 600 V for each single strip. Figure 7.13 gives an overview of the homogeneous currents.

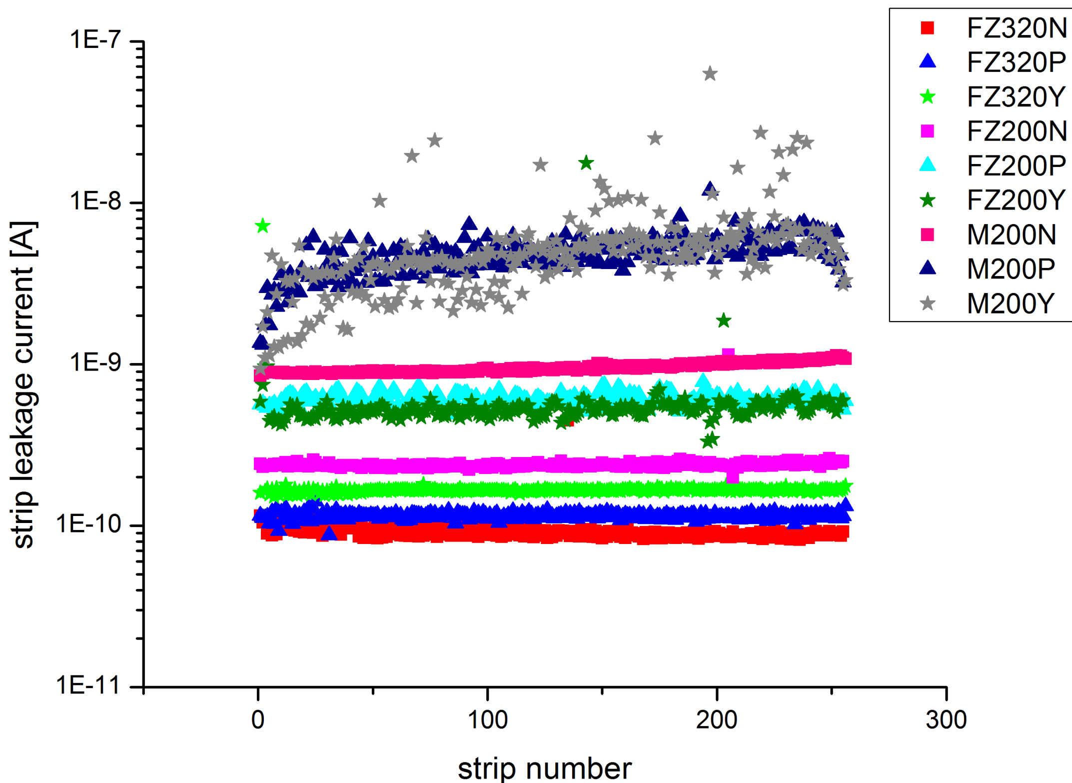

Figure 7.13.: Illustration of the strip leakage current for non irradiated Baby_Std sensors. The behavior is similar to the leakage current already shown. The magnetic Czochralski sensors and the FZ200 sensor have higher currents than the FZ320.

The sum of the strip leakage currents of a sensor approximately results in the sensor leakage

current shown in 7.2.2. As an example, for the FZ200N sensor is:

$$\sum_{i=1}^{N_{strips}} I_{leak_i} = 6.17 \times 10^{-8} A \tag{7.3}$$

which is close to the total leakage current at 600 V taken from the IV curve shown in figure 7.6, which is 6.58×10^{-8}A. As the strips do not cover the whole sensor, there is a small difference of 6.7% between the total current of the sensor and the sum of the strip leakage currents.
After irradiation the strip leakage current is only measured for few strips, performing voltage scans from 1 V to 1000 V. It behaves like the total leakage current. Figure 7.14 shows voltage ramps on different strips of a FZ320Y sensor irradiated to $\Phi_{eq} = 3 \times 10^{14} cm^{-2}$ with protons.

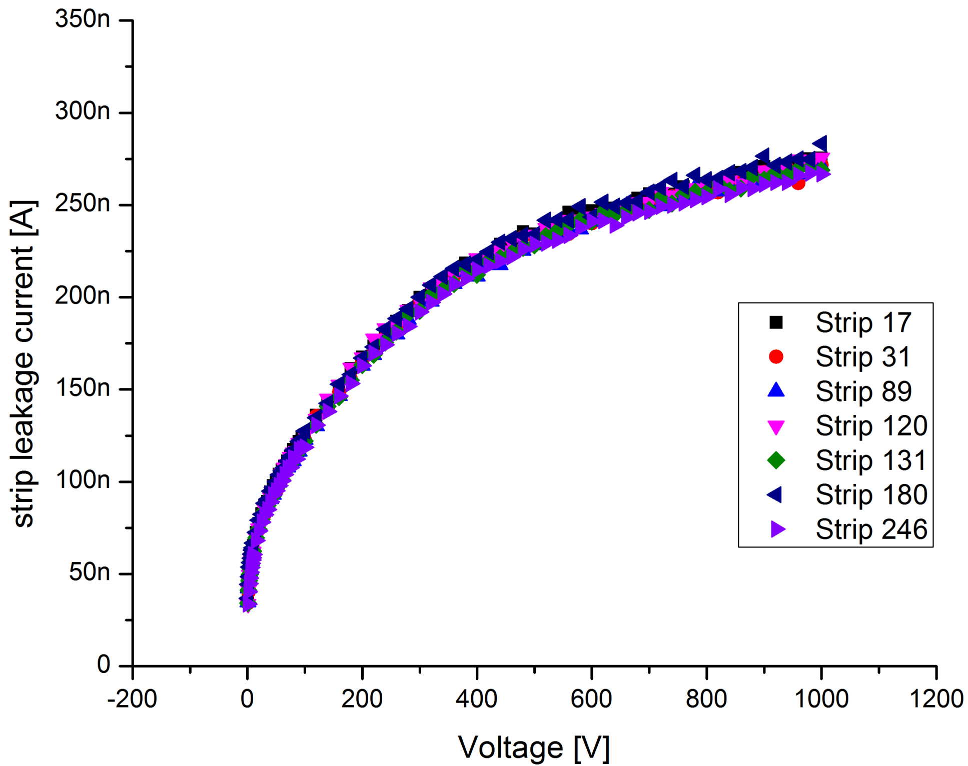

Figure 7.14.: Strip leakage currents after irradiation to $\Phi_{eq} = 3 \times 10^{14} cm^{-2}$ with protons. All strips show an identical current.

The increased strip leakage current at 600 V is in average $2.42 \times 10^{-7} A$ per strip, resulting in a sum of $6.21 \times 10^{-5} A$ for all strips. This is in very good agreement with the total leakage current of $6.34 \times 10^{-5} A$ of this sensor at 600 V.

7.2.4. Coupling Capacitances and Pinholes

The only requirements to the coupling capacitance is to be homogeneous over the whole sensor and to be significantly higher than the inter-strip capacitance as the signal is coupled out from the implant to the readout strip from where it is conducted to the readout chip.
The coupling capacitance can be used to roughly calculate the thickness of the readout oxide, which separates the implant strip and the aluminium readout strip, by using equation 7.1. In figure 7.15 are the coupling capacitance measurements on different sensors before irradiation at 600 V shown. The values for all sensors vary between 83 pF and 92 pF per strip (3.216 cm long) while the coupling capacitance on one sensor is very homogeneous over the complete sensor, with a spread of about 1%. There is a small difference between odd and even strips which can be seen in the two value bands that each sensor has.

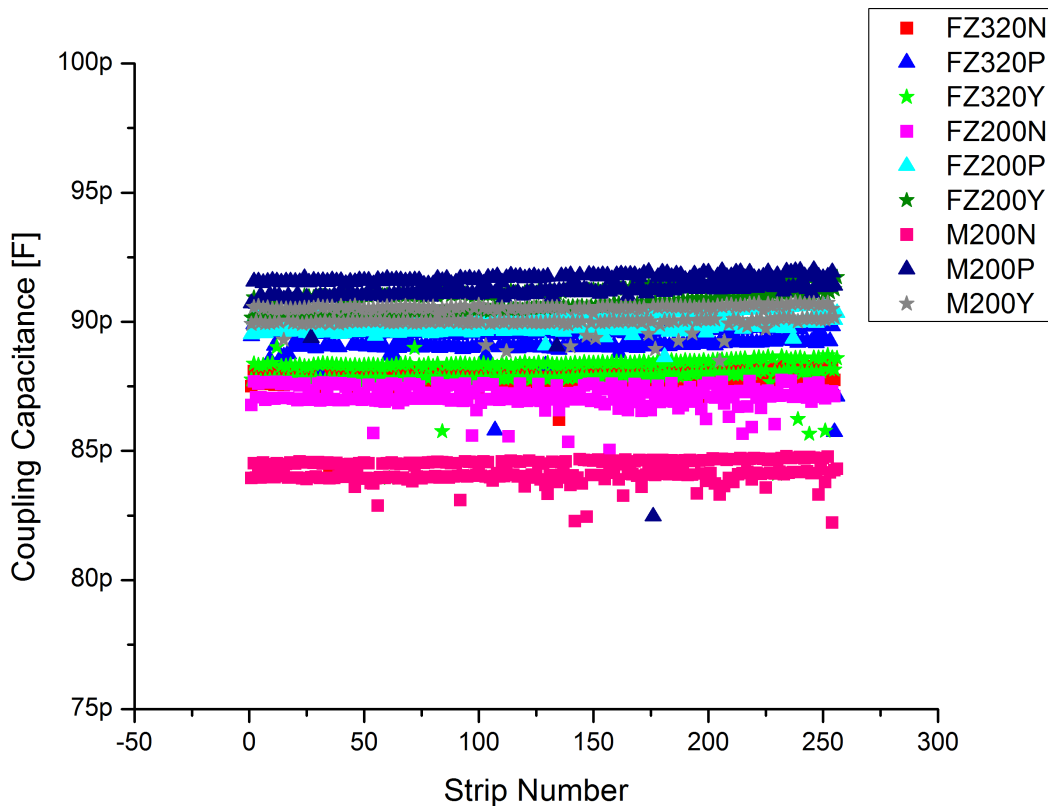

Figure 7.15.: Coupling capacitances for the non irradiated Baby_Std sensors measured at 600 V bias voltage and at 20°C. The values are very homogeneous over the sensors.

Using the measured coupling capacitances to calculate the thickness of the readout oxide d_{SiO_2} gives an approximate thickness of the oxide (most readout oxides are built up of two layers of different materials, a thick layer of SiO_2 and a thin layer of Si_3N_4). Assuming only a layer of $Si0_2$ with $\epsilon_r = 3.9$ and with the strip area of 32160 µm × 24.5 µm table 7.3 shows the calculated readout oxide thicknesses.

Table 7.3.: Overview of the calculated readout oxide thicknesses d_{SiO_2} using the coupling capacitances from figure 7.15.

Baby_Std	FZ320N	FZ320P	FZ320Y	FZ200N	FZ200P	FZ200Y	M200N	M200P	M200Y
CC per strip [pF]	87.717	89.171	88.846	86.824	89.629	89.8	83.9	90.9	90.0
d_{SiO_2} [nm]	310	305	306	313	304	303	324	299	302

Compared with the measured oxide thicknesses in [Tre11] with SiO_2 thickness between 250 nm and 300 nm and Si_3N_4 thicknesses between 50 nm and 100 nm, these approximatively calculated thicknesses fit quite well.
After irradiation the coupling capacitance is not measured for all strips, but for some random chosen strips. The measurement consists of a voltage scan from 1 V to 1000 V. Figure 7.16 shows the evolution of the coupling capacitance with increased fluence for the various sensors, scaled to a strip length of 1 cm.

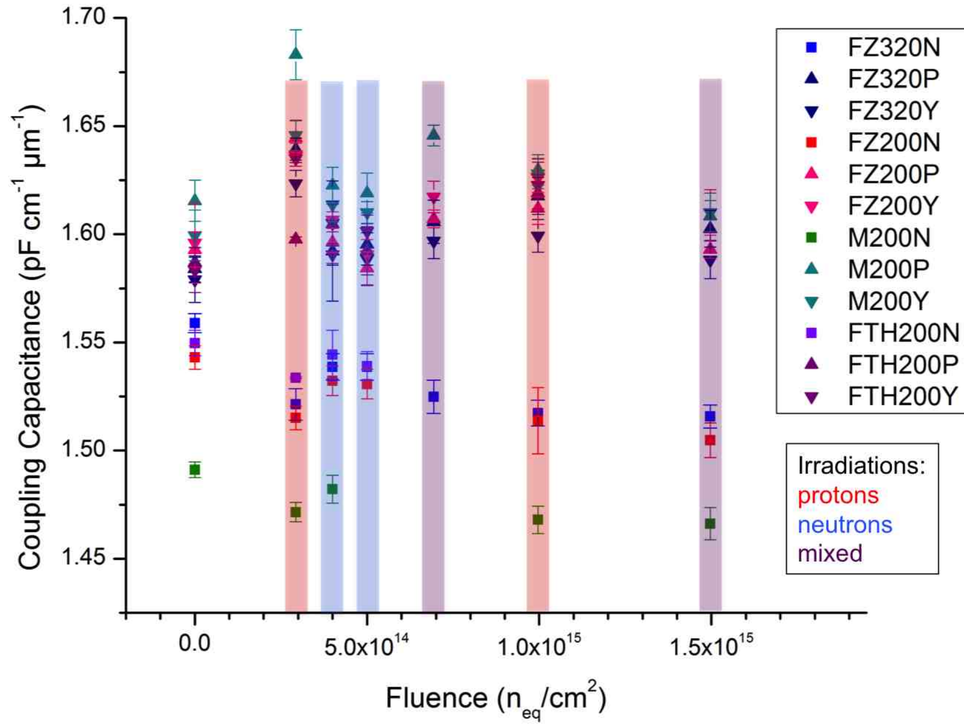

Figure 7.16.: Measured coupling capacitances before (20°C) and after (−20°C) irradiation at 600 V. The values are scaled to the width and the length of the strips.

The coupling capacitance does hardly change after irradiation, there are variations in the order of 4% showing no tendency.

7.2.5. Bias Resistors

The bias resistors are made of heavily doped polysilicon and are used to separate the implanted strips. The bias resistors contribute to the parallel thermal noise of a detector module, as shown in section 2.2.4, therefore their evolution with increasing fluence is important to investigate.
For the non irradiated Baby_Std sensors the values for the bias resistors are meant to be in the range of 1MΩ to 4MΩ. Figure 7.17 shows the results for the bias resistors for all strips on different sensors at 20°C.

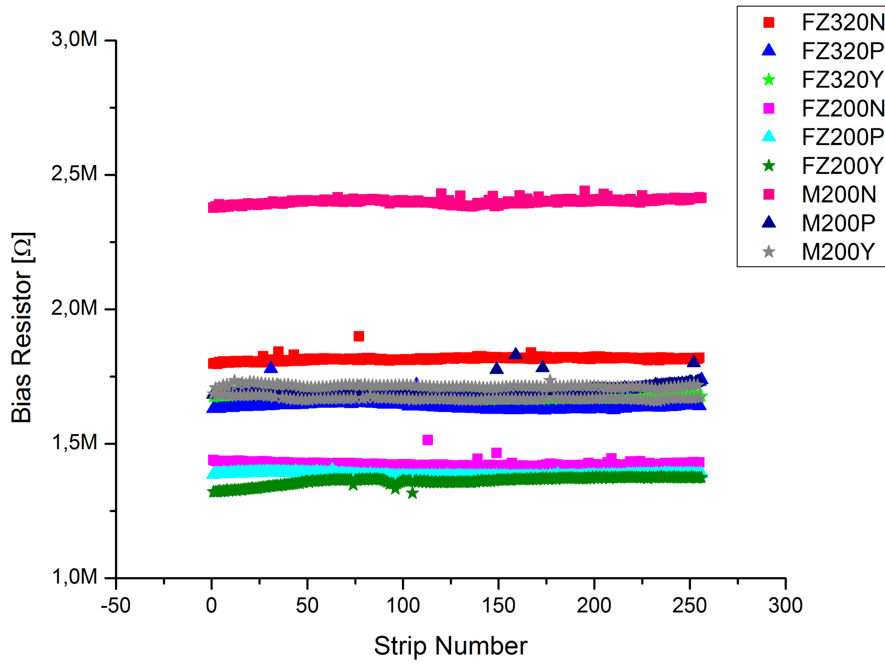

Figure 7.17.: Overview of the homogenous distributed bias resistors on the Baby_Std sensors, measured at 600 V and 20°C.

The measured values for the bias resistors are in between 1.25 MΩ and 2.5 MΩ and very homogeneous with only small variations of less than 1.5% on the sensors.
As the bias resistors are temperature dependent, decreasing temperature leads to an increasing bias resistor. In order to compare the bias resistors before and after irradiation, temperature scans from −20°C to 20°C have been done exemplarily on three non irradiated Baby_Std sensors to parametrize it's temperature dependence, shown in figure 7.18 for N, P and Y type.

The parametrization $y = (a \pm \Delta a) + (b \pm \Delta b) \cdot x$ results in the following formulas:

for n-type: y = (1712940±1661) + (-6110±128) · x

for p-type: y = (1604220±2148) + (-5695±152) · x

for y-type: y = (1818800±3160) + (-7124±223) · x

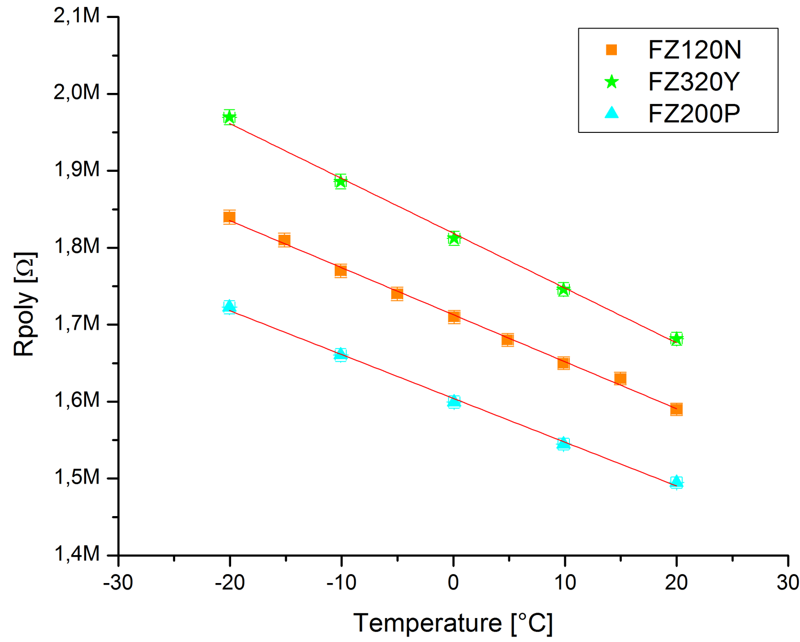

Figure 7.18.: Temperature dependence of the bias resistors. Decreasing the temperature from 20°C to −20°C increases the bias resistors by about 16%.

Using this parametrizations the bias resistors measured at 20°C before irradiation are scaled to −20°C and compared with the bias resistors after irradiation, shown in figure 7.19.

After irradiation a slight increase of the bias resistors is observed. The raise is in a range from a few percentage to a maximum of 15% for the higher fluences. For some lower fluences in between $\Phi_{eq} = 3 \times 10^{14} cm^{-2}$ and $\Phi_{eq} = 5 \times 10^{14} cm^{-2}$ the bias resistors even decrease by 1% to 4%. There is no trend evident.
It is expected, that due to the high doping concentration of the bias resistors, the irradiation only changes them little, without any negative influence on the sensor properties as increasing the R_{bias} even decreases the detector noise, as shown in 2.47.

7.2.6. Inter-strip Resistance

The inter-strip resistance R_{int} is a measure of the sensors strip isolation. For non irradiated sensors R_{int} is typically in the order of several GΩ, guaranteeing a good strip isolation. Figure 7.20 shows the inter-strip resistances for the Baby_Std sensors before irradiation at 600 V and at 20°C.

The values of R_{int} are larger than 1 GΩcm. R_{int} is extracted from a linear fit of a current measurement, for the non irradiated sensors R_{int} is only a lower limit, as the measured currents are almost below the sensitivity of the measurement device.
After irradiation a strong decrease of R_{int} is expected, as the strip isolation gets worse. Figure 7.21 shows the decrease of R_{int} with increasing fluence.

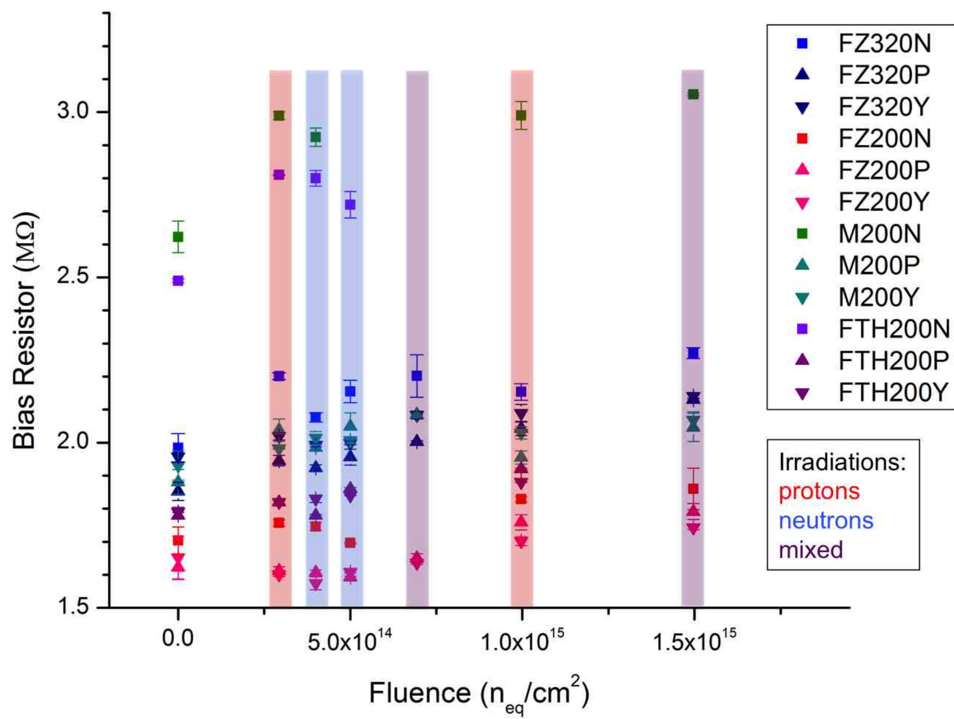

Figure 7.19.: Development of the bias resistors under irradiation. Basically the bias resistors increase by a few percentage.

However, with inter-strip resistances above 100 MΩcm, the values are still high enough to isolate the strips from each other.

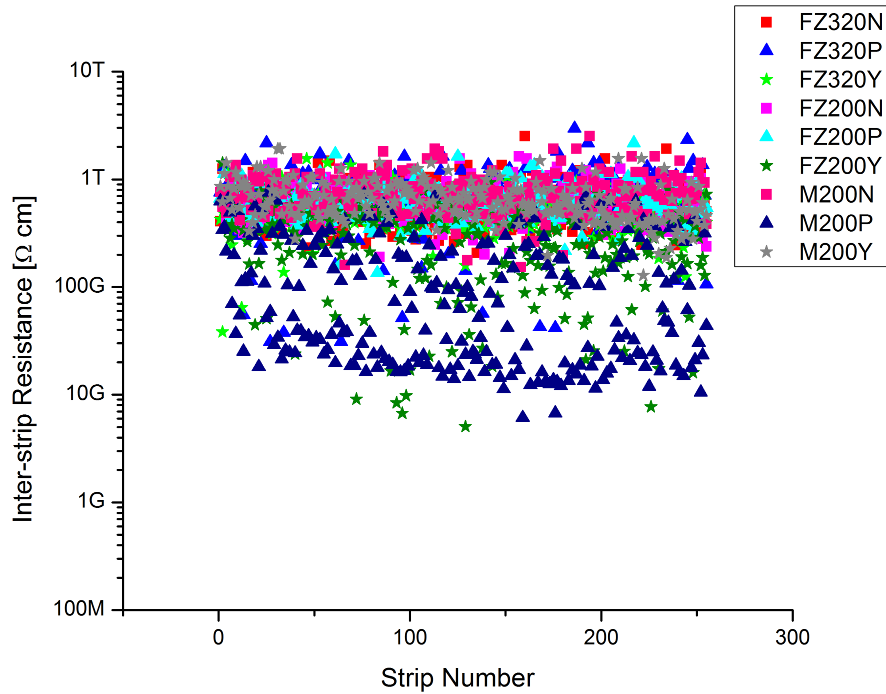

Figure 7.20.: Overview of the inter-strip resistance of the different Baby_Std sensors before irradiation at unit20°C.

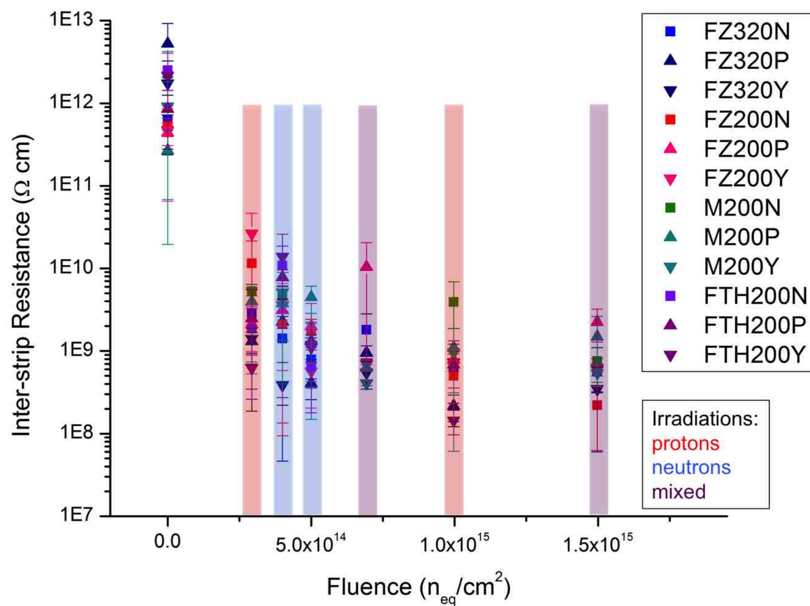

Figure 7.21.: Changes of the inter-strip resistance after irradiation. A strong decrease in the inter-strip resistance can be seen. After irradiation to the lowest fluence of $\Phi_{eq} = 3 \times 10^{14} cm^{-2}$, R_{int} is reduced by three orders of magnitude. Going to higher fluences decreases R_{int} only fractionally. At $\Phi_{eq} = 15 \times 10^{14} cm^{-2}$ the inter-strip resistance is still adequate, with values over 100 MΩcm, to keep the proper strip isolation.

7.2.7. Inter-strip Capacitances

The inter-strip capacitance contributes to the noise as shown in section 2.2.4 and in equation 2.51. C_{int} is measured between one strip and it's neighbor. The measurement is very delicate, as even the position of the needles amongst each other influences the values by about 5%.
Before irradiation the C_{int} values on the Baby_Std sensors range from 1.2 pF to 1.5 pF per strip and are very homogeneous with a maximum mean variation of 4.6% (M200Y). In figure 7.22 are the C_{int} values per strip for the FZ320 (≈ 1.5 pF), FZ200 (≈ 1.35 pF) and the M200 (≈ 1.35 pF) sensors shown. There are no differences between the N, P and Y type sensors, only the sensor thickness influences C_{int}.

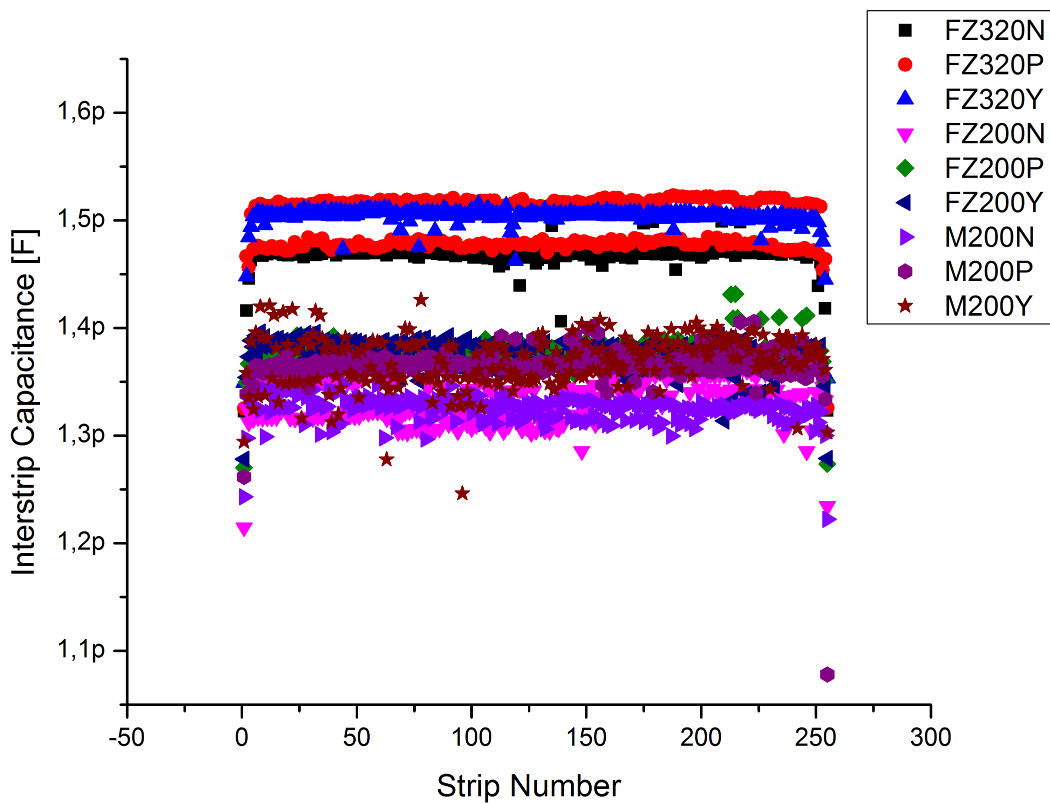

Figure 7.22.: Overview of the C_{int} values per strip length for the different Baby_Std sensors. C_{int} depends on the sensor thickness and is very homogeneous on the sensors.

The change of C_{int}, scaled to a strip length of 1cm, is shown in figure 7.23. After the first irradiation step the values rise by about 5% but stays constant for higher fluences.

7.2.8. Charge Collection

The most important numbers for identifying a good sensor operability are the collected charge, the affiliated charge collection efficiency and the signal-to-noise ratio. In the following the results of

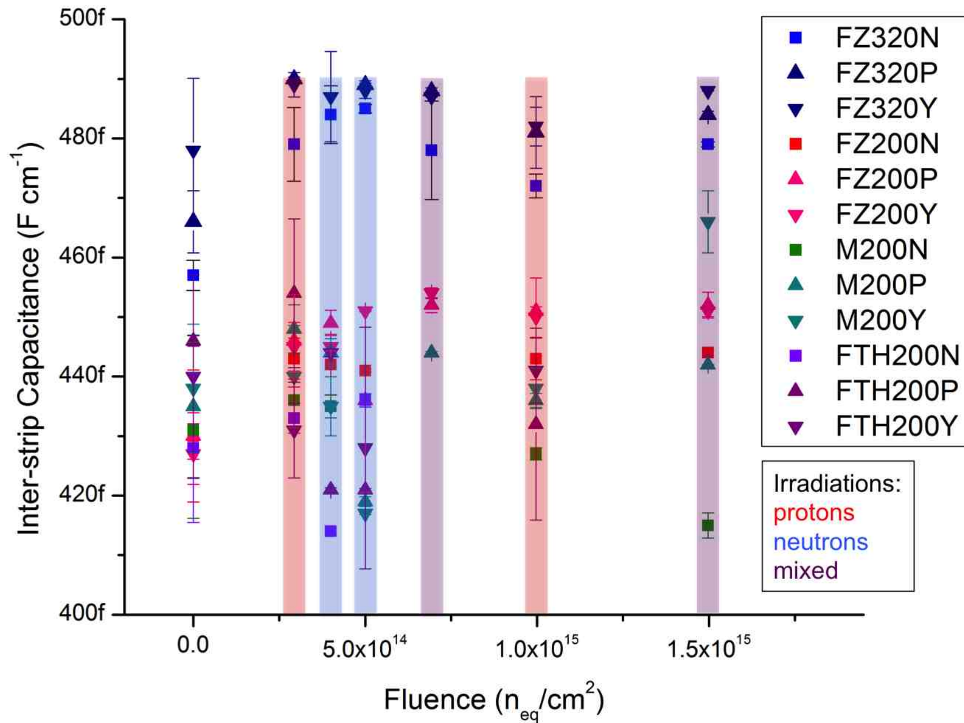

Figure 7.23.: Changes of C_{int} with increasing irradiation. There is hardy any change for C_{int} visible.

the ALiBaVa measurements will be shown, comparing the results at 600 V[2] and 900 V. But first, a short introduction to signal calibration of the different daughterboards is presented.
As the several daughterboards that have been used showed different electron signals, the readout chips had to be calibrated. Therefore, one sensor has been bonded to each daughterboard after another and the collected charge has been measured at different temperatures. Thereby, the collected charge showed a linear dependence on the temperature of the daughterboard T_{DB}, which has also been measured. To calculate the charge from the signal of the chip, the sensor thickness and the theoretical expected number of generated electrons $N_{e^-}^{theo}$ have been used. From the units of the analog digital converter (ADC) the electron signal S has been calculated using:

$$S = \frac{ADC}{a \cdot T_{DB} + b} \cdot N_{e^-}^{theo}$$

whereas a and b are coefficients from the linear fit to the calibration measurements, which in each case are used for the corresponding chip. The calibration measurements and the calibration coefficients can be found in appendix B.1. The error of the electron signal is estimated to 5%.
The measurement of the charge collection has been done with the Sr90 source and the ALiBaVa system as described in section 4.2.2. For each sensor and after each irradiation step a voltage ramp

[2]600 V is the current voltage limit for the CMS tracker

up to 1000 V (700 V for non-irradiated sensors) has been performed. With rising voltage, the charge collection increases until the full depletion voltage is reached and the charge collection saturates. In figure 7.24 the charge collection is plotted for different n-type Baby_Std sensors.

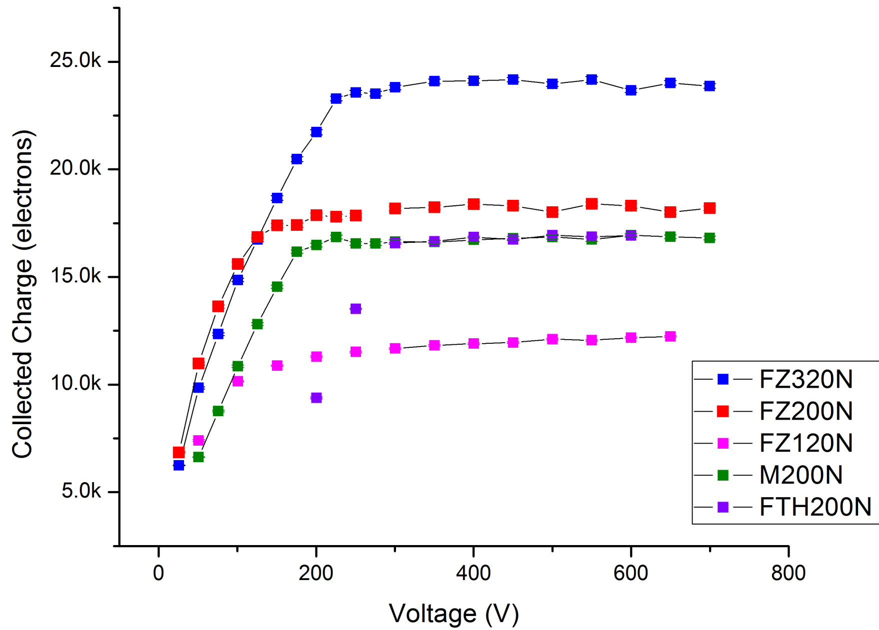

Figure 7.24.: Collected charge for n-type Baby_Std sensors at different bias voltages. The collected charge increases, until the sensors are fully depleted. Thicker sensors collect more charge, but need also higher bias voltages.

The curves show the expected behavior with a saturation of the collected charge after full depletion. The thicker the sensor, the more charge is created by a transversing particle. The 300 µm sensors collect about 22800 electrons, the 200 µm sensors about 15400 electrons, except the FZ200 which are slightly thicker and thus collect about 17300 electrons.

Figure 7.25 shows the changes in the electron signal with increasing fluence at a bias voltage of 7.25(a) 600 V and 7.25(b) 900 V. For better readability, the error bars are left.

The electron signal decreases with rising fluence. Responsible for the signal reduction are on the one hand the created trapping centers in the silicon (3.2.4) and on the other hand the increased depletion voltage (3.2.2). The reduction can be approximated by:

$$d \approx \sqrt{2\mu\rho\epsilon_{Si} \cdot U_{bias}}$$

If $U_{bias} = U_{depl}$, d is the complete sensor thickness D. For a not fully depleted sensor the active

thickness can be calculated using:

$$d_{activ} = D \cdot \sqrt{\frac{U_{bias}}{U_{depl}}}$$

Comparing the electron signals of the non-irradiated sensors, it is obvious that the FZ320 sensors show a higher signal than the 200 µm thick sensors. This primary advantage of the thicker sensors relativizes with increasing fluence. At $\Phi_{eq} = 1 \times 10^{15} cm^{-2}$ the 300 µm sensors show similar signals as the 200 µm sensors. At 600 V the signal reduction occurs much faster than at 900V. This suggests that the signal reduction is partially caused by non-depletion. As it is clear from figure 7.5, the depletion voltage for the FZ320P and FZ320Y sensors at fluences of $1 \times 10^{15} n_{eq} cm^{-2}$ and higher, are beyond 1000 V. Only the FZ320N with a depletion voltage of about 800 V can still be fully depleted.
For the FZ200Y and FZ320N sensors, with the highest measurable depletion voltage of about 950 V, the signal at 600 V is reduced by approximately 20.5% due to the non-depletion. As can be seen in figure 7.27, the signal reduction at $1 \times 10^{15} n_{eq} cm^{-2}$ is much higher than 20%.
But also the influence of the trapping centers lead to a signal reduction. Figure 7.26 shows the electron signal at $\Phi_{eq} = 1 \times 10^{15} cm^{-2}$ in dependence on the bias voltage. For the 200 µm sensors the junction to the saturation is easy to see, especially for the M200 sensors, while the 300 µm sensors do not seem to saturate.

Taking the electron signals at the current CMS tracker voltage limit of 600 V, the real 200 µm sensors (FTH200 and M200) show higher values than the FZ320 and FZ200 sensors. Going to higher voltages above 700 V this changes again.
The charge collection efficiency shown in figure 7.27, illustrates the relative charge reduction with increasing fluence. The reduction is faster for the 300 µm sensors due to the missing full depletion. There is no difference between the P and Y type sensors.

Besides the signal, also the signal-to-noise ratio has an important role. It indicates if the signal created by a transversing particle is still discriminable from the sensor noise and thus detectable. Figure 7.28 visualizes the ratios in dependence on the fluence.

For low fluences the 300 µm sensors show higher signal-to-noise ratios than the 200 µm sensors. From a fluence of $1 \times 10^{15} cm^{-2}$ and higher, there is almost no difference between the thick and the thin sensors, as the thicker sensors have a greater signal decrease. However, the noise changes only minimal and has a mean value of about 1000 electrons. This value confirms to the expected noise of the coming binary readout of the CMS tracker, using CBC chips [FBF+12]. Therefore, this study is representative for the expectations of the experiment. The noise difference between non-irradiated and irradiated sensors to a fluence of $1.5 \times 10^{15} n_{eq} cm^{-2}$ is about 10%. All sensors have, even after an irradiation to $1.5 \times 10^{15} n_{eq} cm^{-2}$ still a signal-to-noise ratio of at least 10.

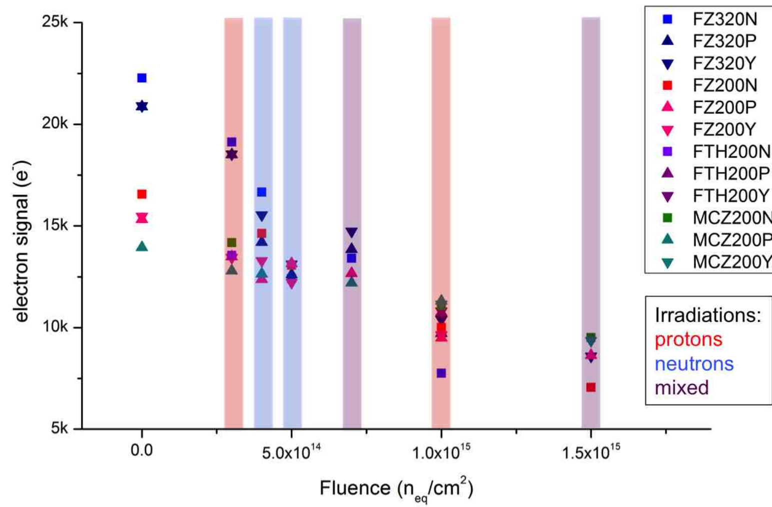

(a) Electron signal at 600 V

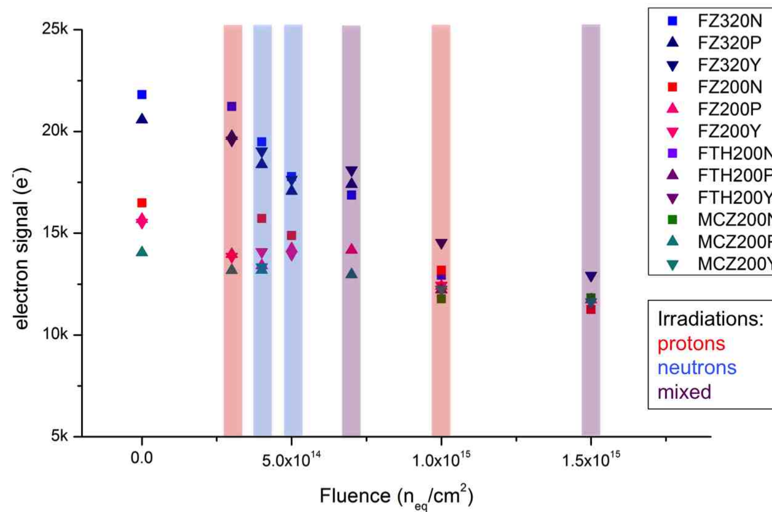

(b) Electron signal at 900 V

Figure 7.25.: Dependence of the electron signal on the fluence at (a) 600 V bias voltage and (b) 900 V bias voltage. For the values of the non irradiated sensors the signal at 700 V has been taken. At 900 V the advantage of the higher signal of the 300 µm sensors can be seen up to $1.5 \times 10^{15} n_{eq} cm^{-2}$, while at 600 V this almost relativizes at $\Phi_{eq} = 7 \times 10^{14} cm^{-2}$

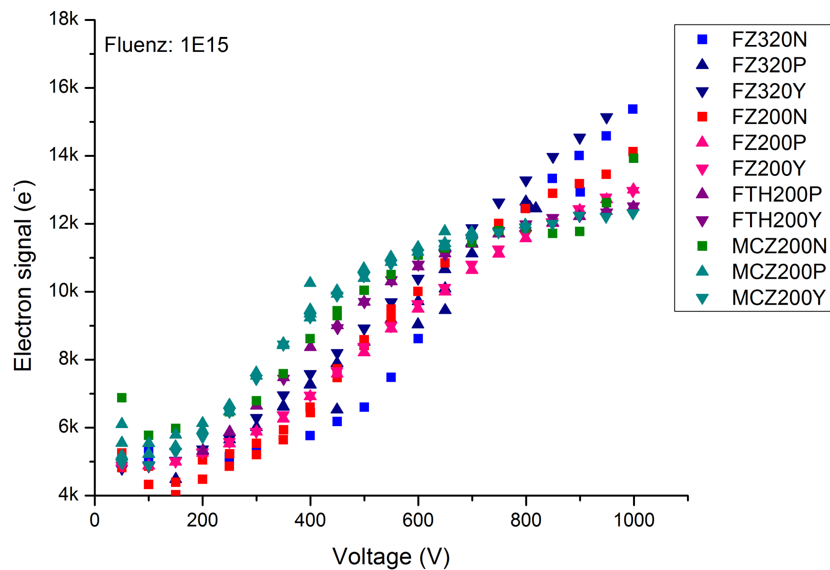

Figure 7.26.: Electron signal for different sensors at $\Phi_{eq} = 1 \times 10^{15} cm^{-2}$ in dependence on the bias voltage. The electron signal for thinner sensors saturates earlier as the electron signal for the thicker sensors which seem not to saturate at all. The 300 µm sensors do not deplete at such a fluence.

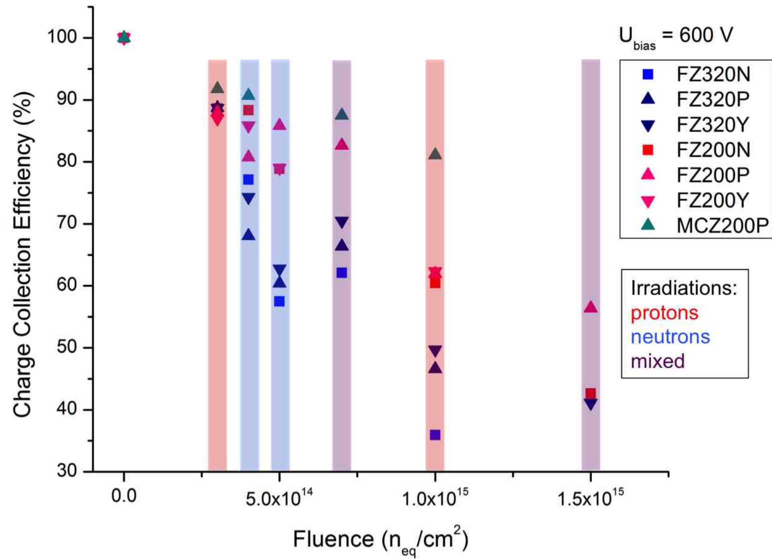

(a) CCE at 600 V

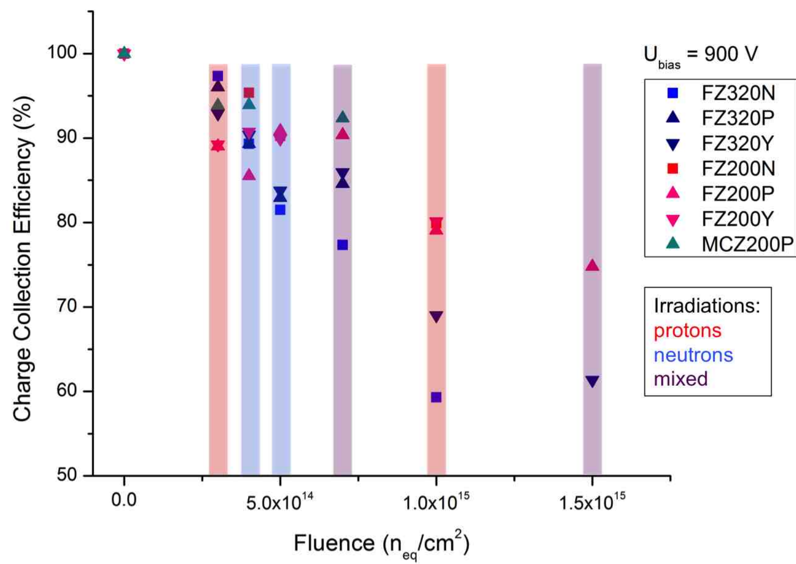

(b) CCE at 900 V

Figure 7.27.: Dependence of the charge collection efficiency on the fluence at (a) 600 V bias voltage and (b) 900 V bias voltage. The charge collection efficiency reduces faster for the 300 µm sensors.

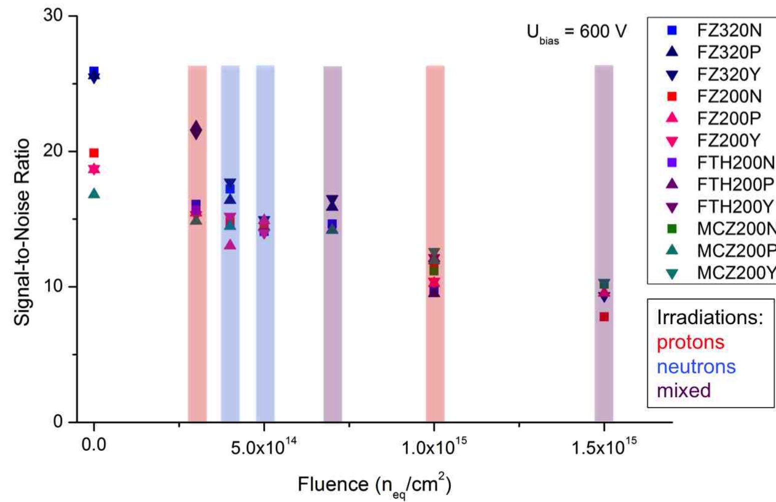

(a) Signal-to-Noise at 600 V

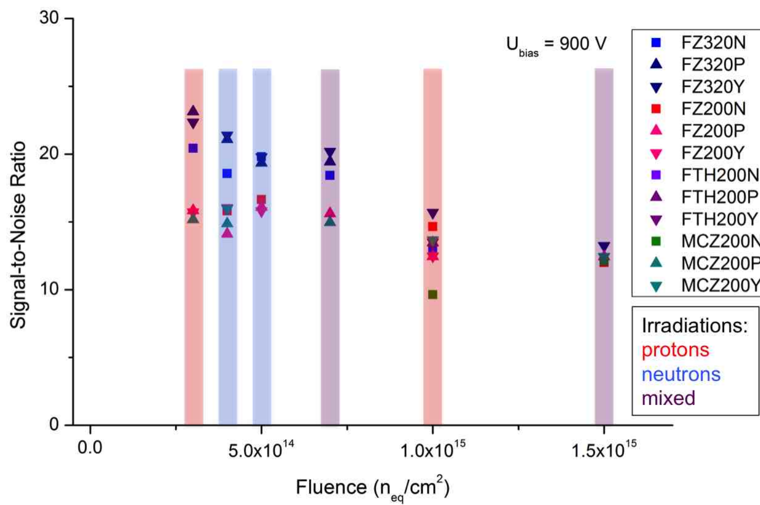

(b) Signal-to-Noise at 900 V

Figure 7.28.: Dependence of the signal-to-noise ratio on the fluence at (a) 600 V bias voltage and (b) 900 V bias voltage. The signal-to-noise ratio is higher at higher voltages (due to the increased depletion region) and there is no visible difference between the thick an the thin sensors or between the p-spray and the p-stop isolation technique.

7.3. Annealing Study

So far, the influence of irradiation on the sensor properties has been investigated. The charge collection and the signal-to-noise ratio decrease with rising fluence, while the leakage current and the depletion voltage increase. The reason for these changes are lattice defects, due to interactions of transversing particles with the silicon crystal lattice (see section 3.1). Some of these defects can recover by a beneficial annealing (see section 3.2.1 and 3.2.2).
Figure 7.29 and figure 7.30 illustrate the changes in the depletion voltage in dependence on the annealing time, after an irradiation to $\Phi_{eq} = 7 \times 10^{14} cm^{-2}$ and $\Phi_{eq} = 1.5 \times 10^{15} cm^{-2}$. The annealing times are stated in equivalent time at 21°C.

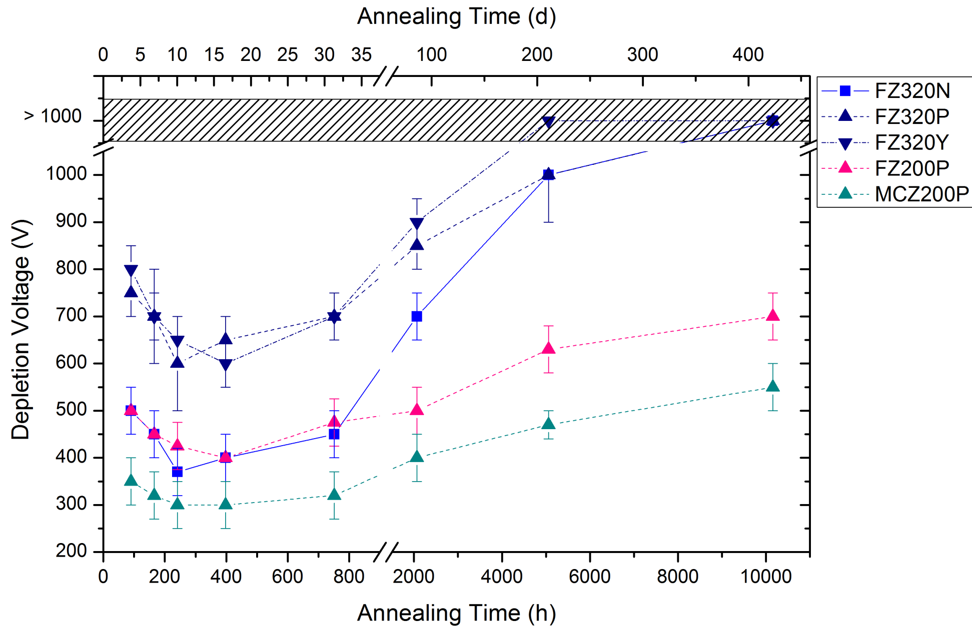

Figure 7.29.: Depletion voltage in dependence on the equivalent annealing time at 21°C, for a fluence of $7 \times 10^{14} cm^{-2}$.

After a decrease in the depletion voltage, which is at a minimum after about 15 days, the depletion voltage rises again. It takes almost 80 days for them to reach the values at no annealing. The depletion voltage for the N type sensor is always below the depletion voltage of the P or Y type sensor. This is due to the fact the N type has a lower depletion voltage right from the beginning and that the generated defects are acceptor-like and as the N type has a high donor concentration more radiation is needed to compensate the donors.

For the leakage current the situation is fundamentally different. After the irradiation the increased leakage current decreases constantly with annealing time. Figure 7.31 shows this behavior for the $\Phi_{eq} = 7 \times 10^{14} cm^{-2}$ and $\Phi_{eq} = 1.5 \times 10^{15} cm^{-2}$ irradiated sensors.

The development of the electron signal is mainly influenced by the depletion voltage. For a bias voltage of 600 V and at a fluence of $7 \times 10^{14} n_{eq} cm^{-2}$ the 200 µm sensors show an almost constant

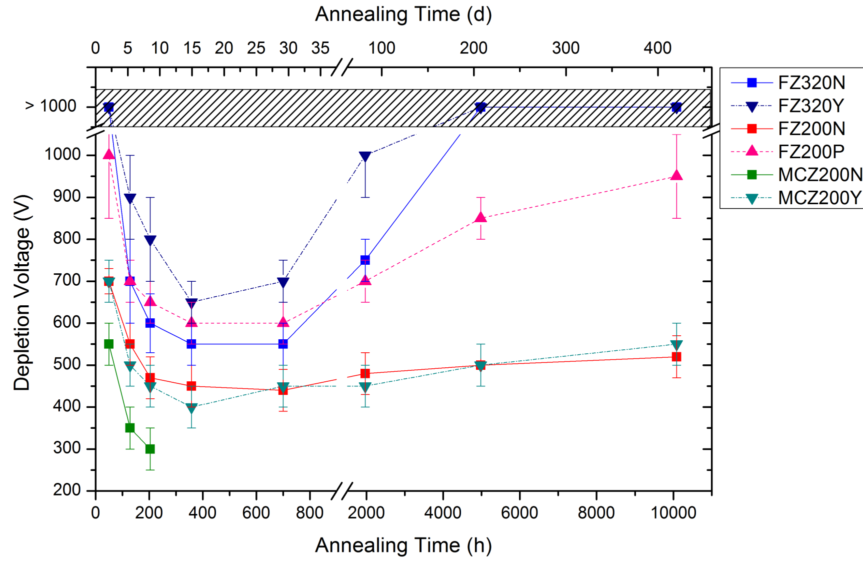

Figure 7.30.: Depletion voltage in dependence on the equivalent annealing time at 21°C, for a fluence of $1.5 \times 10^{15} n_{eq} cm^{-2}$.

electron signal, see figure 7.32(a). The depletion voltages for these sensors are always below 600 V, except for the last two values for the FZ200P where the signal drops slightly.
For the 300 µm thick sensors, the charge collection rises for the first 15 days before it begins to decrease. The gain during the beneficial annealing is not only caused by the reduction of the depletion voltage, as for the 900 V measurements (7.32(b)) all sensors have already been depleted. In contrast, the signal reduction for long annealing times can be explained by the increasing depletion voltage.

At higher fluences of $1.5 \times 10^{15} n_{eq} cm^{-2}$ the situation is similar, see figure 7.33(a) and 7.33(b). After an increase of the electron signals of all sensors for the first 15 days, the signal of the 200 µm sensors keeps almost constant while the signals of the 300 µm sensors decrease rapidly because of the rising depletion voltage.

The reduced signal has a direct impact on the signal-to-noise ratio. Figure 7.34 shows the annealing behavior of the mixed irradiated sensors of $\Phi_{eq} = 7 \times 10^{14} cm^{-2}$ and $\Phi_{eq} = 1.5 \times 10^{15} cm^{-2}$ at 600 V and 900 V. As expected, the signal-to-noise at 600V is lower than at 900 V and at a fluence of $\Phi_{eq} = 7 \times 10^{14} cm^{-2}$ the signal-to-noise is higher than at a fluence of $\Phi_{eq} = 1.5 \times 10^{15} cm^{-2}$.

As the signal-to-noise ratio shows a similar dependence on the annealing time as the electron signal, it can be assumed that the affect of the annealing on the noise is only little. Figure 7.35 illustrates the change in the cluster noise with the annealing time for the two fluences at 600 V and 900 V.

At $\Phi_{eq} = 7 \times 10^{14} cm^{-2}$ the cluster noise does hardly change, while at $\Phi_{eq} = 1.5 \times 10^{15} cm^{-2}$ a noise reduction of 5% is measured.

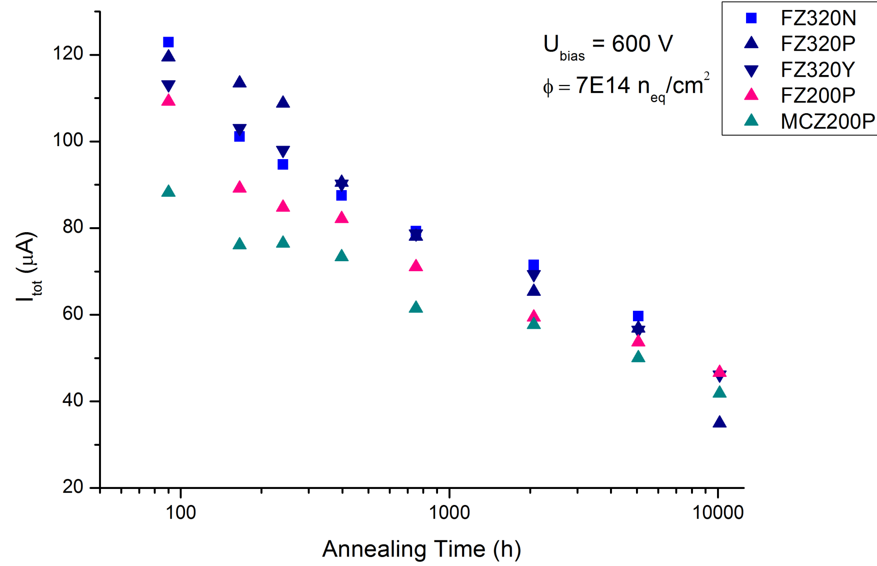

(a) $\Phi_{eq} = 7 \times 10^{14} cm^{-2}$

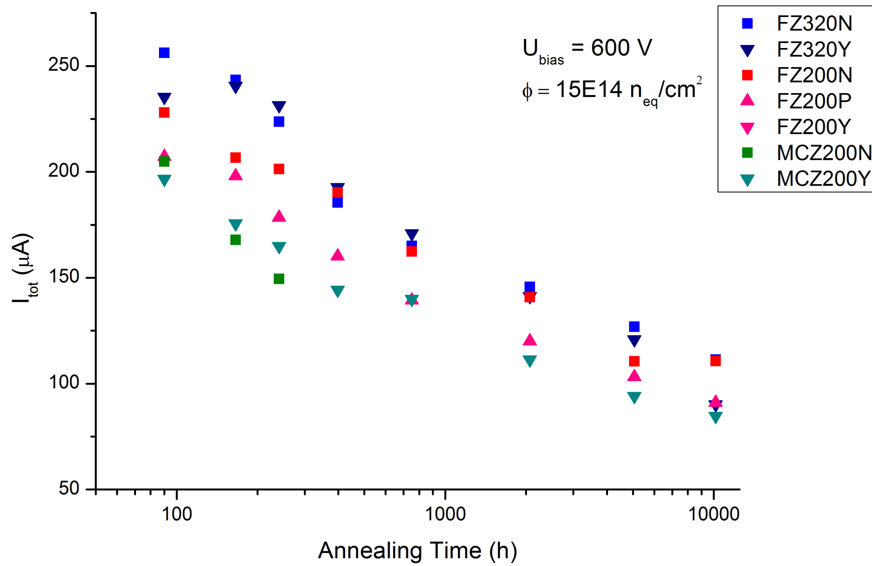

(b) $\Phi_{eq} = 1.5 \times 10^{15} cm^{-2}$

Figure 7.31.: The leakage current plotted versus the equivalent annealing time at 21°C, for a fluence of (a) $7 \times 10^{14} n_{eq} cm^{-2}$ and (b) $1.5 \times 10^{15} n_{eq} cm^{-2}$. The measurement has been done at -20°C at a bias voltage of 600 V.

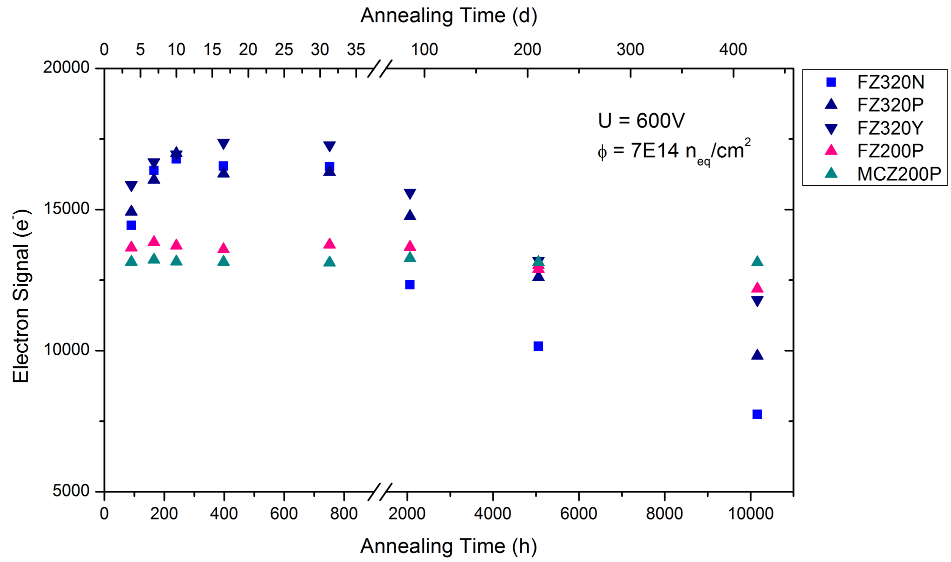

(a) Electron signal at 600V

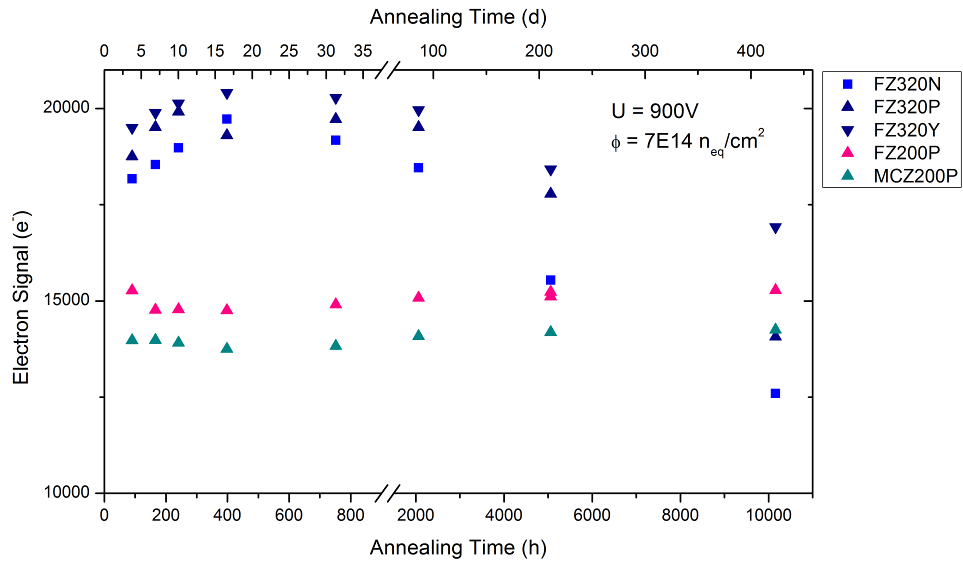

(b) Electron signal at 900V

Figure 7.32.: Dependence of the electron signal of sensors irradiated to $\Phi_{eq} = 7 \times 10^{14} cm^{-2}$ on the annealing time at (a) 600 V and (b) 900 V. The signal of the 200 µm sensors keeps constant, while the signal for the 300 µm sensors decreases. At higher voltages the decreased signal of the 300 µm sensors is still above the signal of the thin sensors even for annealing times of 400 days at 21°C.

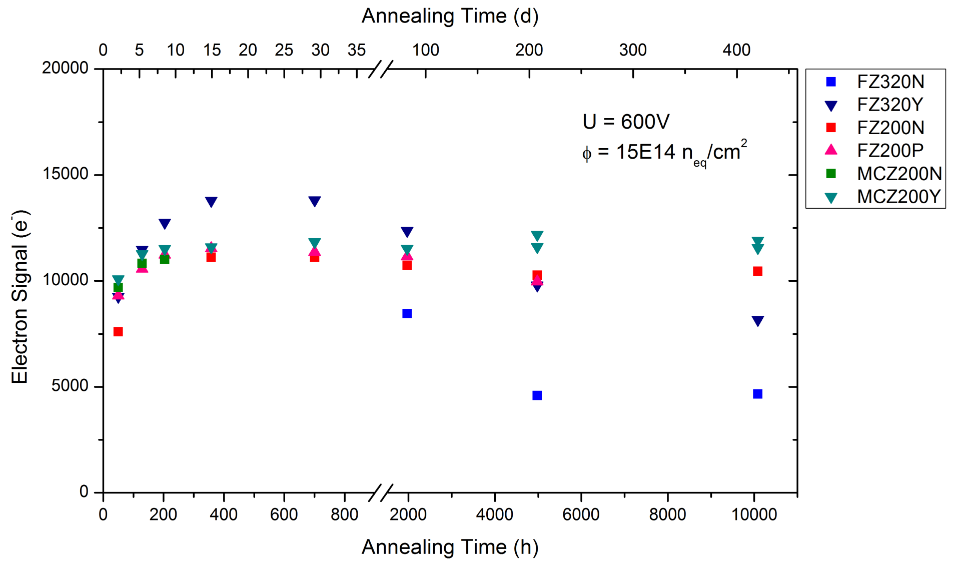

(a) Electron signal at 600V

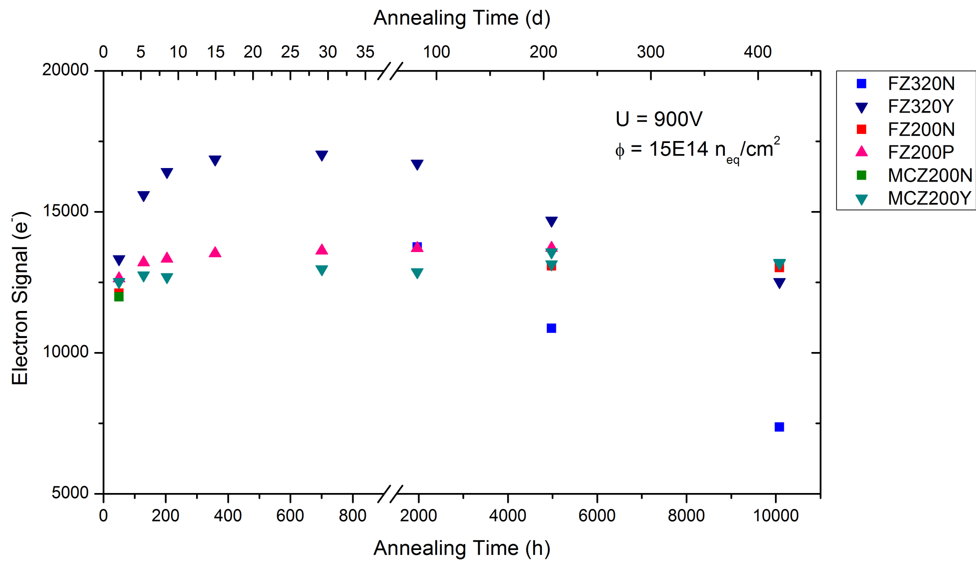

(b) Electron signal at 900V

Figure 7.33.: Dependence of the electron signal of sensors irradiated to $\Phi_{eq} = 1.5 \times 10^{15} cm^{-2}$ on the annealing time at (a) 600 V and (b) 900 V. The signal of the 200 µm sensors keeps constant, while the signal for the 300 µm sensors decreases. At higher voltages the decreased signal of the 300 µm sensors is comparable to the signal of the thin sensors at an annealing time of about 400 days at 21°C. Only the signal of the FZ320N decreases dramatically.

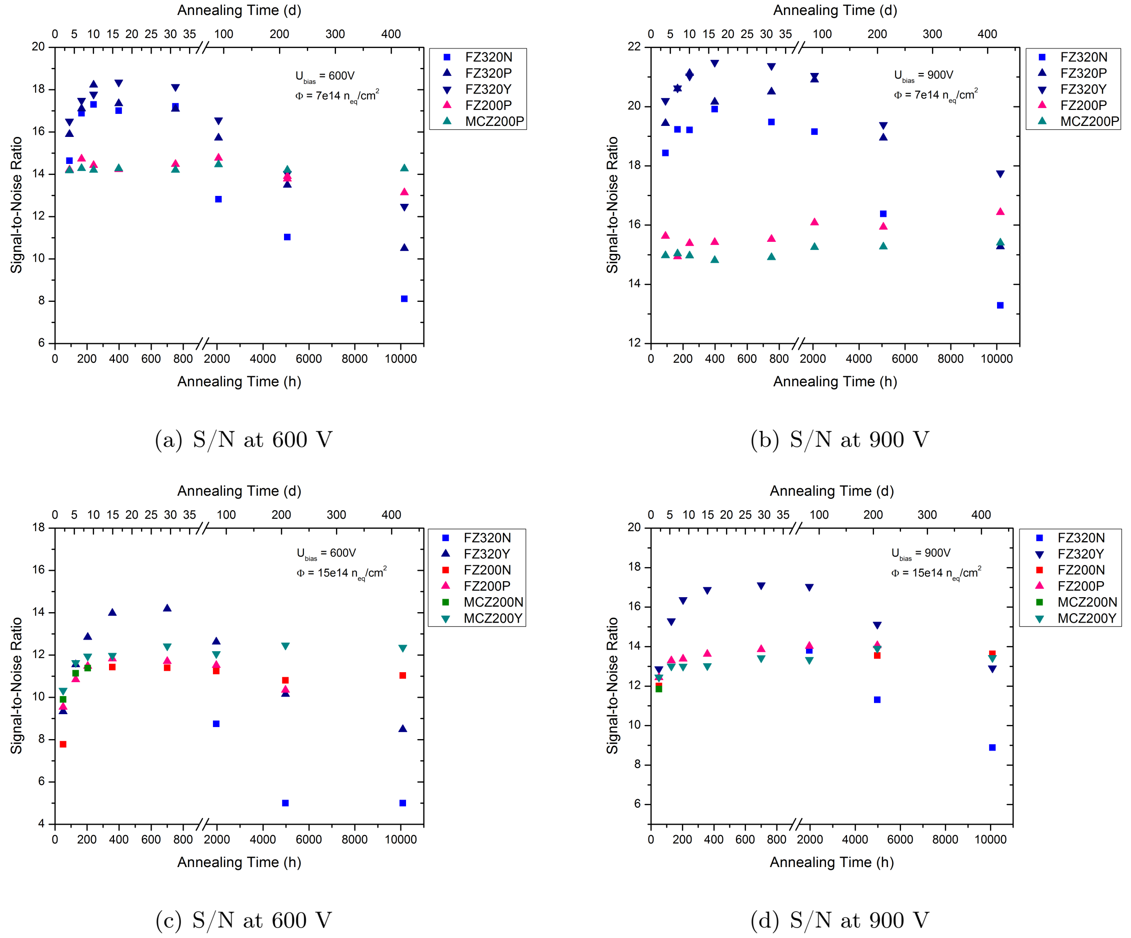

(a) S/N at 600 V

(b) S/N at 900 V

(c) S/N at 600 V

(d) S/N at 900 V

Figure 7.34.: Plot of the signal-to-noise ratio at fluences of $\Phi_{eq} = 7 \times 10^{14} cm^{-2}$ and $\Phi_{eq} = 1.5 \times 10^{15} cm^{-2}$ at 600 V and 900 V versus the annealing time at 21°C. The signal-to-noise behaves similar to the electron signal. At $\Phi_{eq} = 7 \times 10^{14} cm^{-2}$, the signal-to-noise of the 200 µm sensors stays constant but the signal-to-noise of the 300 µm sensors decreases rapidly after a short beneficial annealing. At (a) 600 V the thick sensors show comparable values after an annealing time of 200 days, while at (b) 900 V the values even are comparable up to 400 days annealing time. For $\Phi_{eq} = 1.5 \times 10^{15} cm^{-2}$ at (c) 600 V and (d) 900 V the trend for the thick sensors is similar but worse.

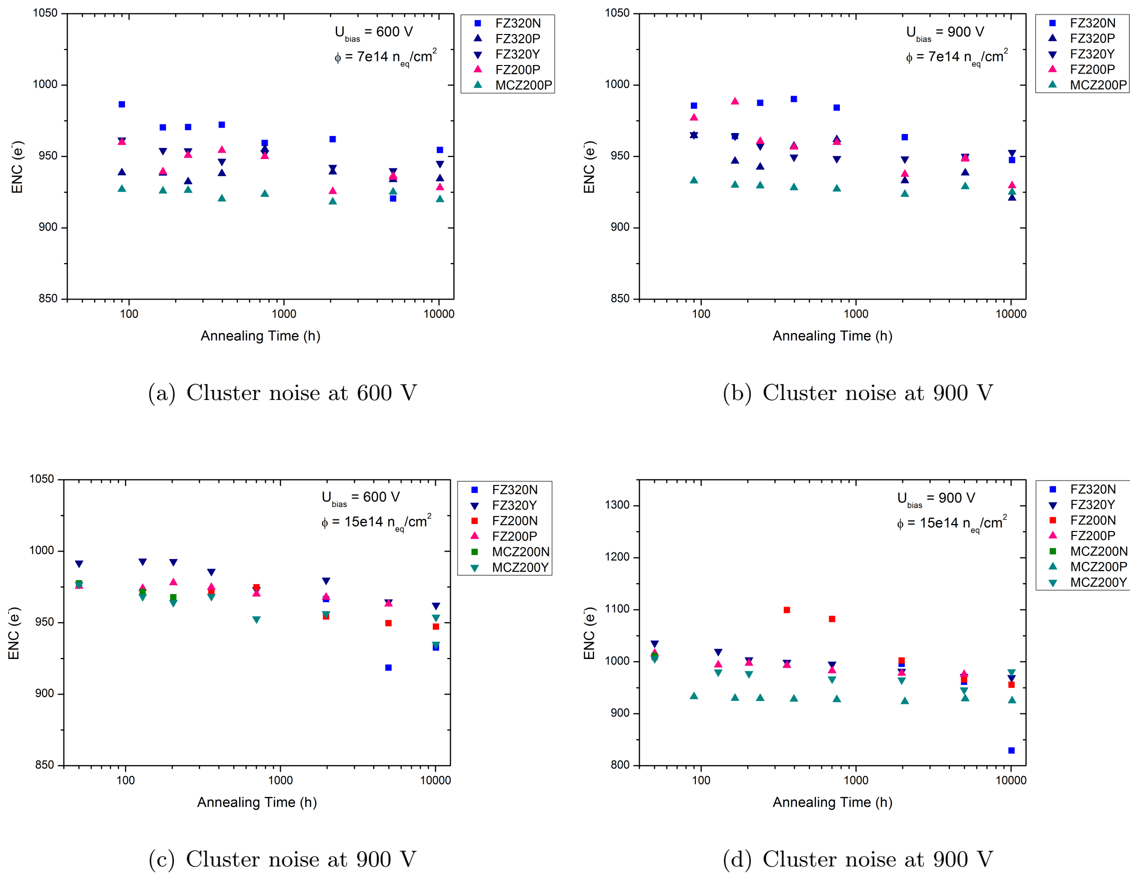

(a) Cluster noise at 600 V

(b) Cluster noise at 900 V

(c) Cluster noise at 900 V

(d) Cluster noise at 900 V

Figure 7.35.: Plot of the cluster noise at fluences of $\Phi_{eq} = 7 \times 10^{14} cm^{-2}$ and $\Phi_{eq} = 1.5 \times 10^{15} cm^{-2}$ at 600 V and 900 V versus the annealing time at 21°C. In all cases, the cluster noise remains constant.

7.4. Conclusion on Material and Technology Study

The qualification of the non irradiated sensors showed a very good production quality. The measured strip parameters have been very homogeneous across the sensors and all parameters were within the desired ranges.
After irradiation the changes of the sensor properties have been investigated and compared to former studies to find the most suitable radiation hard silicon sensors for the high luminosity phase. The full depletion voltage V_{fd} increases, which leads to a loss in the charge collection, if the sensors can not be fully depleted. Especially the 300 μm sensors do not deplete after an irradiation to $7 \times 10^{14} n_{eq} cm^{-2}$, while the 200 μm sensors still deplete below 600 V. The rise of the leakage current with fluence has been compared to former irradiation studies on diodes, and it turned out, that the slope for sensors is slightly higher (16%) and thus also the power consumption of a detector system made up of these sensors.
The sensor strip parameters coupling capacitance and inter-strip capacitance have not been affected by radiation. The increase of the bias resistors by 15% is even beneficial with respect to the noise contribution. The only parameter that has dramatically changed is the inter-strip resistance. R_{int} decreased by almost a factor of 1000 down to about 100 MΩcm, but is still sufficiently high. Even the two different isolation techniques for p-type sensors, p-stop and p-spray, guarantee a good strip isolation up to a fluence of $1.5 \times 10^{15} n_{eq} cm^{-2}$.
A decrease in the charge collection and the signal-to-noise ratio has been measured for all sensor types. From the initial 22800 electrons for the 300 μm sensors and the 15400 electrons for the 200 μm sensors, the charge collection decreases to about 10000 electrons (600V) and 11000 electrons (900V) at a fluence of $1.5 \times 10^{15} n_{eq} cm^{-2}$. Above a fluence of $1 \times 10^{15} n_{eq} cm^{-2}$ there is no difference between the 300 μm and 200 μm thick sensors as well as between the different materials (deep diffusion float zone, thinned float zone and magnetic Czochralski). The development of the signal-to-noise ratio is very similar to that, decreasing from 25 and 18 down to about 10, which is still sufficient for the usage in a tracking detector.
The annealing study, investigating the recovery of radiation defects and their influence on sensor properties after mixed irradiations to fluences of $7 \times 10^{14} n_{eq} cm^{-2}$ and $1.5 \times 10^{15} n_{eq} cm^{-2}$, corresponding to a radial distance to the interaction point of CMS of R=40 cm and R=20 cm has been done in several steps and at defined temperatures. The full depletion voltage showed the expected behavior. After a short (beneficial) annealing, V_{fd} drops to a minimum before it begins to rise with further annealing. The leakage current decreases steadily with annealing time. Charge collection and also signal-to-noise ratio are mainly influenced by the depletion voltage. For the 200 μm sensors, both parameters stay constant during the annealing and for both fluences, as their full depletion voltage remains below the operating voltages of 600 V and 900 V during the annealing study of over 400 days at 21°C. The 300 μm sensors behave different. As the charge collection and S/N depend mainly on the depleted volume, both parameters evolve accordingly to the size of the depletion region. After a short increase during the beneficial annealing, charge collection and signal-to-noise ratio decrease for both fluences, but especially for the $1.5 \times 10^{15} n_{eq} cm^{-2}$. At this fluence, the charge collection and also the signal-to-noise ratio of the FZ320P/Y sensors are

comparable with the signals of the 200 μm sensors. Only the FZ320N shows a very low electron signal.

Chapter 8.

Studies on new Sensor Designs

8.1. Sensor with Fourfold Segmented Strips and Readout at the Edge - FOSTER

The FOSTER, described in detail in chapter 6.3.2, is shown in figure 8.1.

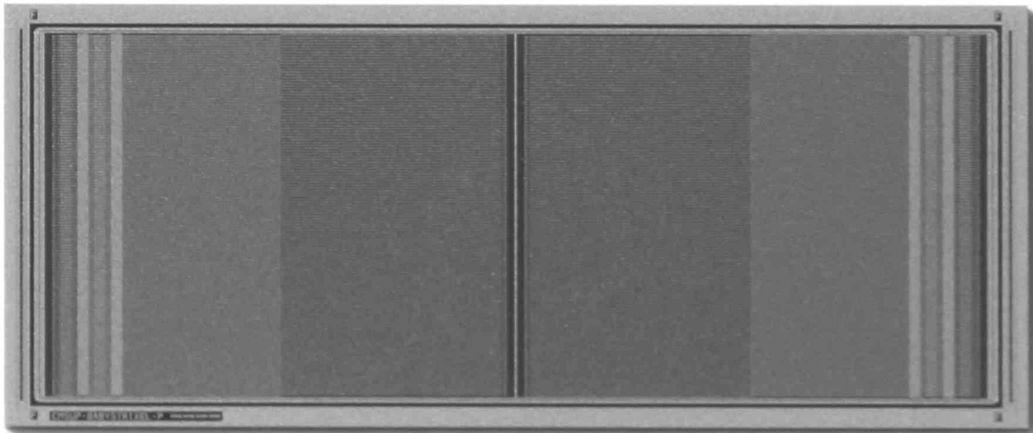

Figure 8.1.: Picture of the FOSTER. This new sensor design increases the granularity and maintains the well know wire bonding at the sensor edge, necessary for the planned 2S module [Abb11].

Looking at the current tracker upgrade plan, which includes trigger-capable 2S modules only, such kind of sensor would even be beyond baseline, meeting all requirements on a sensor for the 2S module. AC pads are placed at the sensor edge to preserve the possibility of standard wire bonding to connect the readout electronics and in addition to have more and shorter strips to increase the granularity.
The following section gives a detailed overview of the characterization of the FOSTER. The first part will show the pre-qualification measurements in the probe-station, investigating especially the production quality of the sensor and the second part will investigate the sensor behavior in terms of signal coupling, which will be accompanied by simulations.

8.1.1. Electrical characterization

The electrical characterization is done on three different sensors, one p-in-n sensor (FZ320N), one n-in-p sensor with p-spray isolation (FZ320Y) and one n-in-p sensor without any strip isolation (FZ320P). Originally the FZ320P was intended to have a p-stop strip isolation similar to the p-stop isolation for the Baby_Std sensors, but due to the narrow spacing the processing was not possible for HPK at that time.
These measurements of sensor and strip parameters give an overview of the production quality and a glimpse of the functionality. All measurements have been done at a temperature of 20 °C and at a relative humidity below 25 %.

Sensor parameters

The global measurements give a first information of the sensor performance. Figure 8.2 depicts the total leakage current measurement (left) and the $\frac{1}{C^2}$ curves (right) for the three sensor types. The total leakage current is in between 3.6 nA/cm^2 and 4.1 nA/cm^2 at 600 V, which is reasonable for that sized sensors and the full depletion voltages extracted from the $\frac{1}{C^2}$ curves indicate values of about 250 V.

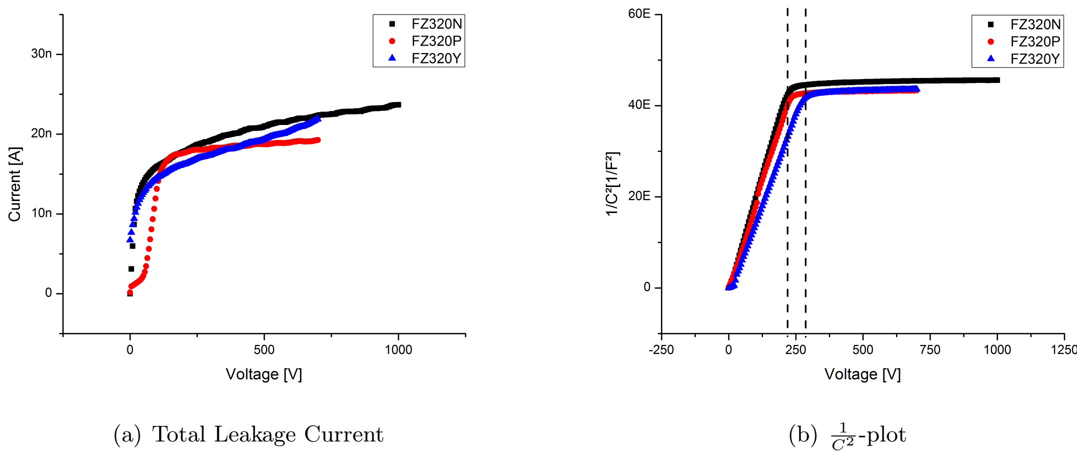

(a) Total Leakage Current

(b) $\frac{1}{C^2}$-plot

Figure 8.2.: Measurements of the total leakage current and the full depletion voltage. (a) The IV curves did not indicate any sensor breakdown up to 700 V with a reasonable current and (b) the $\frac{1}{C^2}$-plot replotted from the CV curves pictures full depletion voltages of about 250 V±15 V.

Strip parameters

The strip measurements show the characteristic parameters or defects of each single strip. The measurements have been done at a bias voltages of 600 V without a guard ring connection. Table 8.1 summarizes the measurement results for the sensor characterization of the three sensors, appendix C.1 shows the results graphically. The measurements show very homogeneous results. There has not been one pinhole and the inter-strip resistances for all strips is larger than 10 GΩ. The good

inter-strip isolation indicates an excellent Si-SiO_2 interface with little oxide charge and therefore no strip-shortening inversion layer in the FZ320P device without p-stop strip isolation.

Table 8.1.: Measurement results for the sensor strip parameters. There is a distinction between far-strips and near-strips for some sensor characteristics due to the different strip geometry (see figure 6.38).

measurement	strips	FZ320N	FZ320P	FZ320Y
		$\bar{x} \pm \sigma_x$	$\bar{x} \pm \sigma_x$	$\bar{x} \pm \sigma_x$
Leakage Current (pA/cm)	near	29.7 ± 4.7	21.3 ± 5.3	52 ± 4
	far	74 ± 5.2	64.6 ± 9.5	83.2 ± 5.4
Bias Resistor (MΩ)	near	1.81 ± 0.01	1.69 ± 0.01	1.73 ± 0.01
	far	1.86 ± 0.01	1.75 ± 0.02	1.79 ± 0.03
Interstrip Capacitance (pF/cm)	near-far	0.57 ± 0.01	0.56 ± 0.01	0.59 ± 0.02
	near-near	0.34 ± 0.01	0.35 ± 0.01	0.39 ± 0.01
	far-far	0.59 ± 0.01	0.6 ± 0.01	0.6 ± 0.01
Coupling Capacitance (pF/cmμm)	near	1.47 ± 0.01	1.37 ± 0.01	1.51 ± 0.01
	far	1.5 ± 0.01	1.42 ± 0.03	1.55 ± 0.02

The inter-strip capacitance shown in table 8.1 is measured between one far-strip and one near-strip but also between two near-strips and two far-strips. The different values for C_{int} can be explained by the different strip geometries (see figure 8.3), as C_{int} mainly depends on the pitch.

To confirm the homogeneity of the sensors, figure 8.4 shows the leakage currents and coupling capacitances for each single strip. The strip leakage currents in figure 8.4(a) are very homogeneous, showing a slightly higher current for the FZ320N and FZ320Y sensors, which is also seen in the IV curves of figure 8.2. The coupling capacitance in figure 8.4(b) is also very uniform over the sensors. There is a slight difference in the capacitance values for the near-strips and far-strips due to their different strip geometry (see figure 6.38).

In total, all strip parameters on the three sensors are homogeneous and fit the requirements. The sensor production is of high quality.

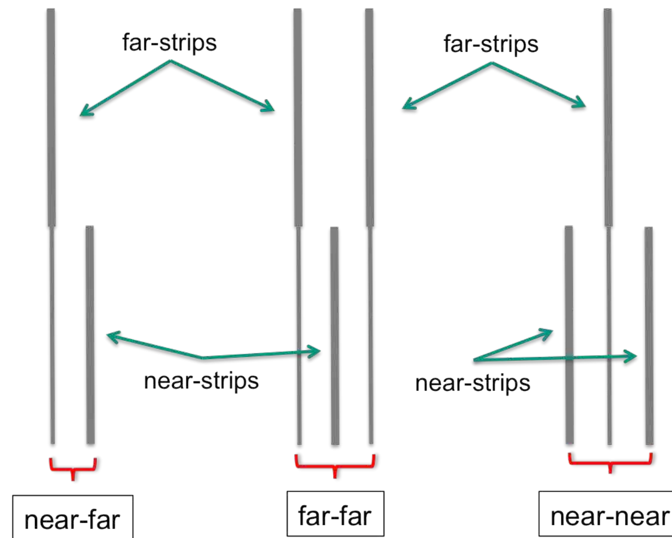

Figure 8.3.: Illustration of the C_{int} measurements on the FOSTER. From left to right, C_{int} is measured between a near- and a far-strip, between two far-strips and between two near-strips. As C_{int} depends on the strip geometry, the C_{int} values change according to strip length and pitch.

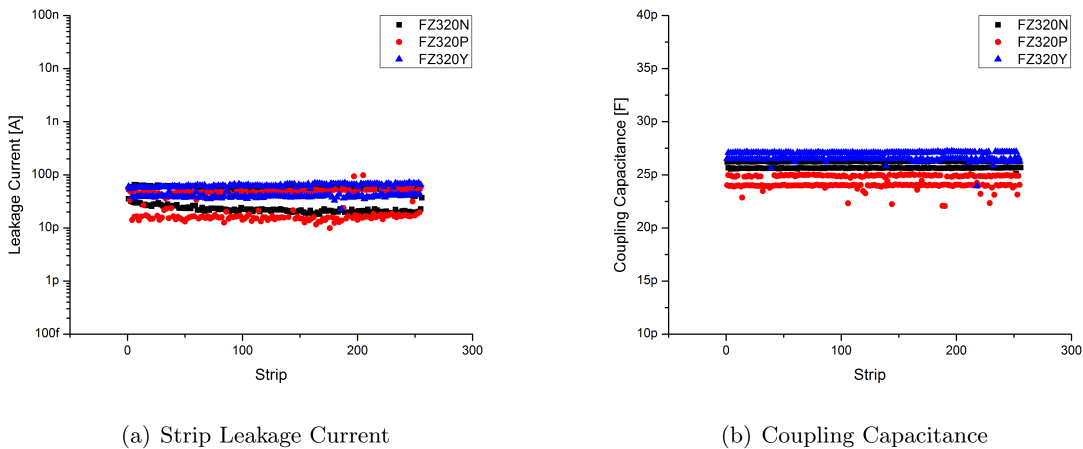

(a) Strip Leakage Current

(b) Coupling Capacitance

Figure 8.4.: Selection of strip measurement results on the three sensor types. Figure (a) and (f) show the uniformity of the strip leakage current and the coupling capacitance. The two levels in the same color reflect the slightly different properties of far-strips (odd strip number) and near-strips (even strip number).

8.1.2. Laser and Source Measurements

To investigate the sensor functionality and especially the signal coupling, the ALiBaVa[1]-system, a portable and fast (25 ns) readout system for silicon microstrip sensors [MH08], has been used. It offers the possibility to perform laser and source measurements, see section 4.2.2.

Laser Measurements

For the FOSTER, especially the charge sharing in the different regions is interesting, also with respect to the three different prototypes. Therefore signal measurements scanning in steps of 1 μm between the strips have been done with a 1060 nm laser at 300V in each region of the sensors. The sensors have been fully depleted and operable. The upper part of figure 8.5 shows a schematic view of the laser scan measurements between strips in the far 8.5(a) and the near region 8.5(b) for the FZ320N FOSTER.

As mentioned in section 6.3.2 the far-strips have odd strip numbers and the near-strips have even strip numbers.
The lower part shows the measurement results, visualizing the signal distribution between the strips. The blueish bars represent the aluminium routings of the far-strips. If the laser hits these lines, the signal vanishes as the laser light gets reflected. In the far region 8.5(a) the signal is equally shared between the far-strips 181 and 183 without any signal coupling to near-strip 182. The sensor works as expected.
In the near region 8.5(b) the signal is not only detectable on the near-strips 182 and 184 but also on the far-strip 183. Different to the design goal, the signal on the far-strip (aluminium routing line) exceeds the signal on the near-strips.
Although only the near region has been hit, the signal coupling to the routing part of the far-strip associates a wrong hit position in the far region. This failure due to the cluster algorithm looking for the highest signal as cluster seed[2] strip would also incident with a binary readout.
These measurements have been repeated on another FZ320N and on the FZ320Y and FZ320P. Figure 8.6 shows the results. All three sensors show the same behavior. While in the far region (plots on the left side) the signal is equally shared between two far-strips, in the near region (plots on the right side) when the laser hits close to the routing line, the signal is coupled to the readout strip of the far-strip. Taking a closer look on the coupled signal heights of the readout strips of the far-strips it can be seen that for the FZ320Y FOSTER the signal is smaller as for the FZ320N or FZ320P. More on that in the simulation section 8.1.3.

[1] **a** **L**iverpool **Ba**rcelona **Va**lencia
[2] strip with highest signal-to-noise, at least larger than 5

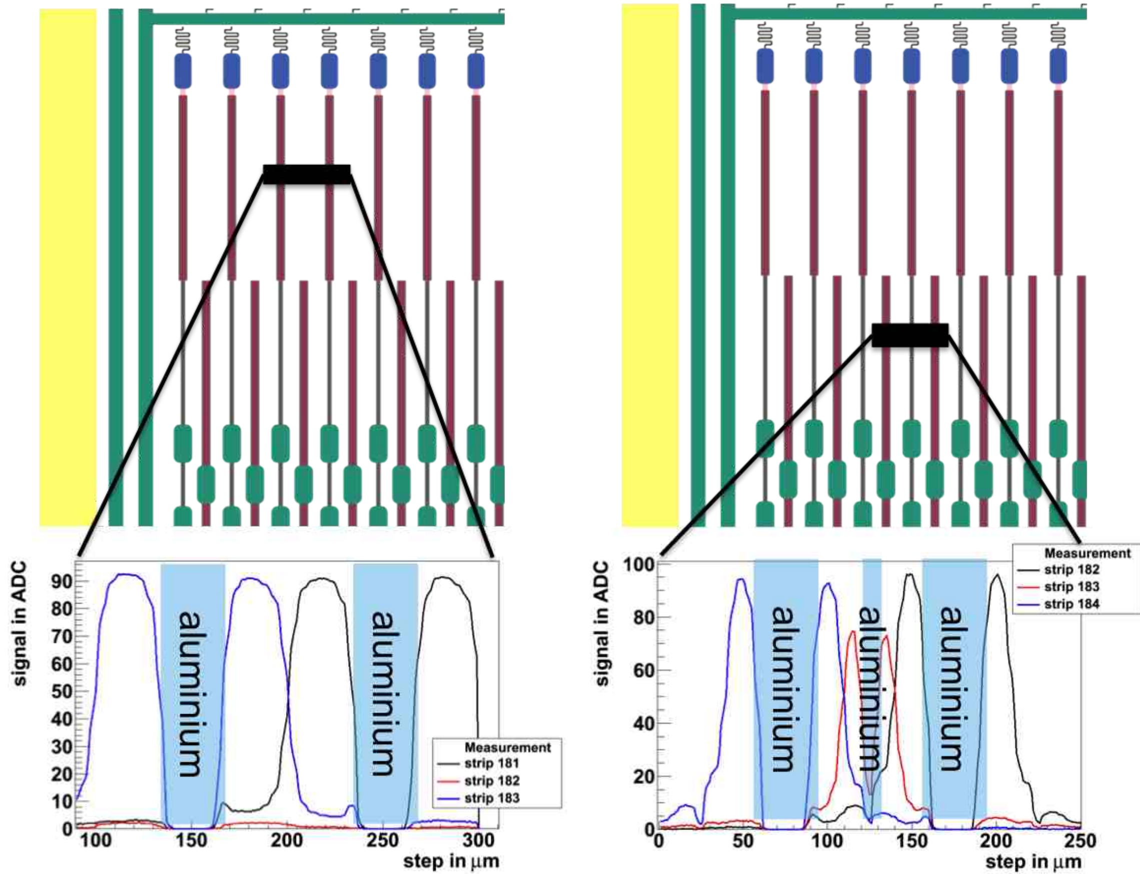

(a) Signal sharing in the far region:
The signal shares only between far-strips 181 and 183.

(b) Signal sharing in the near region:
The signal shares between the near-strips 182 and 184 but is also seen on the far-strips 183.

Figure 8.5.: Laser scan in the (a) far and (b) near region with the corresponding signals of a FZ320N sensor. If the laser, with a spot size of about 15 µm, hits directly on the aluminium routing of a strip, the laser light gets reflected and the signal vanishes.

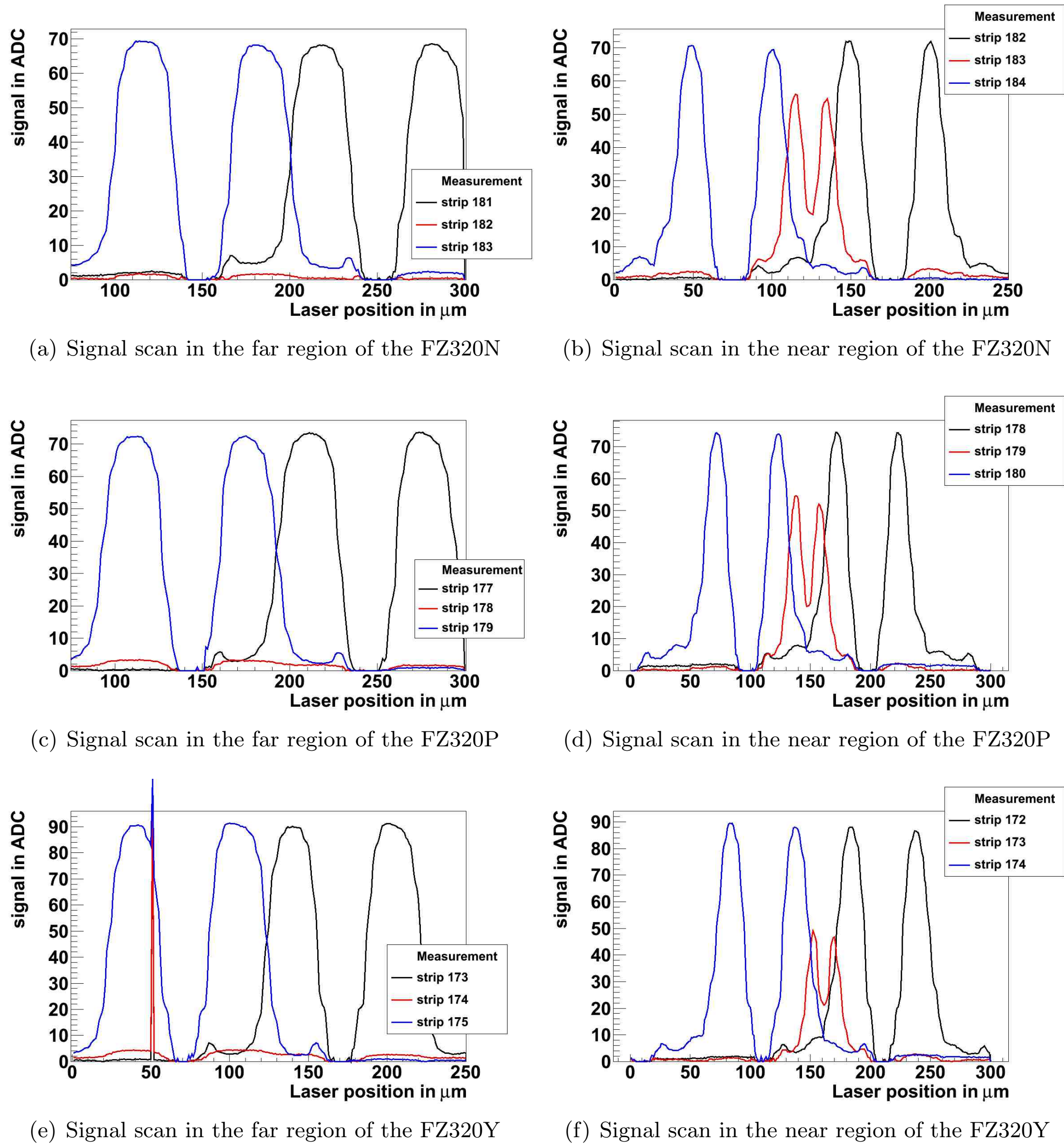

(a) Signal scan in the far region of the FZ320N (b) Signal scan in the near region of the FZ320N

(c) Signal scan in the far region of the FZ320P (d) Signal scan in the near region of the FZ320P

(e) Signal scan in the far region of the FZ320Y (f) Signal scan in the near region of the FZ320Y

Figure 8.6.: Measurements on the three different FOSTER sensors in the far (on the left) and in the near (on the right) region. The signal on the routing lines seems to be smaller for the Y type FOSTER.

Source Measurements

To confirm the signal measurements with the laser, similar measurements have been done with a Sr90-source (beta source).
First a comparison of the charge collected in the near and the far region for the FZ320P and the FZ320N shown in figure 8.7 has been done. There is almost no difference between the N type and the P type sensor. The collected cluster charge is about 24000 electrons for both sensors and in both regions. In detail, the far regions collect marginally more charge.

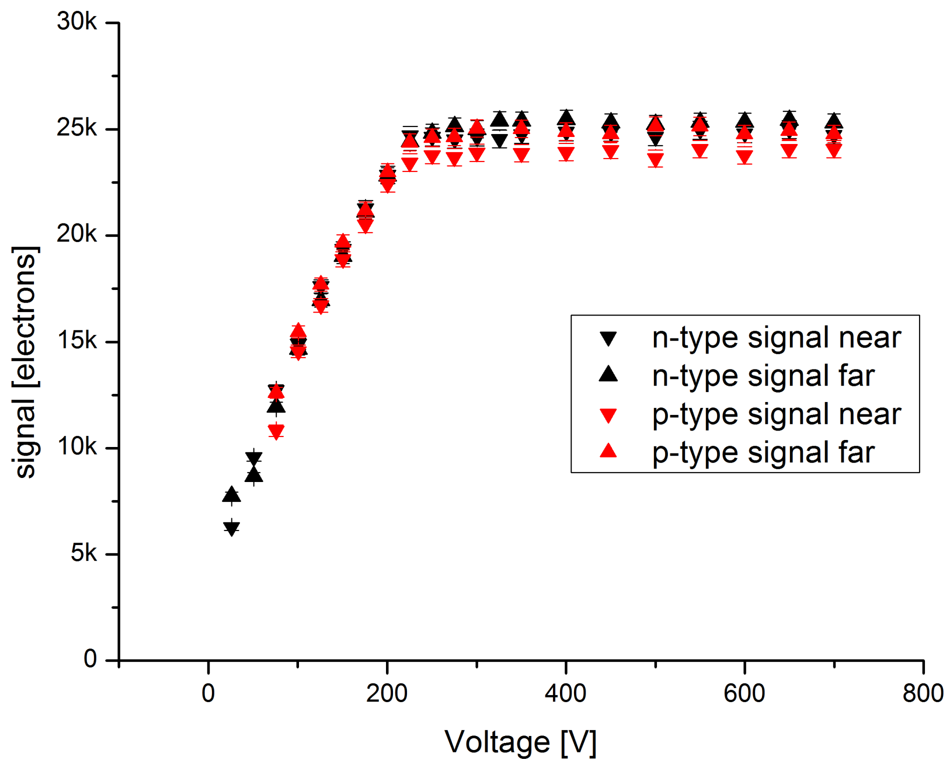

Figure 8.7.: Comparison of the collected charge in the near and the far region for the FZ320N and the FZ320P sensor.

The electron signal rises with increased bias voltage, saturating after reaching full depletion. So the depletion voltage can not only be extracted form the CV curve plotted as $\frac{1}{C^2}$ 8.2(b) but also from the signal over voltage plot, as both curves show exact the same development, see figure 8.8.

To investigate the signal coupling seen in the laser measurements also with the Sr90 source, for each FOSTER type and in each region (near and far) measurements with a Sr90 source have been performed, taking 100000 triggers.
For the FZ320N figure 8.9 shows the signal distribution of the seed strips, depending on which region has been hit by the source. The source is held by a collimator with a window of 0.8 mm diameter and 8 mm depth. The collimator is positioned about 8 mm above the sensor.

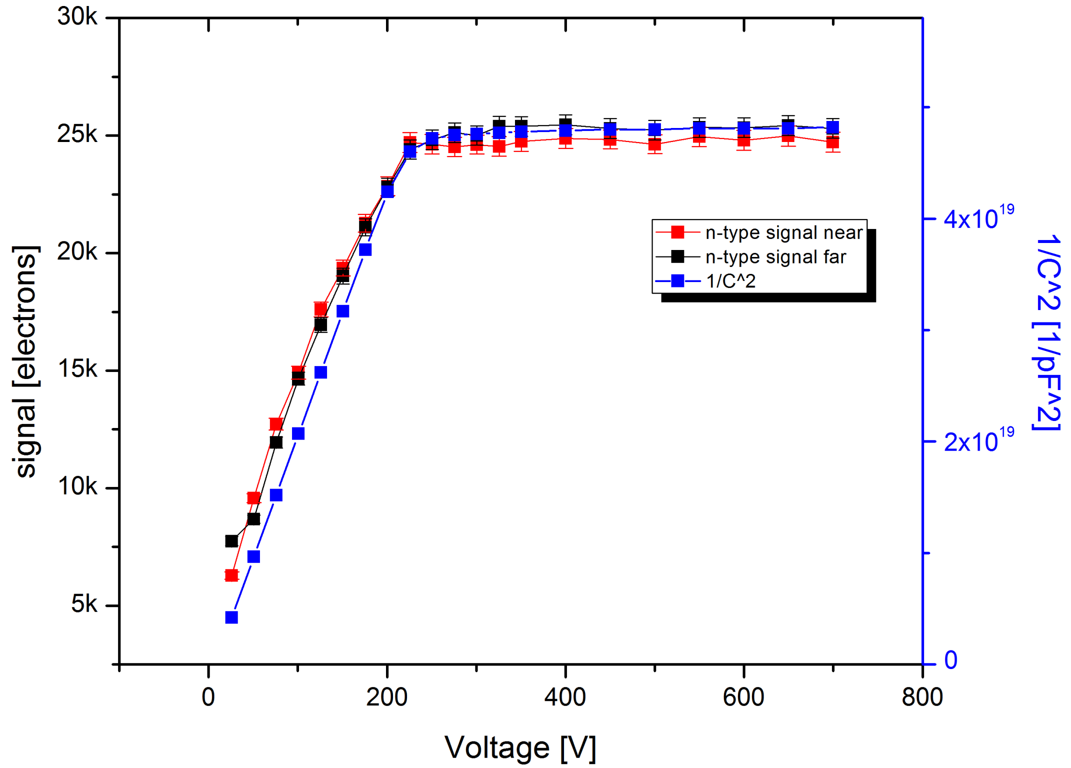

Figure 8.8.: Comparison of the signal over voltage plots in the near and the far region for the FZ320N and the $\frac{1}{C^2}$ plot of the CV curve. The curves indicate the same depletion voltage for the sensor.

If the source is positioned above the far region, the seed strip is in 99.5 % a far-strip(8.9(a)) and in 0.5 % a near-strip(8.9(b)). The few hits, where the seed is a near-strip, although the source is position above the far region, can be explained by the spreading of the source. This has been simulated with GEANT4[3] and is shown in figure 8.10. A beta source, mounted in a collimator as described above, has few betas even at a distance of 10 mm from the peak. As the far region has only a length of 7.6 mm there are actually some electrons hitting in the near region.

Looking at the seed strip distribution, in case that the source is positioned above the near region, the seed strip is in 68.2 % a near-strip but in 31.8 % a far-strip. This high ratio of seed strips identified as far-strips, although the near region was hit, can not be explained by the spreading of the Sr90-source. We observe an induced signal on the routing line of the far-strip by moving charges below the oxide layer.

[3]**GE**ometry **AN**d **T**racking is a platform for "the simulation of the passage of particles through matter," using Monte Carlo methods

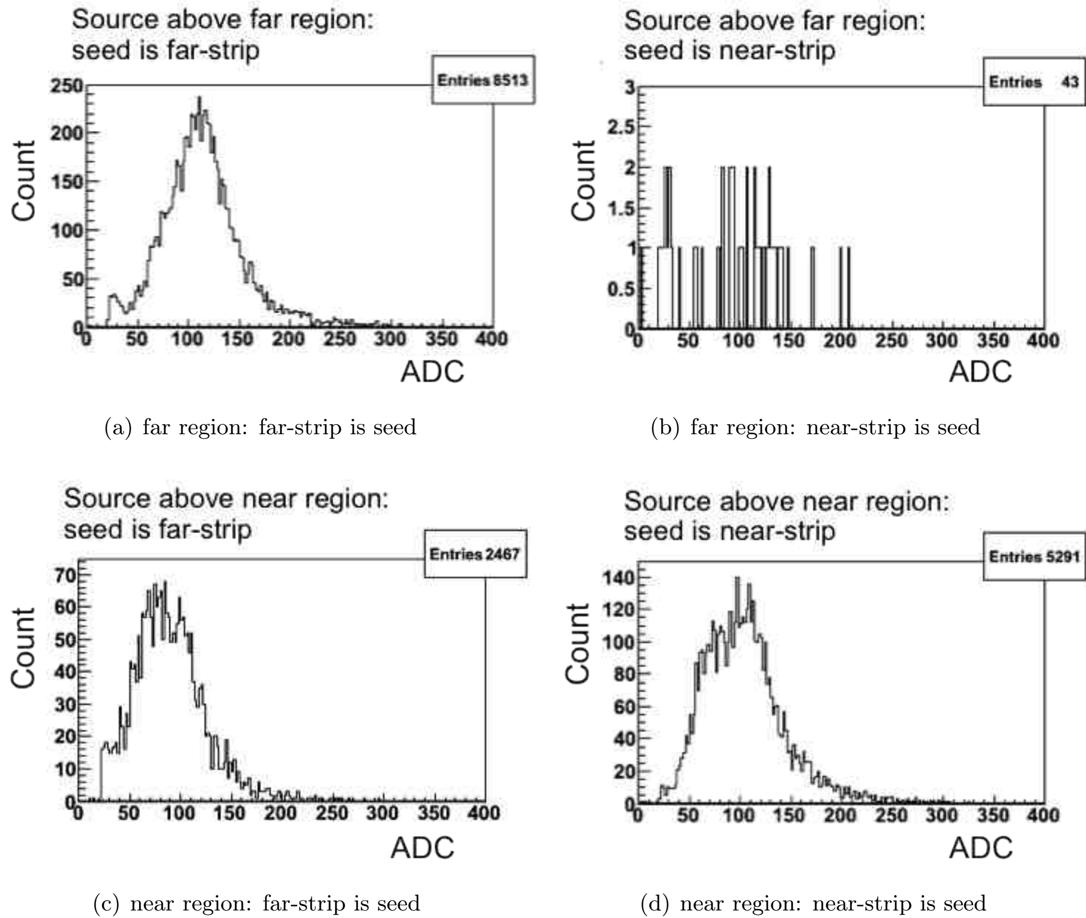

(a) far region: far-strip is seed

(b) far region: near-strip is seed

(c) near region: far-strip is seed

(d) near region: near-strip is seed

Figure 8.9.: FZ320N histograms of the occurrence of seed strips being a far-strip 8.9(a) and 8.9(c) or a near-strip 8.9(b) and 8.9(d) depending on the source position. In the upper part the source is positioned above the far region and in the lower part above the near region of the FZ320N sensor. Even if only the near region is hit, the cluster algorithm finds one-third of the seed strips being far-strips.

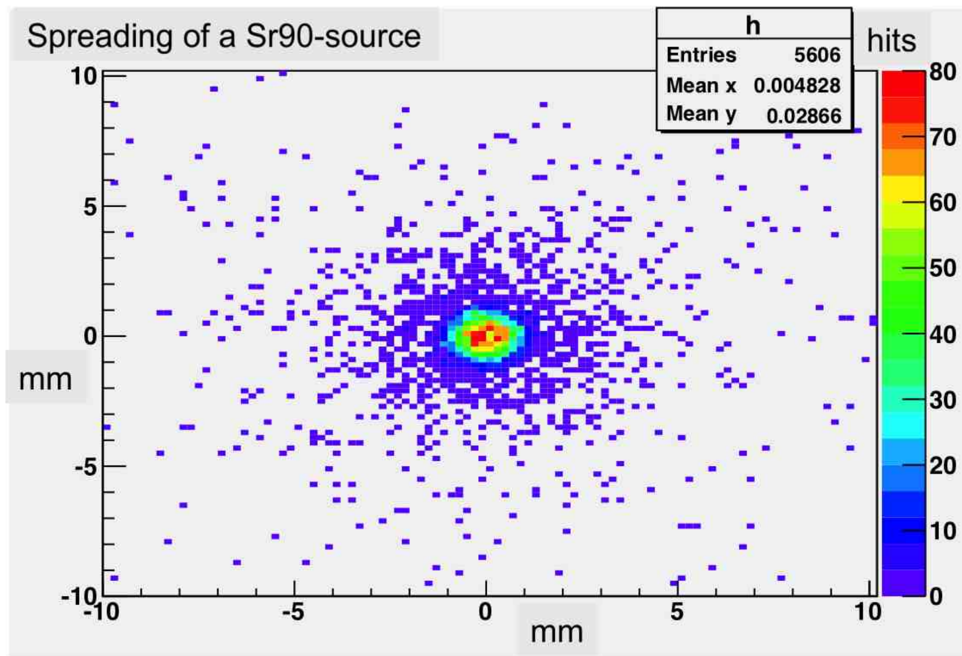

Figure 8.10.: Beam spot of a Sr90 source, mounted on a collimator with a opening window of 0.8 mm diameter and 8 mm depth, positioned in a height of 8 mm. The beamspot has a spreading of about 10 mm.

These seed strip distributions have also been analyzed for the FZ320P and the FZ320Y FOSTER and show similar results, see figure 8.11 and figure 8.12.

While the seed strip is to almost 100 % identified to be a far-strip by hitting in the far region, the seed strip is only to 74 % for P type and 82.6 % for Y type detected to be a near-strip, although hitting in the near region. In 26 % for P type and in 17.4 % for Y type the seed strip is tagged to be a far-strip.

The measurements with the Sr90-source show identical results for all sensor types P, N and Y and confirm the laser measurements. It seems that the Y type FOSTER works slightly better than the others. This may be due to the isolating p-spray layer of the FZ320Y, which is separating the implant strips, as shown in 2.11.
For all three sensors the proper functionality is not given, as the signal coupling to the far-strips leads to a wrong hit position assignment when hitting in the near region.
In addition to the signal measurements, also the time profiles of the cluster signals have been examined. The comparison of the signal time profile for the laser and for the Sr90 measurement at 400V are shown in figure 8.13. The laser pulse measurement is triggered by the motherboard of the ALiBaVa-system while the Sr90 source measurement is triggered by a scintillator. The pulse shapes are unipolar and very similar for both measurements.

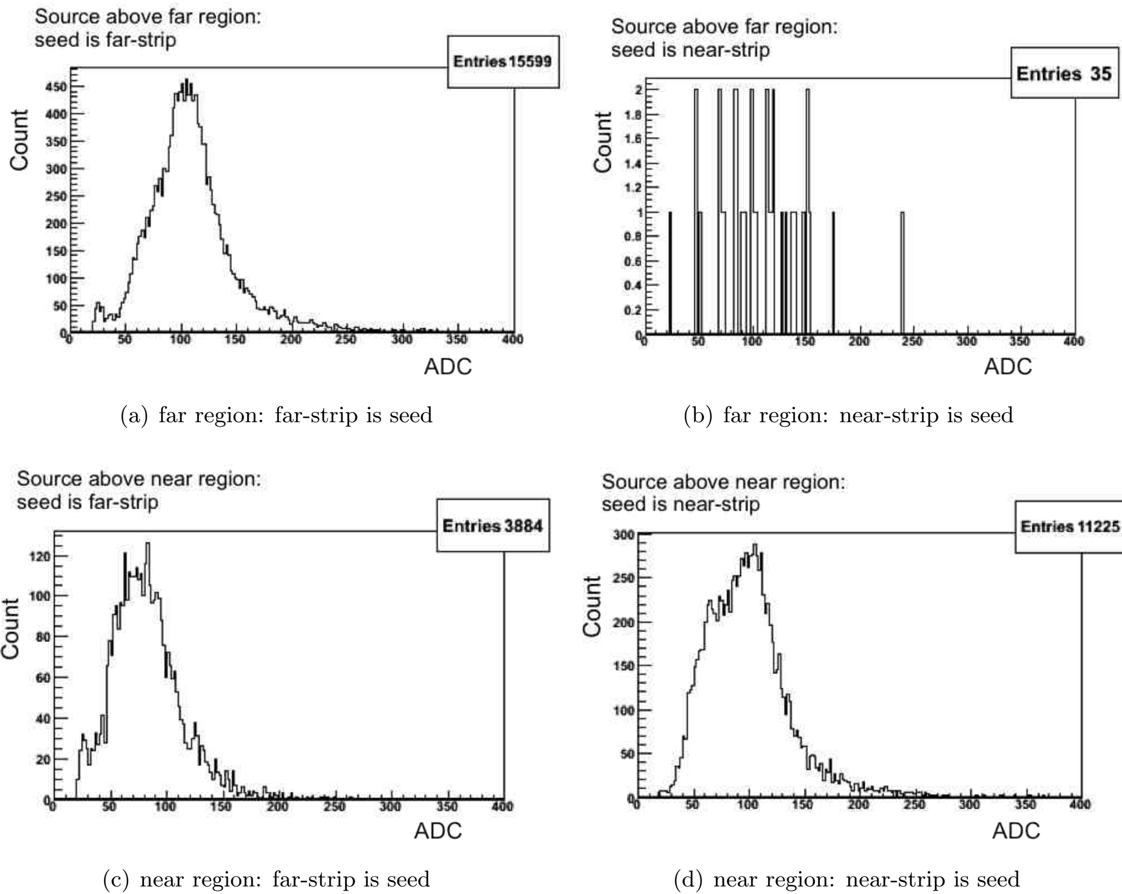

(a) far region: far-strip is seed

(b) far region: near-strip is seed

(c) near region: far-strip is seed

(d) near region: near-strip is seed

Figure 8.11.: FZ320P histograms of the occurrence of seed strips being a far-strip 8.11(a) and 8.11(c) or a near-strip 8.11(b) and 8.11(d) depending on the source position. In the upper part the source is positioned above the far region and in the lower part above the near region. Even if only the near region is hit, the cluster algorithm finds one-forth of the seed strips being far-strips.

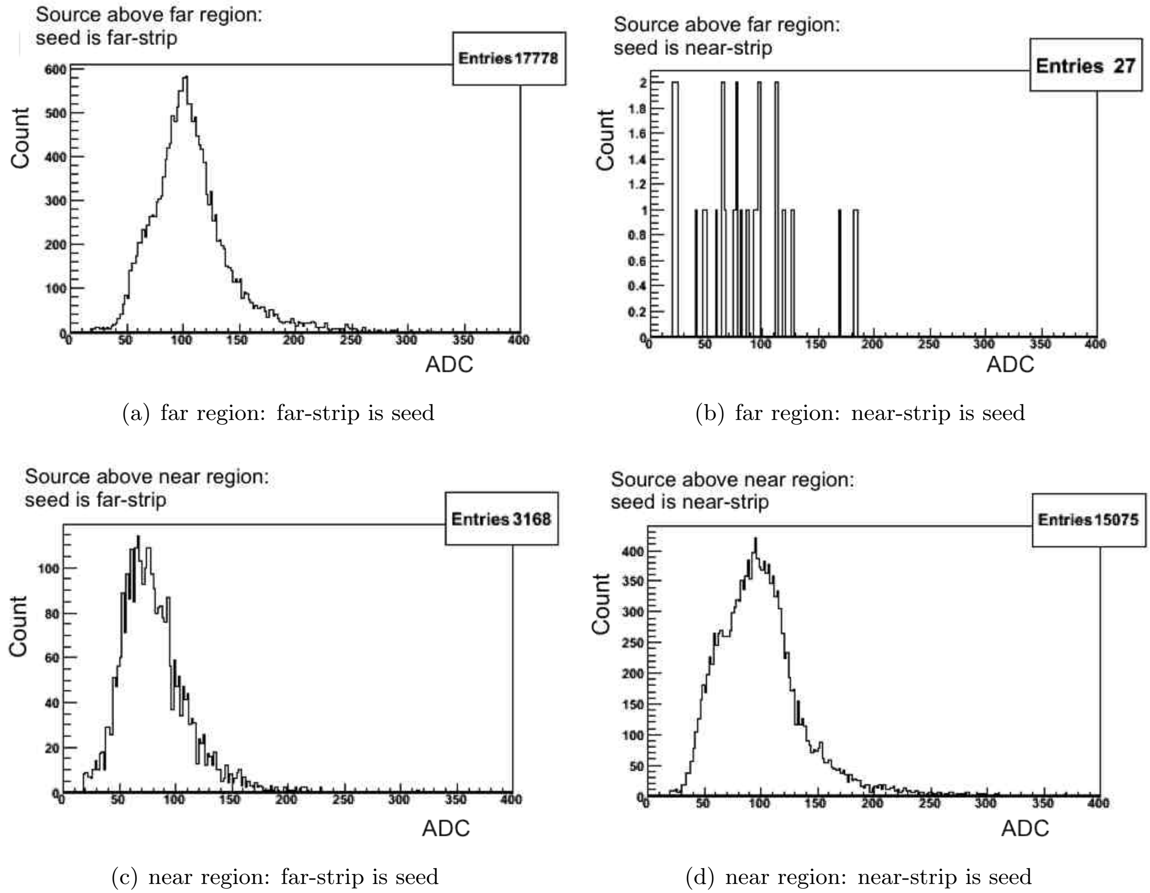

(a) far region: far-strip is seed

(b) far region: near-strip is seed

(c) near region: far-strip is seed

(d) near region: near-strip is seed

Figure 8.12.: FZ320Y histograms of the occurrence of seed strips being a far-strip 8.12(a) and 8.12(c) or a near-strip 8.12(b) and 8.12(d) depending on the source position. In the upper part the source is positioned above the far region and in the lower part above the near region. Even if only the near region is hit, the cluster algorithm finds one-fifth of the seed strips being far-strips.

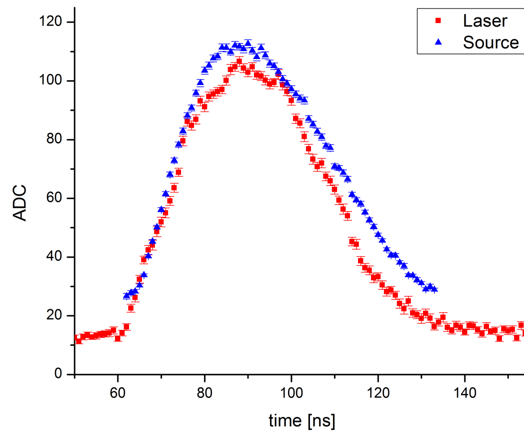

Figure 8.13.: Time profiles of the cluster signals for the laser and for the source measurement on the FZ320Y FOSTER. Both profiles are unipolar and have a similar shape.

8.1.3. Simulations

To investigate the coupling effect of the FOSTER and to verify the laser and source measurement results, the simulation tool Synopsys TCAD[4] has been used to simulate the FOSTER. Therefore the two regions of the FOSTER, near and far, have been rebuilt in a 2D model for N, P and Y type sensors. The simulation uses a heavy ion, configured as a minimum ionizing particle generating 80 electron-hole-pairs per µm along its trace, hitting the sensor vertically. Only the measurement results of the FZ320Y will be compared with the respective simulations, as all three types show identical behavior. Table 8.2 gives an overview of the parameters used to simulate the Y type sensor.

Table 8.2.: Simulation parameters for the FZ320Y sensor. Doping concentrations are specified in peak concentrations with a gaussian shape profile and a depth of 1 µm. The parameters put into the simulations are basically taken from the layout files of the structures and [Tre11].

parameter	value	parameter	value
pitch	100 µm	bulk doping	$3 \times 10^{12}\text{cm}^{-3}$
implantation width	23 µm	implantation concentration	$1 \times 10^{19}\text{cm}^{-3}$
alu strip width	36 µm	back doping	$5 \times 10^{18}\text{cm}^{-3}$
alu routing width	13 µm	oxide charges	$1 \times 10^{11}\text{cm}^{-2}$
thickness	320 µm	p-spray concentration	$2 \times 10^{15}\text{cm}^{-3}$
voltage	−300 V		

Figure 8.14 illustrates the 2D model of the simulated FZ320Y. It shows a section of the near region. The routing line of a far-strip continues between two near-strips. The near-strips implant lies directly beneath the aluminium separated by a thin oxide layer. The surface of the p-bulk is covered with a 1 µm thick gaussian shape p-spray layer to prevent the accumulation of electrons below the oxide layer.

The comparison of the simulated signals and the measured signals in the near region of the FZ320Y FOSTER from the center of near-strip 172 at position 210 µm to the center of near-strip 174 at position 110 µm is shown in figure 8.15. The measured signal (solid lines) is plotted for three strips. The two near-strips 172 and 174 show peak values of about 90 ADC, while the far-strip 173, which in this region only consists of the aluminium routing line, reaches a maximum signal of about 50 ADC. Again the measured signal is vanishing when the laser hits directly on the aluminium (grayish area). The simulated signal (dotted lines) does not show the signal vanishing, as the simulation uses a MIP[5] generating charges in the silicon bulk. The simulated signal is given in units of charge with a maximum of about 4.5×10^{-15}C corresponding to about 28000 electrons generated along the 320 µm track through the bulk.

[4]**T**echnology **C**omputer-**A**ided-**D**esign
[5]Minimum Ionizing Particle is a particle whose mean energy loss rate through matter is close to the minimum

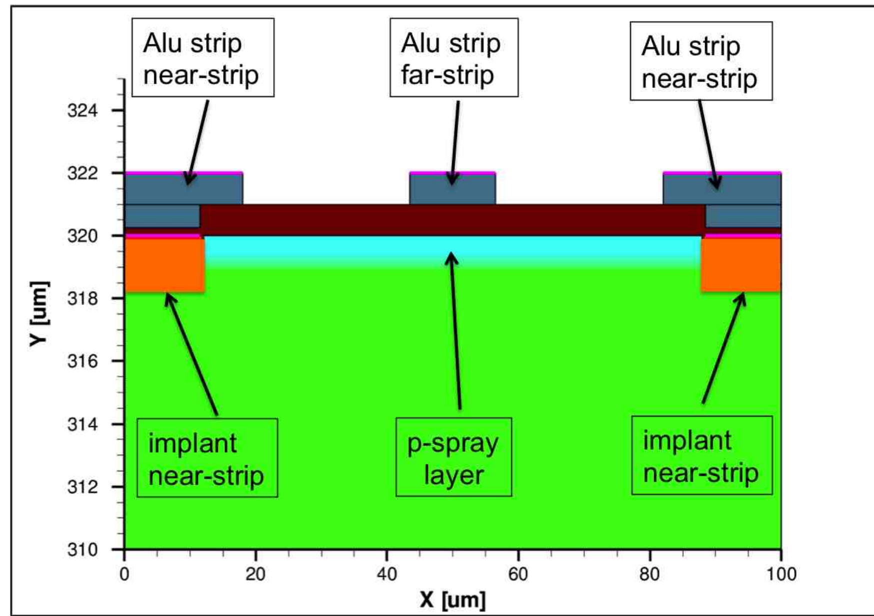

Figure 8.14.: Section of the 2D model of the simulated FZ320Y, illustrating the arrangement of the aluminium strips, the implants and the p-spray layer in the near region. The simulated device is 320 μm × 100 μm and describes the geometry in full thickness from one strip center to the next.

Looking at the signal distributions of the simulation and the measurement there are some differences. The measured signal on the near-strips 172 and 174 has a small shape and the measured signal on the far-strip 173 has a broad shape, which is just the opposite for the simulated signal. These differences can be explained by the finite spot size of the laser, which is larger than 13 μm for the measurements and the point-shaped laser spot in the simulation. While the laser in the simulation only generates charges at the current position and the aluminium routing line of the far-strip only collects charges close beneath, the signal on the far-strip is small but wide on the near-strip. In contrast, the laser spot for the measurement is wide and generates charges not only at the current position, but also within some μm around the position. This leads to a small signal shape on the near-strip and a wide signal shape on the far-strip, as charges are also created close to the aluminium routing line of far-strip 173 and thus induced a signal on it, even if the laser is positioned some μm away. The shift of the signals is almost half the size of the laser spot of about 6.5 μm.
If the FOSTER is hit in the area between the two near-strips, the signal on the far-strip exceeds the signal on the near-strips and indicates a wrong hit position in the far region.

To find the reason for the signal coupling, the electric field of a P type sensor with a routing line between the strips has been simulated. Figure 8.16 illustrates the electric field, represented by the vectors. The electric field points from the strip-side to the backside of the sensor and the electrons move in the opposite direction of the field lines. It is clearly visible, that electrons close to the routing line are attracted to it, inducing a signal.

A suitable solution would be to shield the aluminium routing line. Therefore a structure of highly doped boron can be put below the routing line. As shown in figure 8.17, the implanted structure

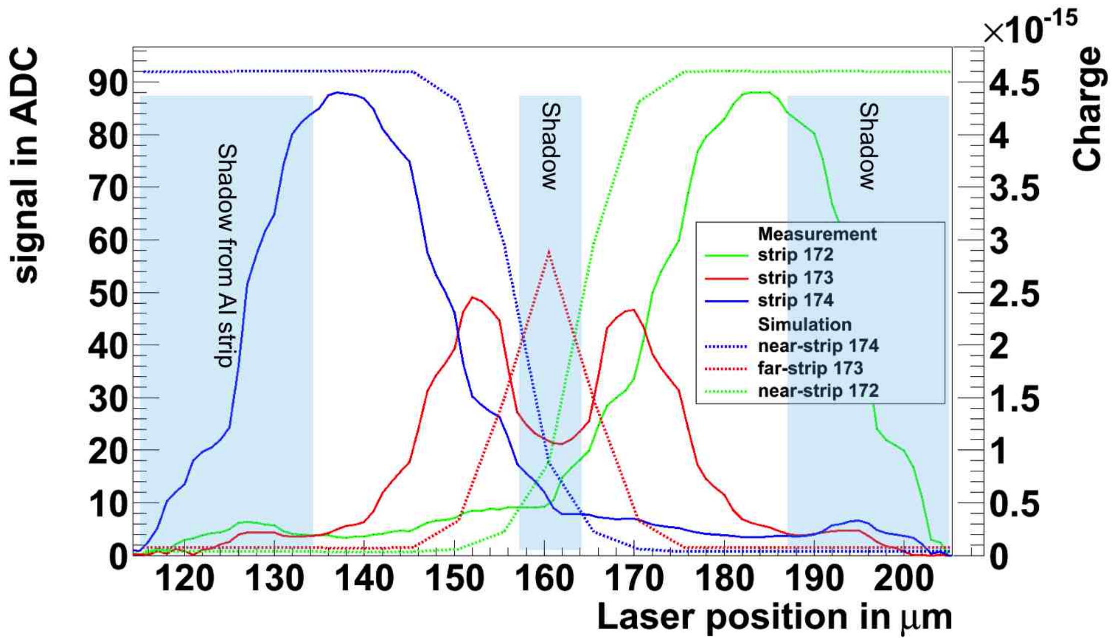

Figure 8.15.: Comparison between the signal of the laser measurements (solid line) and the simulated signal (dotted line) of the FZ320Y. While hitting in the near region the far-strip 173 collects more charge and therefore has a higher signal as the two near-strips 172 and 174. The signal vanishing seen on the laser measurements due to the laser reflection of the aluminium strip does not occur in the simulation of the MIP.

creates a counteracting electric field below the routing line. If the doping concentration of the implanted structure is high enough, the counteracting electric field keeps the electrons, created by a transversing particle, away from the routing line.

This also explains, why the routing line of the FZ320Y FOSTER, shown in figure 8.6, has a smaller signal than the other sensors. The FZ320Y has already a p-spray layer below the routing line, but probably with a to low doping concentration to shield the routing line.

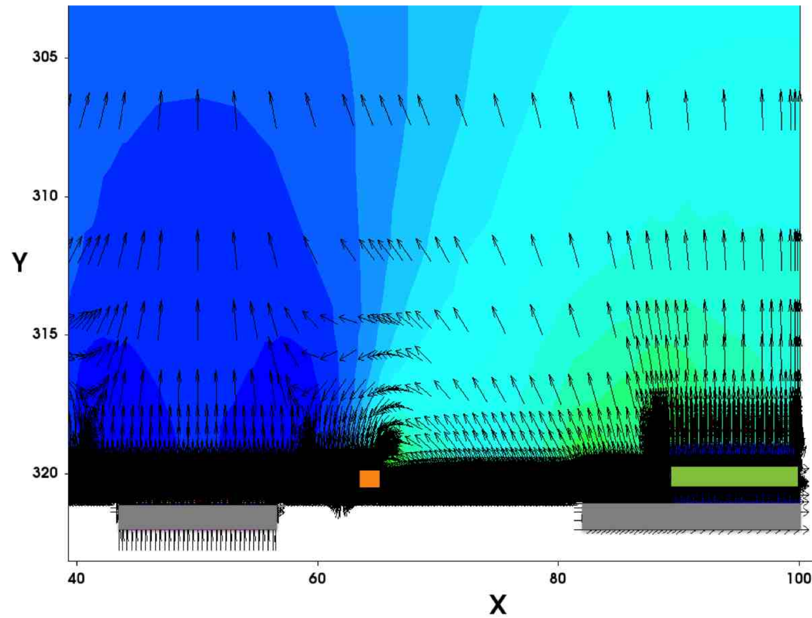

Figure 8.16.: Illustration of the electric field in a P type sensor with a routing line between the strips. The figure shows a section of the simulated device, with the strip (green = implant, grey = aluminium) at the right and the routing line (grey = aluminium) on the left. The orange square represents a p-stop strip isolation.

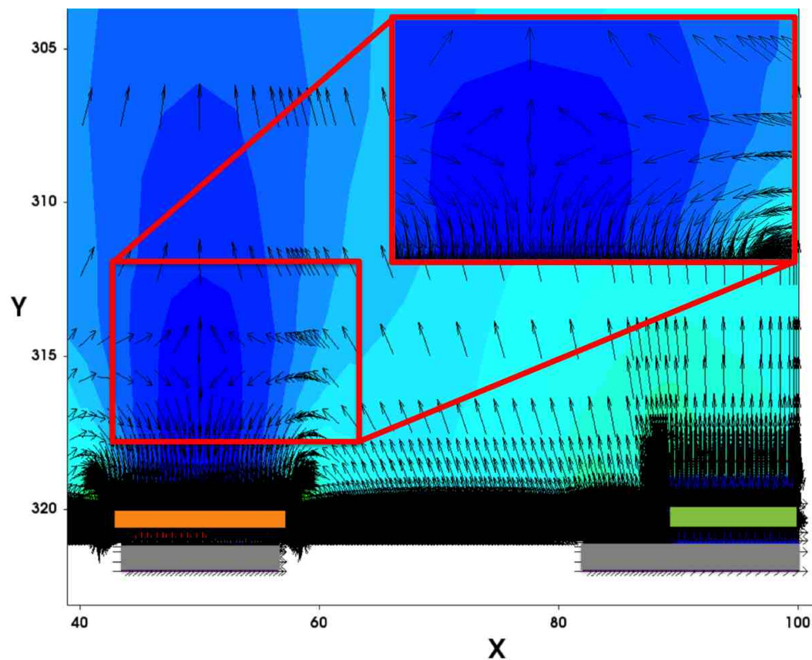

Figure 8.17.: Illustration of the electric field in a P type sensor with a routing line between the strips and a shielding structure of highly doped boron below the routing line. The figure shows a section of the simulated device, with the strip (green = implant, grey = aluminium) at the right and the routing line with shielding below (grey = aluminium, orange = shielding) on the left. The orange square represents a p-stop strip isolation. The red rectangle shows an enlarged view of the region where the electric field due to the shielding structure counteracts the electric field due to the aluminium routing line.

Simulations with various p-spray (boron) concentrations show that a heavy doped layer of p-spray fulfills these shielding requirement. Figure 8.18 plots the signal reduction on the far-strip against the peak concentration of the p-spray layer with a fixed oxide charge concentration of $1\times10^{11}\text{cm}^{-2}$. The simulation points out that the signal on the routing line vanishes for a peak concentration of $4\times10^{15}\text{cm}^{-3}$. Simultaneously to the decreasing signal on the far-strip the signal on both neighboring near-strips rises.

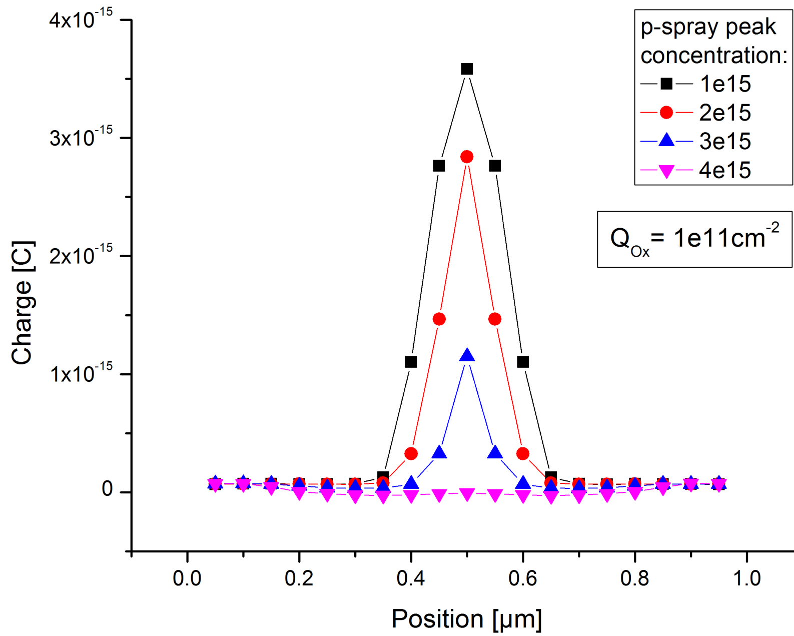

Figure 8.18.: Signal on the far-strip in dependence on the p-spray concentration, while hitting the near region on a FZ320Y sensor. The signal on the routing line drops with increasing peak concentration of the p-spray layer, but the electric field at the intersection of the n^+-implant and the p-spray rises, having a negative effect on the breakdown voltage (see figure 8.19).

Increasing the concentration of the p-spray dose has also an impact on several other important sensor parameters. A high p-spray concentration leads to high electric fields especially at the intersection of the n^+-implant and the p-spray and thus reduces the breakdown voltage. Figure 8.19 shows a comparison of the electric field strength between two p-spray devices at doses of $3\times10^{15}\text{cm}^{-3}$ and $4\times10^{15}\text{cm}^{-3}$ and a p-common structure at a dose of $2\times10^{16}\text{cm}^{-3}$, 100 μm. In both devices the electric field is highest at the edges of the boron implanted layer / structure. The electric field for the p-spray device is almost double the value of the p-common device.

Another sensor parameter that is affected by the p-spray peak concentration is the inter-strip capacitance C_{int} which contributes to the capacitive load at the input of the amplifier and thus on the electronics noise of a sensor module. Increasing the p-spray peak concentration, as shown in [Pie06], leads to growing C_{int} values. Starting with a p-spray peak concentration of $4\times10^{16}\text{cm}^{-3}$ and 0.7 pF/cm, C_{int} increases to 0.9 pF/cm by raising the p-spray peak concentration to $12\times10^{16}\text{cm}^{-3}$.

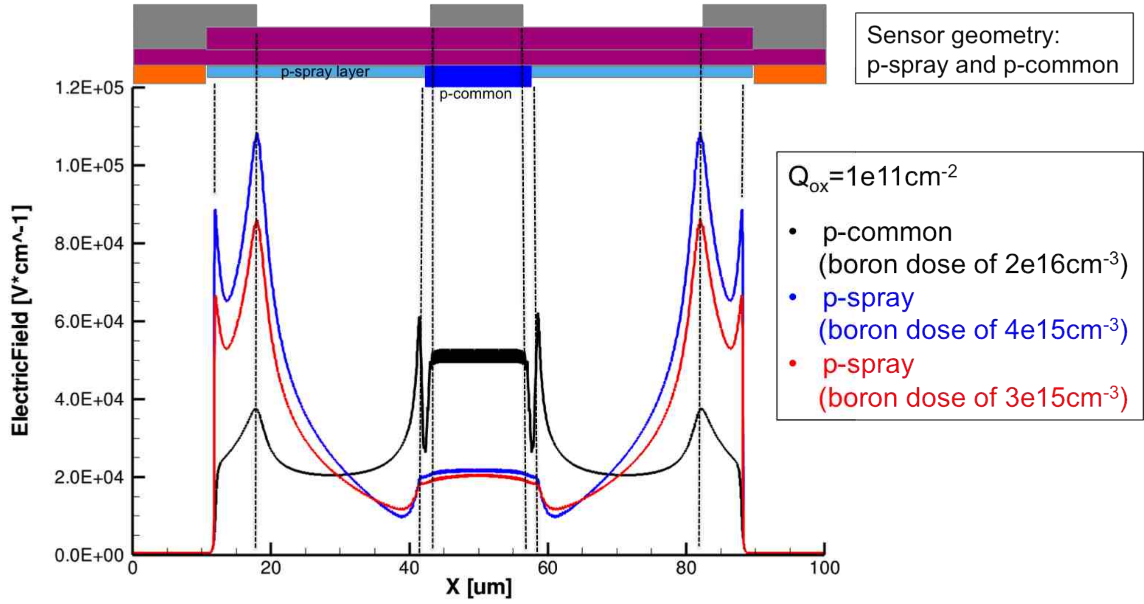

Figure 8.19.: Comparison of the electric field strength of two p-spray devices (figure 8.14) and a device with p-common structure (figure 8.20), 100 μm below the oxide layer in the silicon. Increasing the boron concentration in the p-spray layer from $3 \times 10^{15}\text{cm}^{-3}$ to $4 \times 10^{15}\text{cm}^{-3}$ leads to a higher electric field at the intersection of the n^{+}-implant and the p-spray. For the p-common structure even at a much higher boron concentration of $2 \times 10^{16}\text{cm}^{-3}$ the electric field is only half the value as for the p-spray devices.

The solution for the reduction of the signal coupling on the FZ320Y can be adapted to the P and N type sensors by putting a layer of highly doped boron (FZ320P) or phosphorus (FZ320N) beneath the routing line.
In order to improve the functionality and to get rid of the signal coupling on the FZ320P in the simulation a p-common structure has been put below the routing line to shield it, see figure 8.20.

The p-common structure has 2 μm overhang with respect to the aluminium routing line. It replaces the p-stops used to guarantee the implant strip isolation and makes sure that the generated charges do not couple to the routing line. In the signal simulation shown in figure 8.21 the boron concentration of the p-common structure has a peak concentration of $2 \times 10^{16}\text{cm}^{-3}$. The signal coupling to the routing line of the far-strip is vanished, compared to the signal coupling for the p-stop version, where the signal on the far-strip exceeds the signal on the near-strip.

The improvement of putting a floating, highly doped p-common layer, with a boron dose of $2 \times 10^{16}\text{cm}^{-3}$ and an overhang of 2 μm with respect to the routing line, below the routing line of the far-strip of a FZ320P sensor is shown in the simulation and the functionality of the sensor is established. The same procedure works also for the FZ320N sensor using a highly doped n-common structure.

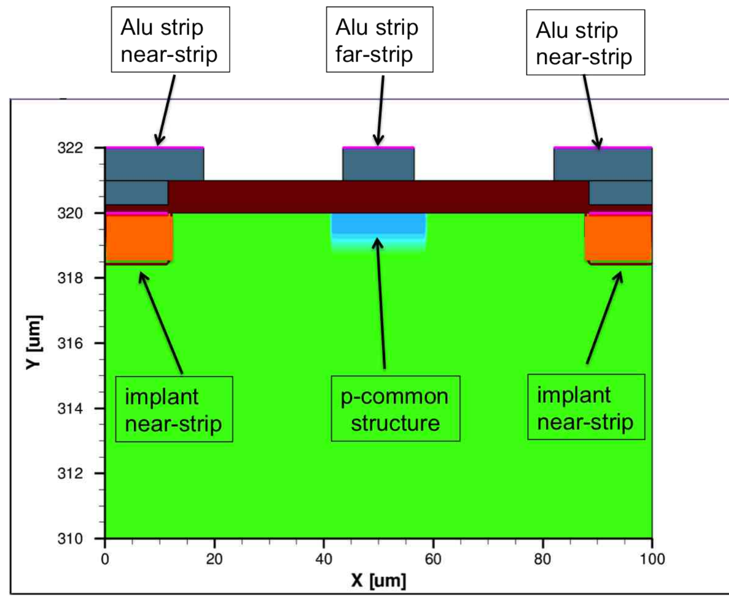

Figure 8.20.: Overview of the improved sensor design with a p-common structure below the aluminium routing line of the far-strip in a p-bulk device.

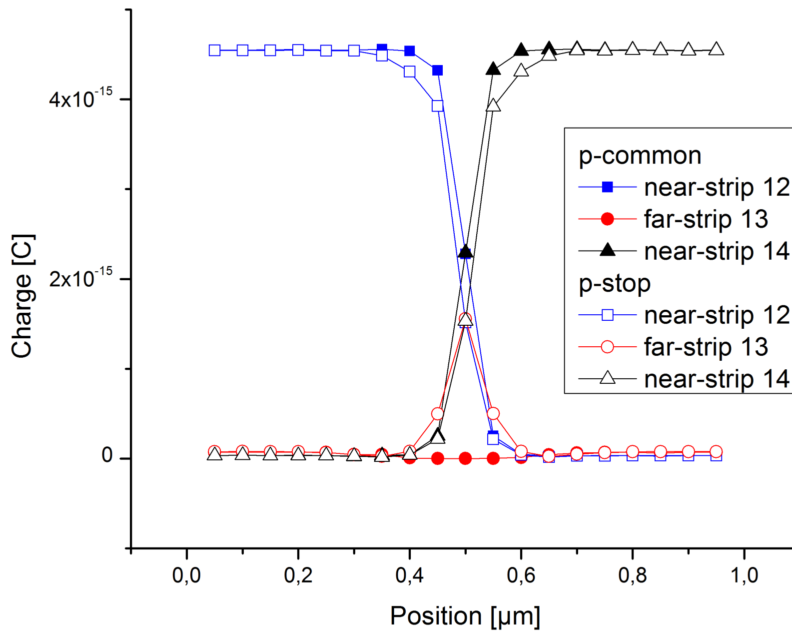

Figure 8.21.: Outcome of the improvement of the sensor design in a p-bulk using a p-common structure. Putting an isolation layer of highly doped boron below the aluminium routing line of the far-strip reduces the signal coupling to the far-strip to almost zero. Without these layer, the sensor with the p-stop shows almost equal signals on the near-strips and far-strips.

8.1.4. Sensor Production with ITE Warsaw

While investigating the FOSTER sensors produced by HPK, we got the opportunity to produce a reworked FOSTER design, using the p-common shielding layer (figure 8.20), with ITE Warsaw. The sensor is p-type with p-stop strip isolation and has a size of about 25.6 mm×5.9 mm and a thickness of 300 μm. First measurements in the probe-station showed that the produced sensors had very low inter-strip resistances in the order of 10 kΩ, typical values for the inters-trip resistance are larger than 10 GΩ. The sensor depletes at about 60 V and has a total current of about 1 μA/cm^2 at 100V which is very high compared to the few nA/cm^2 of the previously analyzed sensors. Figure 8.22 shows the qualification measurements.

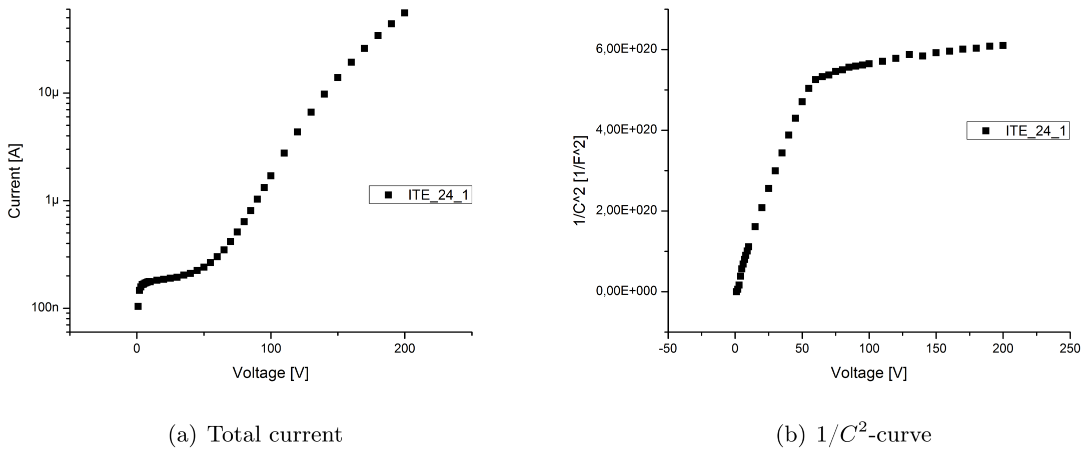

(a) Total current

(b) $1/C^2$-curve

Figure 8.22.: Qualification measurements on the FOSTER sensor produced by ITE. The sensor has a high current of 1 μA/cm^2 at 100V and depletes at about 60V.

The laser scan measurements done on the FZ320 FOSTERs have also been done on the ITE_24_1 FOSTER. Far-strips have odd numbers and near-strips have even numbers. Figure 8.23 shows a laser scan in the far region. First, there is no signal on the near-strip 154, but the far-strips detect a signal, even if the laser is hundreds of μm away. The center of far-strip 153 is at position 330μm and the center of far-strip 155 is at position 230μm. Even if the laser is at position 100μm, both far-strips detect a comparable signal of 60 respectively 85 ADC. This strong signal sharing among the strips makes the sensor useless for standard operation. Responsible for this effect is the very low inter-strip resistance, which does not offer a sufficient strip isolation on this p-type sensor.

As we are mainly interested in the functionality of the reworked design and thus the p-common structure beneath the routing line of the far-strip, the laser scan measurements have also been done in the near region. Figure 8.24 shows the signals for the near-strips 154 and 156 and the far-strip 155. The strong signal sharing among the near-strips over hundreds of μm is also seen, but the signal on the far-strip is clearly lower, being only about a quarter of the signal on the near-strips. It seems that the p-common layer beneath the aluminium readout line of the far-strips is sufficient to reduce the signal coupling to the far-strip.

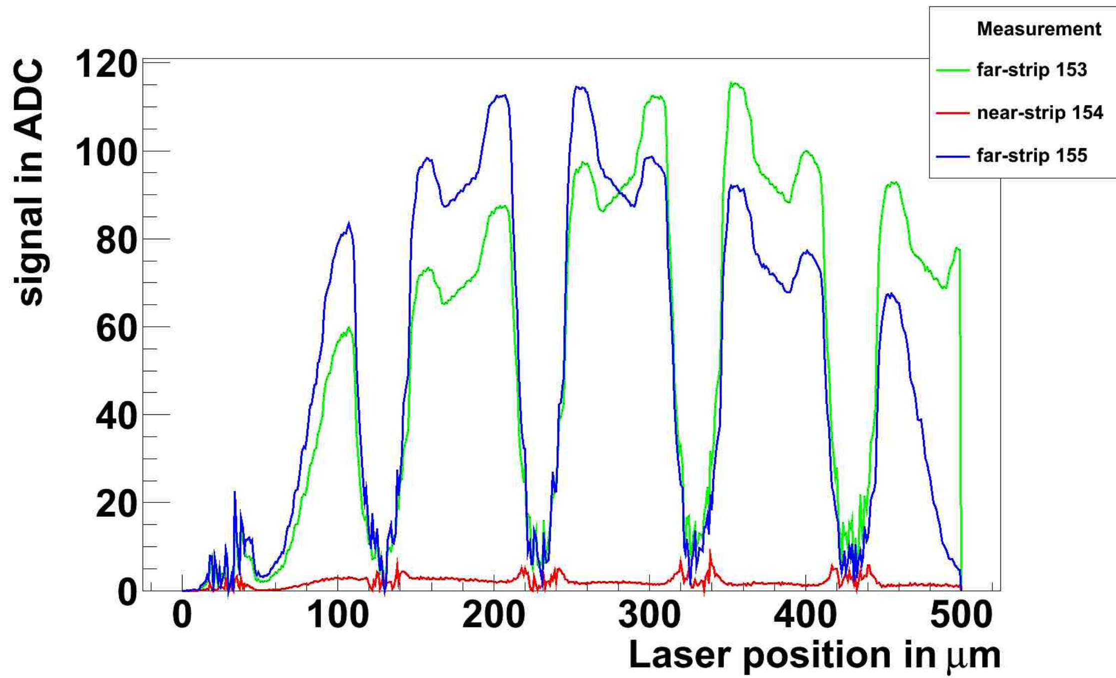

Figure 8.23.: Laser scan in the far region of the revised FOSTER. There is no signal on the near-strip, but a strong signal sharing among the far-strips due to the insufficient strip isolation of the p-type FOSTER.

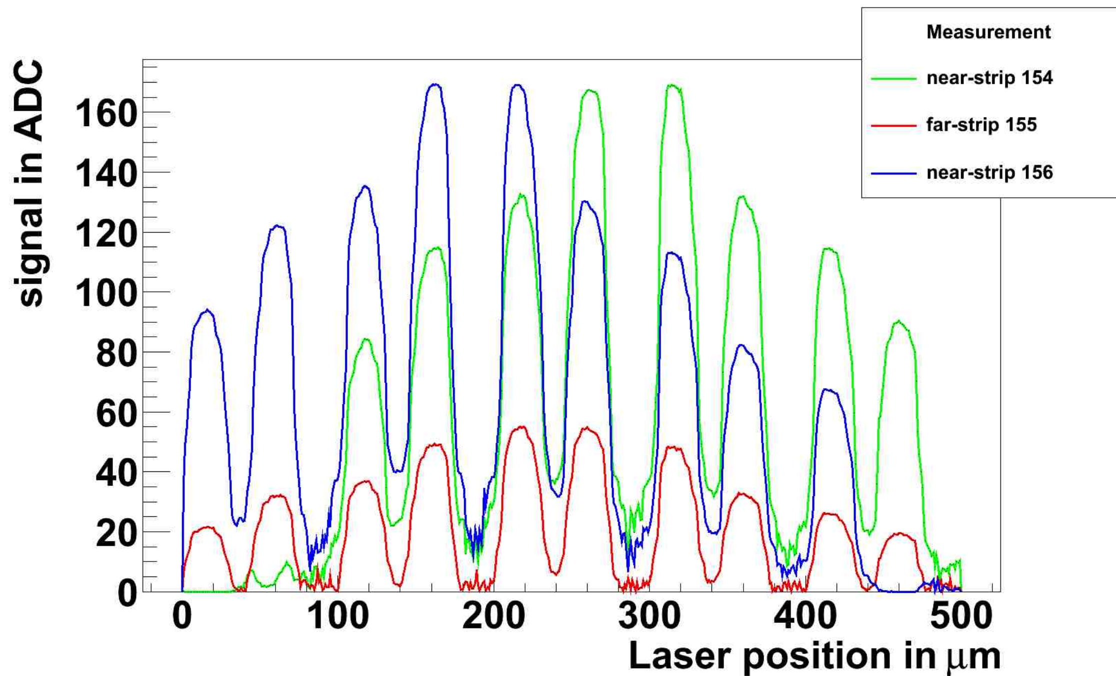

Figure 8.24.: Laser scan in the near region of the revised FOSTER. The near-strips have also a strong signal sharing, comparable to the sharing in the far region, but the signal coupling to the far-strips is clearly lower.

Figure 8.25 shows a comparison of the laser scan measurement in the near region on the HPK FOSTER and the ITE FOSTER. The HPK FOSTER showed a coupling to the aluminum readout strip of the far-strip that led to a wrong hit assignment 8.25(a). The idea to reduce this signal coupling by putting a shielding p-common beneath the aluminium readout strip has been realized in the ITE FOSTER. This sensor has a very low inter-strip resistance and thus an insufficient strip isolation leading to a strong signal sharing between neighboring strips, but the signal to the aluminium readout strip of the far-strips is clearly reduced, see figure 8.25(b).

Another point that indicates the functionality of the shielding p-common layer, is the position of the peak signal value for the far-strip. While for the HPK FOSTER the peak signal was around the aluminium routing line of the far-strip, the peak signal for the ITE FOSTER is shifted and fits exactly the signal shape of the near-strips. This indicated that the signal on the far-strip has the same origin as the signal on the neighboring near-strips, due to the bad inter-strip isolation.

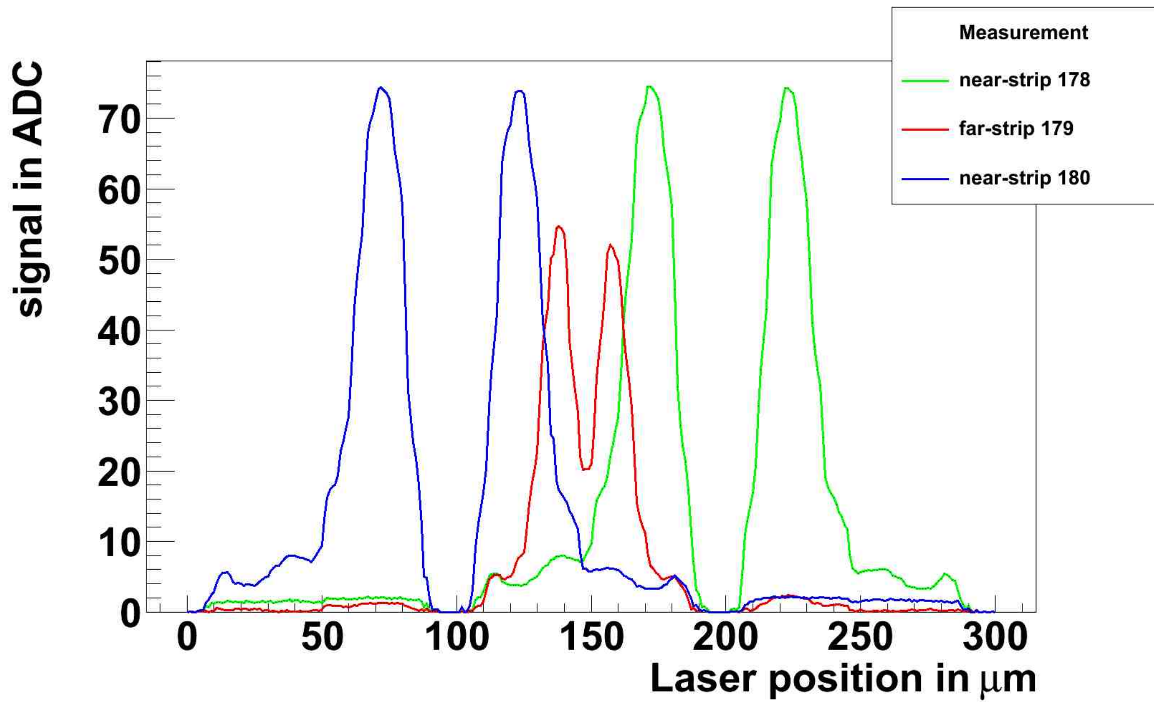

(a) HPK FOSTER

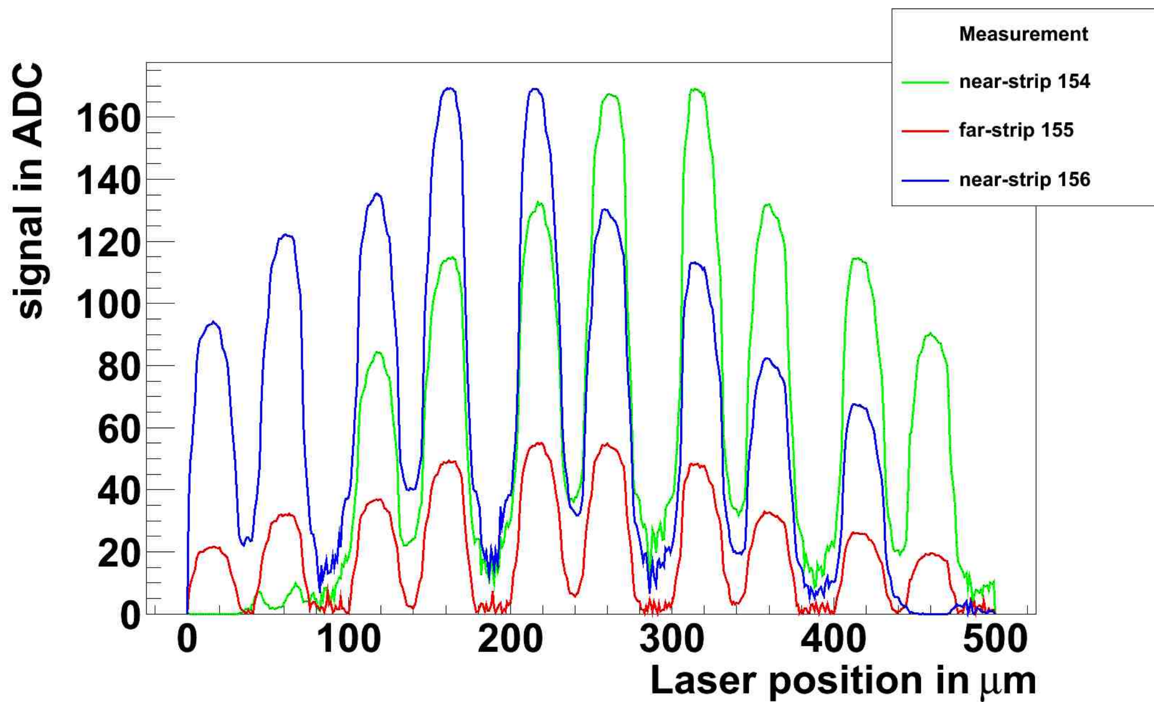

(b) ITE FOSTER

Figure 8.25.: Comparison of the signal coupling to the aluminium readouts strip of the far-strip on the (a) HPK FOSTER and on the (b) ITE FOSTER. Although the ITE FOSTER has poor strip isolation, leading to signal sharing among neighboring strips, the effect of the shielding p-common layer can be seen. The signal on the far-strip of the ITE FOSTER is lower than the signal on the far-strip of the HPK FOSTER.

8.2. Conclusion on new sensor design

The new sensor design with short strips and readout at the edges (FOSTER) has been produced within the campaign of the CEC. The qualification measurements showed homogeneous strip parameters within the requirements indicating a good production quality. The charge collection is in the expected range and the sensors are operable. A problem concerning the signal coupling to the routing line has been found in the near region. Induced signals in this region, where only near-strips should detect the signal, are also detected on far-strips, which are for example for the FZ320P, in 26% identified as seed strips. This leads to a wrong hit assignment in the far region and prevents the proper sensor functionality.

The signal coupling to the routing lines has been investigated by measurements and simulations. Reason for the signal coupling to the routing line is the electric field, which is attracted by the routing line. A suitable solution to shield the routing line and counteract the electric field has been found. Putting a floating, highly doped layer of boron (P-type and Y-type) or phosphorus (N-type) beneath the aluminium routing line in the near region prevents the signal coupling to the far-strip. A new sensor production run, including reworked versions of these sensors with a shielding structure, has been done with ITE Warsaw and started with CNM Barcelona in order to confirm the simulation results. The sensors from ITE Warsaw have already been delivered and tested. These first prototypes give a hint of the working shielding p-common layer, but do not allow to draw final conclusions. A second iteration is already planned.

If the improvements establish the full sensor functionality, the FOSTER would be a promising candidate for the CMS Tracker upgrade, as it fulfills all requirements of the current sensor baseline [Abb11] and could increase the granularity by a factor of two while keeping the dimensions of a sensor covering a 6 inch wafer.

Summary

The work in this thesis has been done within the CMS tracker upgrade collaboration and the central european consortium, in order to identify a sensor baseline for the CMS tracker upgrade in 2022. The main issue related to the upgrade is the higher luminosity and thus the increased radiation damage to the detectors. For CMS a new tracker is needed, built up of suitable silicon material, guaranteeing the sensors to perform well throughout the HL-LHC life time.
As main part of this work, silicon strip sensors of various thicknesses, based on different production techniques, isolation and dopings, fabricated by a single manufacturer have been investigated. The sensors have been irradiated with neutrons and protons, to expected fluences of the CMS tracker during the high luminosity phase. After each irradiation step, the sensors have been electrically characterized in different test stations.
The qualification of the non-irradiated sensors showed a good production quality. The measured strip parameters have been homogeneous across the sensors and all parameters were within the desired ranges.
After irradiation the changes of the sensor properties have been investigated and compared to former studies to find the most suitable radiation hard silicon sensors for the high luminosity phase. The full depletion voltage V_{fd} increases, which leads to a loss in the charge collection, if the sensors can not be fully depleted. Especially the 300 µm sensors do not deplete after an irradiation to $7 \times 10^{14} n_{eq} cm^{-2}$, while the 200 µm sensors still deplete below 600 V. The rise of the leakage current with fluence has been compared to former irradiation studies on diodes, and it turned out, that the slope for sensors is slightly higher (16%) and thus also the power consumption of a detector system made up of these sensors.
The sensor strip parameters coupling capacitance and inter-strip capacitance have not been affected by radiation. The increase of the bias resistors by 15% is even beneficial with respect to the noise contribution. The only parameter that has dramatically changed is the inter-strip resistance. R_{int} decreased by almost a factor of 1000 down to about 100 MΩcm, but is still sufficiently high. Even the two different isolation techniques for p-type sensors, p-stop and p-spray, guarantee a good strip isolation up to a fluence of $1.5 \times 10^{15} n_{eq} cm^{-2}$ and show no different sensor properties.
A decrease in the charge collection and the signal-to-noise ratio has been measured for all sensor types, see section 7.2.8. At a fluence of $1.5 \times 10^{15} n_{eq} cm^{-2}$ there is no difference in the electron signal or the signal-to-noise ratio of the 200 µm and 300 µm sensors, between the different materials (deep diffusion float zone, thinned float zone and magnetic Czochralski) or between irradiations with neutrons or protons.
The influence of the annealing on sensor properties has been investigated in section 7.3. Long annealing times lead to a strong decrease in the charge collection and the signal-to-noise ratio of the

thick n-bulk sensor. Nevertheless, 300 μm p-bulk sensors work sufficient, with a signal-to-noise ratio of 10 (12) at a fluence of $1.5 \times 10^{15} n_{eq} cm^{-2}$, at an operating voltage of 600 V (900 V) and annealing times of about 200 days at 21°C. Thicker sensors show higher signals from the beginning and the p-bulk material is comparable to thin sensors up to $1.5 \times 10^{15} n_{eq} cm^{-2}$, if the material budget does not matter. Thin sensors show no difference between 200 μm n-type and p-type sensors and between sensors with p-stop or p-spray isolation technique and reduce the material budget.
The campaign is not finished yet, further irradiations to higher fluences, corresponding to a radial distance to the interaction point of R=15 cm and R=10 cm are ongoing. Additional sensors with a thickness of 100 μm will also be investigated.
As besides the most suitable material, also aspects like the costs of production and the manageability have to be considered, a final conclusion on the future sensor baseline can not be drawn.
In addition to the material studies, also new layouts of the strip sensors have been investigated. A new sensor with a fourfold segmentation (two near regions at the sensor edge and two far regions in the sensor center) and the readout connection in the near regions at the edge (FOSTER) has been designed. As one plans to increase the sensor granularity by a factor of two to cope with the increased track density, this sensor would even increase the granularity by a factor of four, compared to the current sensors which have strips extending over the entire length of the 10×10 cm^2 sensor. The analysis of this sensor showed very homogeneous strip parameters within the requirements and confirmed the good production quality, already seen on the standard sensors. A signal coupling to the routing line has been found in the near region, as the aluminum routing lines of the far-strips showed higher signals than the near-strips. This leads to a wrong hit assignment and to a non-proper sensor functionality.
The coupling has been investigated by measurements and simulations. The aluminium routing line of the far-strip attracts the electric field and thus the charges close to the routing line. By putting a floating, highly doped layer of boron (p-type) or phosphorus (n-type) beneath the aluminium routing line, a counteracting electric field could shield the routing line.
Hence, a new sensor production run, including reworked versions of this sensor with a shielding structure has been done with ITE Warsaw to confirm the simulation results. The sensors from ITE Warsaw have been tested and give a hint on the functioning of the p-common shielding structure, but do not allow to draw final conclusions, as the boron doping concentration of the p-stop is not sufficient. A second iteration is already planned.
If the improvements establish the full sensor functionality, this sensor is an alternative candidate for the CMS Tracker upgrade, as it fulfills all requirements of the current sensor baseline and increases the granularity by a factor of two, keeping the dimensions of a sensor covering a 6 inch wafer.

Appendix A.

Technical Drawings

A.1. Jig Design

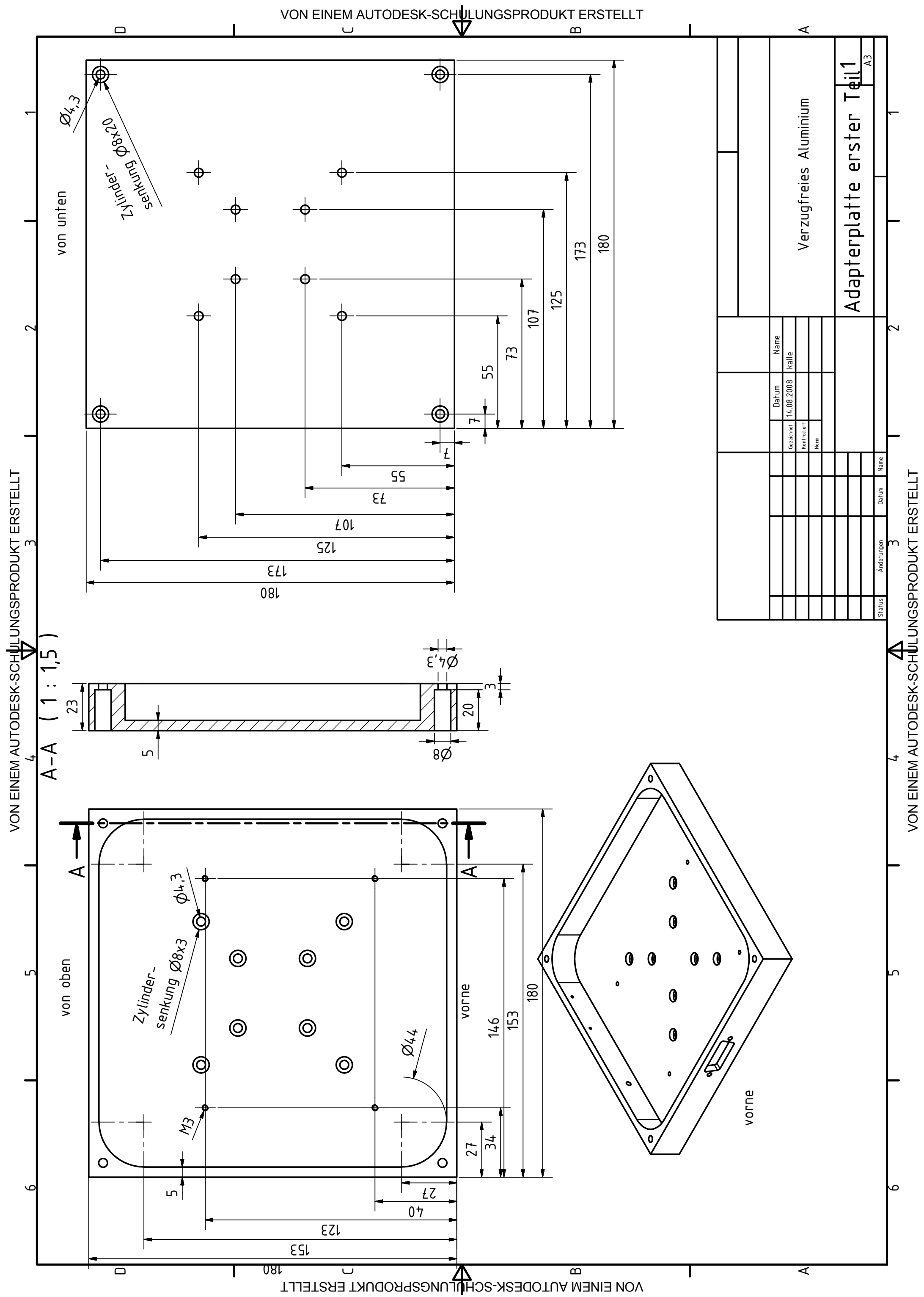

Figure A.1.: Connector plate - part I

Figure A.2.: Connector plate - part II

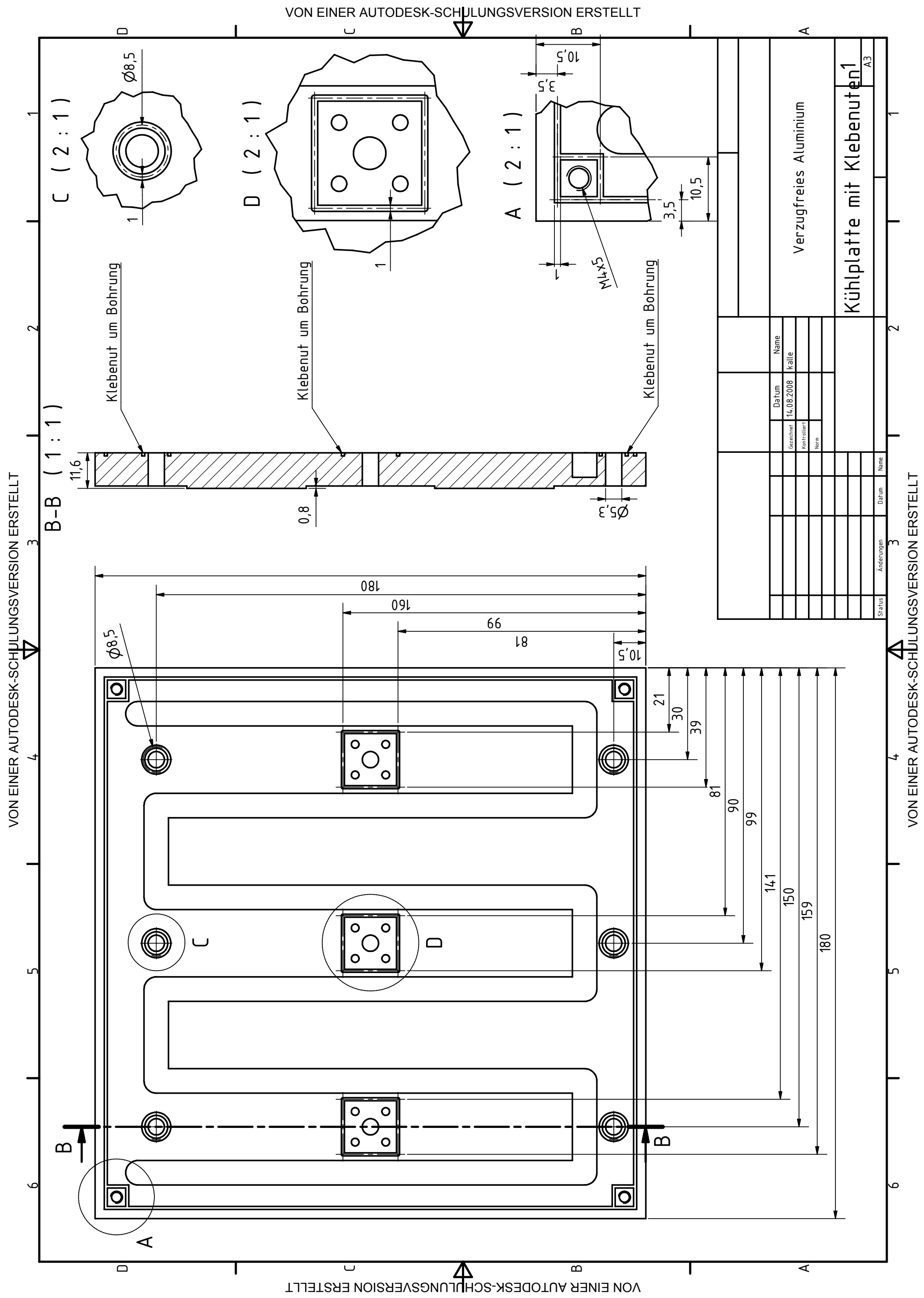

Figure A.3.: Cooling plate with glue flutes.

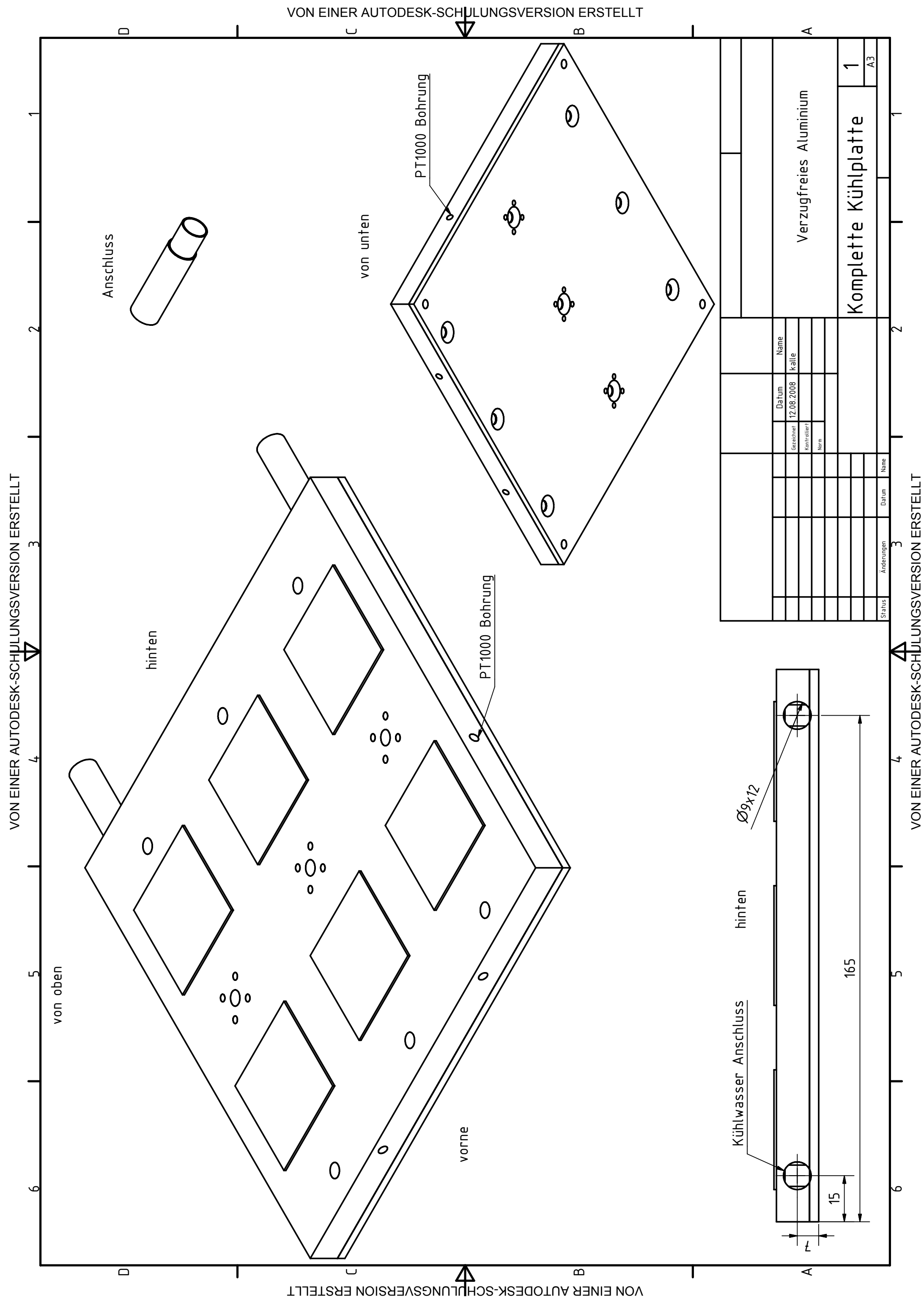

Figure A.4.: Complete cooling plate with connectors.

Figure A.5.: Overview of the vacuum plate and the pipes.

Appendix B.

ALiBaVa

B.1. Charge Calibration

The calibration of the charge has been done with the sensor FZ320N_08_Bstd_2. The active thickness of this sensor has been calculated to 304 µm, using the C_{end} values of the CV curves of the corresponding diodes and the plate condensator equation.
Taking the Bethe-Bloch formula 2.23, one can calculate the number of electron-hole pairs created by a MIP in silicon. The energy to create one electron-hole pair is 3.6eV. Due to the high density of silicon, the average energy loss of about $390\frac{eV}{\mu m}$ for a MIP results in $108\frac{e-h-pairs}{\mu m}$. As for a Landau distribution not the mean, but the most probably value (MPV) is of interest, the charge created in 300 µm silicon is $108\frac{e-h-pairs}{\mu m} \cdot 300\mu m \cdot 0.7$ resulting in about 22500 electron-hole pairs [Har08]. Therefor a transversing particle is estimated to generate about 75 electrons per µm.
So the non irradiated FZ320N_08_Bstd_2 sensor generates a signal of about 22800 e^-.

To calibrate the several daughterboards, the FZ320N_08_Bstd_2 sensor has been measured at different temperatures and voltages. The resulting signal in ADC has been plotted over the daughterboard temperature. The figures B.1, B.2, B.3 and B.4 show the linear fits of the calibration and table B.1 gives an overview. Using the FZ320N_08_Bstd_2, all daughterboards have been calibrated to 22800 e^-.

Table B.1.: Overview of the daughterboard calibration.

Chip	Y-Axis (error)	Slope (error)
10	131.41 (±2.53)	-1.15 (±0.14)
11	126.9 (±1.98)	-1.05 (±0.11)
30	135.16 (±3.83)	-0.99 (±0.21)
31	128.23 (±2.46)	-1.17 (±0.13)
40	148.49 (±5.91)	-1.4 (±0.27)
41	114.27 (±3.54)	-1.01 (±0.16)
50	135.25 (±4.41)	-1.25 (±0.21)
51	127.83 (±2.6)	-1.65 (±0.12)

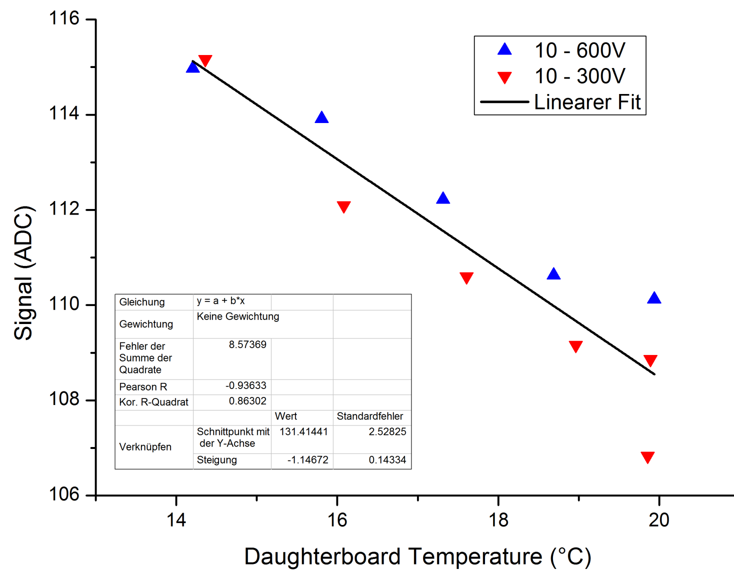

(a) Board 1 Chip 1

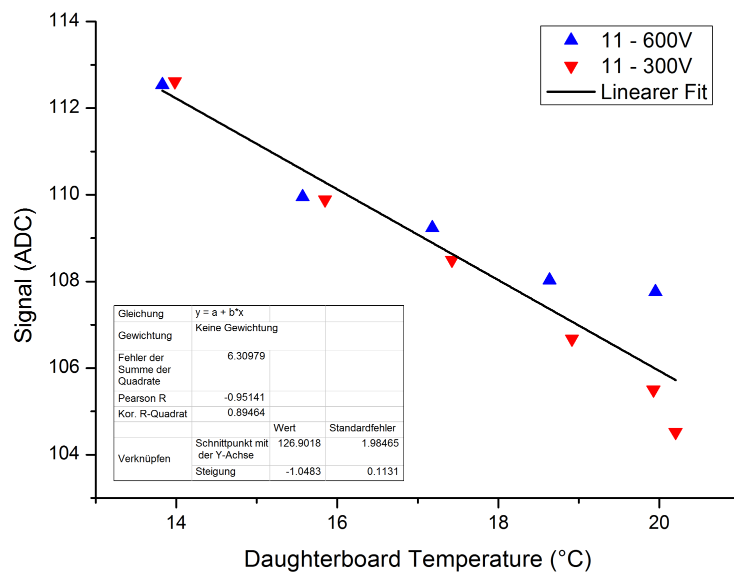

(b) Board 1 Chip 2

Figure B.1.: Calibration of daughterboard 1.

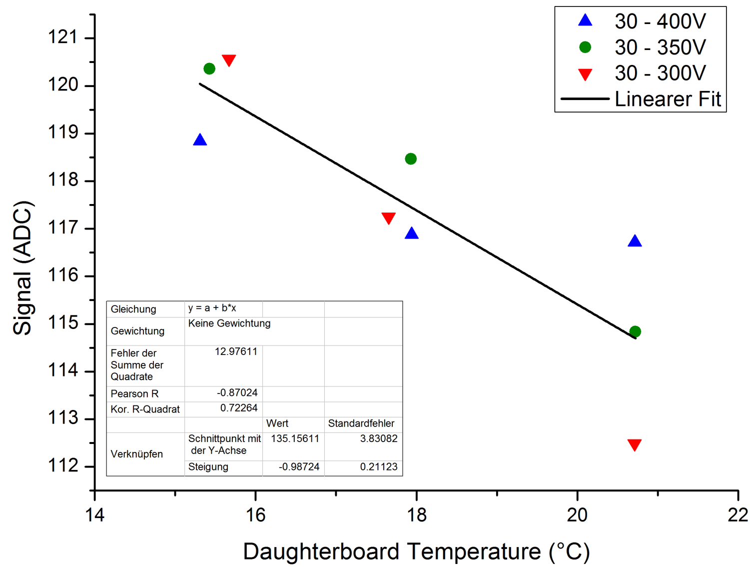

(a) Board 3 Chip 1

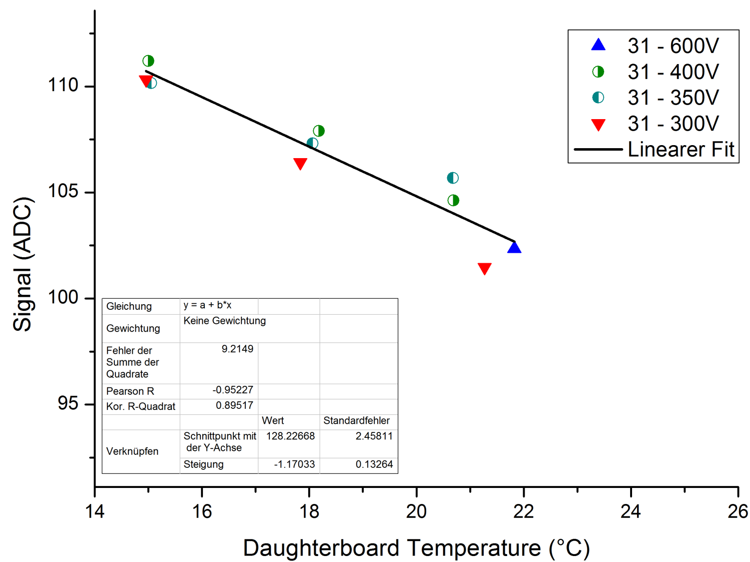

(b) Board 3 Chip 2

Figure B.2.: Calibration of daughterboard 3.

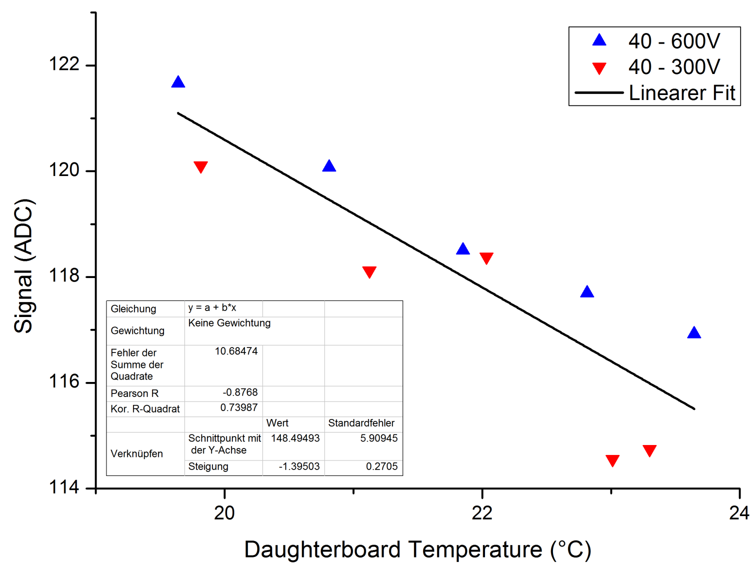

(a) Board 4 Chip 1

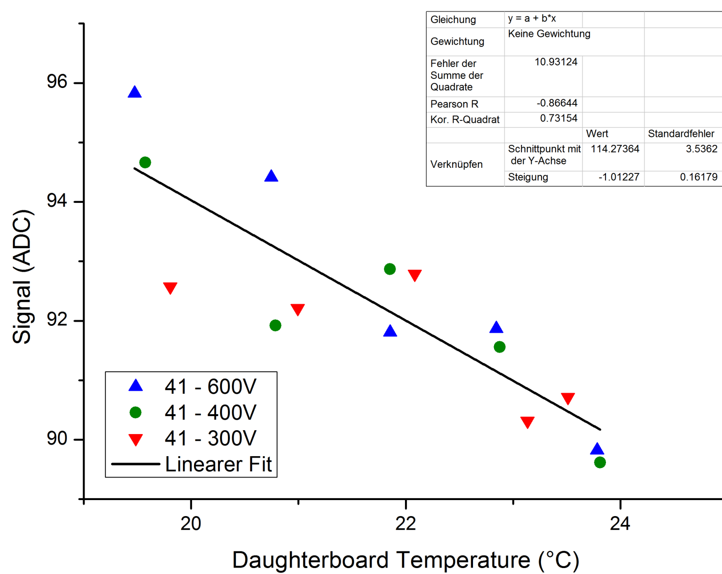

(b) Board 4 Chip 2

Figure B.3.: Calibration of daughterboard 4.

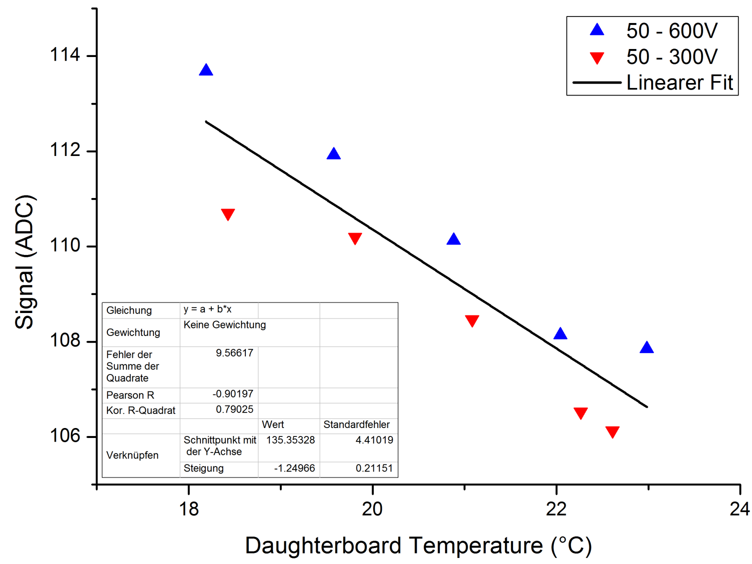

(a) Board 5 Chip 1

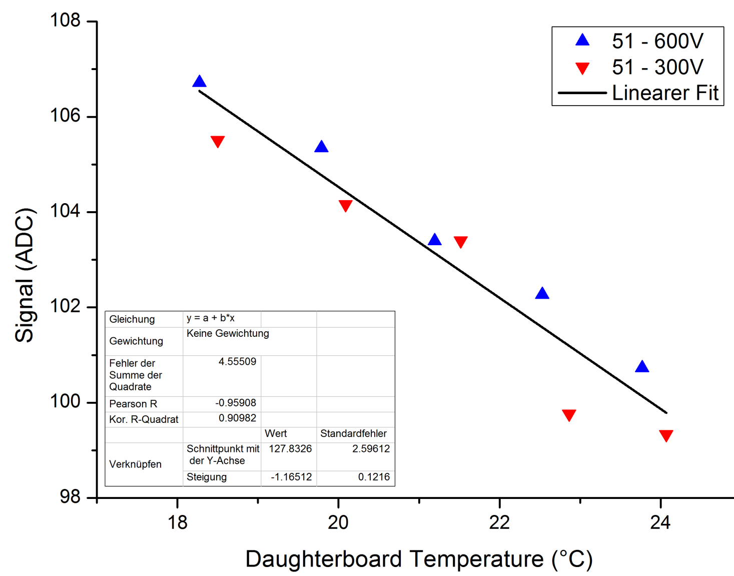

(b) Board 5 Chip 2

Figure B.4.: Calibration of daughterboard 5.

Appendix C.

Measurements

C.1. FOSTER

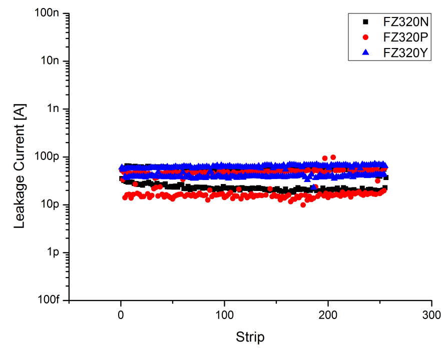

(a) Strip Leakage Current

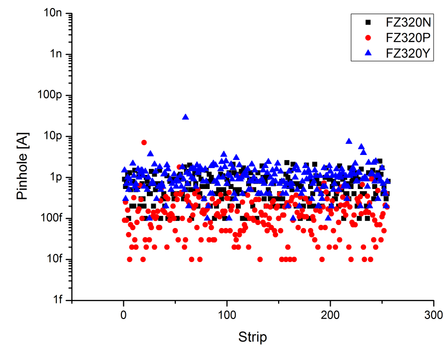

(b) Current over the Dielectric

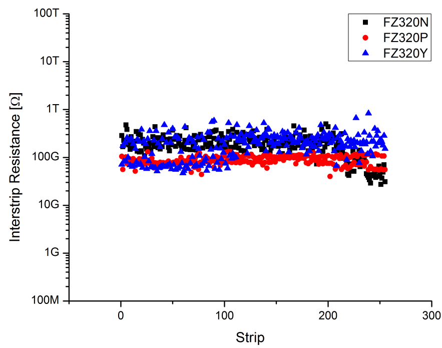

(c) Inter-strip Resistance

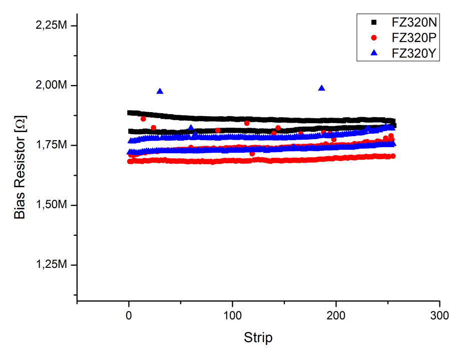

(d) Bias Resistors

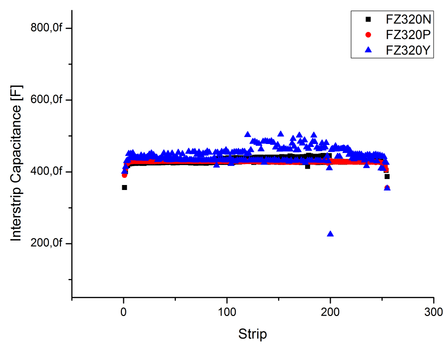

(e) Inter-strip Capacitance

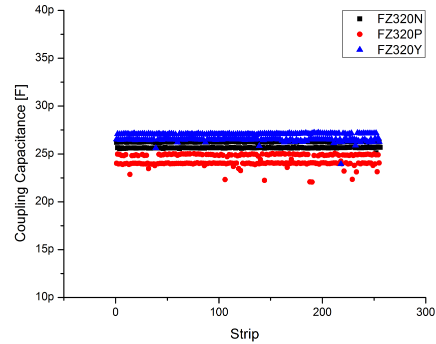

(f) Coupling Capacitance

Figure C.1.: Strip measurements on three FOSTERs. (a) The strip leakage currents are homogenous showing a slightly higher current for the n and y FOSTER. (b) The current over the dielectric in the range of a few pA implies no pinholes. (c) The inter-strip resistance is in the order of several GΩ and (d) the bias resistors are homogeneous within the demanded range. (e) The homogenous inter-strip capacitance and (f) coupling capacitance with small difference for near- and far-strips.

List of Figures

1.1. LHC overview 2
1.2. Overview of the LHC accelerator complex 3
1.3. Expanded view of the CMS detector 4
1.4. CMS tracking 5
1.5. CMS tracker cross-section 6
1.6. LHC upgrade plans 7
1.7. Track density 8
1.8. Signal reduction 9
1.9. Transverse momentum spectrum 10
1.10. Concept of a p_T-module 10
1.11. 3D model of a 2S module 11

2.1. Silicon atoms representation 13
2.2. Energy levels of silicon atoms 15
2.3. Illustration of the band structure 15
2.4. Doped silicon 17
2.5. Illustration of doped semiconductors 22
2.6. pn-junction in thermal equilibrium 23
2.7. Illustration of a pn-junction 24
2.8. MOS structure 26
2.9. Cross section of a silicon strip sensor 28
2.10. 3D sketch of a silicon strip sensor 29
2.11. Isolation techniques for p-type silicon strip sensors 30

3.1. Defects in the silicon lattice 35
3.2. Displacement damage function 36
3.3. Defect energy levels 37
3.4. Fluence dependent leakage current 39
3.5. Current related damage rate 40
3.6. Evolution of full depletion voltage 41
3.7. Influence of carbon and oxygen on V_{dep} and $|N_{eff}|$ 42
3.8. Comparison of V_{dep} and $|N_{eff}|$ for standard FZ and oxygen enriched FZ 43

4.1. Compact Cyclotron Karlsruhe 46
4.2. Irradiation box 47

4.3. TRIGA-Mark-III reactor in Ljubljana 48
4.4. 3D model of the cold jig 50
4.5. GFK and Peltier elements 50
4.6. Picture of the cold jig 51
4.7. Probe-stations in Karlsruhe 52
4.8. ALiBaVa setup in Karlsruhe 54
4.9. Sketch of the 3D model of the ALiBaVa setup 55
4.10. ALiBaVa test board 55

5.1. Wafer layout 62
5.2. Measurement and irradiation sequence 63
5.3. HL-LHC fluences 64
5.4. n-type diode 65
5.5. Metal grid on wafer back side 66
5.6. Complete testing sequence 67
5.7. Lorentz angle measurement scheme 67
5.8. Standard strip sensors 68
5.9. Picture of the MSSD 69
5.10. MSSD module 70
5.11. Picture of the MPix 70
5.12. Pitcture of the Baby_PA 71
5.13. Zoom in the pitch adapter region 71
5.14. Picture of the FOSTER 72
5.15. Schematic view of the FOSTER 73

6.1. Production techniques of single crystal ingots 76
6.2. Silicon rods and wafers 77
6.3. Diffusion process 79
6.4. Channeling effect 79
6.5. Photolithography 80
6.6. Etching - selectivity 81
6.7. Etching - isotropic - anisotropic 81
6.8. plain wafer 82
6.9. Processing - step 1 82
6.10. Processing - step 2 83
6.11. Processing - step 3 83
6.12. Processing - step 4 83
6.13. Processing - step 5 84
6.14. Processing - step 6 84
6.15. Processing - step 7 84
6.16. C++ macro for the LayoutEditor 86

6.17. Complete GDS file . . . 87
6.19. n+ mask . . . 88
6.21. boron mask . . . 89
6.23. aluminium mask . . . 89
6.25. polysilicon mask . . . 89
6.27. polysilicon heads . . . 89
6.29. metal vias . . . 90
6.31. passivation mask . . . 90
6.32. Sensor periphery . . . 92
6.33. Bias and guard ring . . . 92
6.34. Sensor strip region . . . 93
6.35. FOSTER schematic view . . . 94
6.36. FOSTER left corner . . . 95
6.37. FOSTER near-far intersection . . . 95
6.38. near-strip and far-strip geometry . . . 96
6.39. Baby_PA prototype . . . 97
6.40. Zoom in pitch adapter region . . . 98
6.41. Different integrated pitch adapter geometries . . . 99
6.42. Pitch adapter - MPix to extension . . . 99
6.43. Pitch adapter - MPix to TOB_Hybrid . . . 100

7.1. Deep diffusion process . . . 102
7.2. Extraction of the full depletion voltage from a CV curve . . . 103
7.3. Evolution of the $\frac{1}{C^2}$ plot . . . 103
7.4. CV curves in dependence of the sensor thickness . . . 104
7.5. Evolution of V_{fd} with fluence . . . 106
7.6. Total leakage current for the non irradiated n-type Baby_Std sensors . . . 107
7.7. total leakage current for various P type and Y type sensors . . . 108
7.8. DLTS spectra . . . 108
7.9. Leakage current for different diodes . . . 109
7.10. Leakage current for FZ320N and FZ200N scaled to volume . . . 110
7.11. Leakage current at a fluence of $1 \times 10^{15} n_{eq} cm^{-2}$ . . . 110
7.12. Scaled volume current versus fluence . . . 111
7.13. Strip leakage currents for non irradiated Baby_Std sensors . . . 112
7.14. Evolution of strip leakage currents with fluence . . . 113
7.15. Coupling Capacitances of non irradiated Baby_Std sensors . . . 114
7.16. Evolution of coupling capacitances . . . 115
7.17. Bias resistors of the non irradiated Baby_Std sensors . . . 116
7.18. Temperature dependence of the bias resistors . . . 117
7.19. Evolution of bias resistors under irradiation . . . 118
7.20. Inter-strip resistance of the non irradiated Baby_Std sensors . . . 119

7.21. Evolution of the inter-strip resistance . . . 119
7.22. Inter-strip capacitances of the non irradiated Baby_Std sensors . . . 120
7.23. Evolution of the inter-strip capacitance under irradiation . . . 121
7.24. Charge collection for non irradiated n-type Baby_Std sensors . . . 122
7.25. Evolution of charge collection . . . 124
7.26. Charge collection at $\Phi_{eq} = 1 \times 10^{15} cm^{-2}$ . . . 125
7.27. Evolution of charge collection efficiency . . . 126
7.28. Evolution of the signal-to-noise ratio . . . 127
7.29. Annealing of depletion voltage 7e14 . . . 128
7.30. Annealing of depletion voltage 7e14 . . . 129
7.31. Annealing of the leakage current . . . 130
7.32. Signal versus annealing time at $7 \times 10^{14} n_{eq} cm^{-2}$ . . . 131
7.33. Signal versus annealing time at $1.5 \times 10^{15} n_{eq} cm^{-2}$ . . . 132
7.34. Signal-to-Noise Ratio versus annealing time . . . 133
7.35. Cluster noise versus annealing time . . . 134

8.1. Picture of the FOSTER . . . 137
8.2. IV and CV on the FOSTER . . . 138
8.3. C_{int} measurements on the FOSTER . . . 140
8.4. Some selected strip measurements on the FOSTER . . . 140
8.5. Signal sharing on the FOSTER . . . 142
8.6. Signal scans on the different FOSTERs . . . 143
8.7. Charge collection in near and far region . . . 144
8.8. Charge collection versus CV curve . . . 145
8.9. Occurrence of seed strips in the different regions for the FZ320N . . . 146
8.10. Beam spot of a Sr90 source . . . 147
8.11. Occurrence of seed strips in the different regions for the FZ320P . . . 148
8.12. Occurrence of seed strips in the different regions for the FZ320Y . . . 149
8.13. Time profile of the measurements . . . 149
8.14. 2D model for the FOSTER simulation . . . 151
8.15. Comparison between measurement and simulation . . . 152
8.16. E-Field with routing line . . . 153
8.17. E-Field with routing line and shielding . . . 153
8.18. Signal in dependence of p-spray concentration . . . 154
8.19. Electric fields of p-spray and p-common device . . . 155
8.20. Improved FOSTER design . . . 156
8.21. P-common signal reduction . . . 156
8.22. ITE FOSTER qualification . . . 157
8.23. Laser scan in the far region . . . 158
8.24. Laser scan in the near region . . . 158
8.25. Comparison between ITE FOSTER and HPK FOSTER . . . 160

A.1. Connector plate - part I 166
A.2. Connector plate - part II 167
A.3. Cooling plate with glue flutes. 168
A.4. Complete cooling plate with connectors. 169
A.5. Overview of the vacuum plate and the pipes. 170

B.1. Calibration of daughterboard 1. 172
B.2. Calibration of daughterboard 3. 173
B.3. Calibration of daughterboard 4. 174
B.4. Calibration of daughterboard 5. 175

C.1. FOSTER - characterization 178

List of Tables

2.1. Properties of silicon [Har08]. 14

3.1. Interaction of radiation 34
3.2. Annealing parameters from Moll 39
3.3. Beneficial and reverse annealing 41

5.1. HKP wafer submission 61
5.2. Overview of the fluences 63
5.3. Overview of the annealing steps. 63
5.4. Overview of the different regions of the MSSD. All length in μm. 68
5.5. Overview of the different regions of the MPix. All length in μm. 69

6.1. Overview of the layers and their function 88
6.2. Overview of the geometrical specifications of the sensors 100

7.1. Full depletion voltages for non irradiated Baby_Std sensors 104
7.2. Calculated sensor thicknesses 105
7.3. Calculated readout oxide thicknesses 115

8.1. FOSTER characterization 139
8.2. Simulation parameters 150

B.1. Daughterboard calibration 171

Bibliography

[A+01] S. Albergo et al. Optimization of the silicon sensors for the cms tracker. *Nuclear Instruments and Methods in Physics Research Section A: Accelerators, Spectrometers, Detectors and Associated Equipment*, 466(2):300 – 307, 2001. 4th Int. Symp. on Development and Application of Semiconductor Tracking Detectors.

[Abb11] Duccio Abbaneo. Upgrade of the cms tracker with tracking trigger. *Journal of Instrumentation, JINST 6 C12065*, Volume 6, 2011.

[Bar11] Andrew R. Barron. *Chemistry of Electronic Materials.* http://cnx.org/content/col10719/latest/, 2011.

[Ber04] T. Bergauer. Process Quality Control of Silicon Strip Detectors for the CMS Tracker. Master's thesis, Institut für Hochenergiephysik der Österreichischen Akademie der Wissenschaften und Atominstitut der Österreichischen Universitäten, 2004.

[BM05] A. G. Bates and M. Moll. A comparison between irradiated magnetic Czochralski and float zone silicon detectors using the transient current technique. *Nuclear Instruments and Methods in Physics Research A*, 555:113–124, December 2005.

[Car98] Jean-Luc Caron. Overall view of lhc experiments.. vue d'ensemble des experiences du lhc. AC Collection. Legacy of AC. Pictures from 1992 to 2002, May 1998.

[CER] CERN. Lhc. `http://press.web.cern.ch/public/en/LHC/LHCExperiments-en.html`.

[Chi11] A. Chilingarov. Generation current temperature scaling, 2011. Technical note, `http://rd50.web.cern.ch/rd50/doc/recommendations.html`, accessed 20.09.2012.

[D+00] N. Demaria et al. New results on silicon microstrip detectors of cms tracker. *Nuclear Instruments and Methods in Physics Research Section A: Accelerators, Spectrometers, Detectors and Associated Equipment*, 447(1-2):142 – 150, 2000.

[Die] A. Dierlamm. `https://twiki.cern.ch/twiki/pub/CMS/SLHCSensorDevelopment/HPK_measurement_specs_V2.7.pdf`, accessed 17.12.2012.

[Die03] Alexander Dierlamm. Studies on the radiation hardness of silicon sensors, 2003.

[Die09] Alexander Dierlamm. CMS tracker upgrade issues and plans. *Nuclear Instruments and Methods in Physics Research Section A: Accelerators, Spectrometers, Detectors and*

Associated Equipment, 604(1-2):273 – 276, 2009. Proceedings of the 8th International Conference on Position Sensitive Detectors.

[Dra10] M. Dragicevic. The new silicon strip detectors for the cms tracker upgrade, 2010.

[ea92] D. Pitzl et al. Type inversion in silicon detectors. *Nuclear Instruments and Methods in Physics Research Section A: Accelerators, Spectrometers, Detectors and Associated Equipment*, 311(1-2):98 – 104, 1992.

[ea02] S. Braibant et al. Investigation of design parameters for radiation hard silicon microstrip detectors. *Nuclear Instruments and Methods in Physics Research Section A: Accelerators, Spectrometers, Detectors and Associated Equipment*, 485(3):343 – 361, 2002.

[Erf09] Joachim Erfle. Entwicklungen für neue silliziumstreifensensoren und deren qualitätskontrolle. Master's thesis, Institut für Experimentelle Kernphysik, an der Fakultät für Physik der Universität Karlsruhe, 2009.

[FBF+12] W Ferguson, D Braga, J Fulcher, G Hall, J Jacob, L Jones, M Pesaresi, M Prydderch, and M Raymond. The cbc microstrip readout chip for cms at the high luminosity lhc. *Journal of Instrumentation*, 7(08):C08006, 2012.

[Fel09] M. Felcini. The trigger system of the CMS experiment. *Nuclear Instruments and Methods in Physics Research A*, 598:312–316, January 2009.

[Fre04] Stefanie Freudenstein. Materialanalyse und fehlerstudien an hochspannungsfesten silizium-mikrostreifendetektoren für das cms-experiment. Master's thesis, Institut für Experimentelle Kernphysik, an der Fakultät für Physik der Universität Karlsruhe, 2004.

[Fur05] Alexander Furgeri. Quality assurance and irradiation studies, 2005.

[Gia05] F. Gianotti. Physics potential and experimental challenges of the lhc luminosity upgrade, 2005.

[Gor02] I. Gorelov. Electrical characteristics of silicon pixel detectors. *Nuclear Instruments and Methods in Physics Research Section A: Accelerators, Spectrometers, Detectors and Associated Equipment*, 489(1-3):202 – 217, 2002.

[H+08a] F. Hartmann et al. Calibration and measurement specifications. `http://www-ekp.physik.uni-karlsruhe.de/~hartmann/Calibration_and_final_measurement.3.doc`, accessed 17.09.2012, 2008.

[H+08b] F. Hartmann et al. R&D proposal for an R&D project to develop materials, technologies and simulations for silicon sensor modules at intermediate to large radii of a new CMS Tracker for SLHC. R&D Proposal, `http://cmsdoc.cern.ch/cms/electronics/html/elec_web/docs/slhcusg/proposals/08_02.pdf`, accessed 13.03.2012, 2008.

[Hal10] G. Hall. Conceptual study of a trigger module for the cms tracker at slhc. *Nuclear Instruments and Methods in Physics Research Section A: Accelerators, Spectrometers, Detectors and Associated Equipment*, 2010.

[Hal11] Conceptual study of a trigger module for the cms tracker at slhc. *Nuclear Instruments and Methods in Physics Research Section A: Accelerators, Spectrometers, Detectors and Associated Equipment*, 636(1, Supplement):S201 – S207, 2011. 7th International.

[Har08] Frank Hartmann. *Evolution of Silicon Sensor Technology in Particle Physics*. Springer, 2008.

[Hil08] Ulrich Hilleringmann. *Silizium-Halbleitertechnologie: Grundlagen mikroelektrischer Integrationstechnik*. Vieweg+Teubner, 2008.

[HJ01] Louis-Andre Hamel and Manuel Julien. Comments on ramo's theorem. pages 255–263, 2001.

[Hof08] K.-H. Hoffmann. Studien zu Strahlenschäden an Siliziumstreifensensoren für CMS. Master's thesis, IEKP-KA/2008-9, Universität Karlsruhe (TH), 2008.

[JMI06] JMIssMJ. Standard model of elementary particles. `http://upload.wikimedia.org/wikipedia/commons/0/00/Standard_Model_of_Elementary_Particles.svg`, accessed 08.03.2012, June 2006.

[Jun11] Alexandra Junkes. Influence of radiation induced defect clusters on silicon particle detectors, 2011.

[KCM+10] G. Kramberger, V. Cindro, I. Mandic, M. Mikuz, M. Milovanovic, M. Zavrtanik, and K. Zagar. Investigation of irradiated silicon detectors by edge-tct. *Nuclear Science, IEEE Transactions on*, 57(4):2294 –2302, aug. 2010.

[Kit05] Charles Kittel. *Einführung in die Festkörperphysik*. Oldenbourg Wissenschaftsverlag, 2005.

[Kor11] Andreas Kornmayer. Untersuchungen zur signalkopplung an neuartigen siliziumstreifensensorgeometrien. Master's thesis, Institut für Experimentelle Kernphysik, an der Fakultät für Physik der Universität Karlsruhe, 2011.

[Kra12] Manfred Krammer. Instrumentation at the lhc - "the silicon tracking systems". *Nuclear Instruments and Methods in Physics Research Section A: Accelerators, Spectrometers, Detectors and Associated Equipment*, 2012.

[L+01a] G. Lindström et al. Developments for radiation hard silicon detectors by defect engineering - results by the cern rd48 (rose) collaboration. *Nuclear Instruments and Methods in Physics Research Section A: Accelerators, Spectrometers, Detectors and Associated Equipment*, 465(1):60 – 69, 2001. http://www.sciencedirect.com/science/article/pii/S0168900201003473.

[L+01b] G Lindström et al. Radiation hard silicon detectors - developments by the rd48 (rose) collaboration. *Nuclear Instruments and Methods in Physics Research Section A: Accelerators, Spectrometers, Detectors and Associated Equipment*, 466(2):308 – 326, 2001. 4th Int. Symp. on Development and Application of Semiconductor Tracking Detectors.

[Lap12] Marzena Lapka. CMS document 5835-v3. International Masterclass at CMS, `http://cms.web.cern.ch/org/cms-presentations-public`, accessed 19.04.2012, March 2012.

[Lau] Philipp Laube. http://www.halbleiter.org/en/waferfabrication/doping/.

[Lef09] Christiane Lefevre. LHC the guide. *CERN-Broschure-2009-003-Eng*, 2009.

[Lin79] V. A. J. Van Lint. *Mechanisms of Radiation Effects in Electronic Materials.* Univ Microfilms Intl, 1979.

[Lin03] Gunnar Lindström. Radiation damage in silicon detectors. *Nuclear Instruments and Methods in Physics Research Section A: Accelerators, Spectrometers, Detectors and Associated Equipment*, 512(1-2):30 – 43, 2003. Proceedings of the 9th European Symposium on Semiconductor Detectors: New Developments on Radiation Detectors.

[LN62] J. Lindhard and V. Nielsen. Nuclear collisions and ionisation fluctuations in charged particle detectors. *Physics Letters*, 2(5):209 – 211, 1962.

[Lut] Gerhard Lutz. *Semiconductor Radiation Detectors.* Springer.

[M+08] M. Manelli et al. R&D for thin single-sided sensors with hpk. R&D Proposal, `http://cms-tracker.web.cern.ch/cms-tracker/TKSLHC/HPK_Thin%20Sensor.pdf`, accessed 15.03.2012, 2008.

[Mar05] Jacek Marczewski. *Bulk Silicon Detectors of Ionizing Radiation - The role of the depletion layer.* Institute of Electron Technology, Warsaw, 2005.

[MBM11] Steffen Müller, W Boer, and T Müller. *The Beam Condition Monitor 2 and the Radiation Environment of the CMS Detector at the LHC. oai:cds.cern.ch:1319599.* PhD thesis, Karlsruhe, U., Karlsruhe, 2011. Presented on 14 Jan 2011.

[MH08] Ricardo Marco-Hernandez. A portable readout system for microstrip silicon sensors (alibava). In *Nuclear Science Symposium Conference Record, 2008. NSS '08. IEEE*, pages 3201 –3208, oct. 2008.

[MH10] Ricardo Marco-Hernández. A portable readout system for silicon microstrip sensors. *Nuclear Instruments and Methods in Physics Research Section A: Accelerators, Spectrometers, Detectors and Associated Equipment*, 623(1):207 – 209, 2010. 1st International Conference on Technology and Instrumentation in Particle Physics.

[Mol99] Michael Moll. Radiation damage in silicon particle detectors, 1999.

[Mol08] Michael Moll. Recent rd50 developments on radiation tolerant silicon sensors, 2008.

[Moy55] J.E. Moyal. Xxx. theory of ionization fluctuations. *Philosophical Magazine Series 7*, 46(374):263–280, 1955.

[NoPDG11] K. Nakamura and others (Particle Data Group). The review of particle physics. *J. Phys. G 37*, 2011. 075021 (2010) and 2011 partial update for the 2012 edition.

[Pie06] Claudio Piemonte. Device simulations of isolation techniques for silicon microstrip detectors made on p-type substrate. *IEEE Transactions on Nuclear Science*, 2006.

[RBF+12] M Raymond, D Braga, W Ferguson, J Fulcher, G Hall, J Jacob, L Jones, M Pesaresi, and M Prydderch. The cms binary chip for microstrip tracker readout at the slhc. *Journal of Instrumentation*, 7(01):C01033, 2012.

[Ruz00] A Ruzin. Recent results from the rd-48 (rose) collaboration. *Nuclear Instruments and Methods in Physics Research Section A: Accelerators, Spectrometers, Detectors and Associated Equipment*, 447(1-2):116 – 125, 2000.

[Sap94] B. Sapoval. *Physics of Semiconductors*. Springer, 1994.

[SHR+02] V. Savolainen, J. Heikonen, J. Ruokolainen, O. Anttila, M. Laakso, and J. Paloheimo. Simulation of large-scale silicon melt flow in magnetic czochralski growth. *Journal of Crystal Growth*, 243(2):243 – 260, 2002.

[Sut12] Christine Sutton, editor. *CERN Courier*, volume 52. IOP Publishing Ltd, March 2012.

[SvT12] Luka Snoj, Gašper Žerovnik, and Andrej Trkov. Computational analysis of irradiation facilities at the jsi triga reactor. *Applied Radiation and Isotopes*, 70(3):483 – 488, 2012.

[Sze81] S.M. Sze. *Physics of Semiconductor Devices*. Wiley & Sons, 1981.

[Tay] Lucas Taylor. http://cms.web.cern.ch/news/cms-detector-design.

[Thi] Jürgen Thies. Layouteditor. http://www.layouteditor.net/.

[Tre11] Wolfgang Treberspurg. Manufacturing process of silicon strip sensors and analysis of detector structures. Master's thesis, Institut für Hochenergiephysik der Österreichischen Akademie der Wissenschaften und Atominstitut der Österreichischen Universitäten, 2011.

[unk] unknown. http://en.wikipedia.org/wiki/file:wafer_2_zoll_bis_8_zoll_2.jpg.

[Vir03] Tejinder S Virdee. Requirements from experiments in year 1. Technical Report CMS-CR-2003-011, CERN, Geneva, Jun 2003.

[ZJOEC] Ltd Zhejiang Jinsheng Optical Electronic Co. Silicon rods.

Prüfungserklärung

Hiermit versichere ich, dass ich die vorliegende Arbeit selbständig verfasst, noch nicht anderweitig für Prüfungszwecke vorgelegt, keine anderen als die angegebenen Quellen oder erlaubten Hilfsmittel benutzt, sowie wörtliche oder sinngemäße Zitate als solche gekennzeichnet habe.

Karlsruhe, den 1. Februar 2013

Acknowledgement

This thesis covers various topics and I would like to thank all those, without whose help and support I would not have been able to do this work.

I wish to express my sincere gratitude to Prof. Dr. Thomas Müller giving me the opportunity to perform this work, for the freedom he gave me to organize my work and the trust he placed in me. Prof. Dr. Wim de Boer I want to thank for taking the co-reference.

I thank Dr. Frank Hartmann for his support and many fruitful discussions.
My special thanks to Dr. Alexander Dierlamm for being a prudent supervisor, sharing his knowledge and useful suggestions.

I want to thank Dr. Hans-Jürgen Simonis for solving many computer and network problems and the many interesting discussions during coffee break.
For many helping hands, I wish to thank our electronics and workshop team: Tobias Barvich for his never ending helpfulness concerning all mechanical problems and for many interesting insights into our workshop, Felix Bögelspacher for his support in all tasks related to electronics and for the irradiations he prepared and performed and a big thank you to Pia Steck for her patient module assembly and the fast and reliable bonding, next to all the detail work she does along the way.

For helping me carrying out the measurements and keeping the setups running I would like to extend my thanks to my colleagues, as they are in alphabetical order: Lokman Altan, Robert Eber, Joachim Erfle, Sabine Frech, Martin Frey, Stefan Heindl, Ewa Holt, Andreas Kornmayer, Andreas Nürnberg, Mike Schmanau and Martin Strelzyk.

For keeping administrative problems as far away as possible I am thankful to Diana Fellner and Brigitte Gering, also for the nice chats on the wing.

And many thanks to all the students and colleagues of the IEKP who accompanied me over the years. I have found not only nice and helpful colleagues, but also good friends.
The cyclotron crew at Karlsruhe and the reactor crew at Ljubljana I want to thank for their support during the preparation and the execution of the irradiations.
Thanks a lot to all the members of the CEC and the CMS tracker upgrade collaboration for their many contributions to my presentations and work.

This work is supported by the Initiative and Networking Fund of the Helmholtz Association, contract HA-101 ("Physics at the Terascale").

The research leading to these results has received funding from the European Commission under the FP7 Research Infrastructures project AIDA, grant agreement no. 262025.

Finally I would like to warmly thank my parents Katharina and Hans for their unconditional support.

My biggest gratitude goes to my wife Stefanie for supporting me and for always being there for me during all the years we have spent together.

Go placidly amid the noise and haste, and remember what peace there may be in silence.
As far as possible without surrender be on good terms with all persons.
Speak your truth quietly and clearly
and listen to others, even the dull and the ignorant,
they too have their story.

Avoid loud and aggressive persons, they are vexations to the spirit.
If you compare yourself with others, you may become vain and bitter,
for always there will be greater and lesser persons than yourself.
Enjoy your achievements as well as your plans.
Keep interested in your own career, however humble,
it is a real possession in the changing fortunes of time.

Exercise caution in your business affairs,
for the world is full of trickery.
But let this not blind you to what virtue there is,
many persons strive for high ideals,
and everywhere life is full of heroism.

Be yourself.
Especially, do not feign affection.
Neither be cynical about love,
for in the face of all aridity and disenchantment,
it is as perennial as the grass.
Take kindly the counsel of the years,
gracefully surrendering the things of youth.
Nurture strength of spirit to shield you in sudden misfortune.
But do not distress yourself with dark imaginings.
Many fears are born of fatigue and loneliness.
Beyond a wholesome discipline, be gentle with yourself.

You are a child of the universe, no less than the trees and the stars,
you have a right to be here.
And whether or not it is clear to you, no doubt the universe is unfolding as it should.
Therefore be at peace with God, whatever you conceive Him to be,
and whatever your labors and aspirations, in the noisy confusion of life keep peace with your soul.

With all its sham, drudgery, and broken dreams, it is still a beautiful world.
Be cheerful. Strive to be happy.

Max Ehrmann, Desiderata, Copyright 1952.